UNIVERSITY OF SOUTHAMPTON

Aeroacoustic Interactions of Installed Subsonic Round Jets

by

Jack Lawrence

A thesis submitted in partial fulfillment for the
degree of Engineering Doctorate

in the
Faculty of Engineering and the Environment
Institute of Sound and Vibration Research

July 2014

UNIVERSITY OF SOUTHAMPTON

ABSTRACT

FACULTY OF ENGINEERING AND THE ENVIRONMENT
Institute of Sound and Vibration Research

Engineering Doctorate

AEROACOUSTIC INTERACTIONS OF INSTALLED SUBSONIC ROUND JETS

by Jack Lawrence

Additional noise sources are generated when an aircraft engine is mounted beneath a wing. The two main installation sources include: (1) reflection of the exhaust jet mixing noise from the underside of the wing, and (2) interaction between the turbulent jet plume and the trailing edge of the wing, or deployed flap. The strength, directivity and frequency content of these particular sources all serve to increase the time-averaged flyover aircraft noise level heard on the ground by residents beneath the flight path. As the bypass ratio and nacelle diameter of modern turbofan engines continues to increase, constraints on ground clearance are forcing under-wing-mounted engines to be coupled more closely to the wing and flap system, which, in turn, serves to accentuate both of these noise sources. Close-coupled nacelle-airframe designs are now a critical issue surrounding efforts to meet the future environmental targets for quieter civil aircraft.

This research is principally aimed at understanding and predicting the ground-propagating noise generated by the latter of these two installed jet noise sources. In order to characterise the jet-surface interaction noise source, however, it is first necessary to isolate it. A small $1/50^{\text{th}}$ model-scale acoustic experiment, therefore, is conducted in a semi-anechoic university laboratory using a single stream jet installed beneath a flat plate. Both far-field acoustic and near-field plate surface pressure data are measured to investigate the jet-surface interaction noise source. Results from this fundamental experiment are then used to help drive a larger, and more realistic, $1/10^{\text{th}}$ model-scale test campaign, at QinetiQ's Noise Test Facility, where 3D wing geometry effects, Reynolds number scaling effects and static-to-flight effects are investigated. A jet-flap impingement tonal noise phenomenon is also identified and investigated at particularly closely-coupled jet-wing configurations. Finally, the first version of a fast, semi-empirical engineering tool is developed to predict the additional noise caused by jet-wing interaction noise, under static ambient flow conditions. It is hoped that this tool will serve to inform future commercial aircraft design decisions and, thus, will help to protect the acoustic environment of residents living beneath flight paths.

"If a book falls on your head then you've only got yourshelf to blame."

Anon

Contents

List of Figures

List of Tables

Declaration of Authorship

I, Jack Lawrence, declare that this thesis entitled, 'Aeroacoustic Interactions of Installed Subsonic Round Jets' and the work presented in it are my own. I confirm that:

- This work was done wholly or mainly while in candidature for a research degree at this University.
- Where any part of this thesis has previously been submitted for a degree or any other qualification at this University or any other institution, this has been clearly stated.
- Where I have consulted the published work of others, this is always clearly attributed.
- Where I have quoted from the work of others, the source is always given. With the exception of such quotations, this thesis is entirely my own work.
- I have acknowledged all main sources of help.
- Where the thesis is based on work done by myself jointly with others, I have made clear exactly what was done by others and what I have contributed myself.

Signed: _____

Date: _____

Acknowledgements

This research is sponsored by EPSRC and QinetiQ and has been carried out, in part, at the Rolls-Royce University Technology Centre, within the Institute of Sound and Vibration Research (ISVR), at the University of Southampton. I owe significant thanks to the UK Technology Strategy Board for choosing to fund the SYMPHONY project and my Engineering Doctorate degree therein.

I would also like to acknowledge several key individuals who have made this research possible and who have kept my enthusiasm alive throughout. First, and foremost, to my academic supervisor, Dr. Rod Self, I thank you for your constant support, your generosity, your sense of humour and, above all, your patience...your bottle of whisky is in the post! Secondly, to Dr. Mahdi Azarpeyvand, thank you for your support and friendship throughout my degree - you have taught me a great deal indeed. Thirdly, to my industrial supervisor, Mr. Craig Mead, and to all of my other friends at the NTF, thank you so much for supporting me through what was an incredibly intense but extremely exciting year at QinetiQ. I will forever appreciate the colossal team effort that goes into the successful completion of such a large and complex test campaign. Fourthly, to Mr. Richard Pinker, thank you for always taking the time to pass on your invaluable expertise, particularly at the start of my degree when I was totally incompetent! My thanks also go to Dr. Paul Strange and Dr. Kevin Britchford at Rolls-Royce, Derby, and to Mr. Jérôme Huber at Airbus, Toulouse, for the insightful technical discussions and for ensuring my research always remained relevant to the real world.

I strongly believe that my happiest experiences are those shared with great people. To all of the lecturers, technicians and friends at the ISVR (you know who you are!), you have all made studying here a total pleasure, so thank you. And to my family, you guys are pretty amazing too! Thank you for your constant positivity and belief in me. Finally, to Héloïse - I can only imagine how awful it must have been to live with me over the past year. You are my rock and I definitely could not have done this without you. I thank you with all my heart...

Abbreviations

5HP	**5** **H**ole Aerodynamic **P**robe
ACARE	**A**dvisory **C**ouncil for **A**eronautics **R**esearch in **E**urope
ALF	**A**erodynamic **L**ogging **F**acility
AR	**A**rea **R**atio
BEM	**B**oundary **E**lement **M**ethod
BPF	**B**lade **P**assing **F**requency
BPR	**B**y**p**ass **R**atio
CAA	**C**ivil **A**viation **A**uthority
CAD	**C**omputer-**A**ided **D**esign
CFD	**C**omputational **F**luid **D**ynamics
CNC	**C**omputer **N**umerical **C**ontrol
DOAK	**Doak** Laboratory (University of Southampton, UK)
EPNL	**E**ffective **P**erceived **N**oise **L**evel
ISVR	**I**nstitute of **S**ound and **V**ibration **R**esearch
JFI	**J**et-**F**lap **I**mpingement
JSI	**J**et-**S**urface **I**nteraction
JSR	**J**et-**S**urface **R**eflection
LDA	**L**aser **D**oppler **A**nemometry
LE	**L**eading **E**dge
LES	**L**arge **E**ddy **S**imulation
LVDT	**L**inear **V**ariable **D**ifferential **T**ransformer
MTOM	**M**aximum **T**ake-**o**ff **M**ass
NTF	**N**oise **T**est **F**acility (QinetiQ, Farnborough, UK)
PIV	**P**article **I**mage **V**elocimetry
PR	**P**ressure **R**atio

PSD	**P**ower **S**pectral **D**ensity
RANS	**R**eynolds-**A**veraged **N**avier-**S**tokes
SEmp	**S**emi-**Emp**irical Installed Jet Noise Prediction Model
SHW	**S**tationary **H**ot-**W**ire
SMHW	**S**huttle-**M**ounted **H**ot-**W**ire
SPL	**S**ound **P**ressure **L**evel
SYMPHONY	**SY**stem **M**anufacturing and **P**roduct design t**H**rough c**O**mponent **N**oise technolog**Y**
TE	**T**railing **E**dge
TBL	**T**urbulent **B**oundary **L**ayer
TDC	**T**op **D**ead **C**entre
TR	**T**emperature **R**atio
TSB	**T**echnology **S**trategy **B**oard
OASPL	**O**vera**l**l **S**ound **P**ressure **L**evel
UWM	**U**nder-**W**ing-**M**ounted
VR	**V**elocity **R**atio
WPS	**W**ing **P**ositioning **S**ystem
WSS	**W**ing **S**upport **S**tructure

Physical Constants

Acoustic reference pressure	p_{ref}	=	20 μPa
Kinematic viscosity of dry air (at 20°C)	ν	=	1.4×10^{-6} m^2 s^{-1}
Specific gas constant for dry air	R_c	=	287.1 J kg^{-1} K^{-1}

Symbols

Roman			
a_0	ambient speed of sound	m s^{-1}	pg. 20
a_1	sub-peak power law exponent for asymptotic weighting function		pg. 84
a_2	sur-peak power law exponent for asymptotic weighting function		pg. 84
b	airfoil half-chord	m	pg. 41
B_u	velocity decay constant (empirical)		pg. 15
c	airfoil chord	m	pg. 41
$C_2(x)$	Fresnel integral		pg. 43
C_K	Kolmogorov's constant		pg. 61
C_p	specific heat capacity at constant pressure	J $kg^{-1}K^{-1}$	pg. 29
D	jet nozzle exit inner diameter	m	pg. 15
D_{ref}	reference jet nozzle exit inner diameter	m	pg. 72
$D(\theta_e)$	polar directivity factor (relative to mid-span point on trailing edge)	m	pg. 49
e_{ij}	$(\text{i,j})^{\text{th}}$ component of the viscous stress tensor of a fluid		pg. 20
$E(x)$	error function		pg. 48
$E^*(x)$	complex error function		pg. 43
f	cyclic frequency	Hz	
h	radial distance from jet geometric centreline to wing/flap trailing edge	m	pg. 51
$H(f)$	Heaviside function		pg. 31

$H_a(\omega)$	acoustic transfer function between loudspeaker and transducer		pg. 185
I	far-field sound intensity	W m^{-2}	pg. 23
J_c	jet exit conditions		pg. 172
k	acoustic wavenumber	m^{-1}	pg. 27
K	aerodynamic wavenumber	m^{-1}	pg. 42
$\bar{K}$	non-dimensional aerodynamic wavenumber		pg. 42
K_1	streamwise aerodynamic wavenumber	m^{-1}	pg. 43
$\bar{K_1}$	non-dimensional streamwise aerodynamic wavenumber		pg. 45
K_2	spanwise aerodynamic wavenumber	m^{-1}	pg. 43
$\bar{K_2}$	non-dimensional spanwise aerodynamic wavenumber		pg. 45
l	axial distance from nozzle lip to wing/flap trailing edge	m	pg. 51
L	total plate length	m	pg. 90
$\mathfrak{L}$	characteristic length-scale	m	pg. 33
M	jet exit aerodynamic Mach number		pg. 65
M_a	jet exit acoustic Mach number		pg. 66
$M_{a_{\text{ref}}}$	reference jet exit acoustic Mach number		pg. 72
p	fluid pressure	Pa	pg. 20
p'	fluctuating component of pressure	Pa	pg. 20
P_a	far-field acoustic power	W	pg. 23
r	far-field observer distance from source at emission time to observer at reception time	m	pg. 32
r_0	distance from source to field point	m	pg. 36
r_e	distance from field point to trailing edge	m	pg. 36
r_{lip}	radial distance from jet lip-line	m	pg. 60
r_s	shortest distance from nominal edge of jet shear layer to microphone	m	pg. 67
R	far-field observer distance from the centre of the (bypass) nozzle exit plane	m	pg. 23
R_0	axial quadrupole source size	m	pg. 61

R_e	distance from the source point to the field point	m	pg. 37
R'_e	distance from the image source point to the field point	m	pg. 37
R_s	shortest distance from the source point to the field point passing via an edge	m	pg. 38
Re	Reynolds number		pg. 15
$s_{\text{kulite}}(\omega)$	Kulite surface pressure transducer sensitivity		pg. 185
$s_{\text{ref}}(\omega)$	reference microphone sensitivity		pg. 183
S	total plate span	m	pg. 47
$S_2(x)$	Fresnel integral		pg. 43
St_D	Strouhal number based upon the jet diameter and the jet exit velocity		pg. 24
St_r	Strouhal number based upon the radial distance from the jet lip-line and the jet exit velocity		pg. 78
T_0	ambient chamber temperature	K	pg. 66
T_s	jet static temperature	K	pg. 65
T_t	jet total temperature	K	pg. 65
T_{ij}	Lighthill stress tensor	N m^{-2}	pg. 20
U	mean flow velocity	m s^{-1}	pg. 19
U_c	mean flow convection velocity	m s^{-1}	pg. 114
U_{jc}	mean jet centreline velocity	m s^{-1}	pg. 15
u'	fluctuating component of flow velocity	m s^{-1}	pg. 19
v	acoustic particle velocity	m s^{-1}	pg. 23
V_1	loudspeaker voltage	V	pg. 185
V_2	transducer voltage	V	pg. 185
V_{ref}	output reference transducer voltage	V	pg. 185
W_1	asymptotic weighting function		pg. 84
W_2	polynomial-exponential weighting function		pg. 85
x	axial distance from jet nozzle exit plane (+/ve downstream)	m	pg. 15
x_0	axial distance from jet nozzle exit plane to virtual jet origin (based on β_1)	m	pg. 15

X	non-dimensional axial distance from field point to trailing edge		pg. 42
y	spanwise radial distance from centreline of jet nozzle	m	pg. 15
$y_{0.5}$	radial distance from the jet centreline to the point at which the velocity is half that of the centreline velocity	m	pg. 15
y_b	jet shear layer half-thickness	m	pg. 16
y_{b_1}	jet shear layer half-thickness upstream of the potential core	m	pg. 17
y_{b_2}	jet shear layer half-thickness downstream of the potential core	m	pg. 17
Y	non-dimensional spanwise distance from field point to trailing edge		pg. 45
z	vertical radial distance from centreline of jet nozzle	m	pg. 15
z_0	vertical distance from source point to field point	m	pg. 36
z_e	vertical distance from field point to trailing edge	m	pg. 36
Z	non-dimensional vertical distance from field point to trailing edge		pg. 42
Z_0	characteristic acoustic impedance of air	Pa s m^{-1}	pg. 23

Greek

α	normalized turbulence intensity		pg. 40
β_1	jet spreading angle upstream of the end of the potential core	degrees	pg. 14
β_2	jet spreading angle downstream of the end of the potential core	degrees	pg. 14
γ	ratio of specific heats		pg. 29
Γ^2	acoustic coherence function		pg. 183
δ	deployed flap angle (relative to the wing chord)	degrees	pg. 51
δ_{ij}	Kronecker delta function		pg. 20
$\delta(x)$	Dirac delta function		pg. 22

ϵ	dissipation rate of energy per unit mass	$m^2\ s^{-3}$	pg. 61
ϵ_1	streamwise separation between surface transducers	m	pg. 114
ϵ_2	spanwise separation between surface transducers	m	pg. 115
ζ	integration limit angle	degrees	pg. 38
η	ratio of free stream velocity to convection velocity		pg. 43
θ_j	polar field point angle (relative to the jet axis)	degrees	pg. 15
θ_0	polar source point angle (relative to the trailing edge)	degrees	pg. 36
θ_e	polar field point angle (relative to the trailing edge)	degrees	pg. 36
λ	acoustic wavelength	m	
λ_h	hydrodynamic/instability wavelength	m	pg. 60
Λ_y	spanwise correlation length	m	pg. 115
μ	dynamic viscosity	$kg\ s^{-1}\ m^{-1}$	pg. 20
μ_f	normalised frequency		pg. 84
ν	kinematic viscosity	$m^2\ s^{-1}$	pg. 15
ξ	flight stream incident flow angle (relative to the jet axis)	degrees	
$\pi(k)$	pressure-spectrum function		pg. 61
$\Pi_{p_1p_1}$	auto-spectral density function		pg. 183
ρ	fluid density	$kg\ m^{-3}$	pg. 20
ρ'	fluctuating component of density	$kg\ m^{-3}$	pg. 20
σ	eddy correlation radius	m	pg. 20
τ	retarded time (emission time)		pg. 22
φ	phase angle	rad	pg. 113
ϕ	local azimuthal observer angle	degrees	pg. 15
ϕ_s	velocity potential		pg. 61
Φ	NTF global chamber azimuthal observer angle	degrees	pg. 134
$\Psi_{p_1p_2}$	cross-spectral density function		pg. 183
ω	angular frequency	$rad\ s^{-1}$	

Subscripts

f	flight stream
i, j, k	local vector coordinates
inst	installed jet
isol	isolated jet
j	single stream jet
jfi	jet-flap interaction
jsi	jet-surface interaction
jsr	jet-surface reflection
p	primary (core) jet
p_1	near-field trailing edge surface pressure signal
p_2	far-field pressure signal
s	secondary (bypass) jet

For Anderson and Juan...

Chapter 1

Introduction

Every aircraft engine has a specific acoustic signature that can be measured in isolation either directly, on a full-size test bed, or indirectly, in a model-size test facility. When an engine is installed on an aircraft, however, its acoustic signature is altered. Both the modification of existing noise sources and the addition of new sources help explain this difference. Examples of such effects include: (1) reflection and shielding of sound by the airframe, (2) attenuation, or blockage, of sound as it passes through the hot, turbulent jet exhaust plume, and (3) generation of sound from the aeroacoustic interaction between the exhaust jet and the wing and flap system. Collectively, these effects are referred to as *installation effects* and their understanding and prediction is very important both academically, within the field of aeroacoustics, and socially, for those adversely affected by aircraft noise.

The principal aim of this thesis is to investigate the latter of the above examples - specifically the jet-surface interaction (JSI) and jet-flap impingement (JFI) noise sources - for closely-coupled under-wing-mounted (UWM) aircraft. As the aviation industry strives to reduce its acoustic footprint, this research is funded to predict and reduce noise from future aircraft. Two model-scale experimental test campaigns, therefore, were designed to address this problem. The data have been examined and a semi-empirical prediction tool has been developed. The following section details an outline of the thesis highlighting the key results and original contributions.

1.1 Thesis Outline

In the following chapter, a brief review of aircraft noise is given. A literature review of isolated jet noise is then presented in order to set the problem of installed jet noise in context. The reader is reminded of the key outcomes of Lighthill's fundamental concept of jet noise generation and then Lilley's subsequent formulation for parallel shear flows. A brief review of the source distribution and directivity of isolated jets is also introduced. The fluid-structure interaction noise literature is then summarised - from Curle's theory of aerodynamic surface noise generation to Ffowcs-Williams and Hall's formulation for trailing edge noise and then from Amiet's trailing edge noise model to Roger and Moreau's back-scattering correction. Finally, a critical review of experimental installed jet noise literature is presented together with a more detailed formulation of the current installed jet noise problem.

Chapter 3 examines the jet source in isolation. Some time is spent detailing the pressure field generated by a subsonic, single-stream, unheated, axisymmetric, round jet since it will later play an important role in the analysis and prediction of the installed jet noise sources. The first novel aspect of work is also presented here - a revised definition of the 'near-field' of an isolated jet that includes an acoustic Mach number dependency. Additionally, a semi-empirical hydrodynamic pressure spectrum prediction tool is also detailed here.

In Chapter 4, the author discusses the design of, and results from, a $1/50^{\text{th}}$ model-scale, static, installed jet acoustic experiment. This fundamental experiment was carried out in the anechoic, jet noise Doak Laboratory (DOAK), at the University of Southampton's Institute of Sound and Vibration Research (ISVR), UK. In short, a large flat plate was installed next to a single-stream jet (parallel to the jet axis). The trailing edge of the plate was then positioned at various axial and radial locations from the jet nozzle exit. The jet-surface interaction noise source, SPL_{jsi}, is then successfully separated from both the isolated jet mixing noise, SPL_{isol}, and the jet-surface reflection noise, SPL_{jsr}, sources, whereupon both near-field and far-field jet-surface interaction spectral trends are discussed in detail. The second novel aspect of work is presented here - experimental evidence is provided to match the jet-surface interaction noise polar directivity pattern to a semi-empirical expression derived by Miller [1].

In Chapter 5, the author discusses the design and completion of a much larger $1/10^{\text{th}}$-scale installed jet experimental test campaign at QinetiQ's Noise Test Facility (NTF), in Farnborough (UK). Far-field acoustic results are discussed in detail including a read-across between the DOAK and NTF facilities. The fourth novel aspect is presented here concerning the Reynolds number scaling effects that exist

between small university laboratories and large industrial test facilities. Novel results are also discussed concerning the propagation path taken by the jet surface interaction noise source over the topside of the wing.

In Chapter 6, a new tonal noise installation effect is identified over a particular range of jet-flap impingement configurations and jet flow conditions. Following a brief literature review, the important geometrical and aerodynamic parameter ranges are detailed followed by a discussion of the mechanism involved. Suggestions are also made regarding techniques capable of attenuating such a tonal noise source.

Chapter 7 introduces a new, fast and robust semi-empirical engineering tool for predicting the additional far-field installed jet noise produced by a single-stream, unheated jet installed in close proximity to a cruise wing, under static ambient flow conditions. The model is developed using the small model-scale DOAK experimental data and is validated against the larger model-scale NTF experimental data. The accuracy, limitations and opportunities for improvement are then discussed in detail. A higher level framework and strategy for future jet installation noise prediction is also presented. The framework is dependent both on the inputs available and the output fidelity required by the user.

Finally, in Chapter 8, a number of conclusions relating to the work are presented together with a list of topics for future research.

Chapter 2

Background and Problem Specification

This chapter presents background information on aspects of aircraft noise and sets the jet installation noise problem in context. The installed jet problem is formulated after a review of both isolated jet and trailing edge noise literature.

2.1 Aircraft Noise

2.1.1 Aircraft noise trends

Aircraft cause a significant amount of environmental noise pollution, especially around airports. As an ever-increasing number of people are demanding to fly (see Figure 2.1), both the size of airports and the number of aircraft in the skies are increasing. The protection of communities surrounding airports from aircraft noise, therefore, has become a major priority for aircraft manufacturers and aviation authorities alike. Even as aircraft size and power has increased, consistent noise reduction at source has been achieved over the last fifty years, principally via an increase in engine bypass ratio (see Figure 2.2). It is, however, becoming increasingly challenging for the aviation industry to keep within the stringent noise regulations set by the International Civil Aviation Organisation (ICAO).

2.1.2 Aircraft noise regulation and future targets

ICAO [3] has suggested a four-pronged management strategy to combat aircraft noise around airports: (1) reduction of noise at source, (2) land-use planning and

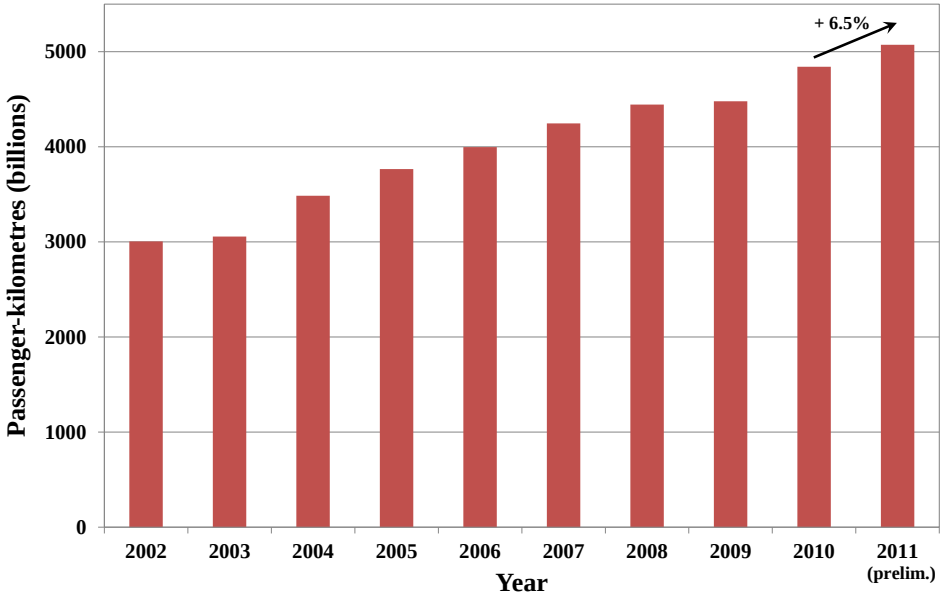

FIGURE 2.1: Total scheduled traffic passenger-kilometres travelled between 2002-2011. [Based on data from reference [2]].

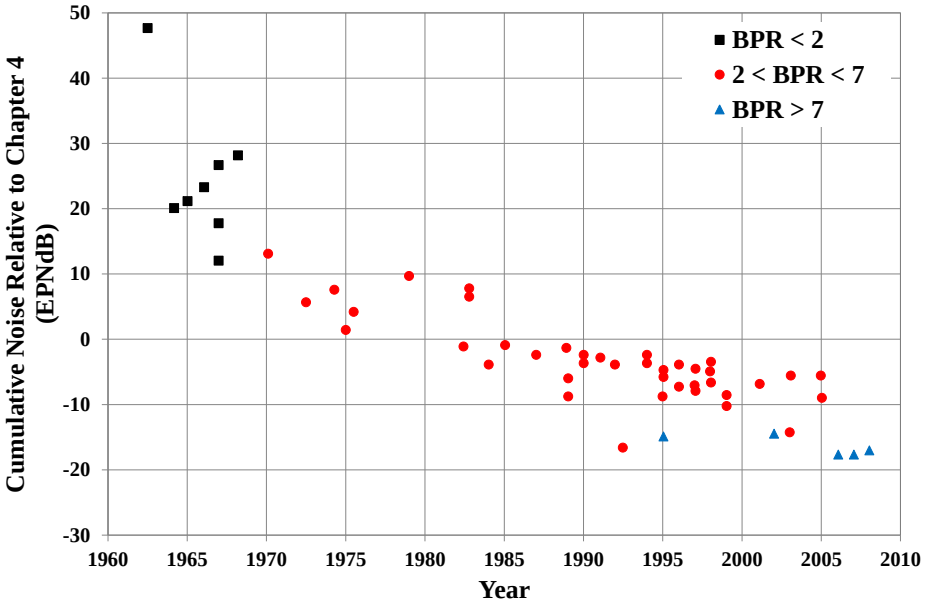

FIGURE 2.2: Progress made in noise reduction at source since implementation of aircraft noise standards - for engine bypass ratio (BPR). [Based on data from ICAO [3]].

management, (3) noise abatement operational procedures, and (4) operating restrictions. In order to encourage noise reduction at source and to monitor and regulate aircraft noise, the Effective Perceived Noise Level (EPNL) metric is used. EPNL is a measure of human annoyance to aircraft noise. It accounts for the human response to sounds with a particular spectral shape, intensity, tonal content and duration. As set by the US Federal Aviation Administration (FAA), in FAR Part 368

[4], and ICAO, in Annex 16.9 [5], each aircraft is certified according to three EPNL values measured at three in-flight reference positions: flyover, sideline and approach (see Figure 2.3). Flyover is defined as a point 6.5 km from the brake release point directly beneath the take-off flight path. The sideline measurement is taken during take-off at the maximum velocity 450 m from the runway axis. The approach position is set 2 km back from the runway threshold directly under the approach flight path. The engines operate at full power along the runway and during the first stage of ascent until a minimum safe altitude has been reached. Sideline measurements, therefore, usually have the highest EPNL values. The aircraft can then continue to climb at a lower thrust setting, known as *cutback*, in order to reduce the noise level at the flyover reference position. For successful certification, the three measured EPNLs of every aircraft must be below a particular cumulative value. This maximum allowable level depends on the Maximum Take-off Mass (MTOM) and the age, or *chapter*, of the aircraft, see Figure 2.4.

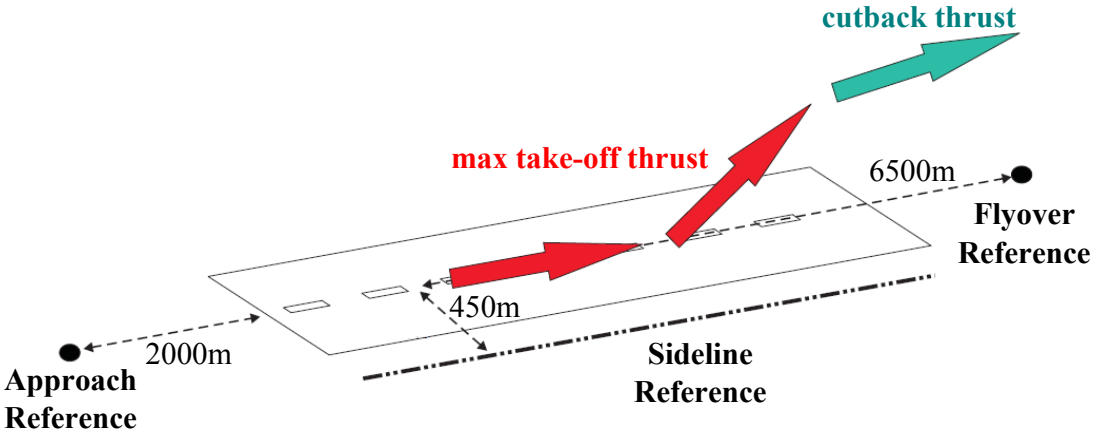

FIGURE 2.3: Aircraft certification measurement positions

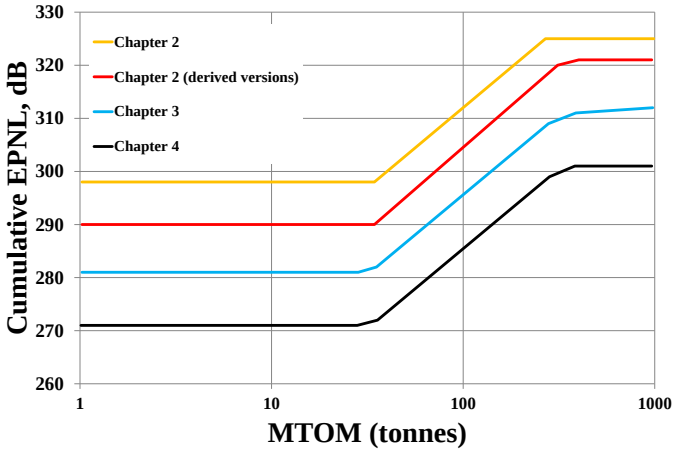

FIGURE 2.4: ICAO cumulative EPNL limits for different aircraft chapters versus Maximum Take-Off Mass [Based on data from reference [6]]

Going forward, regulatory establishments and pan-governmental agencies have set aggressive targets to limit aircraft noise and emissions. The Advisory Council for Aeronautics Research in Europe (ACARE), for example, has set several specific targets for the aviation industry to reach by 2020 [7]. As far as noise is concerned, the aim is to reduce the overall certification EPNL value for new aircraft by 50% whilst increasing aircraft capacity three-fold (compared with 2007 statistics). Figure 2.5 illustrates how technological advances in noise efficiency have already helped to increase the capacity transported without increasing the overall EPNL.

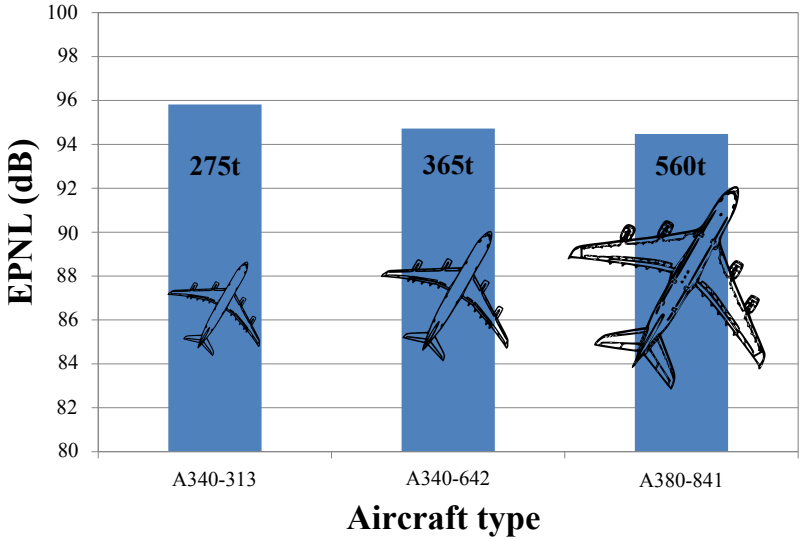

FIGURE 2.5: Increase in aircraft capacity (tonnes) versus effective perceived noise level (EPNL). [Based on data from reference [8]].

ACARE's 2020 target has now been updated by the European Commission's 2050 vision [9]. The current strategy focusses on: (1) optimising both the design and operation of current generation aircraft, and (2) investing in emerging technologies, such as close-coupled under-wing-mounted (UWM) aircraft and open rotors. Although the open rotor addresses the issues of fuel consumption and emissions, promising a fuel saving of up to 20%, the question of noise presents a much greater challenge because there is no nacelle to attenuate the sound generated by the contra-rotating propellers. The trade-off between these three factors is a constant battle for the aviation industry.

2.1.3 Aircraft noise sources

The noise produced by a modern turbofan-powered aircraft is caused both by the airframe and the engine. The high lift devices and landing gear generate most of the aeroacoustic airframe noise, but the engine generates noise in several different ways: (1) as air is drawn in by the fan, (2) as it passes through the compressor, the

combustor and the turbine, and (3) as it is exhausted at the rear of the engine. A more detailed breakdown of these noise sources is presented in the following two sections.

2.1.3.1 Airframe noise sources

The airframe, or non-propulsive, noise sources on a conventional civil aircraft result from flow passing over three main components: (1) the landing gear, (2) the leading edges of the slats and (3) the side and trailing edges of the clean wing, deployed flap and tail [10]. A 'clean' wing (or 'clean' aircraft) is one whose high-lift devices (and undercarriage) are stowed. Of all of these three components, the landing gear is the dominant source of airframe noise on approach [11]. As the ambient airflow passes over the various cavities and sharp edges within and around the undercarriage, the flow separates inducing an unsteady force onto the surface and producing a turbulent wake downstream of the separation point. Noise is generated from this induced surface force and its intensity varies approximately with the sixth power of the aircraft speed [12].

The second major source of airframe noise concerns unsteady flow within the leading edge slat region of the aircraft's high-lift system. Lockard and Lilley [13] hypothesise the mechanism for tonal slat noise as being the resonance between the vortex shedding from the trailing edge of the slat and the gap between the slat and the main wing section. Instabilities in the slat cove shear layer are also believed to produce the broadband component of slat noise.

Third and finally, flap noise has been seen to originate from two different parts of the flap. The first region relates to separated airflow close to the flap side edges. Experiments by Guo *et al.* [14–16] and Stoker *et al.* [17] show that strong vortices form due to the sharp discontinuity in lift between the deployed and undeployed flap portions of the wing. The second part of the flap concerns the trailing edge (TE). TE noise originates from a scattering of a convecting hydrodynamic pressure field by an edge. Various experiments [18] and theories [19, 20] on trailing edge noise demonstrate that the far-field noise intensity varies approximately with the fifth power of the free-stream velocity. We will revisit this particular source in more detail later on, in Section 2.3.2.

Measurements of airframe noise show that the landing gear, leading edge slats and flap side edges are the dominant airframe noise sources for a typical civil aircraft on approach [17, 21]. To give some idea, the deployment of the high-lift devices and the landing gears can increase the overall airframe noise level of a clean (i.e. undeployed flap) aircraft by approximately 10 dB [12].

2.1.3.2 Engine noise sources

A modern turbofan engine generates different types of noise from several components. Figure 2.6 shows the main noise sources of a modern turbofan engine together with the character of noise each generates. Rotating machinery like the fan, compressor and turbine will generate both tonal and broadband noise. Tones, for example, are generated at multiples of the Blade Passing Frequency (BPF) when a rotor blade interacts with a non-uniform incident airflow. The tonal frequency, therefore, depends upon the number of rotor blades and the rotation speed. If stator vanes exist downstream from the rotor, a fluctuating vane loading will be induced by the rotor wakes, which can also be linked directly to noise emission.

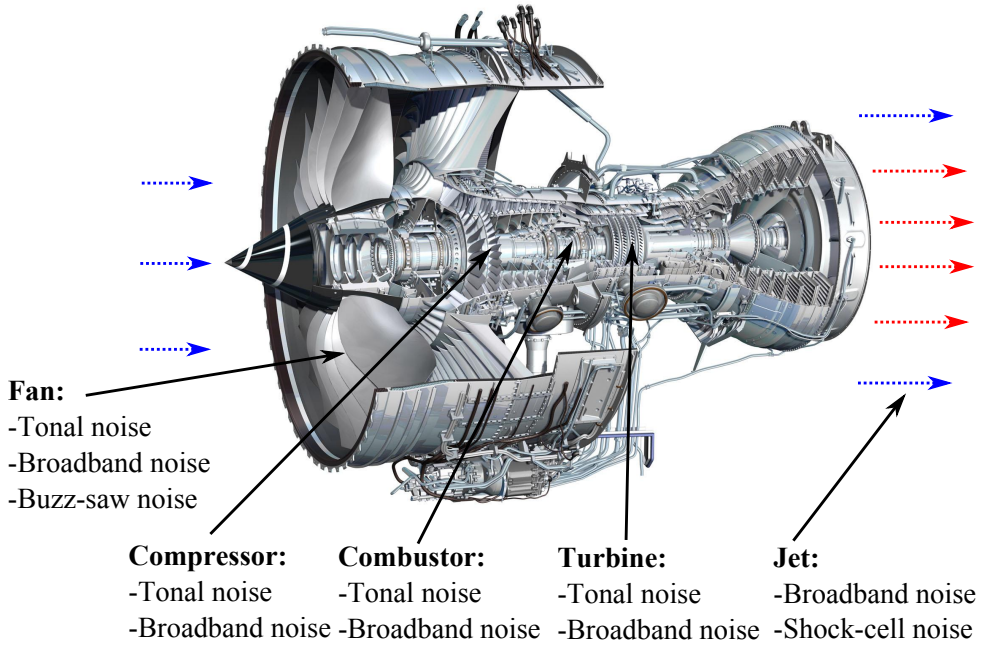

FIGURE 2.6: Cutaway of a Rolls-Royce Trent 1000 turbofan engine detailing the main noise generating components and the character of each noise source

At supersonic relative fan tip speeds, different tones occur at harmonics of the shaft rotation frequency. The supersonic relative speed of the inlet flow to the fan blade creates shocks, which results in *buzz-saw noise*.

Fans also produce broadband noise due to three principal mechanisms: (1) rotor-stator interaction noise, (2) trailing edge noise and (3) inlet turbulence-rotor tip interaction noise. Turbulent flow, which either impinges upon the leading edge of a stator or interacts with the trailing edge or the tip of a blade, will induce fluctuating loading forces on a surface to create a fluctuating pressure field that radiates as noise.

The exhaust flow, or jet, at the rear of the engine also creates broadband noise when both the hot, fast core and the slow, cold bypass flows mix with each other and the

ambient air stream. The jet noise source is distributed in nature, which means that the highest frequency noise, created by the smaller eddies, is generated closest to the nozzle. While small eddies exist throughout the jet, those closer to the nozzle are more energetic. Lower frequency noise is generated further downstream as the eddies 'roll-up' and increase in size. This jet mixing process will be discussed in more detail in Section 2.2.2. Supersonic jet flows can also produce both a tonal and a broadband shock-associated high frequency noise, however, most of today's civil aircraft engine nozzles are designed in such a way as to prevent this.

Fuel ignited within the combustor generates both tonal and broadband noise. The tonal component includes both spiralling waves (or modes) and thermo-acoustic effects. Combustion noise, however, is more prevalent when the aircraft is in-flight, when jet noise levels are significantly reduced. Other secondary noise sources warrant consideration at certain times in the flight cycle. One such example is bleed valve noise, which occurs when high pressure air from the engine core is discharged into the bypass duct on approach.

Acoustically absorbent liners within the nacelle casing can, themselves, also become additional noise sources if not maintained sufficiently. 'Bald' patches, for example, can scatter noise from otherwise cut-off modes into cut-on modes, which propagate to the far-field.

Different sources tend to dominate at different times in the flight cycle. The following section provides a component breakdown of the various noise source levels at the take-off and approach certification measurement positions.

2.1.3.3 Significance of different sources

Figure 2.7 shows a breakdown of the relative EPNL values of the main noise sources present on a typical modern medium range turbofan-powered aircraft at the take-off, sideline and approach certification positions. As one might expect, during acceleration on the ground at take-off, the dominant noise source is the engine. However, due to the advent of high-bypass ratio turbofan engines and other achievements in low-noise engine technology, the airframe noise level of conventional transport aircraft is now comparable to the engine noise at approach. Any further reduction in aircraft noise on approach, therefore, can only be achieved if both engine and airframe noise are reduced simultaneously.

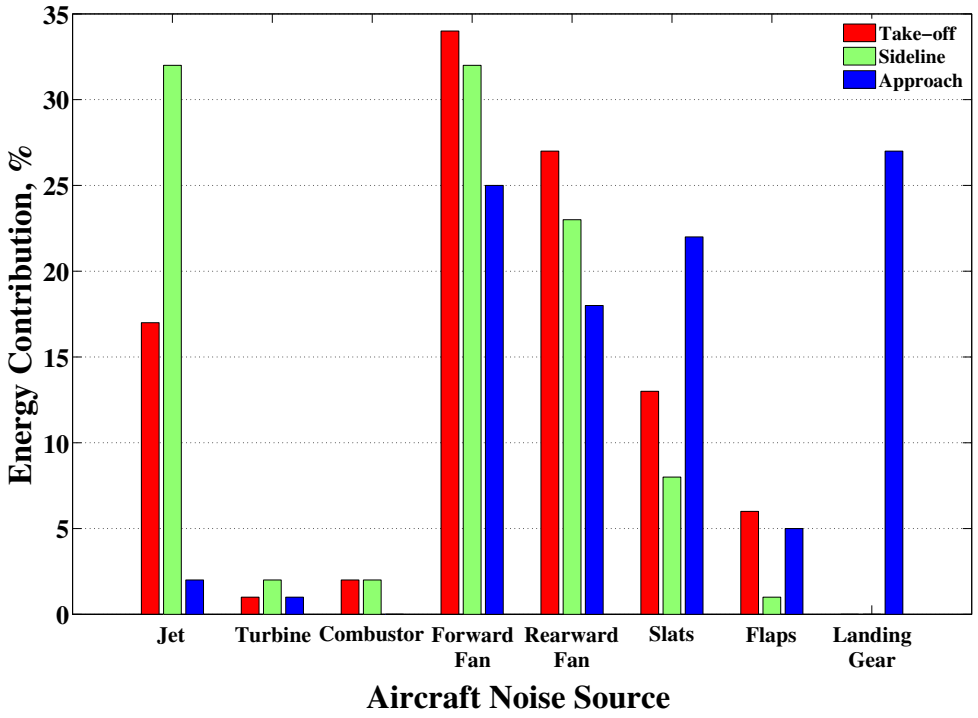

FIGURE 2.7: A breakdown of the relative noise levels of components of a typical modern medium range turbofan-powered aircraft at the take-off, sideline and approach certification positions. [Based on data courtesy of Airbus].

2.1.4 Installation effects

When an engine is installed beneath the wing of an aircraft (see Figure 2.8), additional noise is generated and measured on the ground at all certification measurement positions. All engine sources will incur a degree of installation effect, however, those situated at the rear of the engine are particularly affected due to the presence of the wing and flap surfaces. Three main jet installation effects exist on a modern turbofan aircraft. The first effect is a broadband, high frequency reflection of the jet mixing noise from the underside of the wing - jet-surface reflection (JSR) noise, SPL_{jsr}. The second effect is a relatively low frequency broadband source generated by the passing of the jet's near pressure field over the trailing edge of the wing - jet-surface interaction (JSI) noise, SPL_{jsi}. The third installed jet effect is a mid-frequency noise whose origin is currently contested. It is either created by the impact, or 'scrubbing', of the turbulent flow upon the deployed flap surface or by the reflection of the jet mixing noise from the angled flap surface. For the purposes of this thesis, this third effect will be referred to as jet-flap interaction (JFI) noise, SPL_{jfi}. All three effects are broadband in character however JFI noise can also contain a tonal component at certain nozzle-airframe configurations and at particular jet operating conditions. Research into these latter two effects forms the core of this thesis. A more detailed review of the

literature of jet installation effects will be presented later in Section 2.4. The following section, however, introduces the isolated jet noise source, SPL_{isol}, itself.

FIGURE 2.8: An under-wing-mounted modern turbofan jet engine [photo courtesy of Rolls-Royce plc.]

2.2 Isolated Jet Literature Review

In this section, the jet is examined in more detail since it forms an integral part of the installation effects problem. The sound generated by the flow is then discussed with reference to Lighthill's acoustic analogy and scaling laws. Lilley's adjusted equation for parallel sheared flow is then briefly introduced too. Some time is taken to discuss the source distribution and directivity of jet noise because these properties are important in determining the characteristics of jet installation sources.

2.2.1 Jet aerodynamics

The simplest example of a jet is the discharge of a fluid with a uniform initial velocity profile through an orifice into a quiescent, homogeneous ambient medium, see Figure 2.9. Initially, the layer between the two fluids has very small thickness, however, flow instabilities cause strong turbulent fluctuations, or eddies, to form. Thus, a transverse transfer of momentum and heat, or 'mixing', occurs between the jet and the ambient medium. The 'potential core' is an initial region of nominally laminar, parallel flow. The region of sheared flow between the potential core and the ambient fluid is called the turbulent boundary (or shear) layer and it continues to grow with axial distance downstream from the nozzle as more ambient fluid is entrained into the jet. The initial entrainment (or spreading) rate over the length of the potential core is defined by the angle β_1. In this initial mixing region, the jet has a 2-dimensional self-similarity. As one moves downstream, the non-viscous potential core gradually reduces until, at approximately five nozzle diameters, D, downstream, it has completely disappeared and the start of the transition region is reached. From here, the jet continues to spread at a greater rate, with angle β_2.

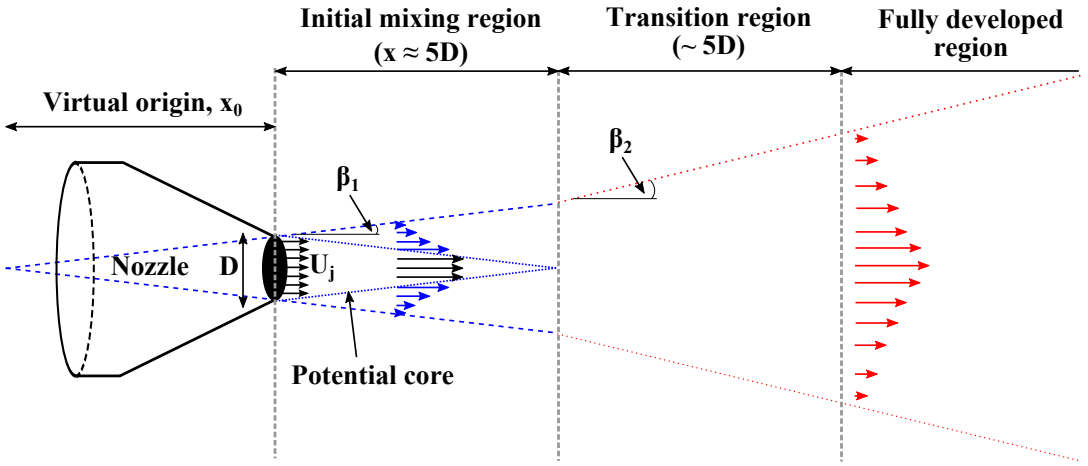

FIGURE 2.9: Schematic of a simple jet flow

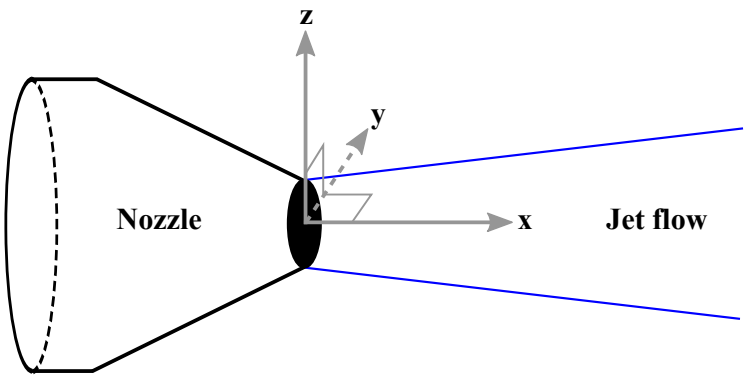

FIGURE 2.10: Global jet coordinate system

The global jet coordinate system used throughout this thesis is depicted in Figure 2.10. The polar observer angle θ_j is defined in the x-z plane and the azimuthal observer angle ϕ is defined in the y-z plane. Over the years, many jet flows have been studied experimentally. Since too many exist to report here, a comprehensive review of the early experimental findings can be found in Abramovich's book entitled, 'The Theory of Turbulent Jets' [22]. The key data sets used, however, include work from Wygnanski and Fiedler [23], Panchapakesan and Lumley [24] and Hussein *et al.* [25], who all show that, downstream of the end of the potential core, for a top-hat jet, the jet centreline velocity, U_{jc}, has the following inverse relationship with axial distance,

$$U_{jc} = \frac{U_j B_u}{\left(\frac{x}{D} - \frac{x_0}{D}\right)}\,, \tag{2.1}$$

where U_j is the jet exit mean velocity, B_u is the velocity decay constant, D is the jet nozzle exit inner diameter, x is the downstream axial distance from the jet nozzle exit plane and x_0 is the axial distance from the jet nozzle exit plane to the virtual jet origin based upon β_1, see Figure 2.9. Both B_u and x_0 are empirically-derived constants (see Table 2.1 for typical values). Similarly, the jet spreading rates before and after the end of the potential core are also found experimentally. Technically, the spreading rate of a jet is defined as,

$$\beta = \tan^{-1}\left(\frac{dy_{0.5}}{dx}\right)\,, \tag{2.2}$$

where $y_{0.5}$ is the radial distance from the jet centreline to the point at which the velocity is half that of the centreline velocity. Table 2.1 shows several examples of all three of these empirically-derived constants for different Reynolds number jets. The Reynolds number of a jet is defined as,

$$\mathrm{Re} = \frac{U_j D}{\nu}\,, \tag{2.3}$$

where ν is the kinematic viscosity of dry air. Although higher Reynolds number jets

contain smaller turbulent structures, it is important to recognise here that both the mean velocity decay and the jet spreading (or entrainment) rates are independent of the Reynolds number, Re. This, therefore, implies that the type of turbulence within a jet is statistically *self-similar* at different scales [26]. The jet is considered to be two-dimensionally self-similar over the first half of the potential core in the initial mixing region and fully axisymmetrically self-similar, or annular, downstream of this point.

It is difficult to establish the true value of the entrainment properties of a jet without a detailed experimental survey (or a large-eddy simulation) because each turbulent jet is very sensitive to its own unique initial conditions [27, 28]. For the majority of this thesis, we will focus on the region of the jet upstream of the end of the potential core. Thus, we will assume that the potential core length is approximately equal to $4D$. Within this region it can also be assumed that the jet centreline velocity is equal to that at the jet exit, i.e. $U_{jc} = U_j$.

	Wygnanski & Fiedler (1969) [23] SHW data	Panchapakesan & Lumley (1993) [24] SMHW data	Hussein *et al.* (1994) [25] SHW data	Hussein *et al.* (1994) [25] LDA data
Re	84903	10795	93560	93560
B_u	5.70 ($x/D < 50$) 5.00 ($x/D \geq 50$)	6.06	5.90	5.80
β_2	4.92	5.48	5.82	5.37

TABLE 2.1: Empirical constants for the jet velocity decay, B_u, and spreading angle downstream of the potential core, β_2 [for $x/D < 100$]

It has also been shown experimentally [23, 25, 29] that the mean radial velocity profile, at a given axial location within a jet, follows a Gaussian-type function of the distance from the jet centreline,

$$\frac{U(x,y)}{U_{jc}} = f\left(\frac{\Delta y_{0.5}}{y_b}\right) , \tag{2.4}$$

where U_{jc} is the velocity on the centreline of the jet, $\Delta y_{0.5}$ is the radial distance between a point y in the jet and the point at which the velocity is half that of the jet centreline $y_{0.5}$, and y_b is the radial distance between two points in the jet where the velocity is 90% and 1% of the jet centreline velocity, respectively. This latter dimension can be thought of as a finite 'thickness' approximation for what is, theoretically, an asymptotic boundary layer profile. Many experiments have been performed with both round and rectangular shaped, submerged (i.e. discharging into stationary, ambient air), axisymmetric, jet nozzles at different Reynolds numbers. Figure 2.11 shows radial mean velocity profile data from two different round jet experiments - Trüpel [29] ($\mathrm{Re} = 5.13 \times 10^6$) and Wygnanski *et al.* [23] ($\mathrm{Re} = 0.85 \times 10^5$). The fact that all of the data points sit on the same trend line over a range of axial locations is further evidence

of the self-similarity property of jets. This characteristic will help us in the following section to derive the governing equations for the acoustic energy produced by free turbulence. Using these two data sets, the following empirical expression can be used to calculate the local mean velocity within a self-preserving jet,

$$U = U_{jc} e^{-\left(\frac{y}{1.2 y_{0.5}}\right)^2} , \tag{2.5}$$

where $y_{0.5}$ is often assumed to be equal to the jet shear layer half-thickness, y_b. We can define y_b relative to the axial position upstream, y_{b_1}, or downstream, y_{b_2}, of the end of the potential core,

$$y_{b_1} = 2x \tan \beta_1 \qquad \text{for } x < x_0 \tag{2.6}$$

$$y_{b_2} = 2x_0 \tan \beta_1 + (x - x_0) \tan \beta_2 \qquad \text{for } x > x_0 \, . \tag{2.7}$$

Combining Equations 2.1 and 2.5, we can write down the following expression for the local mean jet velocity at a point, (x, y), downstream of the potential core within a round, axisymmetric, self-preserving jet,

$$U \approx \frac{U_j B_u}{\left(\frac{x}{D} - \frac{x_0}{D}\right)} e^{-\left(\frac{y}{1.2b}\right)^2} . \tag{2.8}$$

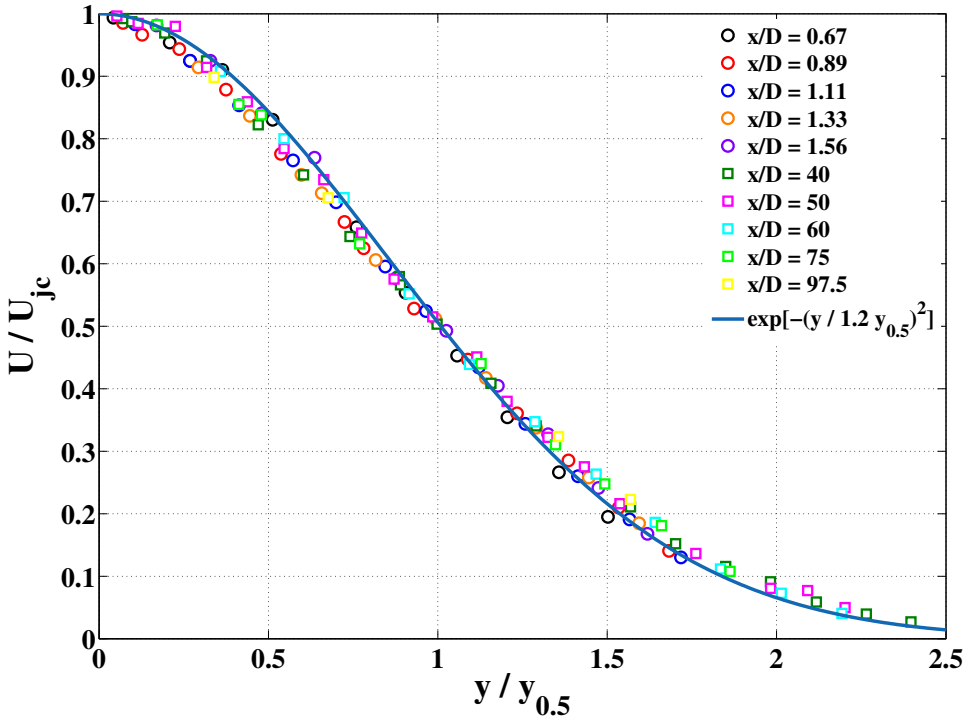

FIGURE 2.11: Dimensionless radial mean velocity profiles for axially symmetric, submerged, round jets. [Circles from Trüpel [29]; squares from Wygnanski & Fiedler [23]]

The final important aspect to mention regarding jet flow is the speed with which turbulent structures travel within the jet mixing shear layer. The 'eddy' convection velocity, U_c, in the mixing region has been quantified by several experiments [30–32]. Figure 2.12 shows that the convection velocity within the initial mixing region is relatively independent of axial distance downstream of the nozzle exit and that it approximately equals $0.62U_j$ at the centre of the mixing region (i.e. on the jet nozzle lip line). The pressure fields generated by the decay of the turbulence within the shear layer are believed, however, to be a frequency-dependent convection velocity. This property will be further explored later in the thesis (see Section 4.3.3.4).

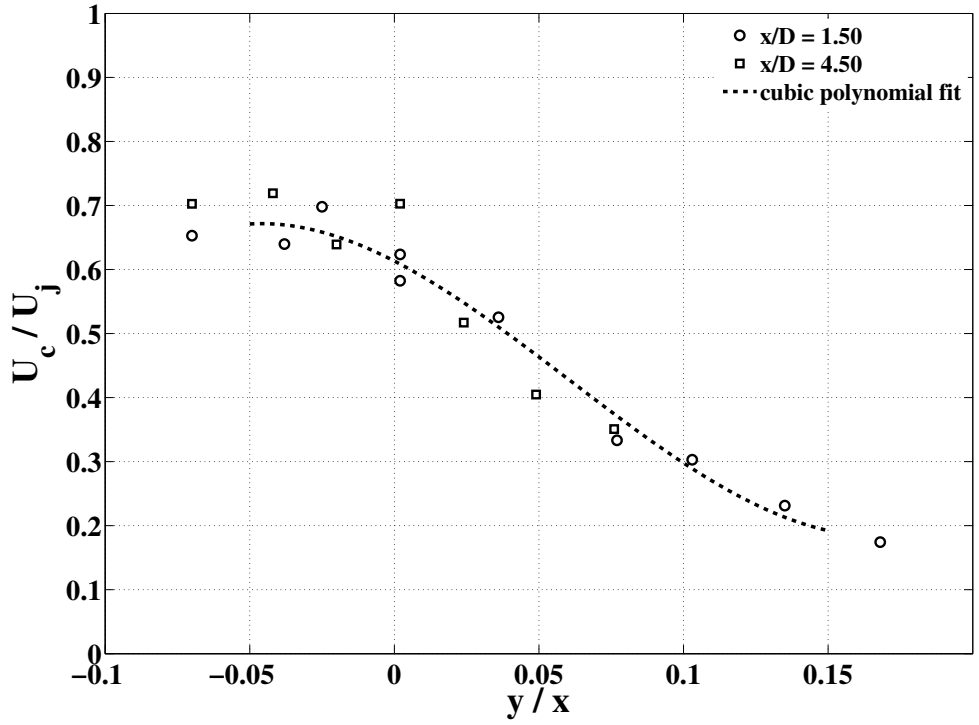

FIGURE 2.12: Eddy convection velocity radial profile. [Data from Davies *et al.* [30]]

2.2.2 Jet acoustics

The velocity at any point within a jet can be decomposed into a time-averaged (mean) component plus a randomly fluctuating (turbulent) component,

$$u_i = U_i + u_i' \,. \tag{2.9}$$

Put simply, fluctuations in the transfer of momentum within a jet are balanced by pressure fluctuations which propagate as sound. Jet noise correlates directly with turbulence intensity and, thus, little noise is generated in the laminar flow region within the potential core. Most of the noise from a single stream, submerged, subsonic jet comes from the mixing region, or shear layer, between the core and the ambient flow, where the turbulence intensity is greatest, see Figure 2.13. The peak turbulence intensity $u'_{\max}$ is fairly constant ($u'_{\max} \approx 0.16(U_j - U_0)$, where U_0 is the velocity of the ambient medium) until well into the transition region. It then falls off as x^{-2} in the fully developed region.

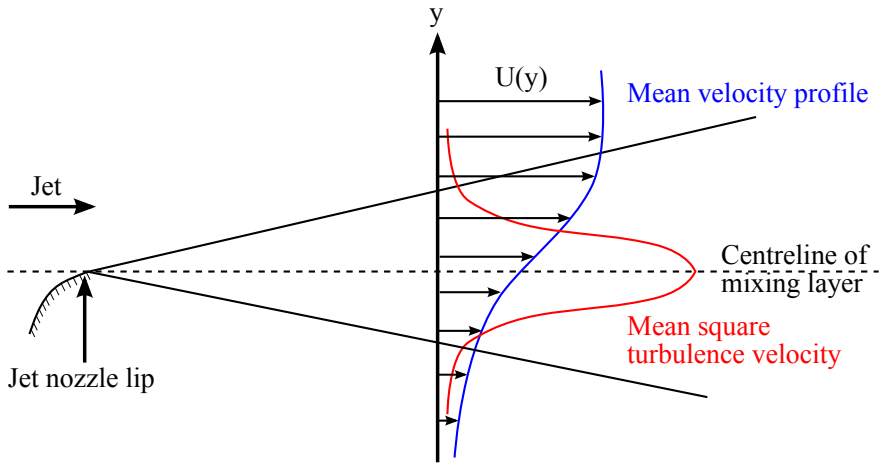

FIGURE 2.13: Jet mixing layer profiles

As indicated in the figure, most of the turbulent energy is confined to a narrow region at the centre of the mixing layer. The size of the turbulent structures, or 'eddies', in the shear layer relate to the frequency of the noise generated. The higher frequency sources are, therefore, created by smaller eddies closer to the nozzle and vice versa - i.e. $f \propto 1/x$.

2.2.2.1 Lighthill's acoustic analogy

In 1952, when attempting to tackle the problem of jet noise, Lighthill [33] realised that the density fluctuations from a turbulent flow region, when seen at large distances, should behave like acoustic waves. He, therefore, set about drawing an analogy

between the full non-linear fluid flow problem and the inhomogeneous acoustic wave equation. This analogy forms the basis of aeroacoustics and can be applied to calculate the acoustic radiation from any small turbulent flow region embedded in an infinite homogeneous fluid, in which the speed of sound, a_0, and the density, ρ_0, are constant. First, Lighthill took the exact equations of mass and momentum conservation for a perfect gas,

$$\frac{\partial \rho}{\partial t} + \frac{\partial (\rho u_j)}{\partial x_j} = 0 \,, \tag{2.10}$$

$$\rho \left(\frac{\partial u_i}{\partial t} + u_j \frac{\partial u_i}{\partial x_j} \right) = -\frac{\partial p}{\partial x_i} + \frac{\partial e_{ij}}{\partial x_j} \,, \tag{2.11}$$

where ρ and p are the fluid density and pressure, respectively, and e_{ij} is the (i,j)$^{\text{th}}$ component of the viscous stress tensor. For a Newtonian fluid, the viscous stress tensor can be expressed in terms of velocity gradients as,

$$e_{ij} = \mu \left(\frac{\partial u_i}{\partial x_j} + \frac{\partial u_j}{\partial x_j} - \frac{2}{3} \delta_{ij} \frac{\partial u_k}{\partial x_k} \right) \,, \tag{2.12}$$

where μ is the fluid viscosity and δ_{ij} is the Kronecker delta function ($\delta_{ij} = 1$ when $i = j$ and $\delta_{ij} = 0$ when $i \neq j$). Note also that the flow variables are composed of both a mean and a fluctuating component such that,

$$p = p_0 + p' \tag{2.13}$$

$$\rho = \rho_0 + \rho' \,, \tag{2.14}$$

where the zero subscript denotes the reference values of the properties at large distances from the turbulent flow and the prime denotes the small perturbations. Multiplying the mass continuity Equation 2.10 by u_i and adding the result to the momentum Equation 2.11 yields,

$$\frac{\partial}{\partial t} \rho u_i = -\frac{\partial}{\partial x_j} (\rho u_i u_j + \delta_{ij} p - e_{ij}) \,. \tag{2.15}$$

By adding and subtracting the term $a_0^2 \partial \rho / \partial x_i$, we then arrive at,

$$\frac{\partial \rho u_i}{\partial t} + a_0^2 \frac{\partial \rho}{\partial x_i} = -\frac{\partial T_{ij}}{\partial x_i} \,, \tag{2.16}$$

where T_{ij} is Lighthill's instantaneous turbulence stress tensor. The exact expression for T_{ij} for viscous, compressible flow is,

$$T_{ij} = \rho u_i u_j + \delta_{ij} \left(p' - a_0^2 \rho' \right) - e_{ij} \,, \tag{2.17}$$

where $\rho u_i u_j$ is the Reynolds stress term. Now, for high Reynolds number jets we can ignore any viscous contributions (i.e. the third term) and if we also assume an isothermal (almost isentropic) flow, we can say that $p' \sim a_0^2 \rho'$ and disregard the second dipole density fluctuation term too. Finally, if we take a subsonic jet we may replace ρ by the mean density ρ_0 and approximate Lighthill's stress tensor as,

$$T_{ij} \sim \rho_0 u_i u_j \, . \tag{2.18}$$

Since only a very small fraction of the energy within the flow gets radiated as sound, this Reynolds stress term can be determined, either through measurements or estimates, without any prior knowledge of the sound field. Lighthill's wave equation can finally be reached by subtracting the divergence of Equation 2.16 from the time derivative, with respect to t, of Equation 2.10,

$$\frac{\partial^2 \rho'}{\partial t^2} - a_0^2 \nabla^2 \rho' = A(\boldsymbol{x}, t) \, , \tag{2.19}$$

where the source term is,

$$A(\boldsymbol{x}, t) = \frac{\partial^2 T_{ij}}{\partial x_i \partial x_j} \, . \tag{2.20}$$

Mathematically, Equation 2.19 is a hyperbolic partial differential equation, which describes a wave propagating at the speed of sound in a medium at rest, on which fluctuating forces are externally applied in the form described by the right hand side of the equation. Within inhomogeneous wave equations, source terms that involve $\partial/\partial t$, $\partial/\partial x_i$, $\partial^2/\partial x_i \partial x_j$ and $\partial^3/\partial x_i \partial x_j \partial x_k$ are known as monopole, dipole, quadrupole and octopole sources, respectively. It is clear, therefore, that the noise source term, $A(\boldsymbol{x}, t)$, is quadrupole in nature. In essence, Lighthill shows us that a quadrupole source distribution (of strength T_{ij}) within a stationary acoustic, homogeneous medium will generate small amplitude density fluctuations that are analogous to the density fluctuations in any real flow. The problem, however, comes when attempting to calculate T_{ij} since, effectively, it requires solving the complete non-linear flow equations, which is an impossible task for most flows. Fortunately, however, there exist certain types of flow where estimates can be made that produce adequate representations of the sound field, albeit in the far-field.

This notion of a *far-field* solution is particularly important for isolated jet mixing noise problems, when T_{ij} is not well known, and when the source (or volume distribution of turbulent eddies) is acoustically compact - i.e. the acoustic wavelength within the source region is much greater than the characteristic length-scale of the source region itself. A far-field solution will also automatically account for the inefficiency of the quadrupole sources within the region of the flow field. Assuming no solid boundaries

exist to influence the sound field, the solution to Equation 2.19 can be expressed in terms of the following free-space, no-flow Green's function,

$$G_0(\boldsymbol{y},\tau|\boldsymbol{x},t) = \frac{1}{4\pi r}\delta\left(\tau - t + \frac{r}{a_0}\right) . \tag{2.21}$$

where r is the distance from the flow disturbance at emission time to the observer point at reception time (i.e. $r \equiv |\boldsymbol{x}(t) - \boldsymbol{y}(\tau)|$), τ is the retarded time taken for the sound to propagate from the flow disturbance to the observer point at the ambient speed of sound (i.e. $\tau = t - (r/a_0)$) and $\delta(x)$ is the Dirac delta function ($\delta(x) = +\infty$ when $x = 0$ and $\delta(x) = 0$ when $x \neq 0$). Thus, by carrying out the integration with respect to τ, the solution to Equation 2.19 can be written down as,

$$\rho'(\boldsymbol{x},t) = \frac{1}{4\pi a_0^2}\frac{1}{r}\int \left[\frac{\partial^2 T_{ij}}{\partial x_i \partial x_j}(\boldsymbol{y},\tau)\right]_{\tau=t-(r/a_0)} d^3\boldsymbol{y} . \tag{2.22}$$

This expression can be simplified by assuming the observer is located in the far-field (i.e. when $|\boldsymbol{x}| \to \infty$ and $|\boldsymbol{x}| \gg |\boldsymbol{y}|$). In such a case, the following approximations can be made,

$$|\boldsymbol{x} - \boldsymbol{y}| \approx |\boldsymbol{x}| - \frac{\boldsymbol{x}\cdot\boldsymbol{y}}{|\boldsymbol{x}|} \tag{2.23}$$

$$\frac{1}{|\boldsymbol{x} - \boldsymbol{y}|} \approx \frac{1}{|\boldsymbol{x}|} \tag{2.24}$$

and, thus, the following space and time derivatives become interchangeable,

$$\frac{\partial}{\partial x_i} \leftrightarrow -\frac{1}{a_0}\frac{x_i}{|\boldsymbol{x}|}\frac{\partial}{\partial t} . \tag{2.25}$$

Finally, if we: 1) assume that the sources are compact (thereby neglecting any retarded time differences), 2) replace the spatial derivatives with time derivatives and 3) use the isentropic, ideal gas relationship, $p' = a_0^2\rho'$, it is possible to rewrite Equation 2.22 in terms of a far-field fluctuating pressure,

$$p'(\boldsymbol{x},t) = \frac{1}{4\pi a_0^2}\frac{x_i x_j}{x^3}\int_V \frac{\partial^2 T_{ij}}{\partial t^2}(\boldsymbol{y}, t - \frac{r}{a_0})d\boldsymbol{y} . \tag{2.26}$$

It is important to note that this final formulation is set within a fixed frame of reference - i.e. the acoustic sources have the same constant properties, ρ_0 and a_0, as the ambient fluid at rest, external to the flow. The application of the above equation is also restricted to subsonic flows since it does not account for shock-associated noise.

2.2.2.2 Jet noise scaling

In order to determine the magnitude of p' in Equation 2.26, a characteristic velocity, U, and length-scale of the turbulent sources (i.e. the energy-containing eddies) are defined. For the following analysis, the nozzle diameter, D is chosen to be the characteristic length-scale. Lighthill [33] states that the characteristic frequency of the turbulent fluctuations can be written as,

$$f \sim \frac{U}{D} \,. \tag{2.27}$$

From Equation 2.18, the density fluctuations can be represented in dimensional terms as,

$$\frac{\partial^2 T_{ij}}{\partial t^2} \sim \frac{U^2}{D^2} \rho_0 U^2 \,. \tag{2.28}$$

Equation 2.26, therefore, can now be rewritten as,

$$p' \sim \frac{D}{x} \frac{\rho_0}{a_0^2} U^4 \,. \tag{2.29}$$

Now, the acoustic intensity is the time-averaged product of sound pressure and particle velocity,

$$\boldsymbol{I} = \frac{1}{T} \int_0^T p'(t) \boldsymbol{v}(t) dt \,, \tag{2.30}$$

where $\boldsymbol{v}(t)$ is the acoustic particle velocity (i.e. the speed of a parcel of fluid as it moves back and forth in the direction of the passing acoustic wave). In the far-field, for a plane progressive wave, the acoustic pressure and particle velocity are both in-phase and so are related by $v = p/Z_0$, where $Z_0 = \rho_0 a_0$ is the characteristic acoustic impedance of air. Thus, we can write down the acoustic intensity as,

$$\boldsymbol{I} = \overline{p'^2}/Z_0 \,, \tag{2.31}$$

where the over-bar represents a time-averaged quantity. Finally, since the acoustic power P is defined as the rate of acoustic energy flow across a specified surface [34], it can be expressed as follows,

$$P_a = \int_S \boldsymbol{I} \cdot d\boldsymbol{S} = \boldsymbol{I} \cdot A = \boldsymbol{I} \cdot 4\pi R^2 \,, \tag{2.32}$$

over a sphere at a distance R. Substituting Equation 2.29 into Equation 2.31, we can produce the following far-field acoustic power scaling result,

$$P_a \sim \rho_0 a_0^{-5} D^2 U^8 \,. \tag{2.33}$$

This is Lighthill's famous 'eighth power law', which has been confirmed experimentally [35–37].

2.2.2.3 Characterising jet noise

In order to characterise the jet noise source, one must understand its frequency content, directivity, source strength and source distribution. The frequency content of the far-field noise generated by a single stream, axisymmetric, cold, subsonic jet at a variety of polar angles, θ_j, can be seen in Figure 2.14. The horizontal frequency axis has been non-dimensionalised, using the jet nozzle diameter and the jet exit velocity, to a Strouhal number,

$$\mathrm{St}_D = \frac{fD}{U_j} \,. \tag{2.34}$$

From this plot, it is clear to see the broadband nature of jet noise as well as the relative differences in source strength and directivity at each frequency.

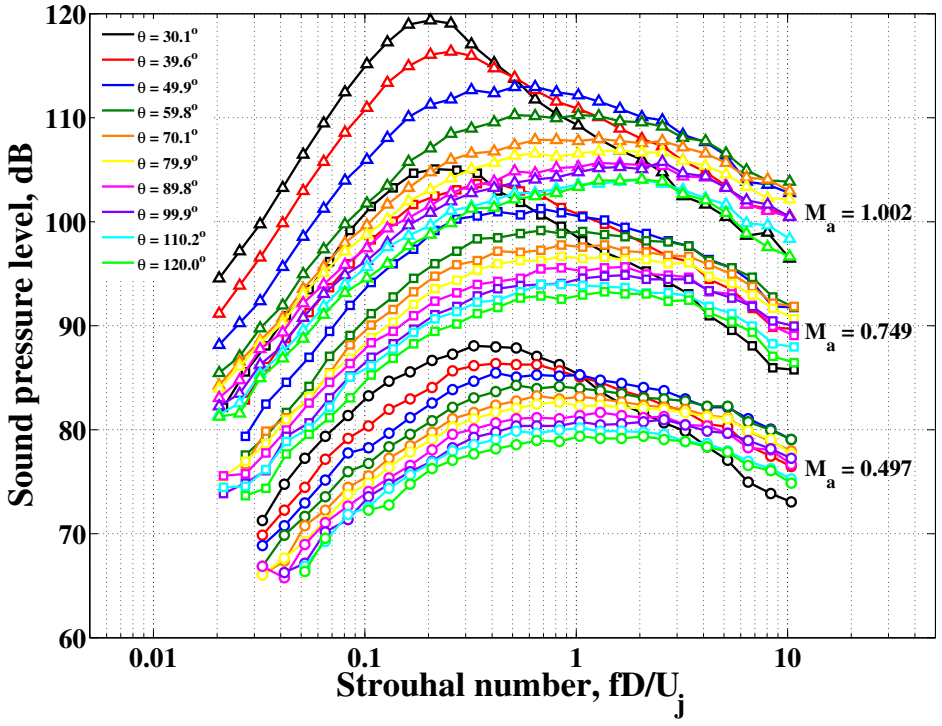

FIGURE 2.14: Single stream, axisymmetric, cold, subsonic jet far-field $1/3^{\mathrm{rd}}$-octave band sound pressure level spectra at a range of polar observer angles and flow acoustic Mach numbers. [Data from JEAN project [38]]

Regarding the directivity of jet noise, the acoustic far-field polar directivity generated by a single stream, axisymmetric, cold, subsonic jet can be seen in Figure 2.15. It is apparent from this plot that the low frequency sources (i.e. $\mathrm{St} < 0.50$) tend to peak toward the smaller polar jet angles, at $\theta_j = 30°$, whereas the higher frequency (i.e. $\mathrm{St} > 5$) sources tend to peak closer to $\theta_j = 60°$. There are two reasons why this

particular directivity pattern exists. The first is a convective amplification effect due to the presence of the mean flow field. This effect was Lighthill's final addition to his eighth power law,

$$I(R,\theta_j) \sim \frac{\rho_0 D^2 U^8}{a_0^5 R^2}(1 - M_c \cos\theta_j)^{-6}\,, \tag{2.35}$$

where M_c is the source convection Mach number (i.e. the local mean flow velocity at the source position). This convective, or Doppler, amplification term, however, has since been refined, by Ffowcs-Williams [39], for application to a subsonic jet, as $(1 - M_c \cos\theta_j)^{-5}$.

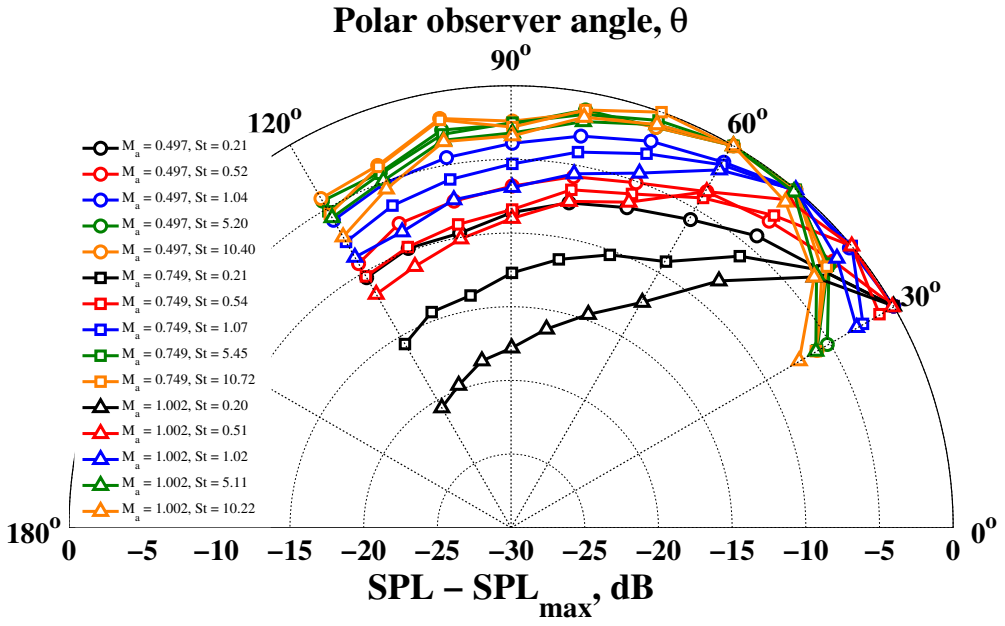

FIGURE 2.15: Single stream, axisymmetric, cold, subsonic jet far-field sound pressure level polar directivity, θ_j (relative to jet axis), for a range of jet exit Mach numbers and Strouhal numbers. [Data from JEAN project [38]]

In 1971, however, Lush [35] compared this theory with experimental data and found that a further factor was missing. This factor was particularly noticeable at high frequencies and at high subsonic flow Mach numbers, see Figure 2.16. Lush suggested that flow-acoustic interaction effects were responsible. To explain this, if you imagine a volume distribution of point sources within a jet, when each source emits an acoustic ray, the ray will be subject to a degree of refraction by the jet flow itself. The degree to which each ray is redirected will, therefore, depend on: (1) the ratio of the wavelength of the ray to the sound path length within the jet, (2) the local jet velocity profile and (3) the incidence of the ray to the flow profile. This effect gives rise to the phenomenon of the *cone-of-silence*, for example, where, at small polar angles to the jet axis, a large proportion of acoustic rays are bent away from the axis. This then results in a region, at $\theta_j < 45°$, of reduced acoustic intensity. Figure 2.17 will help to visualise all of the above-mentioned directivity effects more clearly.

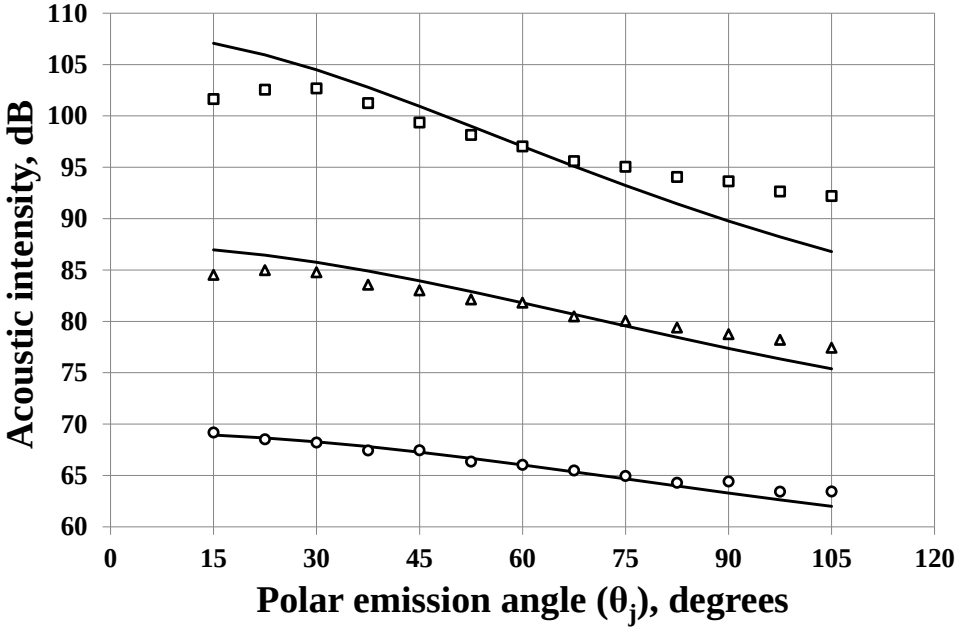

FIGURE 2.16: Single stream, axisymmetric, cold, subsonic jet far-field acoustic intensity polar directivity, θ_j (relative to jet axis), for a range of jet exit Mach numbers; [circles - $U_j = 125$ m/s; triangles - $U_j = 195$ m/s; squares - $U_j = 300$ m/s; solid lines - theory (Equation 2.2.2.3)]. [Data from Lush [35]]

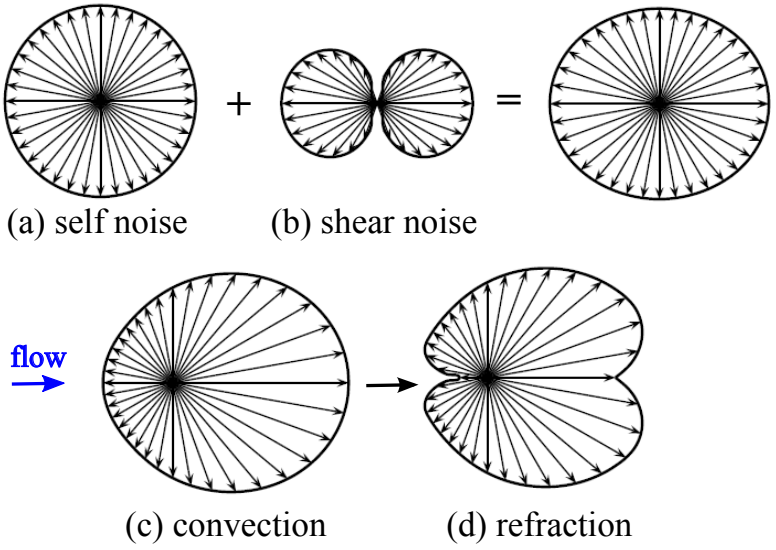

FIGURE 2.17: Illustration of the noise pattern generated by: (a) turbulence alone (self noise), (b) turbulence-mean shear flow interaction (shear noise), (c) convective amplification and (d) flow-acoustic interaction. [Figure courtesy of Andersson [40]]

Lush [35] also realised that if the spectral density results were plotted in $1/3^{\text{rd}}$-octave bands, an additional Doppler shift and Strouhal number weighting factor was also required to ensure that a particular source within a jet was located in a geometrically similar position regardless of emission angle, jet diameter and jet velocity. The final

frequency-dependent expression for far-field acoustic intensity, therefore, became,

$$I(\omega, R, \theta_j) \sim \frac{\rho_0^2 D^2 U^8}{a_0^5 R^2}(1 - M_c \cos\theta_j)^{-5} \left[\frac{\omega D}{U}(1 - M_c \cos\theta_j)\right] . \tag{2.36}$$

The final acoustic characteristic of a subsonic jet concerns the source distribution. Using microphone measurement techniques, like 'polar correlation' and 'beamforming', it is possible to establish the strength and location of different frequencies of sound produced within a distributed noise source. The polar correlation technique, for example, uses cross-spectral far-field measurements to form a one-dimensional source image along the jet axis. Figure 2.18 shows a schematic of the polar correlation set-up, developed by Fisher, Harper-Bourne and Glegg, in 1977 [41]. An important caveat to using this technique, however, is the assumption that individual sources at a particular frequency all have the same directivity.

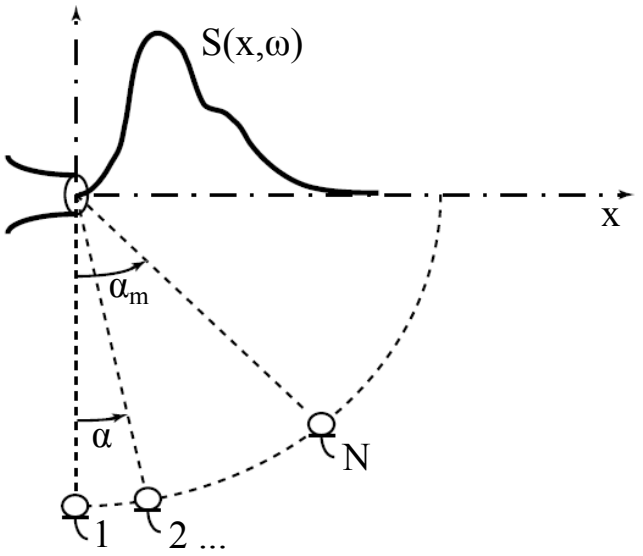

FIGURE 2.18: Schematic of the polar correlation source location technique. A polar array of N microphones are distributed over an aperture α_m. [Figure courtesy of Battaner-Moro [42]]

A typical example of the frequency-dependent source strength per unit length, $S(x, \omega)$, for a single stream, cold, subsonic jet can be seen in Figure 2.19. The solid red line represents a best-fit based upon the following formula, suggested by Glegg [43],

$$S(x, \omega) = A(\omega) \left[\frac{(m/x_c)^m}{(m-1)!}\right] x^{m-1} \exp(-jkx_c \sin\alpha) , \tag{2.37}$$

where $A(\omega)$ represents the strength of the source, x_c is the centroid position along the downstream axis, $k = \omega/a_0$, m is an adjustable shape factor parameter in the range $m \geq 2$ and α is the polar angle at which each microphone is located relative to a 90° reference microphone. The figure clearly shows evidence that the higher frequency

sources are located closer (axially) to the nozzle exit and occupy a much smaller volume than the low frequency sources downstream.

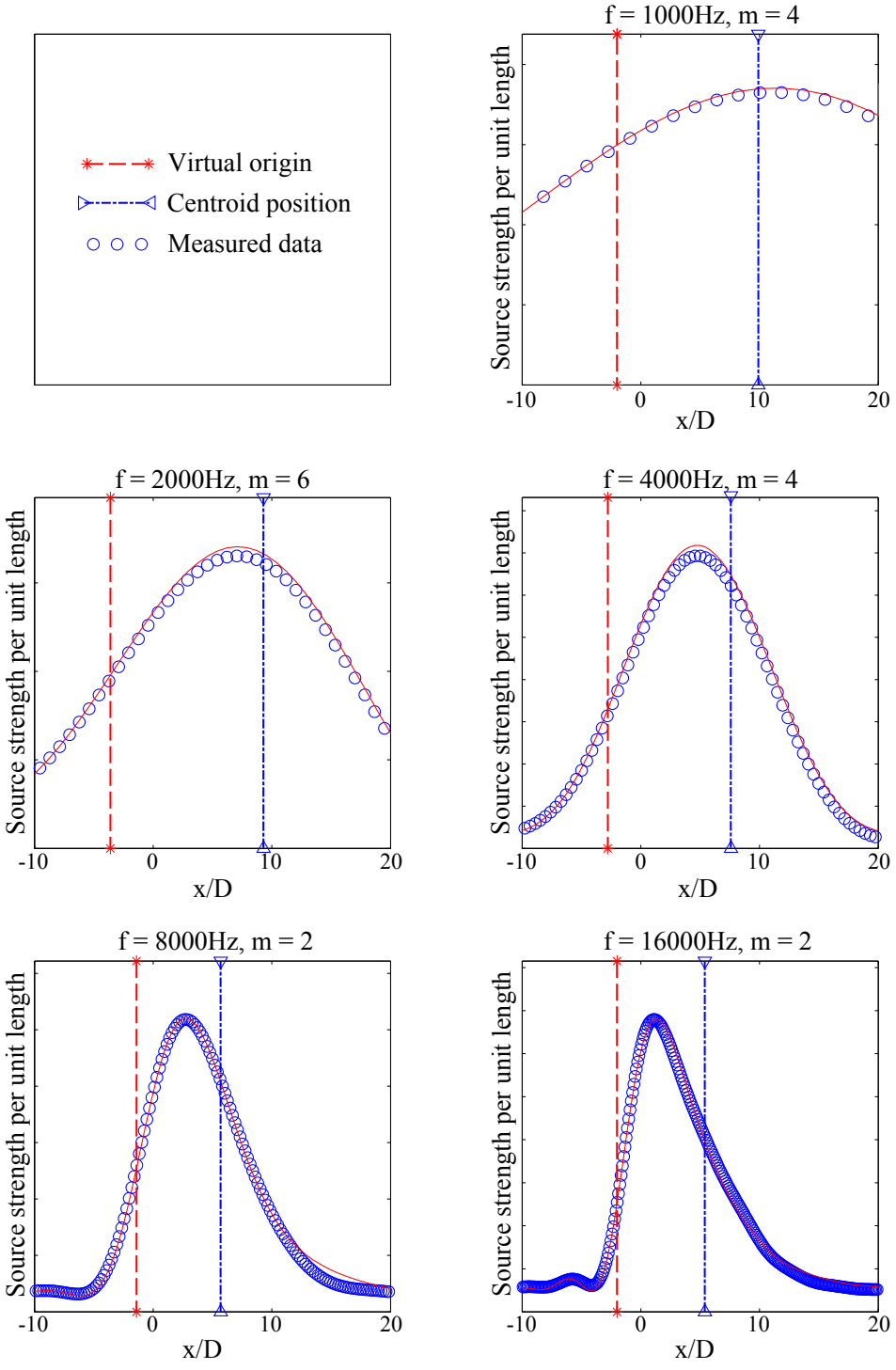

FIGURE 2.19: Typical 1/3$^{\text{rd}}$-octave band source distribution for a single stream, axisymmetric, unheated, subsonic jet; [$D = 45.6$ mm; $U_j = 200$ m/s; $T = 300$ K]. [Data from Battaner-Moro [44]]

2.2.2.4 Lilley's equation

We have seen that Lighthill's jet noise theory treats sound sources as if they were moving parallel to the jet axis through a stationary, uniform medium. The directivity of the noise can then later be accounted for by a convective amplification term and then a refractive term due to velocity and temperature gradients in the vicinity of the source region (i.e. within about one wavelength). It stands to reason, therefore, that the motion of the mean flow in the immediate vicinity of the source, rather than the relative motion at infinity should have the strongest effect on the sound generation process. In fact, when the wavelength of sound is small compared to the dimensions of the jet, the sources essentially become stationary relative to their surroundings. The overall power, therefore, need not warrant a convective amplification term at all. Now, since it is not possible to adjust the source term in Lighthill's equation without prior knowledge of the sound field itself, it is necessary to extend Lighthill's approach by modifying the full non-linear equations into the form of a moving-medium wave equation. Phillips [45] was the first to take this more direct calculation-based approach and his equation is written down below,

$$\frac{D^2\Pi}{D\tau^2} - \frac{\partial}{\partial y_i} a^2 \frac{\partial \Pi}{\partial y_i} = \frac{\partial v_j}{\partial y_i}\frac{\partial v_i}{\partial y_j} - \frac{\partial}{\partial y_i}\frac{1}{\rho}\frac{\partial e_{ij}}{\partial y_j} + \frac{D}{D\tau}\frac{1}{C_p}\frac{DS}{D\tau}\,, \tag{2.38}$$

where C_p is the specific heat capacity of the fluid, at constant pressure,

$$\frac{D}{D\tau} \equiv \frac{\partial}{\partial \tau} + v_j \frac{\partial}{\partial y_j} \tag{2.39}$$

is the material derivative and,

$$\Pi \equiv \frac{1}{\gamma} \ln \frac{p_0 + p}{p_0} \tag{2.40}$$

$$\sim \frac{1}{\gamma} p \qquad \text{if } p << p_0\,, \tag{2.41}$$

where γ is the ratio of specific heats. By applying the material derivative to both sides of Phillips' equation, Lilley then derived the following third order wave equation in which all the propagation effects occurring in a transversely sheared mean flow are accounted for within the wave operator,

$$\frac{D}{D\tau}\left(\frac{D^2\Pi}{D\tau^2} - \frac{\partial}{\partial y_i} a^2 \frac{\partial \Pi}{\partial y_i}\right) + 2\frac{\partial v_j}{\partial y_i}\frac{\partial v_k}{\partial y_j} a_0^2 \frac{\partial \Pi}{\partial y_i} = -2\frac{\partial v_j}{\partial y_i}\frac{\partial v_k}{\partial y_j}\frac{\partial v_i}{\partial y_k} + \Psi\,, \tag{2.42}$$

where

$$\Psi = 2\frac{\partial v_j}{\partial y_i}\frac{\partial}{\partial y_j}\frac{1}{\rho}\frac{\partial e_{ik}}{\partial y_k} - \frac{D}{D\tau}\frac{\partial}{\partial y_i}\frac{1}{\rho}\frac{\partial e_{ij}}{\partial y_j} + \frac{D^2}{D\tau^2}\frac{1}{C_p}\frac{DS}{D\tau}\,. \tag{2.43}$$

To summarise, in Lighthill's theory, the interaction between the sound field and the mean flow (which includes effects such as convection and refraction of sound by the flow) must be accounted for by adjusting the source term - an operation which cannot actually be done until after the equation is solved. In the theories of Phillips and Lilley, however, these effects have, to some extent, been incorporated into the wave operator part of the equation and can, therefore, be calculated as part of the solution - albeit an extremely complex one. A limited number of solutions to Lilley's equation have been derived, for example by Tester and Morfey [46], however, their use is beyond the scope of this thesis. It should be noted that limitations do still exist when using the Lilley analogy. One example of this would be when attempting to quantify the flow-acoustic interaction effects within the jet itself, like for the 'cone of silence' problem. Indeed, the age-old jet noise question still exists: is it physically realistic to separate the mean flow-acoustic field interaction effects completely from the sound generation process?

2.3 Trailing Edge Noise Literature Review

In this section, classical trailing edge noise theory is examined in more detail to prepare the reader for the mechanisms involved in jet-surface interaction (JSI) and jet-flap impingement (JFI) noise.

2.3.1 Unsteady loading noise

In 1955, Curle was the first to assign a mechanism to aerodynamic surface noise generation [47]. He extended Lighthill's theory of quadrupole aerodynamic sound [33] to yield a wave equation with two additional source terms associated with the presence of a solid body. In order to derive these terms, first let us define a closed volume V, which contains the body, a control surface S, a surface velocity $\boldsymbol{v}$ and a normal surface vector $\boldsymbol{n}$. The geometry and movement of S are defined by a scalar function,

$$f(\bar{x},t) = \begin{cases} < 0 & \text{inside } S \\ > 0 & \text{outside } S\,. \end{cases} \tag{2.44}$$

We can also say that $\nabla f = \boldsymbol{n}$ on the control surface. These characteristics can be represented simply by the following Heaviside step function,

$$H(f) = \begin{cases} 1 & \text{for } \boldsymbol{x} \in V \\ 0 & \text{for } \boldsymbol{x} \notin V\,. \end{cases} \tag{2.45}$$

We can also state that,

$$\frac{\partial f}{\partial t} = -\boldsymbol{v}\cdot\boldsymbol{n} = -v_n \quad \text{on } S\,. \tag{2.46}$$

From Lighthill's original density variable $\rho(\boldsymbol{x},t)$, we then create a new 'windowed' (denoted by the overbar) variable $\bar{\rho}(\boldsymbol{x},t)$ which is unchanged outside S but is a constant ρ_0 inside S. Thus,

$$\bar{\rho}(\boldsymbol{x},t) = \rho(\boldsymbol{x},t)H(f) = \begin{cases} \rho(\boldsymbol{x},t) & \text{outside } S \\ \rho_0 & \text{inside } S\,. \end{cases} \tag{2.47}$$

By windowing the density variable, it is important to note the additional terms now introduced on the control surface,

$$\frac{\partial\bar{\rho}}{\partial t} = \frac{\partial(\rho H(f))}{\partial t} = H(f)\frac{\partial\rho}{\partial t} - \rho\delta(f)v_n \tag{2.48}$$

$$\nabla\bar{\rho} = \nabla[\rho H(f)] = H(f)\nabla\rho + \rho\delta(f)\boldsymbol{n}\,. \tag{2.49}$$

We can now rewrite the mass and momentum conservation equations in terms of these windowed variables,

$$\frac{\partial\overline{\rho-\rho_0}}{\partial t}+\frac{\partial\overline{\rho u_i}}{\partial x_i}=[\rho u_n-(\rho-\rho_0)v_n]\delta(f)=Q\delta(f) \tag{2.50}$$

$$\frac{\partial\overline{\rho u_i}}{\partial t}+\frac{\partial}{\partial x_j}(\overline{\rho u_i u_j}+\bar{p}\delta_{ij}-\overline{\tau_{ij}})=F_i\delta(f)\,, \tag{2.51}$$

where Q and F are mass and force sources distributed over the control surface S, respectively. More specifically,

$$F_i=\rho u_i(u_n-v_n)+pn_i-e_{ij}n_j\,. \tag{2.52}$$

Finally, if we make $\overline{\rho'}=\overline{\rho-\rho_0}$, and combine these two equations, we can eliminate $\overline{\rho u_i}$ and reach Curle's wave equation,

$$\frac{\partial^2\bar{\rho'}}{\partial t^2}-a_0^2\nabla^2\bar{\rho'}=\frac{\partial^2}{\partial x_i\partial x_j}[T_{ij}H(f)]-\frac{\partial}{\partial x_i}[F_i\delta(f)]+\frac{\partial}{\partial t}[Q\delta(f)]\,. \tag{2.53}$$

On the RHS of this expression, three source terms are now present. From left to right (and in order of increasing radiation efficiency) a quadrupole, a dipole and a monopole source term exists representing the 'flow alone', 'loading' and 'thickness' noise sources, respectively. The flow alone noise is generated by turbulence, the loading noise by a fluctuating surface force and the thickness by a fluctuating mass flux through the control surface. If we assume that the mean flow is steady and that the body is at rest (i.e. $\partial f/\partial t=0$), as is the case with an aircraft wing above a jet, we can simply neglect the unsteady mass flux, or thickness, term.

2.3.1.1 Loading noise scaling

The solution to Curle's equation can easily be reproduced if we use the following generalised wave equation,

$$\frac{\partial^2\xi}{\partial t^2}-a_0^2\frac{\partial^2\xi}{\partial x_i^2}=\frac{\partial W_{ij\ldots}}{\partial x_i\partial x_j\ldots}\,, \tag{2.54}$$

where ξ and $W_{ij\ldots}$ are generalised functions. The solution to this problem is well-known [48] and can be written down straight away,

$$\xi(\boldsymbol{x},t)=\frac{1}{4\pi a_0^2}\int_{-\infty}^{+\infty}\frac{\partial^n W_{ij\ldots}(\boldsymbol{y},\tau)}{\partial y_i\partial y_j\ldots}\frac{\delta_{ij}(\tau-t+r/a_0)}{r}d\boldsymbol{y}d\tau\,, \tag{2.55}$$

where $r=|\boldsymbol{x}-\boldsymbol{y}|$ is the distance from the source point $\boldsymbol{y}$ to the observer field point $\boldsymbol{x}$. By using the interchangeable derivative property of convolution integrals, it is possible

to rewrite Equation 2.55 as,

$$\xi(\boldsymbol{x},t) = \frac{1}{4\pi a_0^2}\frac{\partial^n}{\partial x_i \partial x_j ...}\int_{-\infty}^{+\infty} W_{ij...}(\boldsymbol{y},\tau)\delta_{ij}(\tau - t + r/a_0)\frac{d\boldsymbol{y}d\tau}{r} \,. \tag{2.56}$$

Finally, by performing the integration over the retarded time τ, it is possible to reach the retarded time result,

$$\xi(\boldsymbol{x},t) = \frac{1}{4\pi a_0^2}\frac{\partial^n}{\partial x_i \partial x_j ...}\int W_{ij...}(\boldsymbol{y},t - r/a_0)\frac{d\boldsymbol{y}}{r} \,, \tag{2.57}$$

where the integral is taken over all space. The solution to Curle's wave Equation 2.53, therefore, is,

$$\rho'(\boldsymbol{x},t) = -\frac{1}{4\pi a_0^2}\frac{\partial}{\partial x_i}\int_S F_i(\boldsymbol{y},t - r/a_0)\frac{d\boldsymbol{y}}{r} \,. \tag{2.58}$$

To extract the key physical insights from this solution, Curle performed a number of simplifications [47]. Firstly, the Curle's surface integral can be simplified in the same way as Lighthill simplified his volume integral. It is first necessary to assume that the observer position $\boldsymbol{x}$ is located within the radiation field of each surface dipole (i.e. $|\boldsymbol{x}| \gg \lambda$) to give,

$$\rho'(\boldsymbol{x},t) = -\frac{1}{4\pi a_0^3}\frac{\partial}{\partial t}\int_S \frac{x_i - y_i}{|\boldsymbol{x} - \boldsymbol{y}|^2}F_i(\boldsymbol{y},t - r/a_0)d\boldsymbol{y} \,. \tag{2.59}$$

Next, he assumed the observer to be located in the far-field. Thus, if the observer distance $\boldsymbol{x}$ was greater than the characteristic length-scale of the body $\mathfrak{L}$ (i.e. $|\boldsymbol{x}| \gg \mathfrak{L}$), the expression further reduced to,

$$\rho'(\boldsymbol{x},t) = -\frac{1}{4\pi a_0^3}\frac{x_i}{x^2}\frac{\partial}{\partial t}\int_S F_i(\boldsymbol{y},t - r/a_0)d\boldsymbol{y} \,. \tag{2.60}$$

Finally, he assumed that the sources were compact. The acoustic wavelength of each dipole source was, therefore, large compared to the body (i.e. $\lambda >> \mathfrak{L}$) and so the retarded time variations within the source region could then be neglected. The far-field solution was then written as,

$$\rho'(\boldsymbol{x},t) = -\frac{1}{4\pi a_0^3}\frac{x_i}{x^2}\frac{\partial}{\partial t}\int_S F_i(\boldsymbol{y},t)d\boldsymbol{y} \,, \tag{2.61}$$

where F_i is the instantaneous force each dipole exerts on the fluid. As shown previously, we know that the turbulent eddies responsible for quadrupole noise can each be considered acoustically compact. For the case of a body of size $\mathfrak{L}$, moving through the air at a speed U, the compact condition is equivalent to $M \ll 1$, assuming

the emitted sound frequency scales according to a Strouhal-type flow mechanism, i.e. as $f \propto U/\mathfrak{L}$.

Using dimensional analysis, as for the quadrupole flow noise (for compact sources), it is now possible to see how the far-field acoustic power from the dipole loading noise scales. We can first deduce the following relationships,

$$\partial/\partial t \sim U/\mathfrak{L} \tag{2.62}$$

$$F_i \approx \rho u_i u_n \sim \rho_0 U^2 \tag{2.63}$$

$$\int_S d\boldsymbol{y} \sim \mathfrak{L}^2 \,, \tag{2.64}$$

From Equation 2.61, the far-field loading noise density fluctuations are now seen to scale as,

$$\rho'(\boldsymbol{x}, t) \sim a_0^{-3} \frac{1}{x} \frac{U}{\mathfrak{L}} \rho_0 U^2 \mathfrak{L}^2 \sim \rho_0 U^3 a_0^{-3} \mathfrak{L} x^{-1} \,. \tag{2.65}$$

In the far-field, pressure and density fluctuations are related adiabatically by $p' = a_0^2 \rho'$. As per Lighthill, we can finally produce the following far-field acoustic power scaling result,

$$P_a \sim \rho_0 a_0^{-3} \mathfrak{L}^2 U^6 \,. \tag{2.66}$$

Curle, therefore, concluded that the radiated sound power induced by unsteady surface force dipoles increases with the sixth power of flow velocity [47].

Regarding the polar directivity pattern of loading noise, Hersh and Meecham [49] successfully observed a classic dipole figure-of-eight, $\sin^2(\theta_e)$, radiation term from their experiments with small, compact airfoils and $M_a = 0.24$ flow, particularly for the high wavelength-to-chord ratios. For higher frequencies, or smaller wavelength-to-chord ratios, however, the $\sin^2(\theta_e)$ pattern no longer held. We shall see in Section 2.3.2, how the above formulation must be modified to account for such non-compact source problems.

2.3.1.2 Extension for moving sources

Lighthill's and Curle's wave equations describe aerodynamic sound generation by sources within an ideal, quiescent atmosphere. This is because the sources are defined within a fixed frame of reference $\boldsymbol{y}$. Since it is easier to specify the source strength in a coordinate system moving with, for example, a surface, Ffowcs-Williams and Hawkings [50] extended Curle's equation and introduced a Lagrangian coordinate system $\boldsymbol{\varsigma}$ fixed

to the rigid body such that,

$$\boldsymbol{y} = \boldsymbol{\varsigma} + \int^{\tau} a_0 \boldsymbol{M}(\boldsymbol{\varsigma}, \tau') d\tau' \,. \tag{2.67}$$

where $\boldsymbol{M}$ is the Mach number vector of the surface (and, therefore, of the sources). Simply put, the sources are now at rest in the $\boldsymbol{\varsigma}$ space, which is moving. Rewriting Equation 2.56 in terms of the $\boldsymbol{\varsigma}$ reference frame, yields the following expression,

$$\xi(\boldsymbol{x}, t) = \frac{1}{4\pi a_0^2} \frac{\partial^n}{\partial x_i \partial x_j ...} \int_{-\infty}^{+\infty} W_{ij...}(\boldsymbol{\varsigma}, \tau) \delta_{ij}(\tau - t + r/a_0) J \frac{d\boldsymbol{\varsigma} d\tau}{r} \,. \tag{2.68}$$

where r is now a function of τ

$$r = \left| \boldsymbol{x} - \boldsymbol{\varsigma} - \int^{\tau} a_0 \boldsymbol{M}(\boldsymbol{\varsigma}, \tau') d\tau' \right| \tag{2.69}$$

and the Jacobian, J, accounts for any divergence of the source during the motion of the transformation,

$$J = \exp \left\{ \int^{\tau} \operatorname{div} c\boldsymbol{M}(\boldsymbol{\varsigma}, \tau') d\tau' \right\} \,. \tag{2.70}$$

The first form of solution to Equation 2.68 can be seen below,

$$\begin{aligned} 4\pi a_0^2 \rho'(\boldsymbol{x}, t) = & \frac{\partial^2}{\partial x_i \partial x_j} \int_V \left[\frac{T_{ij} J}{r|1 - M_r|} \right] d\boldsymbol{\varsigma} - \frac{\partial}{\partial x_i} \int_S \left[\frac{p_{ij} n_j K}{r|1 - M_r|} \right] d\boldsymbol{\varsigma} \\ & + \frac{\partial}{\partial t} \int_S \left[\frac{\rho_0 v_n}{r|1 - M_r|} \right] d\boldsymbol{\varsigma} \,. \end{aligned} \tag{2.71}$$

where M_r is the component of $\boldsymbol{M}$ in the direction of the radiation vector $\boldsymbol{r} = \boldsymbol{x} - \boldsymbol{y}(\boldsymbol{\varsigma}, \tau')$ and K is the ratio of the area elements of the surface S in the $\boldsymbol{y}$ and $\boldsymbol{\varsigma}$ reference frames (just as J is the ratio of the volume elements). The square brackets imply that the contents are to be evaluated at the retarded time (given implicitly by $\tau = t - (r/a_0)$). The volume integral must also be assumed to extend over the region exterior to the surface. In the regions where the source is approaching the quiescent medium (i.e. where $M_r > 0$ and $|1 - M_r|^{-1} > 1$), it is clear to see that an increase in sound intensity results. Conversely, where the source is moving away from the medium, the intensity is reduced. In essence, this solution treats the sound generation as a spatial distribution of time-varying sources. While a more unified solution approach exists, in which the distribution of sources is placed over a 'hypersurface of variable orientation' [50], further discussion is beyond the scope of this thesis.

2.3.2 Scattering of sound by an edge

Having established the physics behind the influence of solid boundaries on aeroacoustic sound generation for compact source regions, the next problem to address concerns the situation whereby the wavelength within the source region is small, or non-compact, compared to the characteristic length-scale of the body (i.e. $\lambda \ll \mathfrak{L}$). In 1970, Ffowcs-Williams and Hall [19] derived an expression to tackle the situation whereby a sharp edge scatters the pressure field from an eddy situated within a wavelength of a half plane, see Figure 2.20.

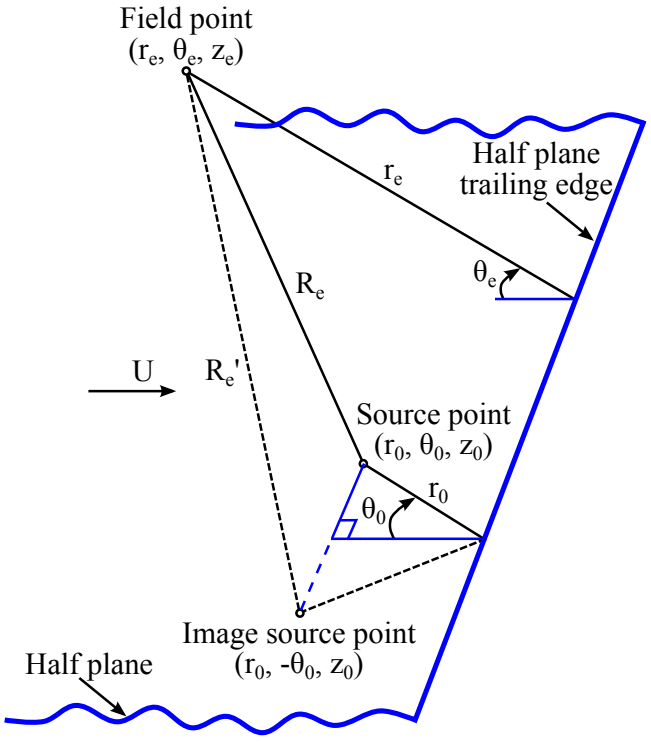

FIGURE 2.20: Trailing edge noise coordinate system schematic

To address this particular problem, details of the potential field in the vicinity of the scattering zone had to be taken into account. Ffowcs-Williams and Hall began, first, by taking Lighthill's wave equation (Equation 2.19) and by neglecting the effects of viscosity. Then, by assuming an isentropic, ideal gas relationship (i.e. $p = a_0^2\rho$), they could reduce the turbulence stress tensor to Equation 2.18. Next, they defined a Fourier transform of the function $f(t)$ such that,

$$f^*(\omega) = \frac{1}{2\pi}\int_{-\infty}^{\infty} f(t)e^{-i\omega t}dt\,. \tag{2.72}$$

Lighthill's wave equation could then be written as the following inhomogeneous Helmholtz equation,

$$\nabla^2 p^* + k^2 p^* = -\left[\frac{\partial^2 \rho u_i u_j}{\partial x_i \partial x_j}\right]^*\,, \tag{2.73}$$

where $k = \omega/a_0$. Now, if we assume that the normal velocity vanishes at the surface of the rigid half plane, the solution of Equation 2.73 can be written down immediately in terms of a Green's function G,

$$p^*(\boldsymbol{x},\omega) = \frac{1}{4\pi}\int_V \left(\frac{\partial^2 \rho u_i u_j}{\partial x_i \partial x_j}\right)^* G d\boldsymbol{y} + \frac{1}{4\pi}\int_S \frac{\partial p^*}{\partial n} G d\boldsymbol{y}\,, \tag{2.74}$$

where
$$(\nabla^2 + k^2)G = -4\pi\delta_{ij}(\boldsymbol{x}-\boldsymbol{y})\,, \tag{2.75}$$

and
$$\frac{\partial G}{\partial n} = 0 \qquad \text{on the half-plane}\,. \tag{2.76}$$

Since there is no normal velocity on the half-plane, the surface integral term in Equation 2.74 vanishes. Finally, if one completes the remaining divergence for the volume integral, using Gauss' theorem, we are left with

$$p^*(\boldsymbol{x},\omega) = \frac{1}{4\pi}\int_V (\rho u_i u_j)^* \frac{\partial^2 G}{\partial x_i \partial x_j} d\boldsymbol{y}\,. \tag{2.77}$$

Using the definitions illustrated in Figure 2.20, Ffowcs-Williams and Hall then converted the above expression into cylindrical polar coordinates.

$$\begin{aligned} 4\pi p^*(r_e,\theta_e,z_e,\omega) = \int \Bigg\{ & \rho u_{r_e}^2 \frac{\partial^2 G}{\partial r_0^2} + \rho u_{z_e}^2 \frac{\partial^2 G}{\partial z_0^2} + \rho u_{r_e} u_{z_e}\left[\frac{\partial}{\partial r_0}\left(\frac{\partial G}{\partial z_0}\right) + \frac{\partial}{\partial z_0}\left(\frac{\partial G}{\partial r_0}\right)\right] \\ & + \rho u_{r_e} u_{\theta_e}\left[\frac{\partial}{\partial r_0}\left(\frac{1}{r_0}\frac{\partial G}{\partial \theta_0}\right) + \frac{2}{r_0}\frac{\partial}{\partial \theta_0}\left(\frac{\partial G}{\partial r_0}\right) - \frac{1}{r_0^2}\frac{\partial G}{\partial \theta_0}\right] \\ & + \rho u_{\theta_e} u_{z_e}\left[\frac{1}{r_0}\frac{\partial}{\partial \theta_0}\left(\frac{\partial G}{\partial z_0}\right) + \frac{\partial}{\partial z_0}\left(\frac{1}{r_0}\frac{\partial G}{\partial \theta_0}\right)\right] \\ & + \rho u_{\theta_e}^2\left(\frac{1}{r_0^2}\frac{\partial^2 G}{\partial \theta_0^2} + \frac{1}{r_0}\frac{\partial G}{\partial r_0}\right)\Bigg\}^* dV_0\,, \end{aligned} \tag{2.78}$$

where $dV_0 = r_0 dr_0 d\theta_0 dz_0$.

From the geometry in Figure 2.20, we can define the separation distance of the source to the field point as,

$$R_e = \{r_e^2 + r_0^2 - 2r_e r_0 \cos(\theta_e - \theta_0) + (z_e - z_0)^2\}^{\frac{1}{2}}\,. \tag{2.79}$$

Similarly, the separation distance of the image source to the field point can be defined as,

$$R_e' = \{r_e^2 + r_0^2 - 2r_e r_0 \cos(\theta_e + \theta_0) + (z_e - z_0)^2\}^{\frac{1}{2}}\,. \tag{2.80}$$

Finally, the shortest distance from the source to the field point passing via the edge can be expressed as,

$$R_s = \{(r_e + r_0)^2 - (z_e - z_0)^2\}^{\frac{1}{2}} . \tag{2.81}$$

Now, assuming the field points are many wavelengths both from the turbulent region and from the edge of the half plane (i.e. $kr_e \gg 1$ and $r_e \gg r_0$), the following straight edge diffraction Green's function solution [51], can be used to solve Equation 2.74 in the far-field,

$$G = \frac{e^{\frac{1}{4}i\pi}}{\sqrt{\pi}} \left\{ \frac{e^{-ikR_e}}{R_e} \int_{-\infty}^{u_{R_e}} e^{-iu^2} du + \frac{e^{-ikR'_e}}{R'_e} \int_{-\infty}^{u_{R'_e}} e^{-iu^2} du \right\} , \tag{2.82}$$

where $$u_{R_e} = \pm[k(R_s - R_e)]^{\frac{1}{2}} , \qquad u_{R'_e} = \pm[k(R_s - R'_e)]^{\frac{1}{2}} . \tag{2.83}$$

From this solution, Ffowcs-Williams and Hall made three further deductions and simplifications. Firstly, they noticed that the majority of the enhancement of the sound field, produced either by quadrupole free turbulence or by scattered edge noise, would arise principally from the derivatives of u_{R_e} and $u_{R'_e}$. Secondly, they noticed that the derivatives of the factors $(R_s + R_e)^{-\frac{1}{2}}$ and $(R_s + R'_e)^{-\frac{1}{2}}$ would not be seen in the far-field. Thus, the two integration limits could be further simplified to,

$$u_{R_e} = (2kr_0 \sin\zeta)^{\frac{1}{2}} \cos\tfrac{1}{2}(\theta_e - \theta_0) \tag{2.84}$$

and $$u_{R'_e} = (2kr_0 \sin\zeta)^{\frac{1}{2}} \cos\frac{1}{2}(\theta_e + \theta_0) , \tag{2.85}$$

where $$\sin\zeta = \frac{r_e}{\sqrt{[r_e^2 + (z_e - z_0)^2]}} . \tag{2.86}$$

Thirdly, the z_0 coordinate was seen to bear no real influence on the far-field sound beyond that produced from a rigid infinite plane (i.e. one without an edge). It was concluded, therefore, that no significant sound enhancement due to longitudinal quadrupoles could be produced if they were aligned parallel with the edge. Furthermore, when looking at the sound field in the plane $\theta_e = \pi$ (and, thus, when $R_e = R'_e$), the general form of the Green's function G reduces to that suitable for solving Lighthill's unbounded fluid problem.

For an eddy situated well within a wavelength of the edge (i.e. when every part of the eddy satisfies the inequality $2kr_0 \ll 1$), Ffowcs-Williams and Hall used the series

expansion properties of Fresnel integrals [52] to rewrite Equation 2.82 as

$$G = \frac{e^{-ikR_e}}{R_e}\left\{1 + \frac{2e^{\frac{i\pi}{4}}}{\sqrt{\pi}}(2kr_0\sin\zeta)^{\frac{1}{2}}\cos\tfrac{1}{2}\theta_0\cos\tfrac{1}{2}\theta_e + O(kr_0)\right\} . \tag{2.87}$$

This expression can now be placed into the solution to the Helmholtz wave Equation 2.74. For the $2kr_0 \ll 1$ condition, if one retains the dominant terms (i.e. those containing the factor $(2kr_0)^{-\frac{3}{2}}$), the following far-field expression is reached,

$$\begin{aligned} -4\pi p^*(r_e,\theta_e,z_e,\omega) = k^2\frac{2e^{\frac{i\pi}{4}}}{\sqrt{\pi}}(\sin\zeta)^{\frac{1}{2}}\cos\tfrac{1}{2}\theta_e \\ \times\int\{\rho u_{r_e}^2\cos\tfrac{1}{2}\theta_0 - \rho u_{\theta_e}^2\cos\tfrac{1}{2}\theta_0 \\ - 2\rho u_{r_e}u_{\theta_e}\sin\tfrac{1}{2}\theta_0\}^*(2kr_0)^{-\frac{3}{2}}\frac{e^{-ikR_e}}{R_e}d\boldsymbol{V_0} . \end{aligned} \tag{2.88}$$

An important point to note about this expression is that, in the presence of the half plane, only three Reynolds stress terms (i.e. $\rho u_{r_e}^2$, $\rho u_{\theta_e}^2$ and $\rho u_{r_e}u_{\theta_e}$) produce pressure fields which are significantly greater than their respective free turbulence values. The remaining $\rho u_{r_e}u_{z_e}$ and $\rho u_{\theta_e}u_{z_e}$ terms increase by a smaller $(2kr_0)^{-\frac{1}{2}}$ factor and the $\rho u_{z_e}^2$ stress has the same pressure field expected from an infinite plane (i.e. without an edge). It is possible to evaluate the volume integrals in Equation 2.74 if, as suggested by Lighthill, we assume the turbulence is divided into regions within which each of the products $(\rho u_{r_e}^2)^*$, $(\rho u_{\theta_e}^2)^*$ and $(\rho u_{r_e}u_{\theta_e})^*$ is perfectly correlated and that each eddy is assumed to be a cylinder (with radius σ) centred on the edge of the half plane. Supposing these two things, the following result can be used,

$$\int \sin\tfrac{1}{2}\theta_0(2kr_0)^{-\frac{3}{2}}dV_0 = \frac{2^{\frac{3}{2}}}{\pi}(k\sigma)^{-\frac{3}{2}}V . \tag{2.89}$$

Next, if we decompose the flow near the edge into a steady part (U_{r_e}, U_{θ_e}, U_{z_e}) and a fluctuating part (u_{r_e}, u_{θ_e}, u_{z_e}), we may approximate terms within Equation 2.88 as follows,

$$(\rho u_{r_e}^2)^* = \rho_0(U_{r_e}^2 + 2U_{r_e}u_{r_e} + u_{r_e}^2)^* \tag{2.90}$$

$$\approx 2\rho_0 U_{r_e}u_{r_e}^* . \tag{2.91}$$

We can see that ρ has been set equal to ρ_0 - the density of the undisturbed fluid. $U_{r_e}^2$ can be neglected because it is independent of time and $u_{r_e}^2$ can also be neglected because it is smaller than the term $U_{r_e}u_{r_e}$ by a factor α, the normalised turbulence intensity (i.e. $\alpha = \frac{u_{r_e}}{U_{r_e}}$). If we then define a typical flow velocity U, we can rewrite

Equation 2.88 as,

$$4\pi p^* = 4\left(\frac{2}{\pi}\right)^{\frac{1}{2}} k^2 \cos\tfrac{1}{2}\theta_e (\sin\zeta)^{\frac{1}{2}} \frac{e^{-ikR_e}}{R_e} \rho_0 U^2 \alpha \sin\bar{\theta_0} \begin{Bmatrix}\cos\\ \sin\end{Bmatrix} \frac{\beta}{2} (k\bar{r}_0)^{-\frac{3}{2}} V \,, \tag{2.92}$$

where $\bar{\theta_0}$ is the angle the mean flow makes with the edge of the half plane and $\bar{r}_0$ and β may be regarded as the r_0 and θ_0 coordinates of the centre of the eddy, respectively. Now, we can express this far-field pressure approximation as an intensity,

$$I(r_e, \theta_e, z_e, \omega) = \frac{k^4 \sin\zeta \cos^2(\frac{\theta_e}{2}) \rho_0 U^4 \alpha^2 \sin^2\bar{\theta_e} \begin{Bmatrix}\cos^2\\ \sin^2\end{Bmatrix} \frac{\beta}{2} V^2}{\pi^3 a_0 R^2 (k\bar{r}_0)^3} \,. \tag{2.93}$$

Setting $\bar{r}_0$ equal to the eddy correlation radius σ and assuming the frequency of the turbulent source scales with a typical Strouhal-type relationship (i.e. $f \propto U/2\sigma$), the acoustic wavenumber k will be of the order $\pi U/a_0\sigma$. The maximum scattered far-field sound intensity from an eddy convecting over an edge, therefore, will take the following form,

$$I_{\max} = \frac{k\rho_0 U^5 \alpha^2 V^2}{\pi^2 a_0^2 R_e^2 \sigma^4} \,. \tag{2.94}$$

This is Ffowcs-Williams and Hall's famous fifth power scaling law, which has been reproduced in other analytical works by Crighton and Leppington [20] and, later, by Chase [53] and Chandiramani [54].

Fink was then the first to verify this trailing edge fifth power law experimentally, using a single stream, circular, subsonic, unheated, jet beneath an airfoil (for $M \leq 0.5$) [55]. Underwood and Hodgson subsequently observed the $\cos^2(\theta_e/2)$ polar directivity behaviour for low Mach number jets (i.e. for $M \leq 0.2$) [56]. Further clarification of this non-compact, semi-baffled directivity was then also given by Meecham *et al.* for baffles, or wings, of finite lengths [57] and then, in more detail, by McInerny *et al.* [58]. The term *semi-baffled* refers to the situation whereby the wavelength of an acoustic source is much smaller than the length of the solid surface (or baffle) from which it radiates, see Figure 2.21. In a later study, Miller proposed that a substantial upstream-travelling component of trailing edge noise was diffracting around the wing leading edge creating an interference pattern seen in the far-field forward arc of the jet [1]. The author will return to discuss this particular observation later on in the thesis, in Section 4.3.2.5.

The final key point to note here is that this formulation is modelled using a surface which is infinitely long upstream of its trailing edge and infinitely wide along the spanwise plane. The source, therefore, is always 'fully non-compact'. In other words, the acoustic wavelength generated by the source is small compared to the dimensions

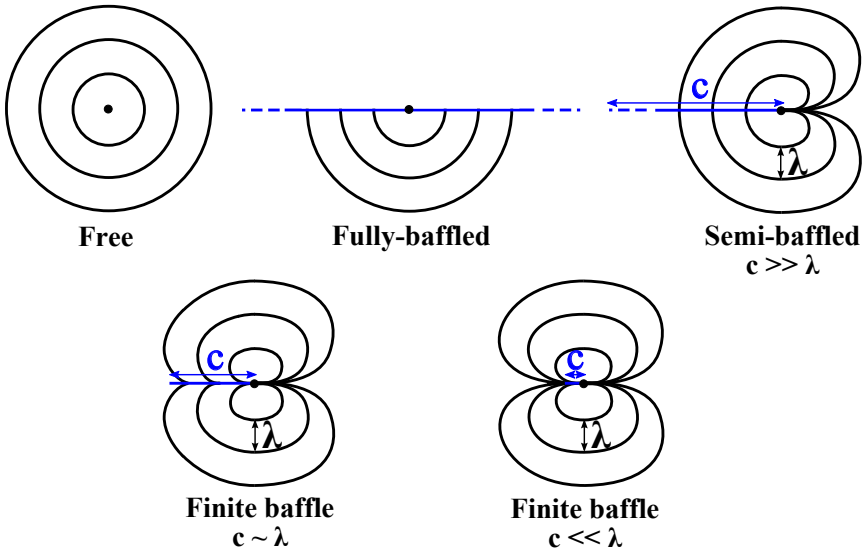

FIGURE 2.21: Illustration of different types of acoustic baffle where c is the length, or chord, of the baffle and λ is the wavelength of the radiated acoustic wave

of the source region itself. We will see in Section 2.3.3.1 how this formulation changes for a rigid body of finite length and span.

2.3.3 Turbulent boundary layer noise

In 1976, Amiet [59] derived an analytical solution for the pressure jump produced by the passage of a two-dimensional gust over the trailing edge of an airfoil, see Figure 2.22a. In order to calculate the disturbance wall pressure field generated when such a convecting incident vortical velocity field is scattered by a trailing edge, Amiet set up the following generic mixed boundary value problem (for any 2D scalar potential field Φ),

$$\begin{aligned} \tfrac{\partial^2\Phi}{\partial x^2} + \tfrac{\partial^2\Phi}{\partial z^2} + \mu^2\Phi &= 0\,, \\ \Phi(x,0) &= f(x)\,, \quad x \geq 0\,, \\ \tfrac{\partial\Phi}{\partial z}(x,0) &= 0\,, \quad x < 0\,. \end{aligned} \tag{2.95}$$

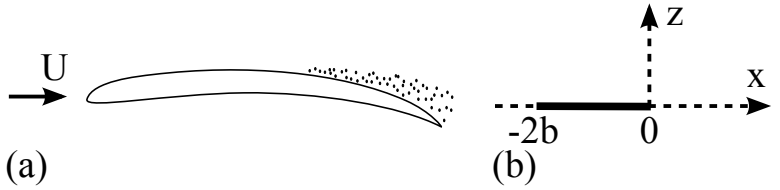

FIGURE 2.22: 2D trailing edge problem schematic with coordinates

It was then possible to attack this problem for any $x < 0$ using Schwarzschild's [60] well-known solution,

$$\Phi(x,0) = \frac{1}{\pi}\int_0^\infty G(x,\xi,0) f(\xi) d\xi \,, \tag{2.96}$$

where

$$G(x,\xi,0) = \sqrt{\frac{-x}{\xi}}\frac{e^{-\mu(\xi-x)}}{\xi - x} \,. \tag{2.97}$$

The disturbance pressure is then seen to act as equivalent acoustic sources and the far-field pressure can be calculated by means of a radiation integral. A key assumption behind this trailing edge model, however, is that the Kutta condition is fully satisfied at the trailing edge (i.e. the two incoming fluid streamlines approaching the edge from above and below the airfoil are unable to travel around the corner of the edge while attached to the surface). Howe, however, has since commented that the Kutta condition may only partially be fulfilled, especially at higher frequencies [61]. Another key assumption of this formulation is that the vortical gust is not statistically changed during the advection process, i.e. the turbulence is 'frozen'.

Amiet's airfoil, in fact, was modelled as a flat plate with zero thickness, zero angle of attack and chord length $c = 2b$, see Figure 2.22b. The plate was assumed to sit within an isotropic homogeneous subsonic flow moving with velocity U, with its trailing edge located at $x = 0$. The trailing edge was also assumed to extend to infinity along the spanwise y-axis. Amiet first defined the disturbance pressure as $p'(x,z,t) = \tilde{P}(x,z)e^{i\omega t}$ in order to reach the following complex convected wave equation in the plane normal to the airfoil,

$$\beta^2\frac{\partial^2\tilde{P}}{\partial x^2} + \frac{\partial^2\tilde{P}}{\partial z^2} - 2ikM_a\frac{\partial\tilde{P}}{\partial x} + k^2\tilde{P} = 0 \,, \tag{2.98}$$

where $k = \omega/a_0$ and $\beta^2 = 1 - M_a^2$. Here, M_a is the free stream acoustic Mach number, $M_a = U/a_0$, and assumed to be less than unity. If the disturbance pressure variable is transformed once more, as $\tilde{P}(x,z) = p(x,z)e^{i(kM_a/\beta^2)x}$, the wave equation becomes,

$$\beta^2\frac{\partial^2 p}{\partial x^2} + \frac{\partial^2 p}{\partial z^2} + \left(\frac{KM_a}{\beta}\right)^2 p = 0 \,, \tag{2.99}$$

where $K = \omega/U$ is the aerodynamic wavenumber. If we make the following final four transformations,

$$X = \frac{x}{b} \,, \qquad Z = \frac{\beta z}{b} \,, \qquad \bar{K} = Kb \,, \qquad \bar{\mu} = \frac{\bar{K}M_a}{\beta^2} \,, \tag{2.100}$$

the problem can be defined in canonical form,

$$\frac{\partial^2 p}{\partial X^2} + \frac{\partial^2 p}{\partial Z^2} + \bar{\mu}^2 p = 0 \,. \tag{2.101}$$

In non-dimensional form, the flat plate extends over $-2 \leq X \leq 0$. In order to determine the main scattering term for the Schwarzschild solution, however, the plate must be extended to infinity upstream (i.e. for $X < 0$). Amiet's surface, therefore, is essentially fully non-compact, as per Ffowcs-Williams and Hall's formulation.

We can now write the incident gust upstream of the trailing edge as $p'(x,0,t) = e^{i\omega t}e^{-i\eta Kx} = e^{i\omega t}e^{-iK_1 x} = P_0 e^{i\omega t}$, where K_1 is the streamwise wavenumber, $\eta = U/U_c$ and U_c is the convection speed of the gust (which must be lower than U). In order to satisfy the Kutta condition, a disturbance pressure P_1 must be added such that $P_0 + P_1 = 0$ for $X \geq 0$. Finally, if the surface is assumed to be perfectly rigid, the normal derivative of P_1 must be equal to zero for $X < 0$. The complete problem can now be expressed as follows,

$$\begin{aligned} \tfrac{\partial^2 p_1}{\partial X^2} + \tfrac{\partial^2 p_1}{\partial Z^2} + \bar{\mu}^2 p_1 &= 0\,, & & \\ p_1 &= -e^{i\bar{K}X[\eta + (M_a^2/\beta^2)]}\,, & x \geq 0\,, & \\ \tfrac{\partial p_1}{\partial Z}(x,0) &= 0\,, & x < 0\,. & \end{aligned} \tag{2.102}$$

For $X < 0$ and $Z = 0$, Schwarzschild's solution gives,

$$p_1(X,0) = -\frac{1}{\pi}\int_0^\infty \sqrt{\frac{-X}{\xi}}\frac{e^{-i\bar{\mu}(\xi - X)}}{\xi - X} e^{-i\bar{K}\xi[\eta + (M_a^2/\beta^2)]}\, d\xi\,, \tag{2.103}$$

$$= -\frac{e^{i\bar{\mu}X}}{\pi}\int_0^\infty \sqrt{\frac{-X}{\xi}}\frac{e^{-i[\eta\bar{K} + (1+M_a)\bar{\mu}]\xi}}{\xi - X}\, d\xi\,. \tag{2.104}$$

Amiet used three further mathematical relationships to reach an exact result for the acoustic source wall pressure. First, he used knowledge of the following property of integrals [62],

$$\int_0^\infty \sqrt{\frac{-X}{\xi}}\frac{e^{-iA\xi}}{\xi - X} d\xi = \pi e^{-iAX}\left[1 - \frac{e^{i\pi/4}}{\sqrt{\pi}}\int_0^{-AX}\frac{e^{-it}}{\sqrt{t}} dt\right]\,. \tag{2.105}$$

He then used the following complex error function,

$$E^*(x) = \int_0^x \frac{e^{-it}}{\sqrt{2\pi t}} dt = C_2(x) - iS_2(x)\,, \tag{2.106}$$

where C_2 and S_2 are Fresnel integrals [63]. Finally, remembering that $\sqrt{2}e^{i\pi/4} = 1 + i$, Amiet's [59] final exact result for the acoustic source wall pressure on an infinite chord is written as,

$$P_1(X,0) = e^{-\eta\bar{K}X}[(1+i)E^*(-[\eta\bar{K} + (1+M_a)\bar{\mu}]X) - 1]\,. \tag{2.107}$$

2.3.3.1 Extension for finite geometry airfoils and 3D gusts

More recently, in 2005, Roger and Moreau [64] modified Amiet's formulation in order that P_1 could satisfy any specified condition on the potential field upstream of the airfoil's leading edge (i.e. for $X < -2$). In short, they derived a back-scattering disturbance pressure correction, again using Schwarzschild's solution, assuming dipoles were distributed normal to the flow along the leading edge. To do this, it was first important to note that the disturbance pressure and potential were related by,

$$Pe^{i\omega t} = -\rho_0 \frac{D\Psi}{Dt} \,, \tag{2.108}$$

where $\Psi = \psi e^{i\omega t}$, ρ_0 is the undisturbed fluid density and D/Dt is the material derivative. In reduced variables, the equation to be solved now becomes,

$$-\frac{b}{\rho_0 U} P = \frac{\partial \psi}{\partial X} + i\bar{K}\psi \,. \tag{2.109}$$

The solution to to this equation, therefore, would take the following form,

$$\psi(X,0) = -\frac{b}{\rho_0 U} \int_{-\infty}^{x} P(\xi,0) e^{i\bar{K}(X-\xi)} d\xi \,. \tag{2.110}$$

In the same way as before, a secondary potential correction ψ_2 is introduced to cancel out the primary potential ψ_1 for $X < -2$ and a change of variable is applied to set up another canonical Schwarzschild problem. After some mathematical manipulation and a simplified integral approximation (consistent with numerical tests [64]), the disturbance potential became,

$$\begin{aligned} \psi_2(X,0) \backsimeq \left(\frac{-b}{\rho_0 U}\right) \frac{(1+i)e^{-4i\bar{\mu}}}{2\sqrt{\pi}(\eta-1)\bar{K}} \frac{1-\Theta^2}{\sqrt{N_1}} e^{i(M_a-1)\bar{\mu}X} \\ \times \left\{ e^{2i\bar{\mu}(X+2)} [1-(1+i)E^*(2\bar{\mu}(X+2))] \right\}^c \,, \end{aligned} \tag{2.111}$$

$$\text{where} \quad \Theta = \sqrt{\frac{N_1}{N}} \,, \qquad N_1 = \bar{K_1} + (1+M_a)\bar{\mu} \,, \qquad N = \bar{K} + (1+M_a)\bar{\mu} \,, \tag{2.112}$$

and where the notation $\{...\}^c$ stands for the imaginary part multiplied by a correcting factor $\varepsilon = (1 + 1/4\bar{\mu})^{-1/2}$. Substituting Equation 2.111 back into Equation 2.109, Roger and Moreau arrived at the following final formulation for the additional leading

edge disturbance pressure,

$$P_2(X,0) \backsimeq \frac{(1+i)e^{-4i\bar{\mu}}}{2\sqrt{\pi}(\eta-1)\bar{K}} \frac{1-\Theta^2}{\sqrt{N_1}} e^{i(M-1)\bar{\mu}X} \times \left\{ i[\bar{K}+(M_a-1)\bar{\mu}]\{-\}^c + \left(\frac{\partial}{\partial X}\{-\}\right)^c \right\} , \tag{2.113}$$

where $\{-\}^c$ represents the imaginary part of the term inside the braces in Equation 2.111 multiplied by the correcting factor ε.

Roger & Moreau [64] subsequently sought to extend the existing 2D formulation to account for streamwise and spanwise wall pressure wavenumber components K_1 and K_2, respectively. At a given frequency, each wavenumber corresponds to an oblique gust and so the scattering problem becomes three dimensional. As before, however, in order to simplify the formulation, the spanwise dimension is assumed to extend to infinity along the y-axis (i.e. so that the side edge effects may be neglected). Therefore, mathematically speaking, this method is only valid provided the span is large compared to the aerodynamic wavelengths $2\pi/K_2$ that carry a significant amount of energy in the incident turbulent pressure field (i.e. the spanwise turbulence correlation lengths). So, the convected wave equation could now be rewritten as,

$$\frac{\partial^2 p'}{\partial x^2} + \frac{\partial^2 p'}{\partial y^2} + \frac{\partial^2 p'}{\partial z^2} - \frac{1}{a_0^2}\left(\frac{\partial}{\partial t} + U\frac{\partial}{\partial x}\right)^2 p' = 0 . \tag{2.114}$$

It follows, therefore, that the solution sought has the following form,

$$p'(x,y,z) = \tilde{P}(x,y,z)e^{i\omega t} , \tag{2.115}$$

where

$$\tilde{P}(x,y,z) = p(x,y,z)e^{i(kM_a/\beta^2)x}e^{-iK_2 y} , \tag{2.116}$$

and that the incident wall pressure gust is now written as $P_0 = e^{-\eta\bar{K}X}e^{-\bar{k}_2 Y}$, where $Y = y/b$. The canonical wave equation then becomes,

$$\frac{\partial^2 p}{\partial X^2} + \frac{\partial^2 p}{\partial Z^2} + \bar{\kappa}^2 p = 0 , \tag{2.117}$$

where

$$\bar{\kappa}^2 = \bar{\mu}^2 - \frac{\bar{K}_2^2}{\beta^2} . \tag{2.118}$$

One proviso with this new parameter, however, is that $\bar{\kappa}^2$ remains positive. Thus,

$$|\bar{K}_2| < \frac{\bar{K}_1 M_a}{\eta\beta} , \tag{2.119}$$

where $\bar{K}_1 = \eta\bar{K}$ is the non-dimensional streamwise wavenumber. Now, when substituting $\bar{\mu}$ for $\bar{\kappa}$, the three main variables in Equation 2.109 change as follows. From Equation 2.107 P_1 becomes,

$$P_1(X,0) = e^{-\eta\bar{K}X}[(1+i)E^*(-[\eta\bar{K}+\bar{\kappa}+M_a\bar{\mu}]X) - 1]\,. \tag{2.120}$$

From Equation 2.111, ψ_2 becomes,

$$\begin{aligned}\psi_2(X,0) \backsimeq \left(\frac{-b}{\rho_0 U}\right)\frac{(1+i)e^{-4i\bar{\kappa}}}{2\sqrt{\pi}(\eta-1)\bar{K}}\frac{1-\Theta^2}{\sqrt{\eta\bar{K}+M_a\bar{\mu}+\bar{\kappa}}}e^{i(M_a\bar{\mu}-\bar{\kappa})X} \\ \times\left\{e^{2i\bar{\kappa}(X+2)}[1-(1+i)E^*(2\bar{\kappa}(X+2))]\right\}^c\,.\end{aligned} \tag{2.121}$$

An finally, from Equation 2.113, P_2 becomes,

$$\begin{aligned}P_2(X,0) \backsimeq \frac{(1+i)e^{-4i\bar{\kappa}}}{2\sqrt{\pi}(\eta-1)\bar{K}}\frac{1-\Theta^2}{\sqrt{\eta\bar{K}+M_a\bar{\mu}+\bar{\kappa}}}e^{i(M_a\bar{\mu}-\bar{\kappa})X} \\ \times\left\{i[\bar{K}+M_a\bar{\mu}-\bar{\kappa}]\{-\}^c + \left(\frac{\partial}{\partial X}\{-\}\right)^c\right\}\,.\end{aligned} \tag{2.122}$$

where
$$\Theta = \sqrt{\frac{\bar{K}_1+M_a\bar{\mu}+\bar{\kappa}}{\bar{K}+M_a\bar{\mu}+\bar{\kappa}}}\,. \tag{2.123}$$

Roger and Moreau [64] comment that, at a given acoustic Mach number, the propagating, or supercritical ($\bar{\kappa}^2 > 0$), gusts contribute most to the radiation. However, at higher frequencies and due to the finite span of the airfoil, the non-propagating, or subcritical ($\bar{\kappa}^2 < 0$), gusts will also begin to contribute. Furthermore, from Equation 2.119, it is clear that with increasing acoustic Mach number, more oblique gusts will also begin to contribute significantly. Using numerical methods, Roger and Moreau found that $\bar{K}_2$ had a negligible effect on the supercritical solution P_1, whereas for the subcritical case, an increase in $\bar{K}_2$ had resulted in a much faster decay upstream from the trailing edge. In this thesis, we will only have time to investigate the supercritical gust solution.

2.3.3.2 Far-field broadband radiation solution

In order to arrive at an expression for the acoustic pressure heard in the far-field, the induced field produced by all gusts must be integrated over the entire airfoil surface. A

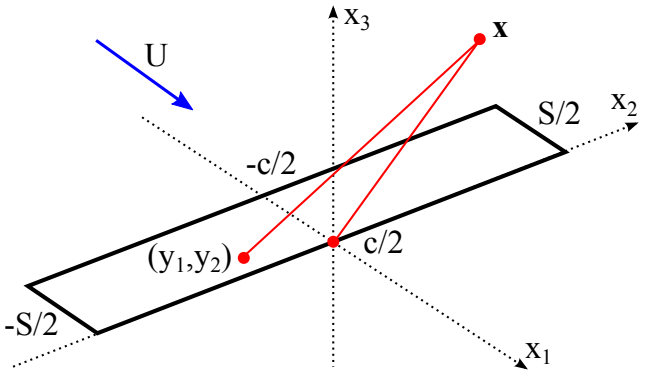

FIGURE 2.23: Radiation schematic [64]

schematic of this situation is depicted in Figure 2.23, where $\boldsymbol{x} = (x_1, x_2, x_3)$ is the observer location relative to the mid-span point on the trailing edge.

If we assume that the disturbance wall pressure has a wavenumber $\boldsymbol{K} = (K_1, K_2)$, we can write down Amiet's radiation integral [65] straight away,

$$p(\boldsymbol{x}, \omega) = \frac{-i\omega x_3}{4\pi c_0 S_0^2} \int_{-2b}^{0} \int_{-S/2}^{S/2} \Delta P e^{i\omega R_t/c_0} dy dx \,, \tag{2.124}$$

where $\Delta P = 2(P_1 + P_2) = 2P$, which represents the two source distributions induced on both sides of the airfoil (i.e. the equivalent lift fluctuations), and S is the total span of the airfoil. The convection of the acoustic waves by the flow is accounted for by the following coordinate modifications,

$$R_t = \frac{1}{\beta^2}[R_u - M_a(x_1 - x)] \,, \tag{2.125}$$

$$R_u = S_0 \left(1 - \frac{x_1 x + \beta^2 x_2 y}{S_0^2}\right) \,, \tag{2.126}$$

$$S_0^2 = x_1^2 + \beta^2(x_2^2 + x_3^2) \,. \tag{2.127}$$

If we now assume that $P = f(X)e^{-i(\bar{K_1}X - \bar{K_2}Y)}$ and that f is the complex amplitude of the source distribution, Equation 2.124 then becomes,

$$\begin{aligned} p(\boldsymbol{x}, \omega) = \frac{-i\omega x_3}{2\pi c_0 S_0^2} b^2 \int_{-2}^{0} \int_{-S/(2b)}^{S/(2b)} f(X) e^{-i(\bar{K_1}X - \bar{K_2}Y)} \\ \times e^{-i\frac{k}{\beta^2}\left[S_0 - \frac{x_1 X + \beta^2 x_2 Y}{S_0} b - M_a(x_1 - bX)\right]} dY dX \,. \end{aligned} \tag{2.128}$$

Now, when integrating with respect to Y (i.e. spanwise), Equation 2.128 reduces to,

$$\begin{aligned} p(\boldsymbol{x},\omega) = \frac{-i\omega x_3 Sb}{2\pi c_0 S_0^2}\mathrm{sinc}\left\{\frac{S}{2b}\left(\bar{K}_2 - \bar{k}\frac{x_2}{S_0}\right)\right\} \\ \times e^{-i(\frac{k}{7}\beta^2)(S_0 - M_a x_1)}\int_{-2}^{0} f(X)e^{-iCX}dX\,, \end{aligned} \tag{2.129}$$

where $$\mathrm{sinc}(x) = \sin(x)/x\,, \qquad C = \bar{K}_1 - \bar{\mu}\left(\frac{x_1}{S_0} - M_a\right)\,. \tag{2.130}$$

Then, when integrating with respect to X (i.e. streamwise), Amiet's supercritical gust radiation solution for the principal P_1 term can be expressed as,

$$\begin{aligned} I_1 &= \int_{-2}^{0} f_1(X)e^{-iCX}dX \\ &= -\frac{e^{2iC}}{iC}\left\{(1+i)e^{-2iC}\sqrt{\frac{B}{B-C}}E^*[2(B-C)] - (1+i)E^*[2B] + 1\right\}\,. \end{aligned} \tag{2.131}$$

where $$B = \bar{K}_1 + M_a\bar{\mu} + \bar{\kappa}\,. \tag{2.132}$$

Roger and Moreau's [64] final back-scattered radiation integral solution for the back-scattered P_2 term, is displayed below,

$$\begin{aligned} I_2 &= \frac{1}{H}\int_{-2}^{0} f_2(X)e^{-iCX}dX \\ &= \left\{e^{4i\bar{\kappa}}[1-(1+i)E^*(4\bar{\kappa})]\right\}^{\,c} - e^{2iF} + i[F + \bar{K} + M_a\bar{\mu} - \bar{\kappa}]G\,, \end{aligned} \tag{2.133}$$

with $$H = \frac{(1+i)e^{-4i\bar{\kappa}}(1-\Theta^2)}{2\sqrt{\pi}(\eta-1)\bar{K}\sqrt{B}}\,, \qquad F = \bar{\kappa} - \bar{\mu}x_1/S_0\,, \tag{2.134}$$

where

$$\begin{aligned} G = (1+\varepsilon)e^{i(2\bar{\kappa}+F)}\frac{\sin(F-2\bar{\kappa})}{F-2\bar{\kappa}} + (1-\varepsilon)e^{i(-2\bar{\kappa}+F)}\frac{\sin(F+2\bar{\kappa})}{F+2\bar{\kappa}} \\ + \frac{(1+\varepsilon)(1-i)}{2(F-2\bar{\kappa})}e^{4i\bar{\kappa}}E^*(4\bar{\kappa}) - \frac{(1-\varepsilon)(1+i)}{2(F+2\bar{\kappa})}e^{-4i\bar{\kappa}}E(4\bar{\kappa}) \\ + \frac{e^{2iF}}{2}\sqrt{\frac{2\bar{\kappa}}{F}}E^*(2F)\left[\frac{(1+i)(1-\varepsilon)}{F+2\bar{\kappa}} - \frac{(1-i)(1+\varepsilon)}{F-2\bar{\kappa}}\right]\,, \end{aligned} \tag{2.135}$$

and where the error function $E(x) = 1 - E^*(x)$. The three expressions required to calculate the far-field acoustic pressure from supercritical gusts, therefore, are

Equations 2.129, 2.131 and 2.133. The latter two of these three equations provide information about the polar directivity pattern generated by a leading edge back-scattered pressure field. The following directivity factor expression will be used later on in the thesis to attempt to explain the jet-surface interaction noise directivity,

$$D(\theta_e) = \frac{kcx_3}{S_0}|I_1 + I_2| \,. \tag{2.136}$$

Now these radiation integrals, Equations 2.131 and 2.133, still only hold for a unit gust with wavenumbers ($\bar{K}_1$,$\bar{K}_2$) at frequency ω. In order to arrive at an expression for the far-field power spectral density, therefore, an integration over all gusts with 2D wavenumbers must be made. As detailed in Amiet's 1975 JSV paper [65], the incident pressure field is assumed to be frozen when convected past the airfoil trailing edge, i.e. $K_1 = \omega/U_c$. The corresponding disturbance pressure distribution P over the airfoil surface, therefore, can be written as,

$$P(x, y, \omega) = \frac{1}{U_c}\int_{-\infty}^{\infty} g\left(x, \frac{\omega}{U_c}, K_2\right) A_0\left(\frac{\omega}{U_c}, K_2\right) e^{-iK_2 y} dK_2 \,, \tag{2.137}$$

where g represents the transfer function between the incident pressure P_0 of amplitude A_0 and the disturbance pressure P (as calculated by the Schwarzschild procedure). One can further analyse P if one assumes that the incident wall pressure field induced by the turbulence on the airfoil is a stationary random process. The corresponding cross-power spectral density between two points on the surface at (x, y) and (x', y'), with $y - y' = \eta$, is then given by,

$$S_{PP}(x, x', \eta, \omega) = \frac{1}{U_c}\int_{-\infty}^{\infty} g\left(x, \frac{\omega}{U_c}, K_2\right) g^*\left(x', \frac{\omega}{U_c}, K_2\right) e^{-iK_2\eta} \Psi_0\left(\frac{\omega}{U_c}, K_2\right) dK_2 \,, \tag{2.138}$$

where Ψ_0 denotes the wavenumber spectral density of the incident gust amplitudes A_0. Finally, we reach the corresponding power spectral density (PSD) of the far-field sound,

$$S_{pp}(\boldsymbol{x}, \omega) = \left(\frac{\omega x_3 L b}{2\pi a_0 S_0^2}\right)^2 \frac{1}{b}\int_{-\infty}^{\infty} \Psi_0\left(\frac{\omega}{U_c}, K_2\right) \mathrm{sinc}^2\left\{\frac{L}{2b}\left(\bar{K}_2 - \bar{k}\frac{x_2}{S_0}\right)\right\} \times \left| I\left(\frac{\bar{\omega}}{U_c}, \bar{K}_2\right)\right|^2 d\bar{K}_2. \tag{2.139}$$

The final simplification we can make to this expression comes if we assume the characteristic scales of the near pressure field close to the trailing edge are small when compared to the chord length. The sinc term in Equation 2.139 can then be written as,

$$\mathrm{sinc}^2\left\{\frac{L}{2b}\left(\bar{K}_2 - \bar{k}\frac{x_2}{S_0}\right)\right\} \simeq \frac{2\pi b}{L}\delta\left(\bar{K}_2 - \bar{k}\frac{x_2}{S_0}\right) \,, \tag{2.140}$$

which results in the selection of an oblique gust off the mid-span plane for each angle of radiation. The final far-field expression for a trailing edge plus leading edge

scattered pressure field produced by a convecting spanwise distribution of turbulent gusts past a trailing edge can be written as follows,

$$S_{pp}(\boldsymbol{x},\omega) = \left(\frac{\omega x_3 b}{2\pi a_0 S_0^2}\right)^2 2\pi L \left|\left(I\frac{\bar{\omega}}{U_c},\bar{k}\frac{x_2}{S_0}\right)\right|^2 \Psi_0\left(\frac{\omega}{U_c},k\frac{x_2}{S_0}\right) . \tag{2.141}$$

It should be stressed at this point that this formulation by Roger and Moreau assumes that this uniform flow contains frozen turbulence and is convected at a subsonic acoustic Mach number along an airfoil (parallel to the chord line) and past its trailing edge. It has yet to be seen, therefore, whether these assumptions are valid for use with a non-uniform, spreading jet flow application containing decaying turbulence. The other important parameter to recognise with this approach is the spanwise correlation length of the pressure field distributed along the trailing edge, Λ_y. Indeed, Brooks and Hodgson [18] and Roger and Moreau [66] have both shown far-field noise to be proportional to this spanwise correlation length. Further discussion surrounding this approach can be found later on in the thesis, in Sections 4.3.2.5 and 4.3.3.5.

2.4 Installed Jet Noise Literature Review

The main focus of the work in this thesis concerns the understanding and prediction of installed jet noise for an under-wing-mounted (UWM) modern turbofan engine, see Figure 2.8. As engine efficiency continues to increase, the size of the nacelle is also set to grow. Due to ground clearance constraints placed on UWM engine aircraft, the axis of the jet must move vertically upwards closer to the wing. Thus, any interaction between the turbulent jet plume and the wing (or deployed flap) trailing edges will also increase. It is crucial, therefore, that the aviation industry is able to predict and guard against the potential additional noise generated by such future closely-coupled jet-wing configurations.

To attack this problem, it is important to understand the physics of the various mechanisms involved. It is helpful, therefore, to simplify the problem. A schematic of the first level of simplification can be see below, in Figure 2.24. While parameters, such as the spanwise sweep angle of the wing (and flap), have not been taken into account here, the problem is still extremely complex. Examples of some of these complex effects include: (1) the presence of the engine pylon, which will add an asymmetry to the development of the upper jet shear layer, (2) the heated, coaxial jet, which will add additional shear terms to the isolated jet noise source, and (3) the presence of the non-parallel incident flight stream, U_f, which will generate a lift force on the wing and redirect the jet away from the wing. Since all of these effects will mask the fundamental jet-wing (or jet-flap) interaction effects, it is necessary to simplify the problem even further. Only then can each source mechanism be isolated and characterised fully.

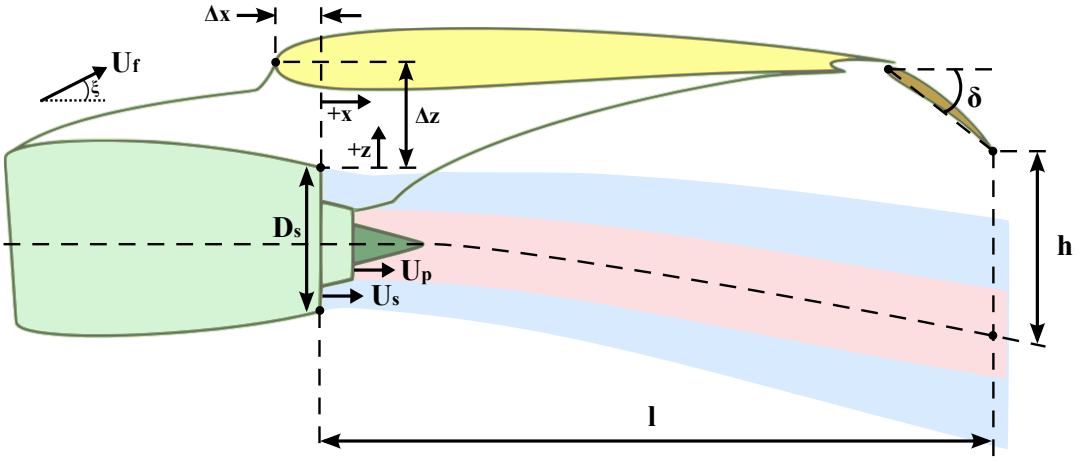

FIGURE 2.24: Installed coaxial jet schematic

In 1976, Head and Fisher [67] published results from a series of small-scale, jet-surface interaction experiments, in which they positioned a static, single stream, circular, subsonic, unheated jet next to a semi-infinite flat plate shield, see Figure 2.25. The

plate was termed 'semi-infinite' because it extended axially far upstream of the jet nozzle exit, preventing the generation of any leading edge noise. Using far-field microphone data above and below the plate (i.e. on the shielded and unshielded sides, respectively), Head and Fisher were able to identify the two principal jet installation effects - jet-surface reflection (JSR) and jet-surface interaction (JSI) noise, see Figure 2.26.

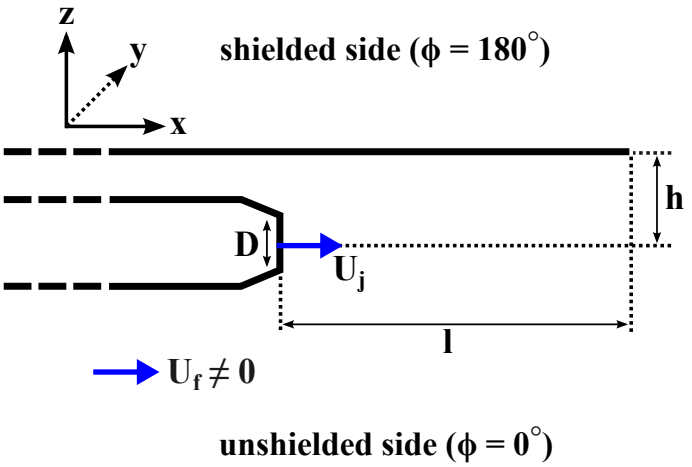

FIGURE 2.25: Schematic of a single stream jet plus a semi-infinite horizontal flat plate

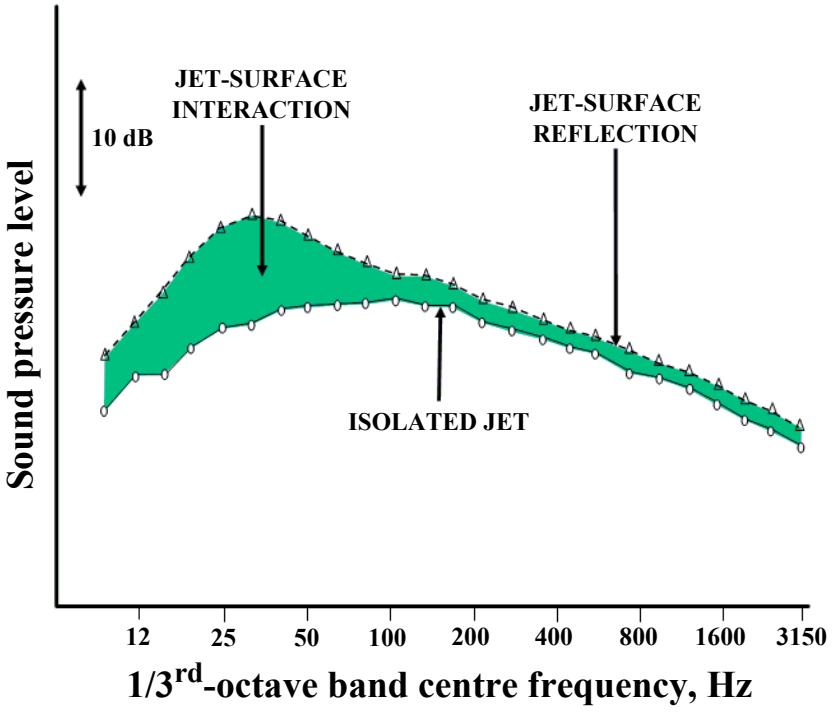

FIGURE 2.26: Typical installed jet noise spectrum (full-scale); $[\theta = 90°, \phi = 0°]$

The JSR noise was seen at high frequencies parallel to, and no more than 3 dB above, the isolated jet noise spectrum, whereas the JSI noise was seen at much lower frequencies and as much as 10 dB above the isolated jet noise spectrum for some

configurations. Regarding the far-field behaviour of parameters h and l, it was found that the JSI noise generally decreased with increasing h and increased with increasing l.

A 180° phase shift was also observed in the far-field signals either side of the shield, suggesting the presence of a dipole. A small number of far-field microphones, however, made it difficult to make robust conclusions about the JSI noise directivity and, hence, the source mechanism itself. Thus, the additional low frequency far-field JSI noise produced was attributed solely to an unspecific dipole source driven by local jet near-field pressures at the plate trailing edge. Yu and Tam's subsequent experiment with a rectangular 'wall jet' (i.e. when a jet flow is blown tangentially along a wall) and a flat plate further confirmed that a highly coherent sound field existed in exact opposition across the trailing edge [68].

On a real full-scale aircraft, Bushell was the first to observe significantly higher installed, in-flight jet noise levels compared to an isolated, static jet on a test bed [69]. Szewczyk [70] and Bryce [71] then formally confirmed the difference between model simulation and experiment flight data as *installation noise*. In the early 1980s, Southern [72], Way and Turner [73], Reddy and Tanna [74], Wang [75] and Underwood and Hodgson [56] all published experimental test results, which further quantified the change in sound pressure level (SPL) due to the installation of a realistic wing above a coaxial jet. The high frequency portion of additional noise was identified as reflected jet noise from the underside of the wing, but was noted to be considerably less than the 3 dB expected from the perfect addition of two incoherent pressure fields. Way and Turner attributed this discrepancy to an attenuation of acoustic rays propagating through the turbulent jet exhaust plume enroute to the far-field [73]. All five of these studies also identified the presence of the low frequency JSI source between the jet and the wing. At the time, however, the source mechanism itself was largely neglected since, at full-scale, the peak frequency of interest was below that which could be perceived by the human ear. Way and Turner [73] also attempted to create an empirical prediction scheme based upon Head and Fisher's far-field data but were unable to match both the JSI noise peak level and frequency satisfactorily for different jet-wing configurations.

Some of the first experiments involving configurations where the exhaust jet impinged upon a deployed flap were also performed by Way and Turner [73]. Compared to the isolated jet case, an increase in noise below 400 Hz (full-scale) was measured, however, further research was deemed necessary to better understand the jet-flap mechanism(s) involved.

Regarding static-to-flight effects, Southern [72] speculated that the JSI noise should reduce in-flight because of two effects. Firstly, the lift produced by the wing would

redirect the jet further away from the trailing edge. Secondly, the spreading rate of the jet would also reduce in flight. Either way, the result would be an increase in vertical separation between jet and wing and, thus, a reduction of the JSI noise source strength itself.

In 1983, further model-scale installed jet data were published by Shearin [76], SenGupta [77] and Miller [1]. SenGupta suggested that the installed noise spectrum consisted of a low frequency fluctuating lift noise, a mid frequency trailing edge noise and a high frequency reflection noise. The low and mid frequency sources depended on whether the wavelength of sound was large or small, respectively, compared to the wing chord. Miller [1] then produced the following empirical polar directivity function to account for the forward-arc interference between two acoustic waves travelling upstream from the trailing edge above and below the wing,

$$D(\theta_e) = \sqrt{1 - \left(R\cos\left(\pi N_w\right)\right)^2}\cos\left(\frac{\theta_e + \delta}{2}\right), \tag{2.142}$$

where
$$R = \left(1 - \frac{\theta_e}{\pi}\right)^{0.25} e^{\left[-\frac{c}{2\pi\lambda}(\theta_e+\delta)\right]}, \tag{2.143}$$

and
$$N_w = \left(r_T - r_L - \frac{c}{1 - M_f}\right)/\lambda\,. \tag{2.144}$$

The variables r_T and r_L are the distances from the trailing and leading edges, respectively, to the far-field observer position, c is the wing chord, δ is the flap deployment angle (relative to the wing chord) and M_f is the flight acoustic Mach number.

The next model-scale installed jet test data were published by Shivashankara and Blackner [78], in 1997. In their 1/20th-scale installed, coaxial, heated jet investigation, the authors noted how the presence of both the wing and the engine pylon modified the axisymmetric shape of the jet. This was particularly relevant for the secondary shear layer of the jet, which was believed to generate much of the flap trailing edge scattering noise and the wing reflection noise.

In the following year, Mead and Strange [79] published an extensive experimental investigation of model-scale jet installation effects using a planform flat plate wing and a single stream jet. Of key note was their conclusion that the addition of an ambient flight stream flow served to reduce the lower frequency jet-surface interaction noise but did not affect the higher frequency reflection installation noise.

Pastouchenko and Tam used numerical methods (parabolized Reynolds-averaged Navier-Stokes equations) to simulate the downwash caused by a flap when scrubbed by

a subsonic jet [80]. Unfortunately, it was not possible to capture the relevant large-scales due to the fine-scale turbulence model used. More recently, Mengle reported another model-scale coaxial jet experimental campaign and concluded that by reducing the radial separation between the jet and flap trailing edge, the far-field installed noise increased [81]. Most recently, Cavalieri *et al.* performed a series of jet plus flat plate acoustic model-scale experiments for a variety of subsonic Mach numbers and vertical jet-plate separations [82]. Their preliminary results supported the theory for the scattering of the irrotational, hydrodynamic jet near-field by the plate trailing edge.

It has, thus, become evident that better clarity of the specific mechanism(s) by which JSI noise is generated and radiated is required.

2.4.1 Jet-surface reflection noise

In principle, jet surface reflection noise is well understood. Moore and Mead [83] and Moore [84] were the first to outline a prediction method based on a 3-dimensional ray-theory approach, where a point source with an empirically prescribed directivity and strength (taken from far-field acoustic data) would represent any part of the jet source. The wing (and flap) geometry would then be represented by a number of flat surfaces.

Berton [85] used an asymptotic method (used in optics) to calculate the diffracted field of engine sources for novel over-wing-mounted turbofans. This configuration was seen successfully to shield the high frequency reflection effects generated by under-wing-mounted engines. Chappuis *et al.* [86] later presented an analytical model on aft fan noise shielding based on diffraction by a semi-infinite flat plate. By applying a predetermined phase difference to a series of monopoles, together with an understanding of the source directivity, they were able to arrive at a reasonable agreement with boundary element method (BEM) numerical and experimental results.

In 1999, Clark and Gerhold [87] published the first experimental acoustic shielding study on a novel Blended Wing Body (BWB) aircraft geometry. This work was followed up by Gerhold *et al.* [88], who used a boundary element method to predict the incident field due to a point source in a nacelle and an equivalent source method to determine the scattered field from the BWB. The results, however, were only limited to relatively simple geometries and low frequencies due to the amount of computational power required. Agarwal *et al.* [89] then, in 2006, published a ray-tracing model to calculate the scattered acoustic field created by the shielding effect of a BWB aircraft.

The model accounts for both edge-diffracted and creeping rays and was validated using model-scale experimental data and numerical boundary element results.

More recently, McLaughlin *et al.* [90] and Young *et al.* [91] each created semi-empirical prediction tools for reflection and shielding configurations, respectively. McLaughlin developed a new three-dimensional ray theory propagation method for sources in a steady inhomogeneous moving medium using an empirical hot jet blockage model, CFD jet velocity profiles and flat plate wing surface segments. Although the method was benchmarked against an analytical solution of the Lilley equation, there still remain questions regarding the validity of the assumptions used for more complex propagation problems, like when a flap is deployed at an angle or when looking at small polar angles close to the jet axis.

2.4.2 Jet acoustic blockage

As acoustic waves attempt to propagate through a jet, their energy is redistributed via two separate mechanisms. The overall effect is known as acoustic jet blockage. The first mechanism involves the refraction of acoustic rays across a velocity and a temperature gradient. The effects are most noticeable, therefore, when the temperature and velocity of the core jet flow are high compared to the bypass or ambient flows. In 2003, Moore and Mead [83] stated that the inclusion of the acoustic blockage by a hot jet is essential in any prediction of under-wing reflection noise. Moore then went on to create the first 3-dimensional semi-empirical hot jet blockage model [84]. In 2008, McLaughlin *et al.* [90] used Lilley's infinite parallel isothermal jet solution, together with a new database of point source propagation data through a realistic jet flow, to develop another high-frequency, far-field semi-empirical engineering prediction tool for jet blockage.

The second mechanism involves energy scattered by the turbulence itself within the jet shear layers. This mechanism is often referred to as hay-stacking when studying tonal noise propagation problems. The highly dissipative shear layer region scatters energy into neighbouring frequency bands and a broader tone with a reduced peak amplitude is then seen in the far-field. This particular research field is currently very active.

2.4.3 Jet redirection and lift effects

If the entrainment properties of a free, axisymmetric jet are restricted due, for example, to the presence of a solid surface, a Coandă, or redirection, effect will result. Under static ambient flow conditions, a flow in close proximity to a surface (e.g. a jet

flow beneath an aircraft wing) will certainly bend towards the surface. Similarly, under in-flight ambient flow conditions, if a lift force is produced by the flow around the airfoil, the high pressure region beneath the airfoil will act to redirect the jet away from the surface. Intuitively, the closer the surface is to the jet, the greater the Coandă or lift redirection effect will be. A greater redirection effect will also result when a smaller relative velocity exists between the jet and the ambient flow beneath the wing. While this particular effect is not extensively studied in this thesis, it is nevertheless important, at least, to acknowledge and keep in mind.

Chapter 3

Near-Field Isolated Jet Noise

As mentioned in the literature in the previous chapter, jet-surface interaction (JSI) noise is currently believed to be generated by diffraction of the jet near pressure field around the trailing edge of an aircraft wing or flap. Understanding the structure and behaviour of the near pressure field of an isolated free jet, therefore, is an important first step to predicting installed jet-surface interaction noise. This chapter investigates the pressure field generated by a subsonic, single stream, axisymmetric, unheated jet under static ambient flow conditions. Previous experimental work is first reviewed before new experimental results are presented detailing both the near and far regimes of the pressure field produced by a model-scale isolated jet. Finally, a read-across is made between a small model-scale university jet and a large model-scale industrial jet.

3.1 Introduction

The pressure field generated by a jet can be divided into two parts: (1) an evanescent hydrodynamic near-field, which does not propagate away from the source region, and (2) a true 'acoustic' field, which propagates to the far-field. The far-field of a source is the region in which the pressure field decays according to the laws of geometrical acoustic spreading (i.e. the inverse square law). This is true for a compact, or point, source where the sound pressure and acoustic particle velocity are in-phase. For every doubling of distance, therefore, the sound intensity measured (under free-field conditions) will decrease by 6 dB. The near-field, however, is the region close to a source where no clear phase relationship exists between the sound pressure and acoustic particle velocity. The acoustic intensity, here, is seen to decay exponentially, or evanescently, with distance. The hydrodynamic pressure fluctuations are generated by vortical structures, or instabilities, which convect downstream within the jet shear

layer. The propagation velocity and amplitude of these pressure waves, therefore, scale with jet velocity (as opposed to the far-field acoustic waves, which propagate at the speed of sound). The corresponding wavelength is known as the hydrodynamic, or instability, wavelength, λ_h, and is defined as follows,

$$\lambda_h = \frac{U_c}{2f}\,, \tag{3.1}$$

where U_c is the instability convection velocity. In 1984, Ho and Lafouasse [92] concluded that, for a circular jet, this hydrodynamic near-field regime extends approximately one hydrodynamic wavelength normal to the jet. This was later also shown to be true for an elliptic jet [93]. If, however, the length-scale associated with the source, $\mathfrak{L}$, is larger than one wavelength, then the hydrodynamic field generally extends out by a factor of $3\mathfrak{L}$.

Due to the differences in wave phase velocity, v, between the hydrodynamic and acoustic jet pressure fields, the respective regimes are better defined in terms of a non-dimensional wavenumber, kr_{lip}, where $k = \omega/v$ and r_{lip} is the radial distance from the nozzle lip-line, see Figure 3.1. The lip-line is chosen because it is the region of maximum turbulence within a free, circular jet upstream of the end of the potential core. Beyond the potential core (i.e. at approximately $x/D > 4$), the area of maximum turbulence gradually moves towards the jet centreline (see dotted red line in Figure 3.1). In the limit as the product of the wavenumber and distance becomes large ($kr_{\text{lip}} \gg 1$), the mean-square pressure exhibits far-field behaviour. This implies that the sound intensity of the acoustic far-field decays as $I \propto (kr_{\text{lip}})^{-2}$.

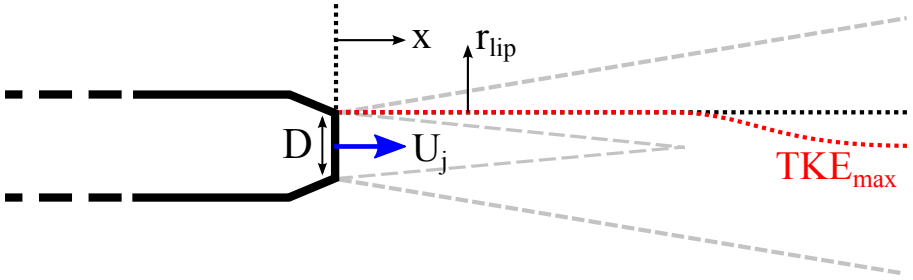

FIGURE 3.1: Isolated jet schematic illustrating the line of maximum turbulence kinetic energy (TKE) within the jet

Within the hydrodynamic near-field, however, two further sub-regimes can be identified: (1) a rotational (non-linear) pressure field and (2) an irrotational (linear) pressure field. Firstly, the rotational pressure regime can be thought of as the large-scale vortical structures, or eddies, in the flow. Previous studies [94–100] have determined that, for a turbulent flow, the maximum contribution to the mean-square pressure fluctuation (i.e. the maximum turbulence kinetic energy within the jet) is from wavenumbers in the energy-containing range (i.e. when the turbulent velocity

spectrum function, $E(k)$, is a maximum). Contributions to the pressure-gradient fluctuations, however, were seen to come from the inertial sub-range (i.e. when $kE(k)$ is a maximum). Kolmogorov [26] defined the spectral shape of this region in his second similarity hypothesis as,

$$E(k) = C_K \epsilon^{2/3} k^{-5/3} \,, \tag{3.2}$$

where C_K is the Kolmogorov constant and ϵ is the dissipation rate of energy per unit mass. In the early 1950s, Batchelor [101] and Inoue [102] were the first to take this velocity spectrum function result and, using dimensional analysis, derive an expression for the pressure-spectrum function, $\pi(k)$, in a free turbulent shear layer,

$$\frac{\pi(k)}{\rho^2} \propto \epsilon^{4/3} k^{-7/3} \,. \tag{3.3}$$

Later on that decade, Kraichnan [103] and Lilley [104] succeeded in deriving the complete expression for the pressure fluctuations in a free turbulent shear flow by decomposing the velocity field into mean and fluctuating parts and ignoring the third-order velocity moments. This then revealed the turbulence-mean-shear and the turbulence-turbulence sources. The latter term matched the previous work by Batchelor and Inoue and has since been validated experimentally by George *et al.* [105]. The rotational jet hydrodynamic pressure intensity, therefore, has been proven to decay as $I \propto (kr_{\text{lip}})^{-7/3}$.

The second component of the non-propagating hydrodynamic jet pressure field is the irrotational pressure regime. In 1997, Arndt *et al.* [106] took the unsteady Bernoulli equation and, assuming unbounded turbulence, used the following spherical wave equation solution [107] to solve for the velocity potential, ϕ_s,

$$\phi_s = \frac{\partial^2}{\partial r_{\text{lip}}^2} \left\{ \frac{-iqR_0^2}{4\pi r_{\text{lip}}} e^{i(\omega t - k r_{\text{lip}})} \right\} \,, \tag{3.4}$$

where q is the source strength and R_0 is the source size. Given the boundary condition for an axial quadrupole,

$$-\left. \frac{\partial \phi_s}{\partial r_{\text{lip}}} \right|_{r_{\text{lip}}=R_0} = iU_0 \cos^2\theta_j e^{i\omega t} \,, \tag{3.5}$$

the following general solution for the mean-square pressure was found,

$$I = \frac{(P - P_\infty)^2}{\rho_0 a_0} = \rho_0 a_0 U_0^2 (kR_0)^2 \left[\frac{R_0}{r_{\text{lip}}} \right]^6 \left| \frac{2 + 2ikr_{\text{lip}} + (ikr_{\text{lip}})^2}{B} \right|^2 \,, \tag{3.6}$$

where

$$B = 6 - 3(kR_0)^2 + i[6kR_0 - (kR_0)^3] \,, \tag{3.7}$$

and where $\rho_0 a_0$ is the acoustic impedance. If one assumes that long-wavelength disturbances are associated with large sources, and vice versa, it is also reasonable to assume that the product kR_0 stays approximately constant. Thus, as $kr_{\text{lip}} \ll 1$ and while $r_{\text{lip}} > R_0$, the following expression is reached for the near-field mean-square pressure intensity,

$$I \propto \rho_0 a_0 U_0^2 (kr_{\text{lip}})^{-6} \,. \tag{3.8}$$

From this result, Arndt's final step was to liken the source velocity, U_0, to the typical jet shear layer turbulence intensity, such that $U_0^2 \sim kE(k)$. Now, given Equation 3.2, the irrotational hydrodynamic intensity within the inertial sub-range was seen to have the following spectral variation,

$$I \propto (kr_{\text{lip}})^{-20/3} \,. \tag{3.9}$$

In summary, Figure 3.2 illustrates the four spectral energy regions of pressure fluctuations generated by a turbulent jet: 1) the low-wavenumber region, at $kr_{\text{lip}} < 0.2$, 2) the energy-containing region, at $0.2 < kr_{\text{lip}} < 0.8$, where the spectral decay is kr_{lip}^{-6}, 3) the inertial subrange, at $0.8 < kr_{\text{lip}} < 2.0$, where $kr_{\text{lip}}^{-20/3}$ and 4) the acoustic far-field, at $kr_{\text{lip}} > 2.0$, where kr_{lip}^{-2}. Arndt *et al.* [106] defined this $kr_{\text{lip}} = 2$ frequency-dependent dividing line between the near-field and far-field regions at low Mach numbers.

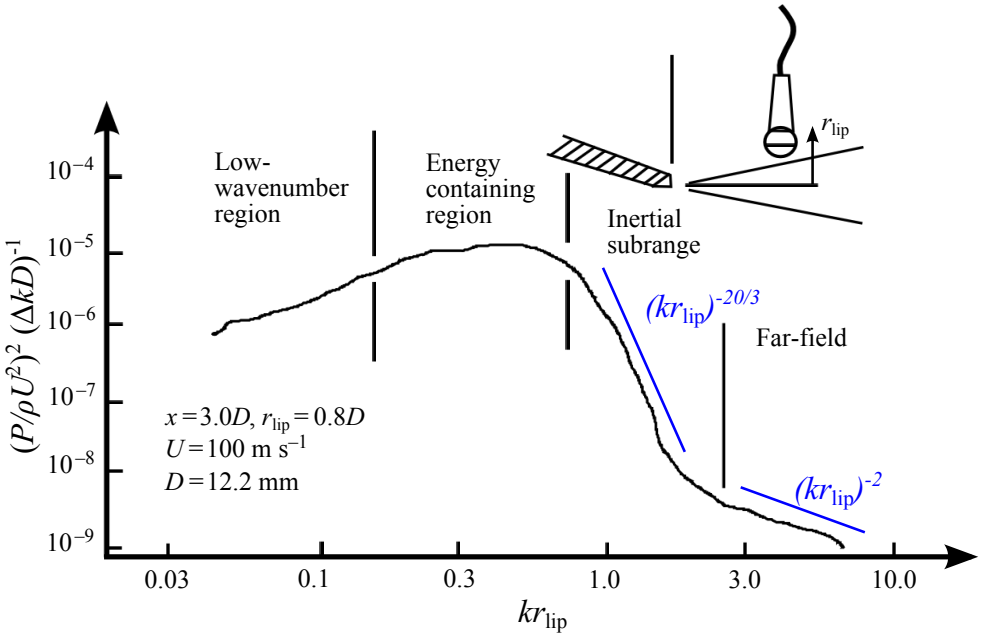

FIGURE 3.2: A typical spectrum illustrating all four regions of the pressure fluctuations generated by a turbulent jet [106]

The rest of this chapter initially describes an experiment designed to verify both the

spectral composition and the spatial decay of the irrotational hydrodynamic near pressure field of a high-speed, subsonic jet. Secondly, a simple, semi-empirical model is developed to predict the near pressure field spectrum of an isolated free jet. Later on, in Chapter 4, this free jet spectrum will then be compared to an 'equivalent' installed surface pressure spectrum measured at the trailing edge of a flat plate installed next to the same single stream, subsonic jet (see Section 4.3.3.2). It is hoped that the far-field installed jet spectrum, eventually, can be recreated quickly from such an isolated jet hydrodynamic pressure model and a simple near-field to far-field propagation model that takes into account the diffraction and scattering of sound from the aircraft wing (see the future work section of Chapter 8).

3.2 Experiment Design

A model-scale isolated jet experiment was undertaken in the Doak Laboratory (DOAK), within the Institute of Sound and Vibration Research (ISVR), at the University of Southampton (UoS), UK. The DOAK jet facility is approximately 15 m x 7 m x 5 m and is fully anechoic down to 400 Hz, see Figure 3.3.

FIGURE 3.3: Photograph of the ISVR Doak Laboratory (approx. $1/50^{\text{th}}$ model-scale)

For this small-scale experiment, an unheated airflow was passed through an upright 'labyrinth' silencer and into a 570 mm parallel pipe section to reach a single stream, 28° convergent, conical test nozzle with a 38.1 mm inner exit diameter, D, see Figure 3.4. This nozzle was chosen so that direct comparisons could be made with QinetiQ's 86.1 mm static, single stream jet nozzle noise database. This is an important exercise since the question of Reynolds number scaling effects from small-scale to large-scale model jets is still a sensitive research topic [108]. This point will be revisited later on, in Section 3.4.2.

The DOAK facility houses 2 horizontal, unheated, circular jet rigs: 1) a 101.6 mm diameter rig, and 2) a 50.8 mm diameter rig. In order to control the mass flow through a 38.1 mm jet, a Fisher 67C control valve was used with the smaller 50.8 mm rig. The jet was then operated over a range of jet acoustic Mach numbers ($M_a = U_j/a_0 = 0.30$, 0.50, 0.75 and 0.90). The conditions of the air stream and acoustic Mach number set points were determined from real-time measurements of total temperature and total

pressure and were kept within tolerances of ±2 m/s. An Omega thermocouple probe was installed well upstream of the nozzle to measure the total temperature of the flow and a Druck PDCR-820 1 bar transducer was fixed to the top of the silencer plenum to record the total pressure. To ensure accurate acoustic propagation representation, ambient temperature, relative humidity and ambient pressure instrumentation were also set up within the laboratory. An Omega HX94V probe recorded the ambient temperature and relative humidity and a Druck DPI-142 barometer recorded the ambient chamber pressure.

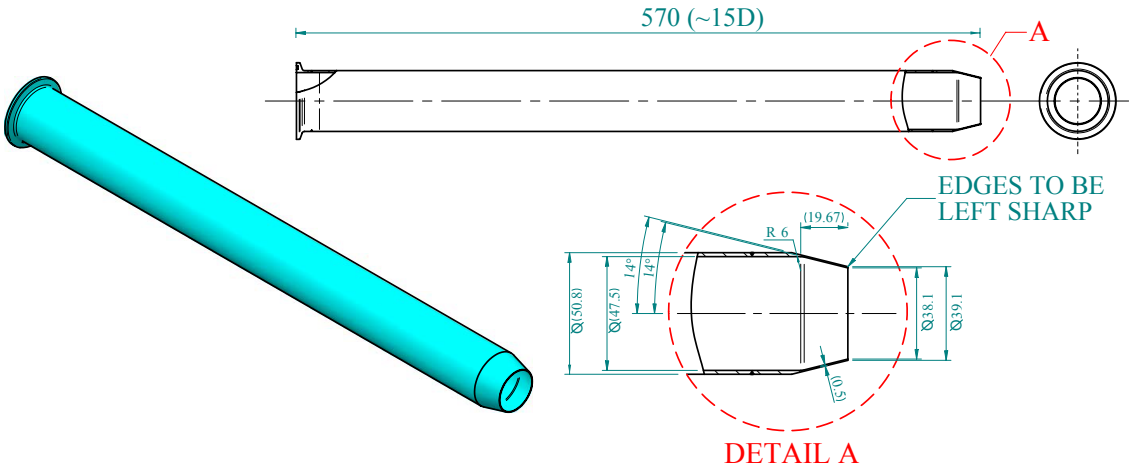

FIGURE 3.4: DOAK 38.1 mm diameter single stream nozzle schematic

The nozzle exit acoustic Mach number set points were calculated using the isentropic, adiabatic compressible flow equations. The pressure ratio, PR, is defined as the ratio between the total pressure, p_T, measured in the plenum and the ambient chamber pressure, p_0, into which the flow is expanded. If one assumes the flow velocity in the plenum is zero, a static pressure, p_s, taken from a plenum surface tapping can be used to represent the total plenum pressure. If $PR = p_T/p_0$, the temperature ratio, TR, can be written down straight away as,

$$TR = PR^{\left(\frac{\gamma-1}{\gamma}\right)}\,, \tag{3.10}$$

where γ is the adiabatic index of dry air ($\gamma = 1.4$ at 20° Celsius). The exit aerodynamic Mach number of the flow, therefore, is,

$$M = \sqrt{\frac{2(TR-1)}{\gamma-1}}\,, \tag{3.11}$$

and so the jet exit velocity, U, will be,

$$U = M \cdot \sqrt{\gamma \cdot R_c \cdot T_s} = M \cdot \sqrt{\gamma \cdot R_c \cdot \frac{T_T}{TR}}\,, \tag{3.12}$$

where R_c is the specific gas constant for dry air and T_s and T_T are the static and total temperatures of the flow, respectively. Finally, to arrive at the jet exit acoustic Mach number, M_a, the following equation must be used to account for the ambient speed of sound,

$$M_a = \frac{U}{\sqrt{\gamma R_c T_0}}\,, \tag{3.13}$$

where T_0 is the ambient chamber temperature.

For this particular test campaign, three acoustic measurement arrays were used: 1) a fixed polar far-field array, 2) a traversable azimuthal far-field array, and 3) a traversable near-field array. The near-field measurements, however, were made separately to the far-field. Further details of the arrays are presented in the following sections.

3.2.1 Far-field acoustic set-up

Polar measurements of the acoustic far-field were made using a fixed array on one side of the jet (at azimuthal angle $\phi = 0°$). The fixed polar array contained ten 1/4-in GRAS Type 40BF condenser microphone capsules, each conditioned with a B&K Falcon Type 2670 pre-amplifier. The microphones were positioned between polar angles $40° \leq \theta_j \leq 130°$ at 10° intervals, where the angle θ_j is defined relative to the jet axis. Each microphone was mounted within a long, thin, rigid tube and attached to a microphone stand at nozzle height. It was important to position the diaphragm of the microphone as far away as possible from the microphone stand to reduce adverse high frequency reflection effects. Each microphone on this array was oriented at 0° incidence to the nozzle.

For the azimuthal far-field array, a further five 1/4-in GRAS Type 40BF condenser microphone capsules (with B&K Falcon Type 2670 pre-amplifiers) populated a semi-circular trilite structure, centred on the jet nozzle, see Figure 3.3. The azimuthal angles ranged between $0° \leq \phi \leq 180°$ at 45° intervals. As with the fixed polar array, the microphones were mounted within long, thin but rigid tubes to reduce adverse reflection effects. The microphones were oriented at 0° incidence to the jet centre-line when the array was positioned at $\theta_j = 90°$. This whole array was then traversed up and down the lab incorporating polar angles $60° \leq \theta_j \leq 130°$. For polar angles away from $\theta_j = 90°$, the appropriate free-field incidence corrections were later applied to the data in the post-processing phase.

All microphone signals were passed through B&K Nexus 2690 signal conditioning and amplifier units and 20 Hz high-pass filters. To achieve a flat sensitivity (particularly above 20 kHz), all microphone capsule protection grids were removed. The resulting

typical frequency response (at 0° incidence) can be seen in Figure 3.5. Each microphone was level-calibrated before, weekly and at the end of the test campaign using a B&K Type 4230 1 kHz calibrator. In addition, a full frequency pressure response calibration (up to 100 kHz) was performed for each microphone capsule at the end of the test. The shortest distance between microphone and nozzle was $R = 53D$. At this distance, according to the inequality $kr_{\text{lip}} > 2$, discovered by Arndt *et al.* [106], spectra measured above 55 Hz can be considered to be in the acoustic far-field.

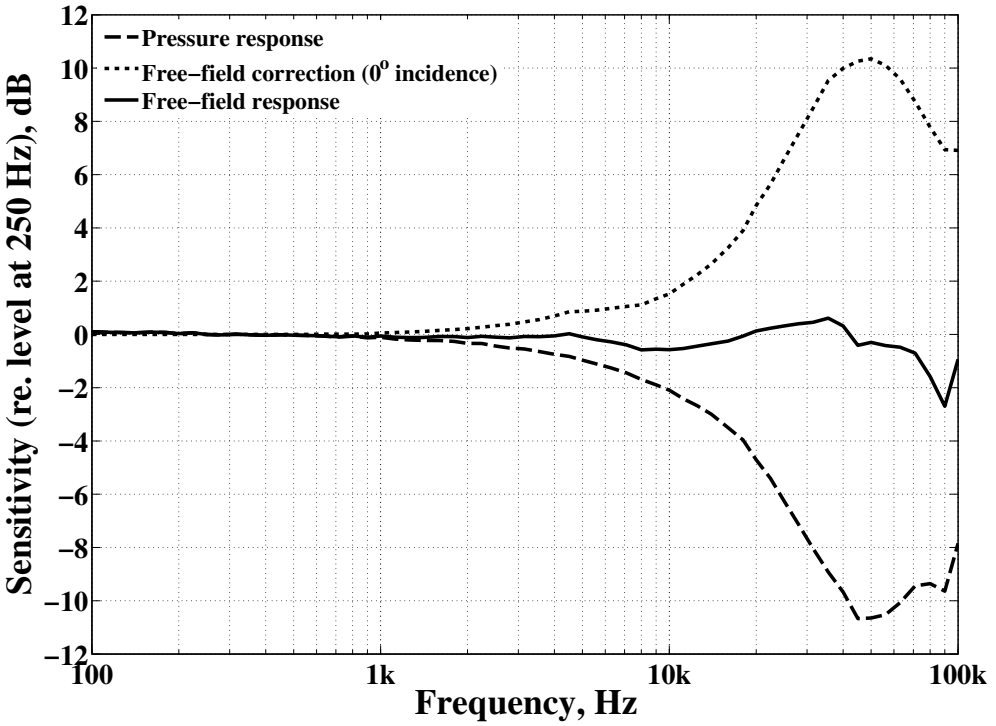

FIGURE 3.5: GRAS Type 40BF typical microphone capsule sensitivity (without protection grids)

3.2.2 Near-field acoustic set-up

Images of the traversable near-field array can be seen in Figure 3.6. The array consisted of eight 1/4-in GRAS Type 40BF condenser microphone capsules (with B&K Falcon Type 2670 pre-amplifiers) and four 1/2-in B&K Type 4191 condenser microphone capsules (with B&K Falcon Type 2669 pre-amplifiers). The array was attached to a TSI T1DE traverse system and was operated remotely by an ISEL C142-4 controller. The array itself was angled parallel to the nominal edge of the jet shear layer, at $\theta_j = 6°$ to the jet axis, so that the transducers could be positioned as close as possible to the jet without being at risk from damage by the jet flow. This also meant that the array would not modify the jet's hydrodynamic pressure field. $\theta_j = 6°$ was chosen based upon previous experimental data, see table 2.1, for the spreading

rate of a typical subsonic jet. The shortest distance between each microphone and the 'edge' of the jet's shear layer was defined as r_s. Weights were also added to stabilise the array. As with the far-field microphones, both the length and diameter of the microphone holders were carefully chosen to reduce adverse reflection effects while maintaining sufficient rigidity to support the microphones. Acoustic foam was added to the surfaces of both the array and traverse system in order to attenuate acoustic wavelengths capable of reflecting back onto the microphones. Since, at these measurement distances, the distributed jet noise sources are non-compact, the microphone diaphragms were oriented at grazing, or 90°, incidence to the jet. Thus, all sources within the jet shear layer would see the same transducer frequency response regardless of their axial position within the jet. All microphone coordinates were recorded axially, with reference to the nozzle exit plane, x, and radially, with reference to the perpendicular distance from the jet lip-line, r_{lip}. The lip-line was chosen since it represents (approximately) the region of maximum turbulence kinetic energy within the jet shear layer. The microphone array extended downstream to $x/D = 14.62$ and was traversed perpendicular to the edge of the jet shear layer, between $0.67 \leq r_{\text{lip}}/D \leq 13.15$.

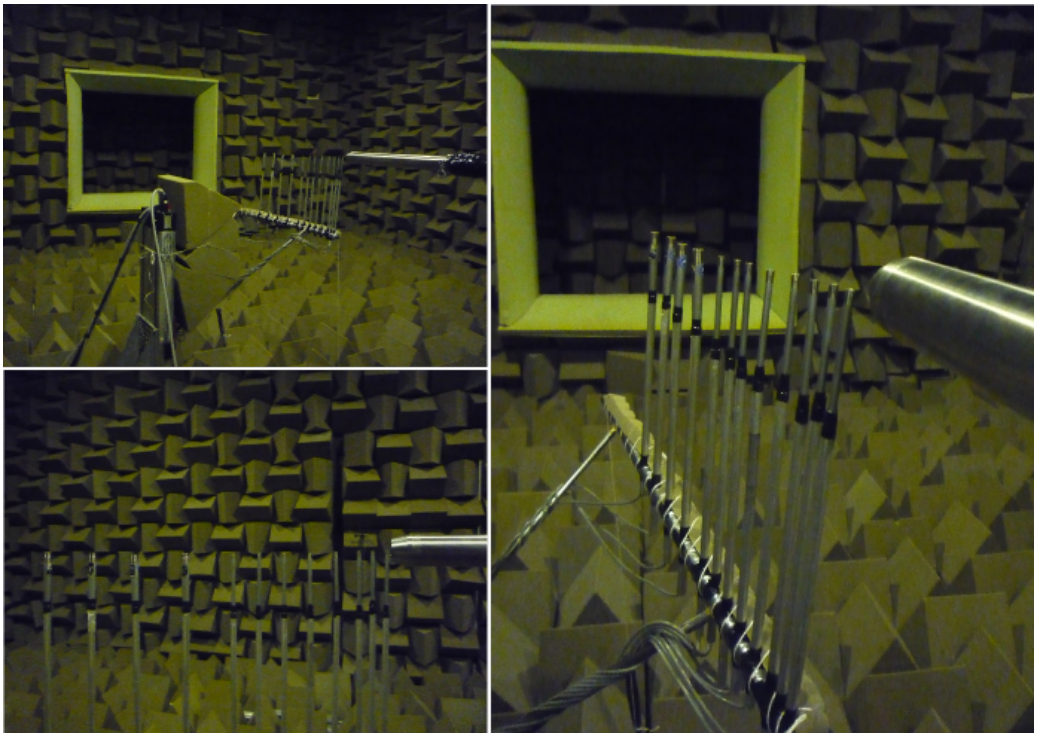

FIGURE 3.6: DOAK isolated jet near-field acoustic set-up

All microphone signals were passed through B&K Nexus 2690 signal conditioning and amplifier units and 20 Hz high-pass filters. All microphone protection grids were not removed since phase information between microphones above 20 kHz was not required. Each microphone was level-calibrated before, weekly and at the end of the test

campaign using a B&K Type 4230 1 kHz calibrator. In addition, a full frequency pressure response calibration (up to 100 kHz) was performed for each microphone capsule at the end of the test.

3.3 Data Acquisition, Processing and Output

All instrumentation was connected up to a 24-bit National Instruments PCI-4472 dynamic signal acquisition system. For the far-field measurements, data test points were acquired in 10 second samples at a sampling rate of 100 kHz. All channels were acquired synchronously. Free-field and incidence level corrections were then applied to the data during the post-processing to account for the frequency response of each microphone capsule. This was particularly important for microphones on the azimuthal array whose incidence angles were dependent upon the traverse polar angle. Atmospheric attenuation level corrections were applied to all far-field acoustic data according to Bass *et al.* [109–111]. Data was also level-corrected to a distance of 1 m from the nozzle exit according to the classical acoustics law of spherical spreading (i.e. $+20\log_{10}(R)$). Finally, each test point was corrected for ambient chamber and electronic system noise using background data measured on the day of testing.

For the near-field measurements, data test points were acquired in 10 second samples at a sampling rate of 50 kHz. Again, all channels were acquired synchronously. Neither atmospheric attenuation nor distance level corrections were applied to these data. Each test point was, however, corrected for background noise.

For all acoustic data presented in this thesis, power spectral density quantities are computed and then converted into sound pressure levels (SPL) relative to $20\log_{10}\left(\frac{p}{p_{\text{ref}}}\right)$, where $p_{\text{ref}} = 20\mu\text{Pa}$. When not otherwise stated, spectra will typically be plotted in 10 Hz narrow frequency bands since this is the standard data format often required by the aviation industry.

3.4 Far-Field Results

Before the near-field data is interrogated, it is important to determine whether the Doak model-scale university jet conforms to the well-established laws of jet noise. The following section, therefore, briefly presents the necessary far-field velocity scaling, spectral and directivity analyses required to benchmark the jet.

3.4.1 Velocity analysis

As seen previously in Equation 2.33, Lighthill was the first to present a formulation for the far-field sound intensity produced by a single turbulent eddy [33]. Thus, if one neglects refraction effects by looking at the $\theta_j = 90°$ far-field observer angle, an axisymmetric jet flow should radiate noise according to this same 'eighth power' law. From studying the circles in Figure 3.7, it is clear that the DOAK jet conforms well with Lighthill's U_j^8 far-field sound power law.

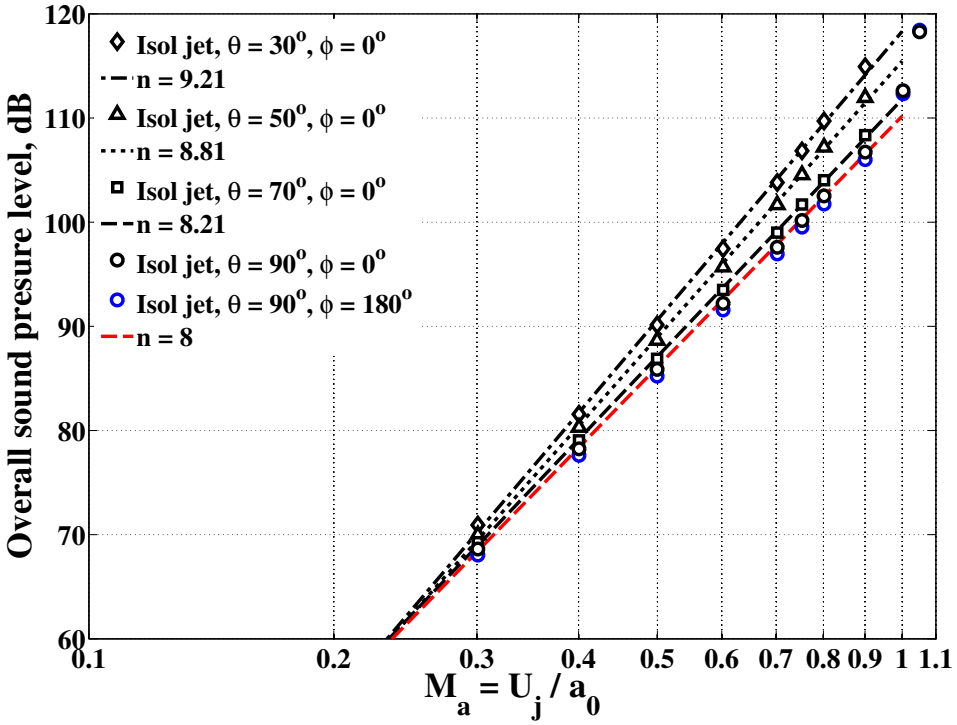

FIGURE 3.7: DOAK isolated jet far-field overall sound pressure level versus jet acoustic Mach number, OASPL $\propto \left(\frac{U_j}{a_0}\right)^n$

There are two additional points worth noting here. Firstly, at $\theta_j = 90°$, as the acoustic Mach number approaches and exceeds $M_a = 1$, the far-field sound intensity data suddenly moves above the $n = 8$ trend line. At these flow speeds, Lighthill's power law no longer holds because additional broadband and tonal shock-associated noise sources

are generated at the nozzle exit. Secondly, as one moves away from the $\theta_j = 90°$ polar angle towards the jet axis, the velocity exponent n is seen to increase. More energy is seen downstream due to a combination of Lighthill's convective amplification directivity term and Lush's flow-acoustic refraction effect, see Figure 2.17. When one integrates the acoustic intensity over all polar and azimuthal angles, the total acoustic power radiated from a jet scales with a velocity exponent n slightly less than 8. This point, however, continues to be contested and falls beyond the scope of this thesis.

3.4.2 Spectral analysis

Let us now compare the DOAK jet spectra with five other larger single stream (unheated) jets to establish what, if any, Reynolds number scaling effects exist. The first obvious comparison to make is with the 86.1 mm single stream QinetiQ nozzle, see Figure 3.8, from which the DOAK jet is scaled directly. This nozzle was tested at QinetiQ's Noise Test Facility (NTF), in 2003, however only $1/3^{\text{rd}}$-octave band data is available. The subsequent comparison, therefore, will be in $1/3^{\text{rd}}$-octave bands. The second single stream jet is the 50.0mm JEAN nozzle (tested at the Martel facility in 2002), see Figure 3.9. The third single stream jet is the 101.6 mm SILOET nozzle (tested at the NTF in 2012), see Figure 3.10. The fourth jet is the 185.7 mm SYMPHONY S33-ASS nozzle (tested at the NTF in 2010), see Figure 3.11. With this particular set-up, a core annular mixer nozzle was designed and buried within the bypass stream. The primary (core) and secondary (bypass) jet velocities, U_p and U_s respectively, were then matched (i.e. velocity ratio, $VR = U_s/U_p = 1$) in order to simulate a single stream jet. The fifth jet is the 200.0 mm CoJeN coplanar coaxial nozzle (tested at the NTF in 2005), see Figure 3.12. Again, as with the SYMPHONY S33-ASS nozzle, the core and bypass jet velocities were matched to simulate a single stream jet. The bypass jet exit diameter was used as the effective single stream jet diameter.

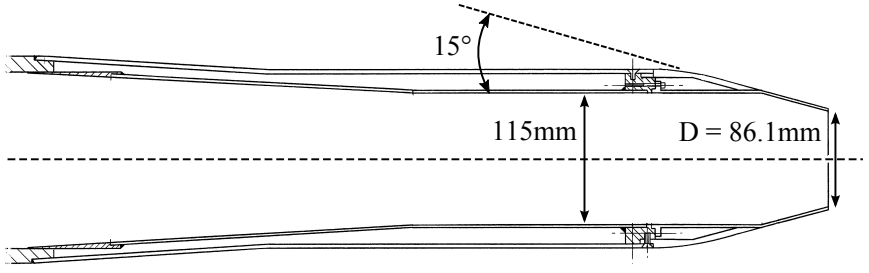

FIGURE 3.8: QinetiQ 86.1 mm diameter single stream nozzle schematic

In order to compare the noise from all of these nozzles, the following three corrections must be applied to the data. Firstly, an amplitude correction must be added to

FIGURE 3.9: Photograph of the JEAN 50.0 mm diameter single stream nozzle

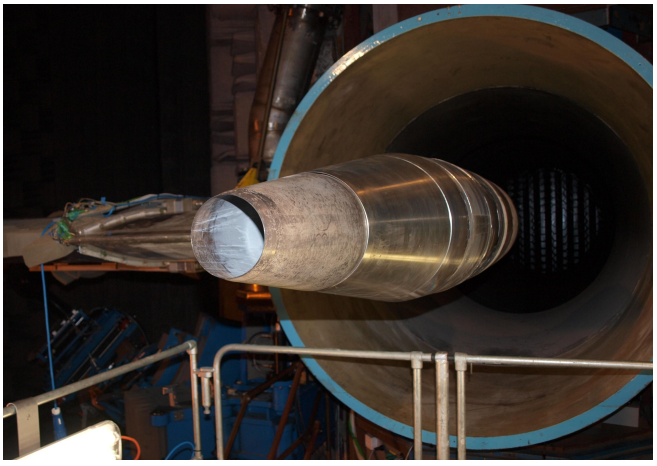

FIGURE 3.10: Photograph of the SILOET 101.6 mm diameter single stream nozzle at the NTF

account for the greater volume of sources produced from a larger diameter jet. Secondly, if the jet exit acoustic Mach number is not identical between jets, the data should also be velocity-corrected. For the subsequent third-octave band analysis, therefore, the following corrected sound pressure level, SPL_c, is defined as,

$$\mathrm{SPL}_c = \mathrm{SPL} + 20\log_{10}\left(\frac{D_{\mathrm{ref}}}{D}\right) + 80\log_{10}\left(\frac{M_{a_{\mathrm{ref}}}}{M_a}\right), \tag{3.14}$$

where D_{ref} is some reference nozzle diameter ($D_{\mathrm{ref}} = 1$ m) and $M_{a_{\mathrm{ref}}}$ is the reference acoustic Mach number (which varies between 0.50, 0.75 and 0.90). Lastly, the frequency axis must be non-dimensionalised to a Strouhal number based upon the nozzle diameter, D, and jet exit velocity, U_j, i.e. $\mathrm{St}_D = fD/U_j$. Figures 3.13-3.15 show the final jet noise spectral comparisons. Clearly the DOAK jet (the black series in the figures) performs well relative to the other historical jets at all three polar angles and at the lowest acoustic Mach number (i.e. at $M_a = 0.50$). With increasing jet velocity,

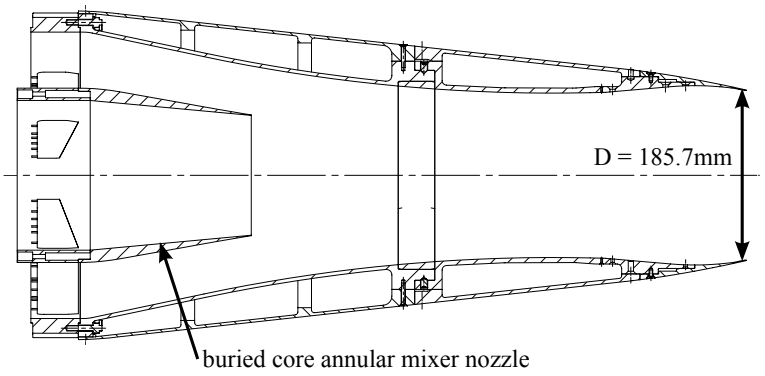

FIGURE 3.11: SYMPHONY S33-ASS 185.7 mm diameter single stream nozzle schematic

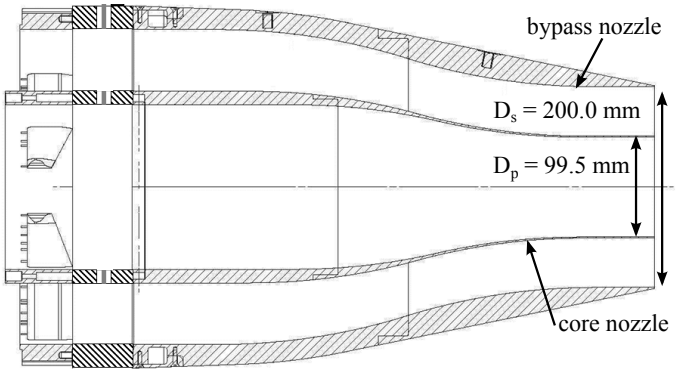

FIGURE 3.12: CoJeN 200.0 mm diameter coplanar coaxial nozzle schematic

however, the read-across with the larger nozzles deteriorates until, at $M_a = 0.90$, where the DOAK jet is, on average, 2 dB above the other jets at all three polar angles. This is in direct contrast, however, to the 50mm MARTEL nozzle data (see red series in the figures), which appears to better match the other larger-scale jets at higher rather than lower jet velocities. There is clearly also some corrupt (spikey) data visible in the MARTEL data at the forward arc microphone position (i.e. at $\theta_j = 120^o$, see Figure 3.15). This is most likely due to reflections from the microphone holder itself. At $M_a = 0.90$, the Reynolds number of the DOAK jet is approximately 0.77×10^6. The disparity in amplitude between the small-scale DOAK nozzle and the other larger nozzles is consistent with previous studies of industrial versus university jets [108, 112]. Without a detailed aerodynamic survey of the lip-lines of these nozzles, however, it is impossible to establish which parameter is responsible for this discontinuity. Has, for example, the development of a thick turbulent boundary layer within the smooth DOAK jet pipe served to increase the percentage turbulence level within the jet? Or are there other rig-related effects responsible?

One final important observation from Figures 3.13-3.15 is that both the SYMPHONY S33-ASS buried core coaxial jet and the CoJeN coplanar coaxial jet can successfully

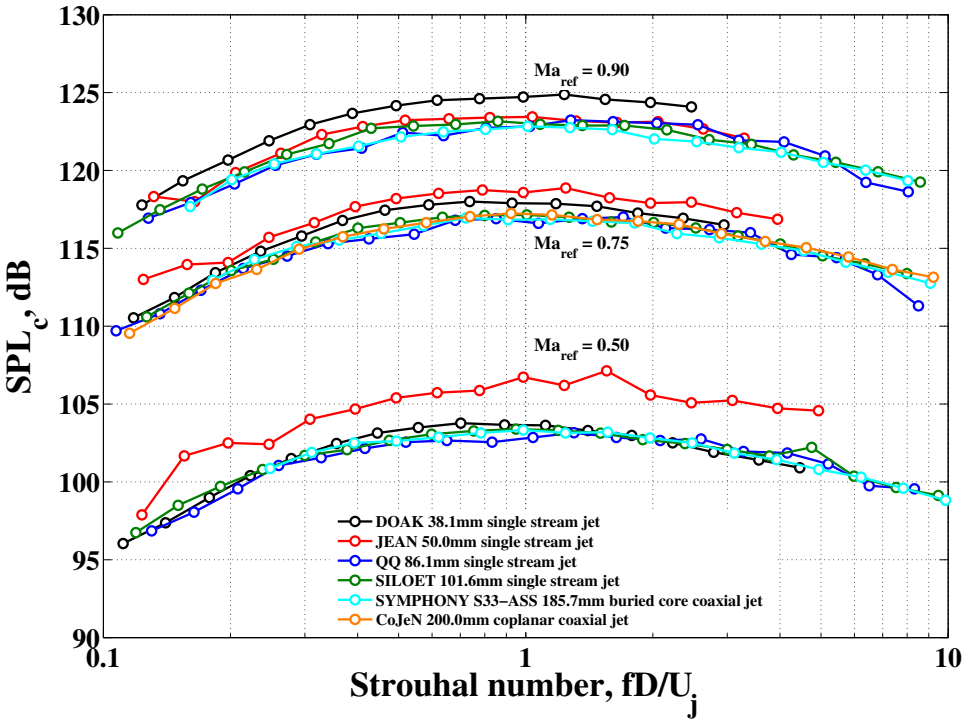

FIGURE 3.13: 1/3$^{\text{rd}}$-octave band isolated, cold, single stream jet spectral comparison $[\theta_j = 90°]$

simulate a single stream jet when they have a velocity ratio equal to unity. This is an important conclusion to which we will refer later on in the thesis.

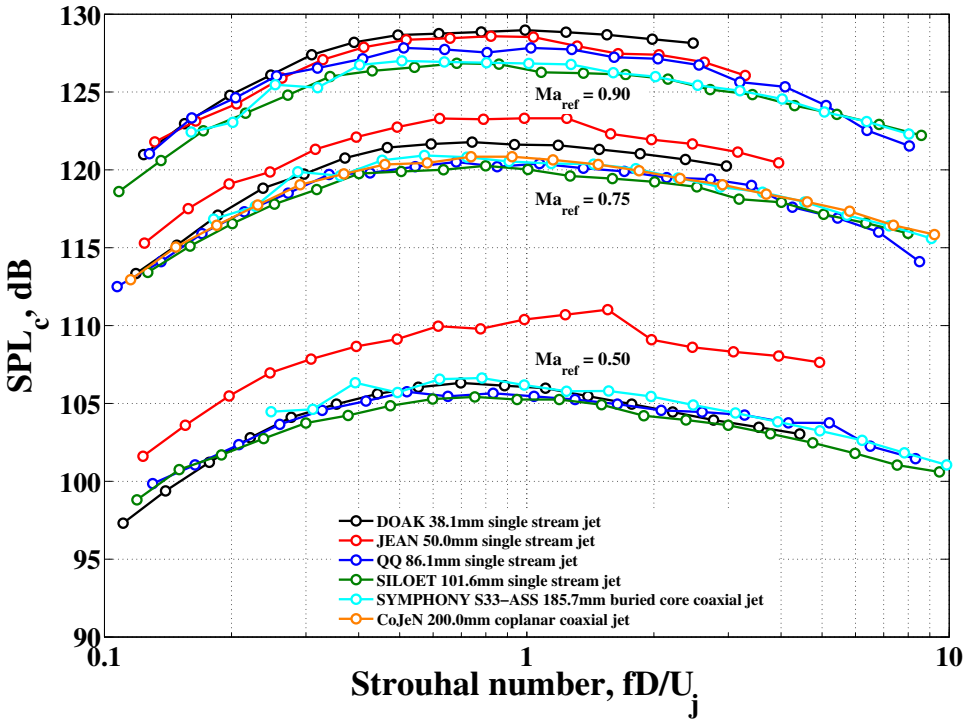

FIGURE 3.14: 1/3$^{\text{rd}}$-octave band isolated, cold, single stream jet spectral comparison $[\theta_j = 60°]$

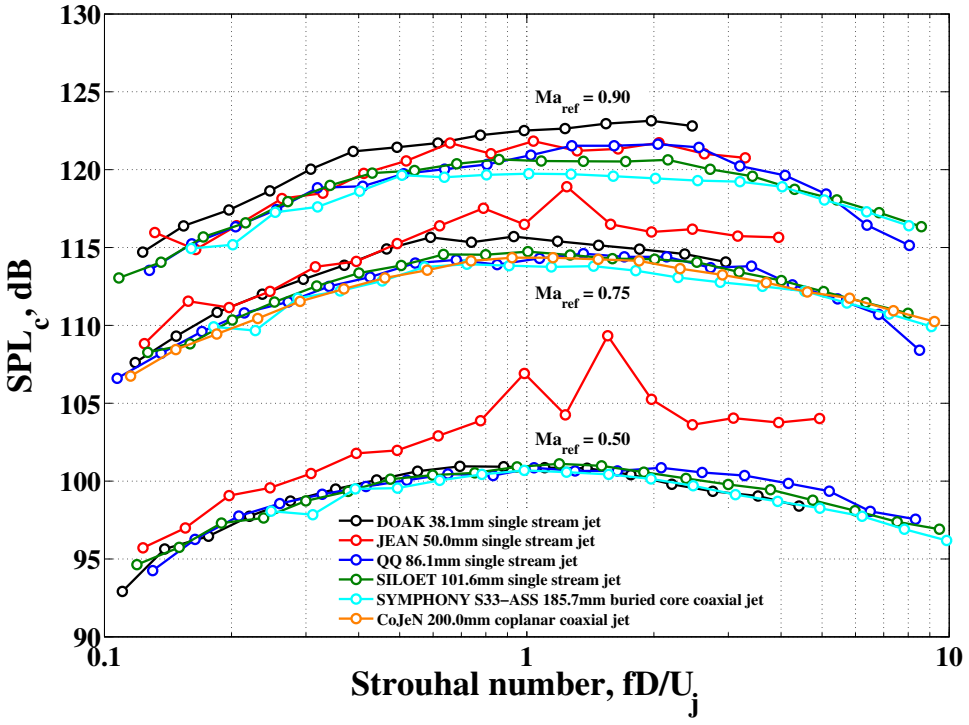

FIGURE 3.15: 1/3$^{\text{rd}}$-octave band isolated, cold, single stream jet spectral comparison $[\theta_j = 120°]$

3.4.3 Directivity analysis

As mentioned in the preceding chapter, the polar directivity of single stream, cold, subsonic jets has been well documented in the past [113, 114]. Figure 3.16 illustrates the far-field polar directivity performance of the DOAK jet between $30° \geq \theta_j \geq 150°$. The amplitude (or z-axis) of this graph is plotted as a ratio of the maximum SPL (i.e. $\text{SPL} - \text{SPL}_{\text{max}}$). We can see that the jet noise appears to peak at, or beyond, $\theta_j \approx 30°$ and at $\text{St}_D \approx 0.2$. As velocity increases above $M_a = 30$, it is possible to see the effects of convective amplification and flow-acoustic refraction as the directivity pattern begins to lobe towards $\theta_j = 50°$.

For completeness, the azimuthal symmetry of the DOAK jet (at $\theta_j = 90°$) is displayed in Figure 3.17. As before, the amplitude of this graph is expressed as a ratio of the maximum SPL. The striking asymmetry of the data within the plots across the azimuthal angles shows that the amplitude calibration of the microphone at $\phi = 135°$ is erroneous (by 1 dB, approximately). Excusing this, however, we can conclude that, at $\theta_j = 90°$, the DOAK jet is azimuthally axisymmetric in the far-field. A similarly uniform azimuthal sound field is also seen to radiate at all other polar angles (i.e. between $60° \leq \theta_j \leq 130°$).

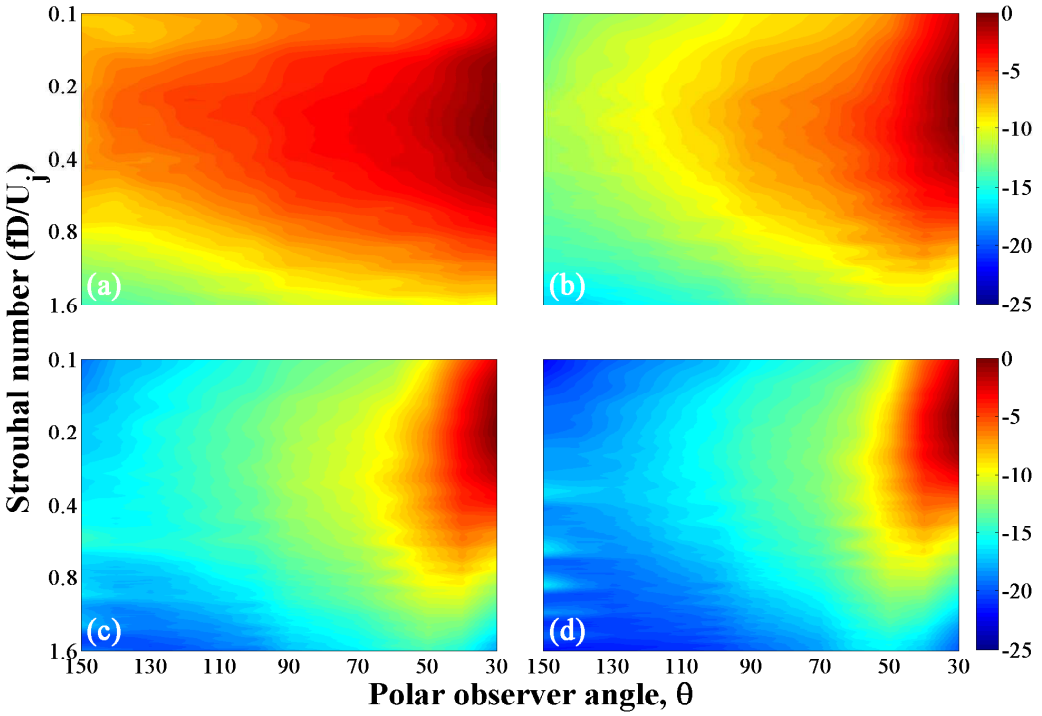

FIGURE 3.16: DOAK isolated jet far-field polar directivity (amplitude displayed as a ratio of the maximum SPL) at four subsonic acoustic jet Mach numbers: (a) $M_a = 0.30$, (b) $M_a = 0.50$, (c) $M_a = 0.75$, (d) $M_a = 0.90$; [$\phi = 0°$]. Colours have been linearly interpolated between $\Delta\theta_j = 10°$ intervals.

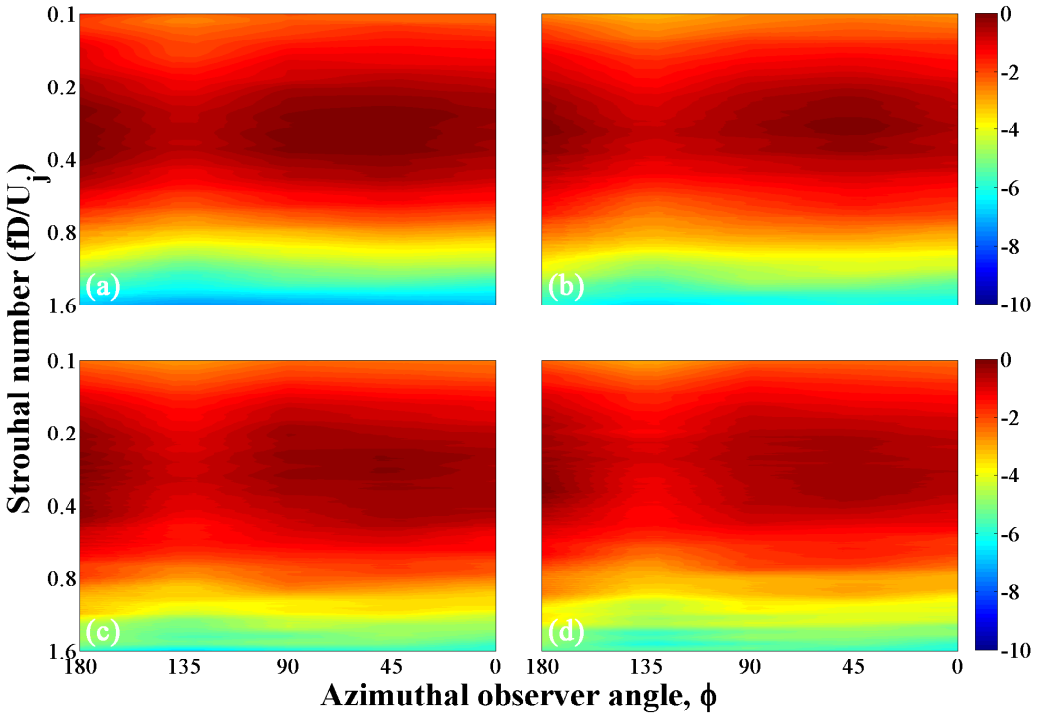

FIGURE 3.17: DOAK isolated jet far-field azimuthal directivity (amplitude displayed as a ratio of the maximum SPL) at four subsonic acoustic jet Mach numbers: (a) $M_a = 0.30$, (b) $M_a = 0.50$, (c) $M_a = 0.75$, (d) $M_a = 0.90$; [$\theta_j = 90°$]. Colours have been linearly interpolated between $\Delta\phi = 45°$ intervals.

3.5 Near-Field Results

In this section, we will characterise the spectral content, velocity scaling and decay of the near pressure field of the single stream, cold, subsonic DOAK jet. Specifically, we are interested in the irrotational hydrodynamic field of the jet and its relative dominance over the acoustic field as one radially approaches the lip-line. It is important to interrogate the jet's hydrodynamic near-field because it will form the starting point for predicting the far-field noise from installed jets later on in the thesis, in Chapter 7.

3.5.1 Peak frequency analysis

Recall the near-field isolated jet schematic, Figure 3.1. The following plot, Figure 3.18, illustrates the pressure spectra measured at an axial location downstream of the nozzle exit, $x/D \approx 2$, for a range of radial distances, $0.67 \leq r_{\text{lip}}/D \leq 13.15$. The axial distance is 'approximate' because the microphone array was traversed radially perpendicular to the edge of the jet (assuming the nominal spreading angle, $\beta_1 = 6°$) rather than perpendicular to the nozzle lip-line. Within each subplot of this figure, therefore, the bottom (quietest) data series refers to the largest radial distance, $r_{\text{lip}}/D = 13.15$ at $x/D = 0.78$, and the top (loudest) series refers to the closest radial distance, $r_{\text{lip}}/D = 0.67$ at $x/D = 2.09$. As radial distance, r_{lip}, decreases towards the nozzle lip-line (see blue arrow), a low frequency augmentation of the pressure spectrum can be observed. This augmentation is the irrotational component of the hydrodynamic jet pressure field.

If we now non-dimensionalise the frequency x-axis to a Strouhal number based upon the radial distance from the jet lip-line, r_{lip}, and the jet exit velocity U_j, we can define a new variable,

$$\text{St}_r = \frac{f r_{\text{lip}}}{U_j} \,. \tag{3.15}$$

Using this scaling, we find that, at this particular axial location, the peak of the irrotational hydrodynamic field collapses onto a single Strouhal number, $\text{St}_r \approx 0.16$, see Figure 3.19. The location of this peak frequency, however, is a strong function of the axial position along the jet. Figure 3.20 shows the dependence of the hydrodynamic peak frequency versus axial distance, x/D. The reader should be aware that the r_{lip}/D values at each axial position, however, are not constant. Instead, the distance from the nominal edge of the jet shear layer is kept constant at $r_s/D = 0.45$. As is typical of a jet source distribution (see Figure 2.19), as axial distance increases, frequency decreases.

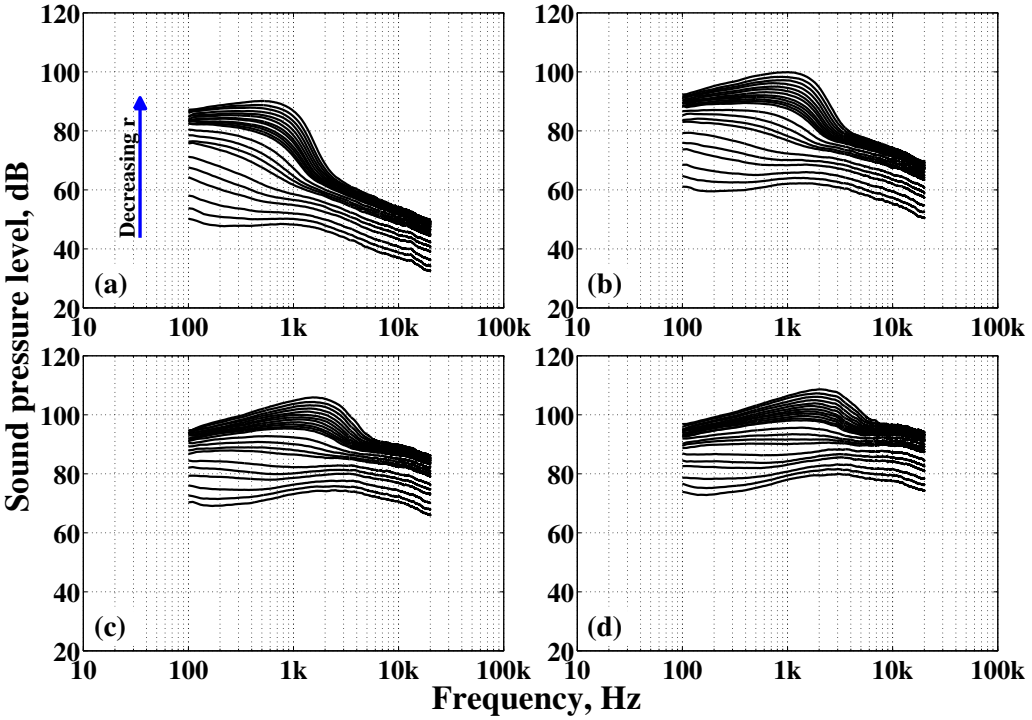

FIGURE 3.18: Spectral content of the near sound pressure field generated by an isolated jet: (a) $M_a = 0.30$; (b) $M_a = 0.50$; (c) $M_a = 0.75$; (d) $M_a = 0.90$; [$x/D \approx 2$; $0.67 \leq r_{\text{lip}}/D \leq 13.15$]

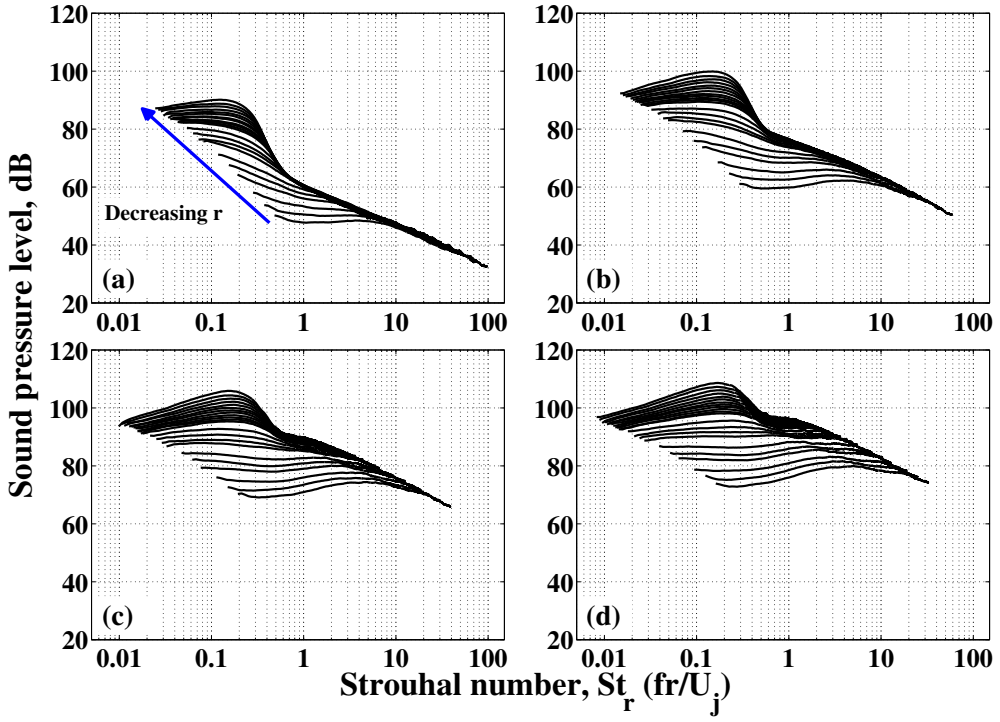

FIGURE 3.19: Strouhal-corrected spectral content of the near sound pressure field generated by an isolated jet: (a) $M_a = 0.30$; (b) $M_a = 0.50$; (c) $M_a = 0.75$; (d) $M_a = 0.90$; [$x/D \approx 2$; $0.67 \leq r/D \leq 13.15$]

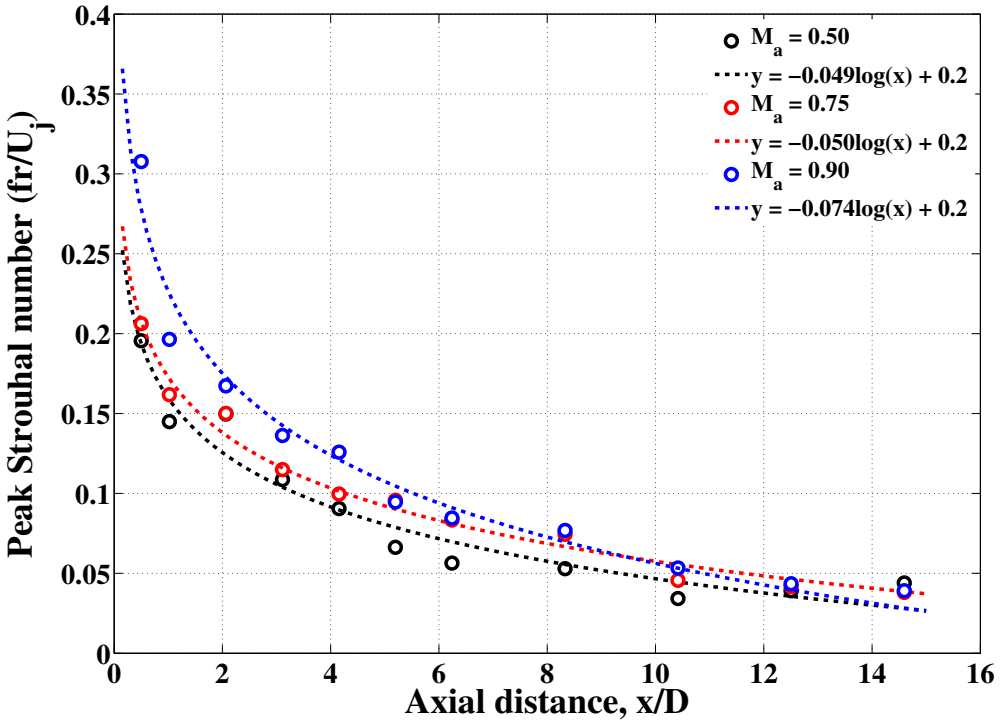

FIGURE 3.20: Axial dependence of the peak Strouhal number of the near sound pressure field generated by an isolated jet; $[r_s/D = 0.45]$

3.5.2 Peak amplitude analysis

According to Lighthill, the fluctuating turbulent Reynolds stress term, T_{ij}, in Equation 2.20, is the source of the near hydrodynamic pressure field [33]. Since this term scales as, $p \propto U^2$, see Equation 2.18, one would expect to see a $I \propto U_j^n$ velocity dependence with $n = 4$. If we plot the peak sound pressure level of the hydrodynamic field generated by the DOAK jet at various axial locations downstream of the nozzle and upstream of the end of the potential core, see Figure 3.21, on average a velocity dependence close to U_j^4 is seen. The velocity exponent, n, however, is seen to vary with axial distance. The reader should also be aware that a slight radial distance dependence will also be wrapped up in this analysis since r_{lip} is not kept constant. An axial variation of the velocity exponent, however, is not unexpected since neighbouring sources both along the nozzle lip-line, as well as vertically above and below the lip-line, all contribute to the sound field measured at a single observer point.

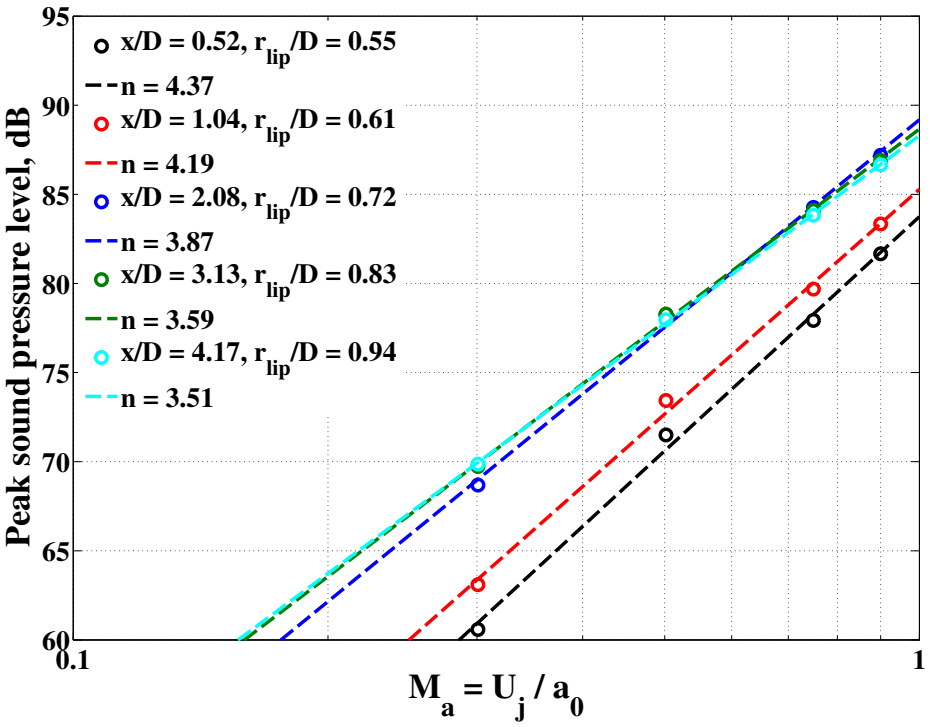

FIGURE 3.21: Dependence of the peak hydrodynamic near sound pressure field generated by an isolated jet with acoustic Mach number

If we fix the velocity exponent to $n = 4$, we can see what type of relationship best fits the axial dependence of the peak hydrodynamic sound pressure level. As before, the distance from the nominal edge of the jet shear layer is kept constant at $r_s/D = 0.45$. Figure 3.22 shows us that a logarithmic-type relationship is the most suitable fit to the data.

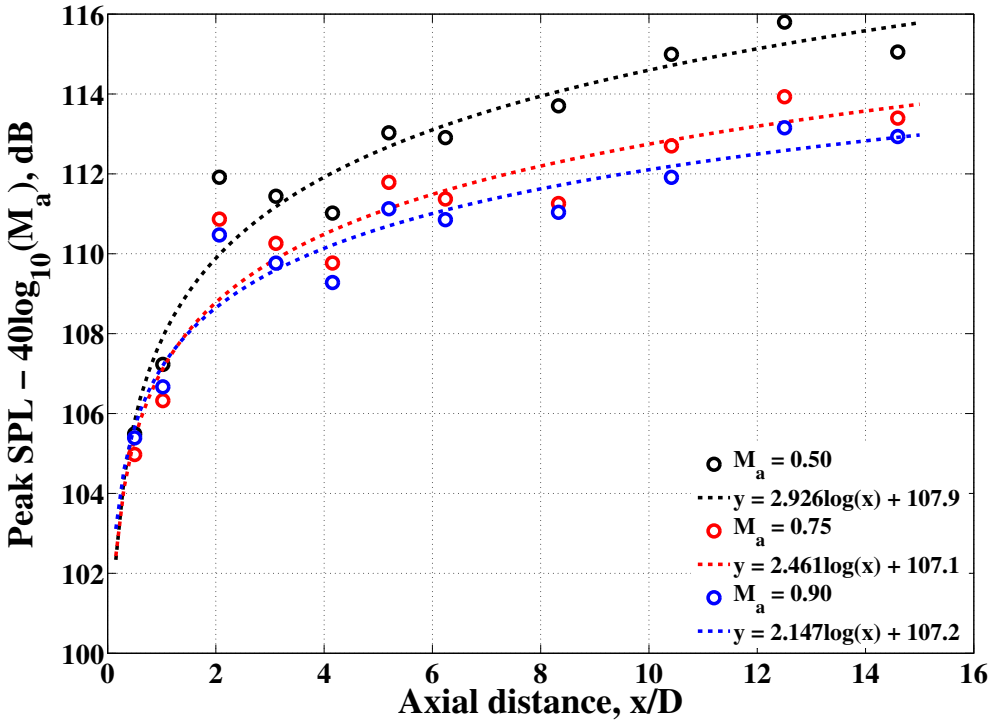

FIGURE 3.22: Velocity-corrected hydrodynamic near-field sound pressure levels generated by an isolated jet versus axial distance; $[r_s/D = 0.45]$

3.5.3 Radial decay analysis

In this section, the relationship between the hydrodynamic peak SPL and radial distance from the jet lip-line, r_{lip}, is examined. If we correct the data in Figure 3.19a by subtracting a $40\log_{10}(M_a)$ velocity correction and we then choose a single Strouhal number close to the hydrodynamic peak frequency, we arrive at Figure 3.23. Clearly the hydrodynamic field decays exponentially, as suggested in the literature. It is also interesting to note that the radial decay of the hydrodynamic field does not appear to depend upon acoustic Mach number.

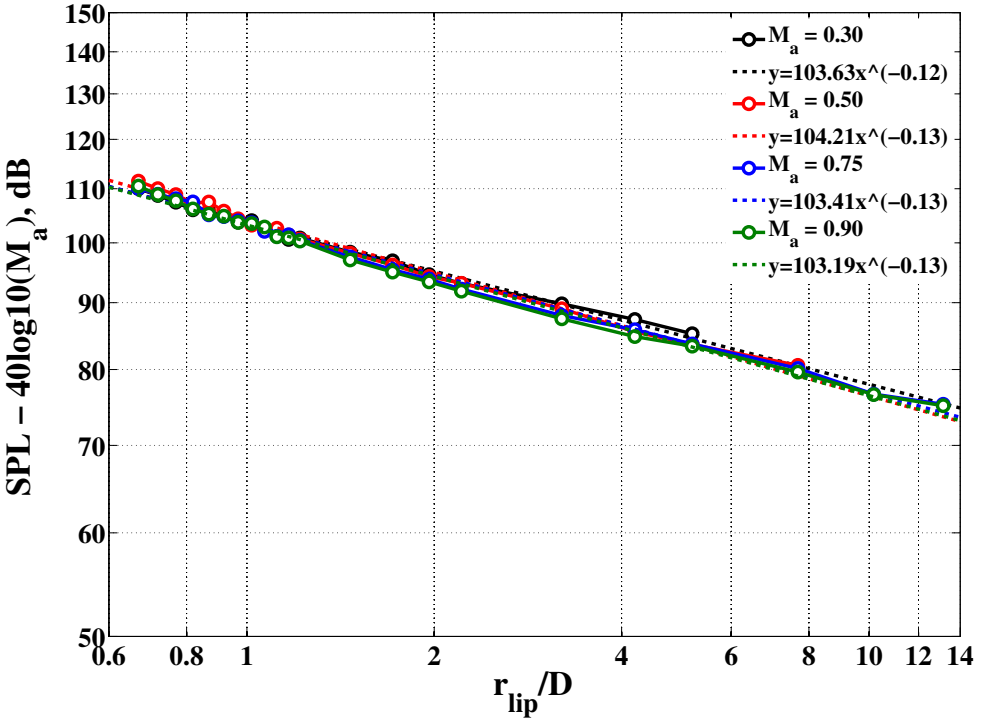

FIGURE 3.23: Velocity-corrected radial decay of near-field sound pressure levels generated by an isolated jet over a range of radial distances and acoustic Mach numbers; $[x/D \approx 2;\ \text{St}_r = 0.2]$

3.5.4 Peak spectral shape analysis

As mentioned in the introduction section of this chapter, previous research by Arndt *et al.* [106] has established that the irrotational hydrodynamic pressure field of a jet decays evanescently with increasing radial distance. If we take a closer look at Figure 3.19a (see Figure 3.24), we can see that the sur-peak gradient of the hydrodynamic spectrum tends to decay according to $I \propto \mathrm{St}_r^{-20/3}$. This power law is consistent with Arndt *et al.* [106]. The acoustic field, seen at $\mathrm{St}_r > 0.7$, however, is seen to decay according to $I \propto \mathrm{St}_r^{-2}$, as one would expect from the classical inverse-square law for spherically spreading acoustic intensity.

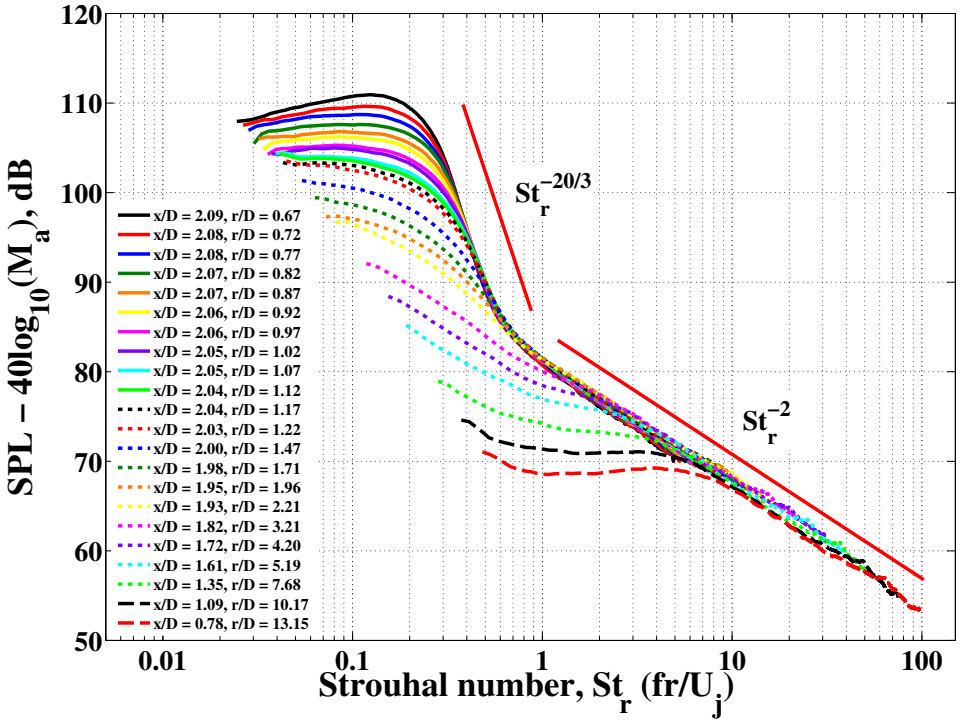

FIGURE 3.24: Spectral decay of the near sound pressure field generated by an isolated jet; $[M_a = 0.30]$

When wanting to predict this irrotational hydrodynamic spectrum, the next step would be to attempt to fit a suitable curve-fit function to this data. Historically, when dealing with broadband jet noise spectra, two curve-fitting functions are often used. The first is a straight forward asymptotic function,

$$W_1(\mu_f) = \frac{(1 - \frac{a}{b})\mu_f^a}{1 - \frac{a}{b}\mu_f^{(a-b)}}\,, \tag{3.16}$$

where μ_f is the normalised frequency (i.e. $\mu_f = f/f_{\mathrm{peak}}$) and a and b are the sub-peak and sur-peak power law exponents, respectively. The second curve-fit is a polynomial-exponential function (used principally for fitting jet source strength

distributions),

$$W_2(\mu_f) = B(A\mu_f)^a e^{-(A\mu_f)^b}\,, \tag{3.17}$$

where $A = \sqrt[b]{a/b}$ and $B = A^{-a}e^{(A^b)}$. These two weighting curves are illustrated more clearly in Figure 3.25.

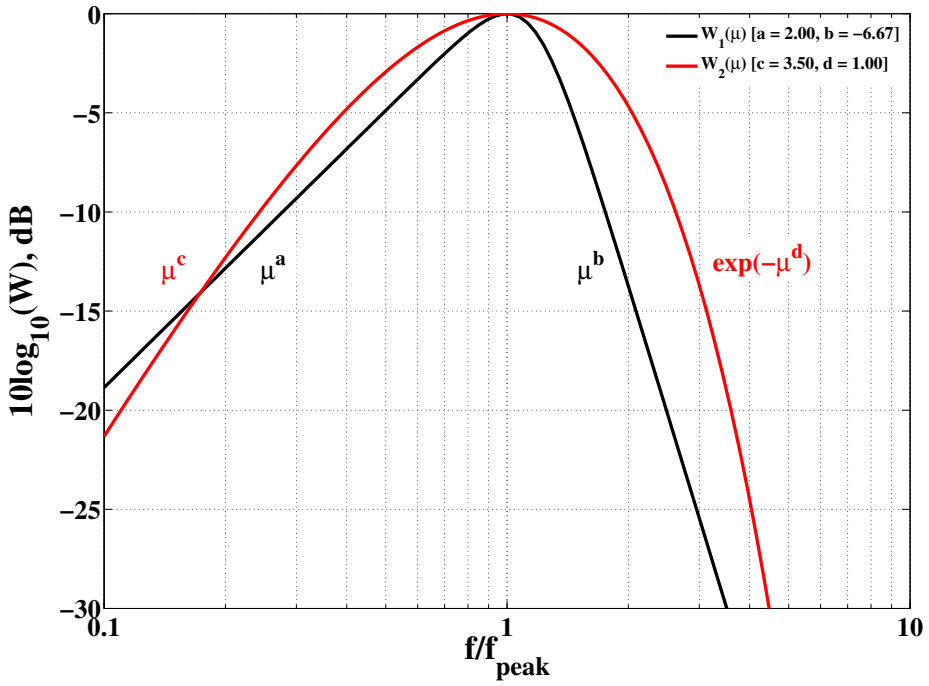

FIGURE 3.25: Example weighting functions for jet noise spectral peak curve-fitting

While Arndt's $b = \frac{-20}{3}$ power law is a reasonable approximation for the spectral sur-peak decay rate at the lowest jet acoustic Mach number ($M_a = 0.30$, see Figure 3.24), it does not hold as flow velocity increases. In order to study the sub-peak and sur-peak gradients more closely, we can normalise the x-axis of Figure 3.24 into a fraction of the peak Strouhal number and define a new variable, $\mu_f = \mathrm{St}_r/\mathrm{St}_{r_{\mathrm{peak}}}$. Then, if we normalise the y-axis and define a peak amplitude ratio, $\mathrm{SPL} - \mathrm{SPL}_p$, we can attempt to match one of the weighting functions to the shape of the peak.

We can see an example of the variation in the spectral shape power law exponents with acoustic Mach number clearly if we plot μ_f against $\mathrm{SPL} - \mathrm{SPL}_p$, see Figure 3.26. Further research is now required to establish the curve-fits necessary to predict these a and b gradient values and complete the semi-empirical prediction model for the hydrodynamic field generated by an isolated, free jet.

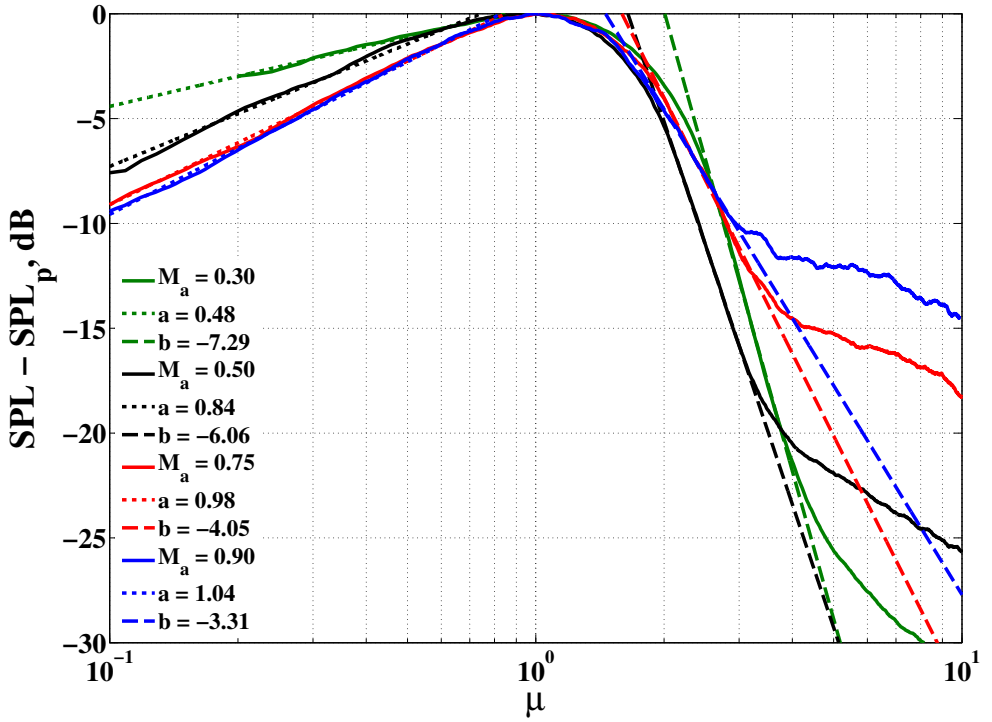

FIGURE 3.26: Asymptotic power law curve-fits to the isolated jet hydrodynamic spectral peak shape at four subsonic acoustic Mach numbers; $[x/D = 2.09;\ r_{\text{lip}}/D \leq 0.67]$

3.6 Conclusions

In this chapter, the near-field and far-field acoustic properties of the Doak Laboratory's 38.1 mm single stream, cold, subsonic jet have been presented and discussed in detail. By studying far-field acoustic data, we have seen that the DOAK jet nozzle performs well against other historical single stream jet nozzles at $M_a = 0.50$, but that it creates more noise than the larger industrial-type nozzles at higher subsonic flow acoustic Mach numbers. A detailed aerodynamic survey of the jet exit plane will generate the necessary data to establish which parameters are responsible for this discrepancy. The current working hypothesis, however, is that a laminar boundary layer has been allowed to grow within the smooth jet pipe resulting in an increased percentage turbulence level within the jet shear layer.

Regarding the near hydrodynamic pressure field, an extensive acoustic experimental survey has also been conducted over a range of subsonic acoustic Mach numbers and at several axial and radial locations near to the jet. At low jet velocities, Arndt *et al.* [106] defined the 'near-field' of a jet by the frequency dependent inequality, $kr_{\text{lip}} < 2$. According to Figure 3.19, however, this inequality can now be redefined to include a jet velocity dependence,

$$fr_{\text{lip}}/U_j < 0.7\,. \tag{3.18}$$

We have also seen that the hydrodynamic peak Strouhal number follows an expected inverse relationship with increasing axial distance downstream of the nozzle. Furthermore, the hydrodynamic peak amplitude is seen to adopt a U_j^4 dependency. The behaviour of the peak amplitude with axial distance, however, is more difficult to interpret without information about the strength of the turbulence within the flow. Future hot-wire and five-hole probe turbulent velocity experiments should help to link the trends observed.

Regarding the radial decay of the hydrodynamic field, as the distance from the jet nozzle lip increases, we have seen that the hydrodynamic peak frequency decays evanescently as expected and is independent of acoustic Mach number.

Preliminary investigation into the hydrodynamic field spectral shape has been completed and has been found to be consistent with the findings of Arndt *et al.* [106]. Once this analysis is complete, the resulting semi-empirical prediction model will be able to compare isolated jet near-field spectra easily with 'equivalent' installed surface pressure spectra on aircraft wing or flap surfaces.

One final important point to note is that as one moves further radially away from the jet lip-line, a greater contribution from the other sources in both the vertical z-plane

and the axial x-plane will begin to contribute to the measured sound field. In other words, the sound field will become more and more three dimensional. Future jet hydrodynamic near-field models created using data at large radial distances (i.e. $r_{\text{lip}}/D > 1$), therefore, should be developed with care.

The understanding gained in this chapter regarding the behaviour of the hydrodynamic near-field will be important in the next chapter, when we install the jet in close proximity to an horizontal flat plate.

Chapter 4

Small Model-Scale Installed Jet Noise

This chapter presents acoustic results from a $1/50^{\text{th}}$ model-scale installed jet experimental test campaign carried out at the University of Southampton's Doak Laboratory (DOAK). The experiment comprised an horizontal flat plate installed close to a single stream, unheated jet, under static ambient flow conditions. A detailed description of the design of the experiment is presented together with a far-field acoustic comparison with previous installed jet experiments. Both near-field and far-field acoustic results are presented to help characterise the fundamental mechanisms underlying installed jet noise.

4.1 Introduction

As stated in Chapter 2, the first significant experiments investigating high subsonic jet-surface interaction (JSI) noise were performed by Head and Fisher [67], in 1976. In their experiments, a flat plate shield was positioned close to a circular, unheated, single stream jet under static ambient flow conditions. The additional low frequency far-field noise produced, see Figure 2.26, was attributed solely to an 'unspecified' dipole-type source driven by local jet near-field acoustic pressures at the trailing edge. A 180° phase shift was observed in the far-field signals either side of the shield, however, the small number of far-field microphones made it difficult to make robust conclusions about the directivity and, hence, the mechanism of the source itself. Since the 1970s, JSI noise has largely been neglected because the equivalent full-scale frequency range over which it was seen to exist was either inaudible to humans or below the threshold for noise annoyance. However, now that larger, ultra high-bypass engines are being

designed, the vertical separation distance, h, between the jet and wing is set to decrease. We will see later on in this chapter that as h decreases, both the amplitude and peak frequency of the JSI noise increases. Thus, more and more of the JSI noise spectrum is set to shift into the audible frequency range. The understanding and prediction of JSI noise, therefore, is becoming increasingly important.

As previously mentioned in Section 2.4, there are two other important sources of installed jet noise. Firstly, high frequency jet mixing noise is reflected by the under-wing surface down to the ground. Detailed investigation into this jet-surface reflection (JSR) noise source, however, falls beyond the scope of this thesis. Secondly, if the edge of a flap is deployed into the jet, an additional mid frequency (i.e. ¡400 Hz full-scale) noise source has been observed in far-field data by Way and Turner [73]. Even less research, however, exists for this jet-flap impingement (JFI) noise source.

The small-scale experiment described in this chapter attempts to isolate the JSI and JSR installed jet noise sources. The JFI noise source is then explored in more detail later on in Chapter 6. The JSI noise can be isolated from the JSR noise by observing the sound which propagates above the wing (i.e. on the shielded side of the jet). The far-field acoustic results can then be compared against those from Head and Fisher [67].

4.2 Experiment Design

In order to understand the fundamental physics of the JSI noise source, a simple jet plus horizontal flat plate experiment was conducted under static ambient flow conditions (i.e. $U_f = 0$), see Figure 4.1. As in Chapter 3, the DOAK single stream, unheated, 38.1 mm diameter jet was operated at four fully-expanded, subsonic acoustic jet Mach numbers: 0.30, 0.50, 0.75 and 0.90.

A 6 mm-thick, rectangular aluminium alloy flat plate was secured to a 2-axis traverse system so that it could be moved incrementally along (axially) or perpendicular (radially) to the jet axis. The total span S of the plate was 1.100 m, extending approximately $15D$ above and below the centre line of the jet. It was sufficiently large, therefore, to prevent the generation of additional noise from flow passing over the side edges. The total plate length L, or chord, of the plate was 0.762 m, or $20D$. The leading edge of the plate, therefore, would always extend upstream of the jet nozzle lip, thus minimising any potential aeroacoustic leading edge effects. Thus, the plate was termed 'semi-infinite'. Finally, the plate trailing edge was machined down (at an angle of 60°) to a thickness of 1 mm.

FIGURE 4.1: Photograph of the Doak Laboratory single stream jet plus horizontal flat plate far-field acoustic set-up (approximately $1/50^{\text{th}}$ model-scale)

The schematic shown in Figure 4.2, illustrates the fundamental parameters investigated: h, l and M_a - where h is the jet-surface radial separation (measured from the jet geometric centre line to the surface of the plate), l is the axial extension of the surface downstream from the nozzle exit plane and M_a is the jet exit acoustic Mach number (i.e. $M_a = U_j/a_0$). The axial plate positions, l/D, were: 1.50, 2.00, 2.50, 3.00, 3.50, 4.00, 7.00 and 10.00. The radial plate positions, h/D, were: 0.67, 1.00, 1.25, 1.50, 2.00 and 4.00. Both realistic future aircraft configurations (i.e. $l/D < 2$ and $h/D < 1$) and less realistic 'diagnostic' configurations (i.e. $l/D > 2$ and $h/D > 1$) were studied in order that robust data trends could be recognised. For the most closely-coupled configurations (i.e. when $h/D = 0.67$), a 1 cm-thick strip of foam was placed between the jet pipe and the plate (see Figure 4.3a) to minimise any vibration-induced noise.

The same far-field polar and azimuthal acoustic measurement arrays were used as per the isolated jet experimental set-up. As before, acoustic data from this far-field array was post-processed into background-corrected, 1 m lossless, 10 Hz narrowband sound pressure levels. In addition, a near-field array of surface pressure microphones was also included to track the convecting acoustic and hydrodynamic pressure fields of the jet along the surface of the plate towards its trailing edge. The near-field surface pressure array was configured as shown in Figure 4.3. Fourteen 2 mm diameter Kulite Type XT-190 pressure transducers were used. Further information regarding the location of these transducers can be found in Section 4.3.3. The calibration technique developed for these transducers is detailed in Appendix A. Acoustic data from this near-field

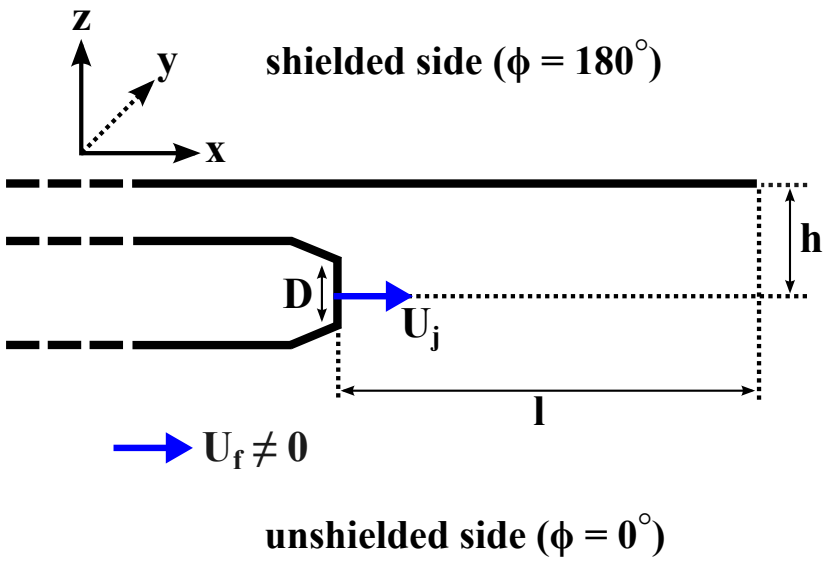

FIGURE 4.2: Schematic of the DOAK single stream jet plus horizontal flat plate set-up

array was post-processed into background-corrected, 10 Hz narrowband sound pressure levels.

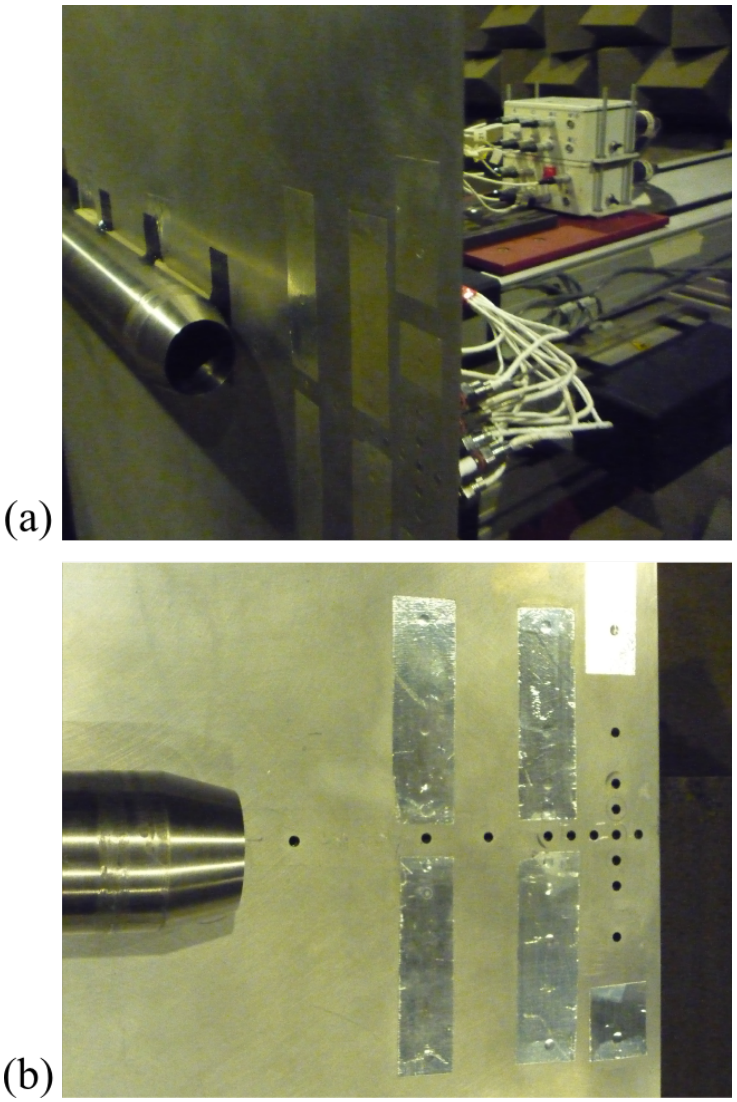

FIGURE 4.3: (a) General near-field set-up for horizontal flat plate installed jet configuration; (b) T-array of near-field surface pressure transducers

4.3 Results and Discussion

This section is divided into four subsections. The first subsection introduces the general far-field acoustic results from the first of the three above-mentioned installed jet experiments - namely, the horizontal flat plate installed jet. The second subsection then focusses more closely on the jet-surface interaction (JSI) noise source itself in isolation. Source characteristics including the frequency content, velocity scaling and directivity are each discussed in turn. The third subsection briefly addresses the far-field acoustic results for the jet-surface reflection (JSR) noise source. Finally, the fourth subsection investigates the near-field surface pressure results, wherein the stream-wise convection velocity, U_c, and spanwise turbulence integral length scale, Λ_y, of both the acoustic and hydrodynamic fields are presented. The overall aim is to further the understanding of the fundamental mechanism(s) involved in installed jet noise and, in particular, JSI noise.

4.3.1 General far-field installed jet noise results

We begin this subsection by looking at the far-field acoustic spectrum produced by the DOAK single stream jet installed in close proximity to the 'semi-infinite' horizontal flat plate. As already seen in Figure 2.26, it is possible to identify the key installation noise source contributions. Figure 4.4 shows results from a parametric study of the main JSI noise variables: h, l and $M_a = U_j/a_0$, as defined in Figure 4.2. All sound pressure level (SPL) data presented here are for the $\theta_j = 90°$ polar observation angle so that no refraction (jet blockage) or Doppler effects need be addressed. Each subplot of Figure 4.4 shows a particular configuration of h and l. Within each subplot there are four sets of data which represent the four acoustic jet Mach numbers, M_a, and then for each M_a, there are three data series: (1) the isolated jet noise (black line), (2) the installed jet noise measured below the surface, i.e. the unshielded or $\phi = 0°$ jet (blue line), and (3) the installed jet noise measured above the surface, i.e. the shielded or $\phi = 180°$ jet (red line).

There are several important points to mention here. Firstly, if one studies the pairs of installed jet spectra (i.e. the blue and red lines), a notch is visible at approximately 400 Hz. This feature is particularly clear at the two smallest acoustic Mach numbers, where the installed jet noise levels are significantly greater than those of the isolated jet. The centre frequency of this notch appears to be insensitive both to the acoustic jet flow Mach number and to the position of the plate next to the jet (i.e. for all data series in Figure 4.4). The author suggests, therefore, that this notch is, in fact, the result of a geometric acoustic interference effect. If we assume that the 'dipolar' JSI

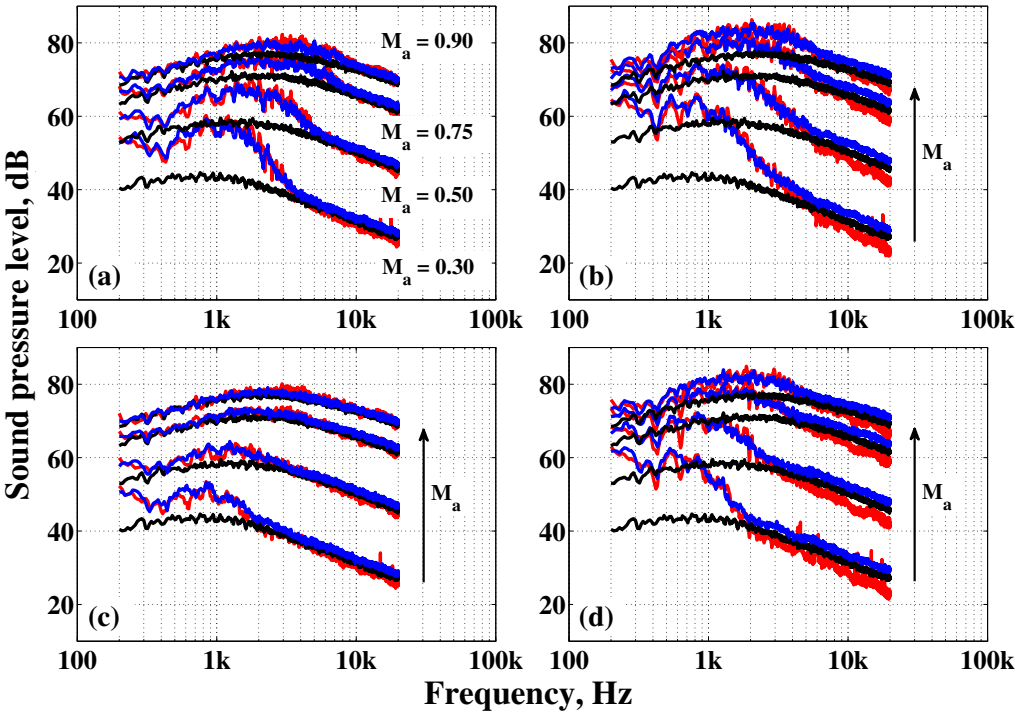

FIGURE 4.4: Far-field, 10 Hz narrowband sound pressure level comparison between an isolated and an installed jet at $\theta_j = 90°$: (a) $h/D = 0.67$, $l/D = 2$; (b) $h/D = 0.67$, $l/D = 4$; (c) $h/D = 1$, $l/D = 2$; (d) $h/D = 1$, $l/D = 4$; [blue lines - installed jet, $\phi = 0°$; red lines - installed jet, $\phi = 180°$; black lines - isolated jet]

noise (as described by Head and Fisher [67]) originates at the trailing edge of the plate, it is possible that the wave travelling above the plate, or the 'shielded' wave, will reach the leading edge of the plate and then diffract back down to the unshielded side of the jet whereupon it interacts with the 'unshielded' wave destructively. If this were the case, a simple relationship would exist between the wavelength of sound and the total length, or chord, of the plate. The plate length is 762 mm, which corresponds to a frequency of 450 Hz. This explanation, therefore, fits well and will be further explored later, in Section 4.3.2.5.

With this logic, one would also expect the side edges of the plate (in the spanwise y direction) to generate an interference pattern. From the centre of the plate, the distance to the spanwise side edges is 550 mm, which corresponds to a frequency of approximately 620 Hz. It is actually possible to see a slight second dip at this frequency, but only in the shielded data (i.e. the red lines in Figure 4.4). So, why would the spanwise interference effect be much weaker than the streamwise interference effect? Ffowcs-Williams and Hall [19] and Chase [53] proved this, mathematically, by concluding that the source is oriented perpendicular to the surface of the half-plane in the direction of the flow. Thus, for a non-swept trailing edge, the maximum sound radiation must propagate perpendicular to the surface and in the

plane of the x-axis (streamwise), rather than obliquely over the span of the plate surface. Further discussion on directivity will continue later, in Section 4.3.2.5.

The second important observation concerns the unshielded installed spectra (i.e. the blue lines in Figure 4.4). Studying these data series, it is possible to identify both the jet-surface reflection (JSR) and the jet-surface interaction (JSI) noise source contributions. Compared to a free jet, the additional JSR noise, $\Delta\text{SPL}_{\text{jsr}}$, can be seen at high frequencies parallel to the isolated jet spectrum. The additional JSI noise, $\Delta\text{SPL}_{\text{jsi}}$, however, is relatively low in frequency and can be seen to protrude substantially above the isolated jet mixing noise, particularly at low acoustic Mach numbers. In order to illustrate these two sources more clearly, we can subtract the isolated jet noise spectra from the unshielded (i.e. $\phi = 0°$) installed jet noise spectra. We can then non-dimensionalise the frequency and define a Strouhal number, St_D, as follows,

$$\text{St}_D = \frac{fD}{U_j}\,, \tag{4.1}$$

where D is the jet diameter and U_j is the jet exit velocity. Finally, if we send the 10 Hz narrowband data through a low-pass filter to remove the high frequency fluctuations, we arrive at the following four 'smooth' sets of plots, see Figures 4.5-4.8.

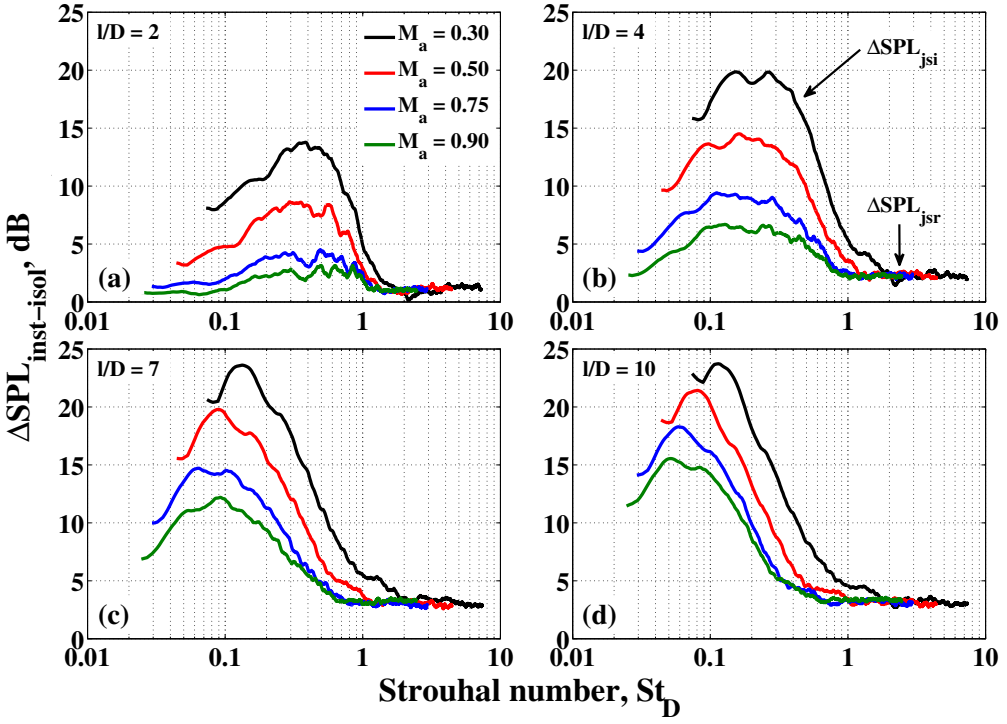

FIGURE 4.5: Far-field, smoothed 10 Hz narrowband installed jet ΔSPL increase above an isolated jet at four subsonic jet exit acoustic Mach numbers, M_a, and four axial plate extensions, l/D: (a) $l/D = 2$; (b) $l/D = 4$; (c) $l/D = 7$; (d) $l/D = 10$; [$h/D = 0.67$, $\theta_j = 90°$, $\phi = 0°$]

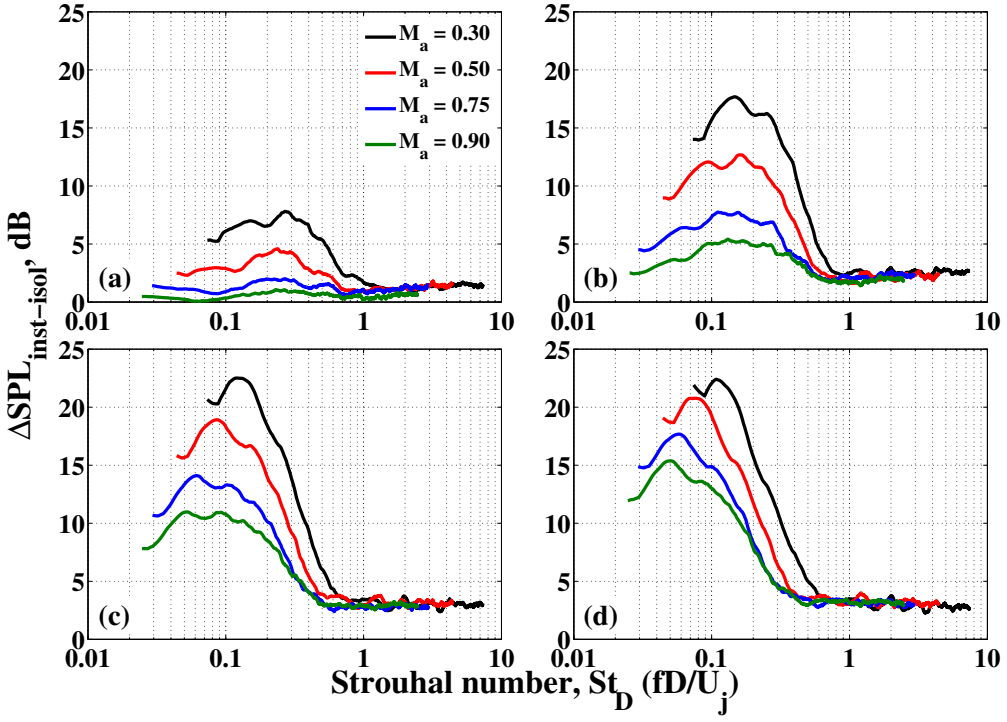

FIGURE 4.6: Far-field, smoothed 10 Hz narrowband installed jet ΔSPL increase above an isolated jet at four subsonic jet exit acoustic Mach numbers, M_a, and four axial plate extensions, l/D: (a) $l/D = 2$; (b) $l/D = 4$; (c) $l/D = 7$; (d) $l/D = 10$; [$h/D = 1.00$, $\theta_j = 90°$, $\phi = 0°$]

The next important observation concerns the success in using the Strouhal number, St_D, to align the JSI peak frequencies for different jet exit velocities. Indeed, this scaling result compares well with the observations of Head and Fisher [67], in 1976. The fact that the jet exit velocity, U_j, is the most suitable velocity means that the far-field JSI noise is governed by global properties of the jet flow rather than, for example, by the convection velocity of the hydrodynamic pressure field local to the plate trailing edge. There are many more observations to make concerning these four figures. Further discussion, however, will take place within the subsequent two sections.

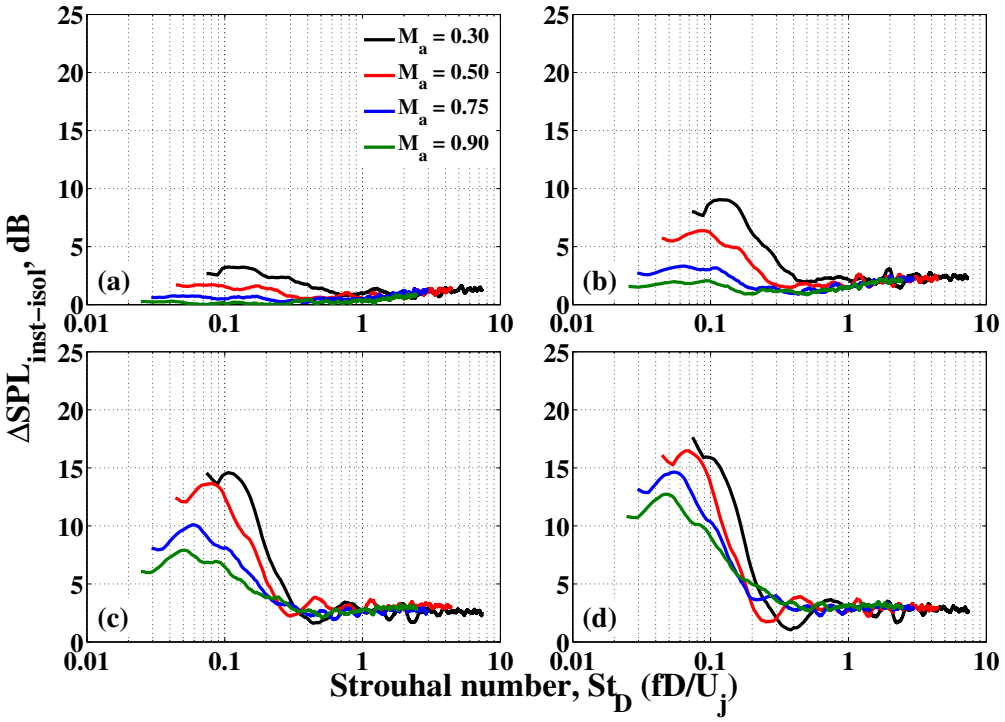

FIGURE 4.7: Far-field, smoothed 10 Hz narrowband installed jet ΔSPL increase above an isolated jet at four subsonic jet exit acoustic Mach numbers, M_a, and four axial plate extensions, l/D: (a) $l/D = 2$; (b) $l/D = 4$; (c) $l/D = 7$; (d) $l/D = 10$; [$h/D = 2.00$, $\theta_j = 90°$, $\phi = 0°$]

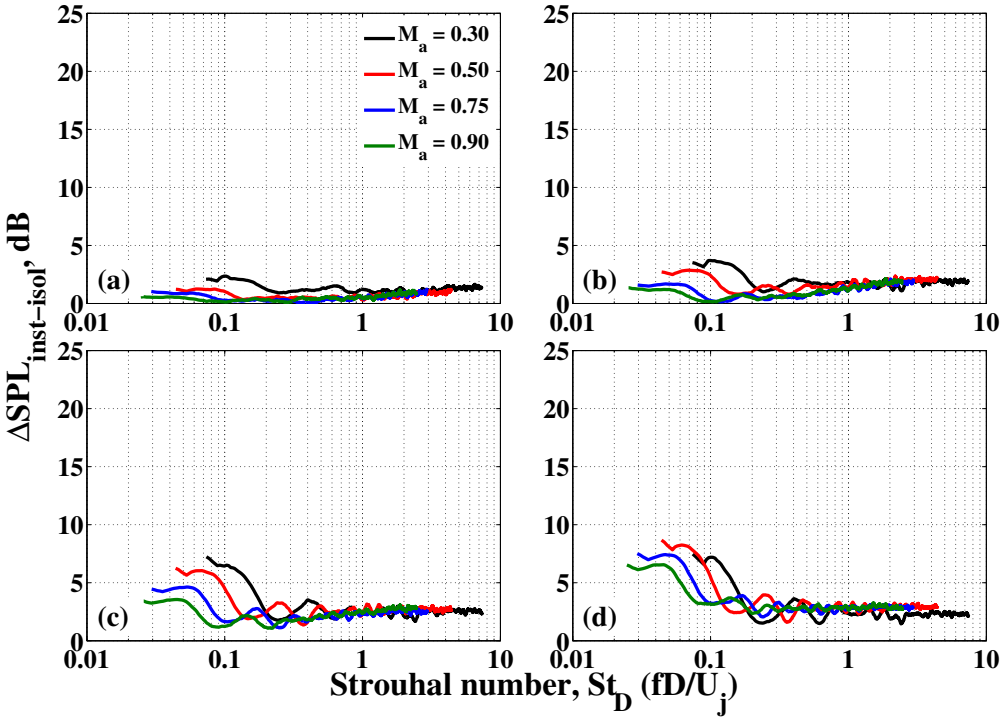

FIGURE 4.8: Far-field, smoothed 10 Hz narrowband installed jet ΔSPL increase above an isolated jet at four subsonic jet exit acoustic Mach numbers, M_a, and four axial plate extensions, l/D: (a) $l/D = 2$; (b) $l/D = 4$; (c) $l/D = 7$; (d) $l/D = 10$; [$h/D = 4.00$, $\theta_j = 90°$, $\phi = 0°$]

4.3.2 Far-field jet-surface interaction noise results

In this section, we will focus on the JSI noise contribution to the far-field installed jet noise spectrum above and below a semi-infinite horizontal flat plate (i.e. at $\phi = 0°$ and $\phi = 180°$, respectively). The shielded azimuthal angle, $\phi = 180°$ (i.e. the red lines in Figure 4.4), has been chosen because the data from this side of the plate does not contain any contributions from the JSR source. The following six subsections, in turn, detail the: (1) overall sound pressure level velocity dependence, (2) peak frequency location, (3) peak sound pressure level velocity dependence, (4) peak sound pressure level radial distance dependence, (5) polar directivity and (6) azimuthal directivity of the JSI noise source.

4.3.2.1 OASPL velocity analysis

When looking at the far-field velocity dependence of a noise source, it is essential to look at the total frequency-integrated energy, or overall sound pressure level (OASPL), radiated to a particular observer location. Thus, if we subtract the isolated jet mixing noise OASPL from the shielded installed jet OASPL, we can plot Figure 4.9 and establish the relationship between the radiated acoustic intensity of the JSI source versus jet acoustic Mach number for various jet-plate configurations. As Lighthill found for quadrupole jet noise, we are looking for a $I \propto U_j^n$ type law. Clearly, a relationship very close to $I \propto U_j^5$ is seen to exist for various installed jet configurations, which is consistent with Ffowcs-Williams and Hall's theory for non-compact scattered sound by an edge [19]. Unfortunately, however, the reliability of the shielded OASPL data deteriorates when h becomes too large because the relative strength of the JSI source above the jet mixing source (i.e. $\Delta\text{SPL}_{\text{jsi}}$) reduces.

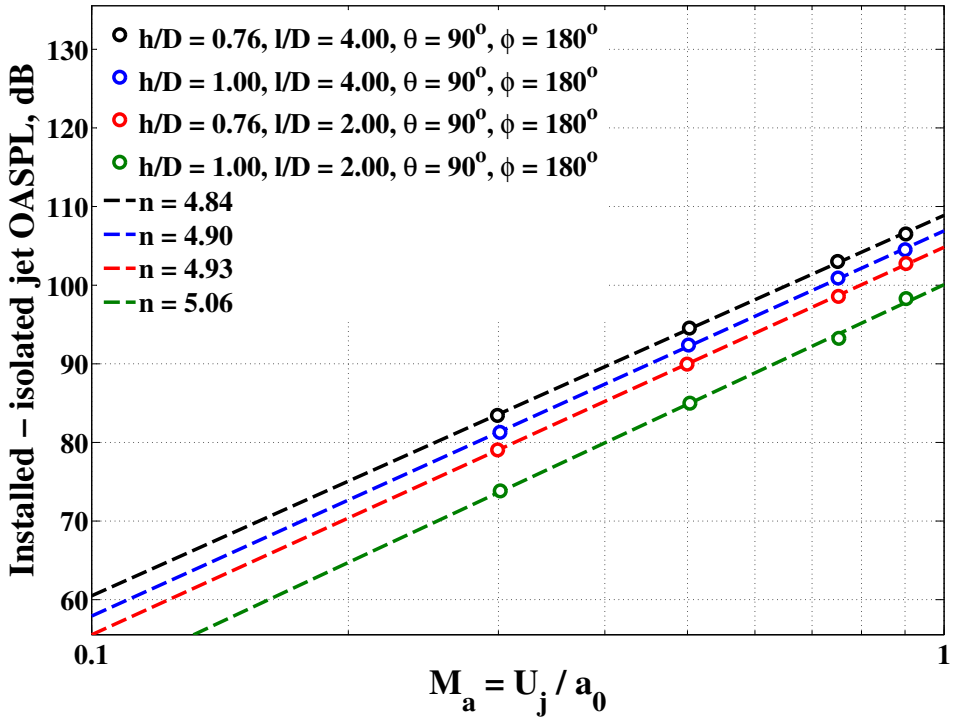

FIGURE 4.9: Far-field installed minus isolated jet $\mathrm{OASPL_{jsi}}$ versus acoustic Mach number for the DOAK jet installed in close proximity to a variety of horizontal flat plate locations. The linear least-squares regression best-fit lines (dashed) are also plotted to illustrate an $I \propto U_j^n$ dependence

4.3.2.2 Peak frequency analysis

If we look back at Figures 4.5-4.8, we notice that as the axial plate length, l, increases, the JSI noise peak frequency decreases. This is expected since, with increasing axial distance downstream from the nozzle exit, the jet shear layer thickness grows allowing increasingly large source eddies to develop. The corresponding peak frequency of the near hydrodynamic jet pressure spectrum generated by these larger eddies, therefore, will also decrease with increasing axial distance. What perhaps is less intuitive, though, is why the JSI noise peak frequency increases with decreasing radial distance, h. This can be explained with knowledge gained in Chapter 3 concerning the behaviour of the jet's hydrodynamic near pressure field as a function of radial distance, r. Recalling Figure 3.18, the reader will remember that as radial distance decreases, acoustic contributions from the higher source frequencies, which are assumed to sit along the lip-line of the jet (i.e. in the middle of the shear layer), increase. Thus, the frequency of the hydrodynamic peak also increases.

If we look at the shielded side of the jet (i.e. $\phi = 180°$) and subtract the isolated jet pressure from the installed jet pressure, we can define the 'pure' JSI noise source as, $\mathrm{SPL_{jsi}}$. Now, if we further smooth out the 10 Hz narrowband data by applying a low-pass filter, we can select the far-field JSI peak Strouhal number and plot it as a function of axial plate length, l. Due to the lower acoustic frequency limit of the anechoic chamber, however, it is only possible to see the peak of the JSI spectrum for plate lengths $l/D \leq 4$. For certain low velocity and large radial separation combinations, this issue is again prevalent. Furthermore, care must be taken when attempting to select the JSI peak for: (a) configuration combinations involving small axial plate lengths and large radial jet-plate separations, and (b) high acoustic Mach number flow conditions, where the $\Delta\mathrm{SPL_{jsi}}$ values are small. For this reason, the range of radial jet-plate separations chosen for this analysis was $0.67 \geq h/D \leq 1.25$. With these factors considered, we arrive at Figure 4.10. The general $1/l$ trend, initially reported by Head and Fisher [67] (i.e. the square series in Figure 4.10), is not inconsistent with the Doak Laboratory data presented here. When looking at the three linear least-squared regression best-fit lines for the Doak data (i.e. the orange lines), however, it is clear that for a constant axial plate length, the peak frequency does increase as radial distance decreases. This behaviour is consistent with the near-field isolated jet observations in Chapter 3. An important caveat to this figure, however, concerns the error introduced by selecting a single peak frequency from a broad spectral hump. While this will almost certainly account for some of the data scatter, the general trend nonetheless remains clear.

The final observation regarding Figure 4.10 can be made from Head and Fisher's [67] results for long plates (i.e. $l/D > 4$). Although the amount of data in this region is scarce, the peak JSI noise Strouhal number is seen to display a much weaker dependence upon l. While this $f \propto 1/l$ trend is a signature of the axial source distribution within an isolated free jet, one other explanation for this observation could concern the restricted growth of the upper jet shear layer due to the presence of the plate. As the jet spreads, the plate trailing edge will eventually become 'wetted' (or 'scrubbed') by the flow. At this point, at the plate trailing edge, the jet's rotational hydrodynamic pressure field will dominate over the irrotational pressure field. The mechanism for noise generation, therefore, would also change from a scattering of the irrotational pressure field to a fluctuating loading force on the trailing edge. The radiated peak frequency would then necessarily be a weak function of l because the source frequency of the fluctuating loading force exerted onto the plate by the fluid would now solely be determined by the size and convection velocity of the eddies convecting along the surface of the trailing edge rather than by the radial position of the edge relative to the sources on the nozzle lip-line, as is the case for the scattered irrotational hydrodynamic field situation.

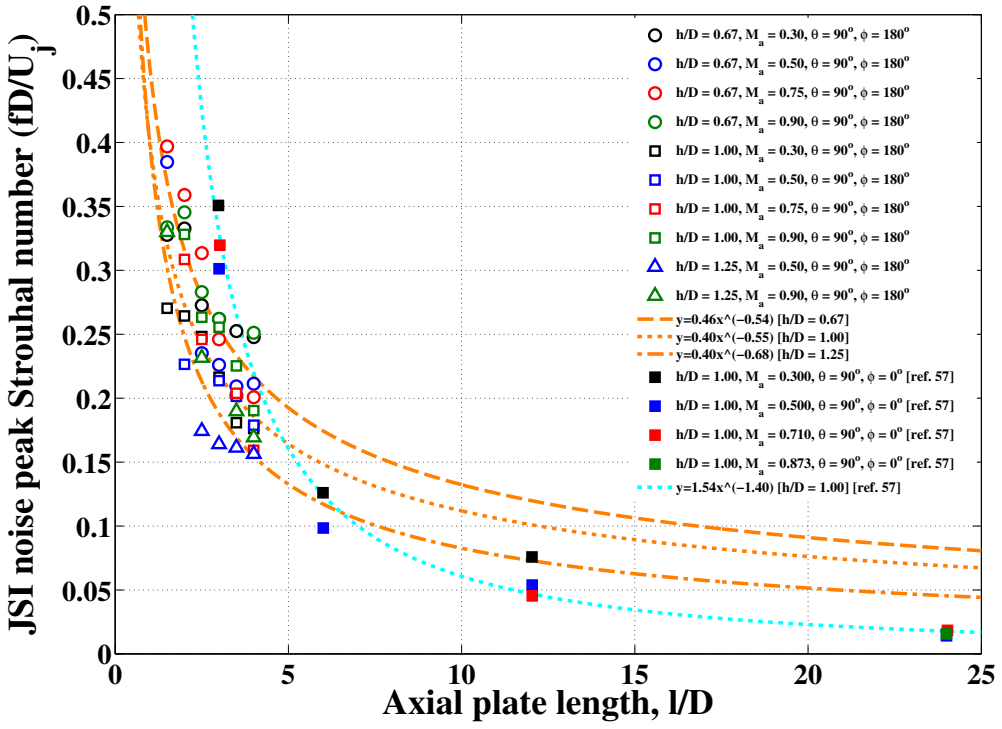

FIGURE 4.10: Far-field jet-surface interaction (JSI) noise peak Strouhal number versus axial plate length; [DOAK data - empty markers; Head and Fisher data - solid square markers]

4.3.2.3 Peak sound pressure level velocity analysis

According to Lighthill [33] (see Section 3.5.2), the amplitude of the hydrodynamic peak is expected to vary with the fourth power of the acoustic Mach number of the jet flow. Thus, if we plot the amplitude of the JSI noise source, $\mathrm{SPL}_{\mathrm{jsi}} - 40\log_{10}(M_a)$, against axial plate length for the same three radial plate separations, we arrive at Figure 4.11. Since the data markers collapse well onto each other, we can conclude that the $40\log_{10}(M_a)$ correction is a successful scaling law to use for both the near-field hydrodynamic and the far-field JSI peak SPLs. It is also apparent from this figure that the dependence of the far-field peak JSI noise level with axial plate length takes on a logarithmic-type dependence.

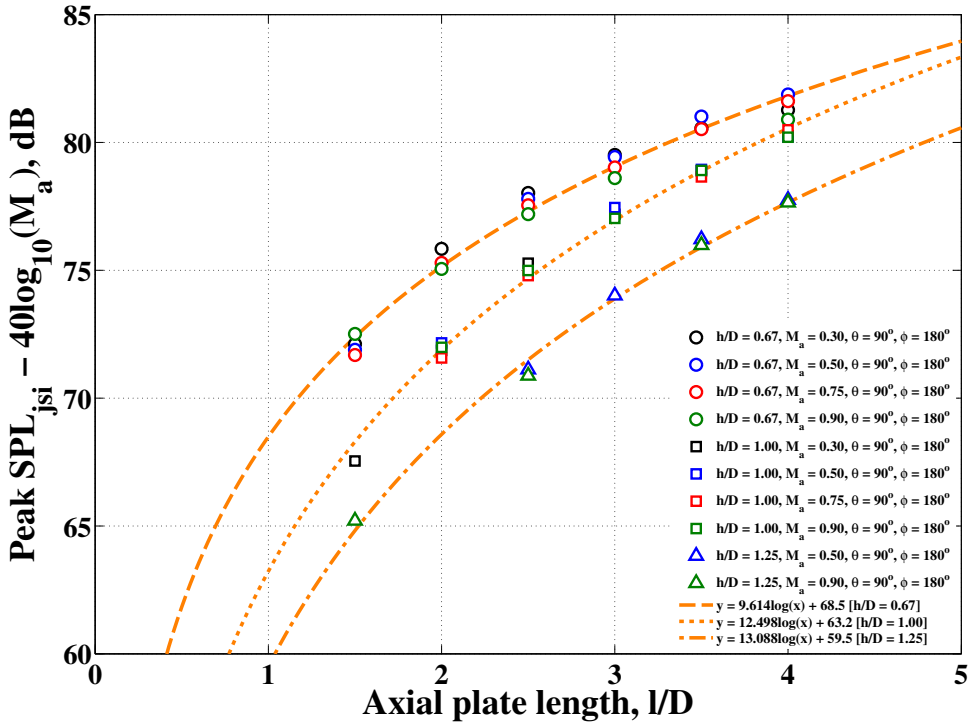

FIGURE 4.11: Far-field jet-surface interaction (JSI) noise peak SPL versus axial plate length

4.3.2.4 Peak sound pressure level radial distance analysis

As with Section 3.5.3, if we now attempt to collapse the JSI peak SPLs in Figure 4.11 further by accounting for the decay of the evanescent hydrodynamic field, we must include another correction factor based upon radial distance, $m10\log_{10}(r/D)$. It is not expected that a single value for m will collapse the data for every plate length. Indeed, as with the isolated jet, a m versus l dependence exists. Using data between $0.67 \leq h/D \leq 1.50$ and $1.5 \leq l/D \leq 4.0$, we can write down the following linear best-fit empirical expression for m,

$$m = -0.27(l/D) + 1.87\,. \tag{4.2}$$

Using this relationship, we can finally collapse all of the far-field JSI peak SPL data onto one logarithmic-type best-fit curve, see Figure 4.12. Future planned aerodynamic research, involving the turbulent statistics produced within the DOAK jet, will hopefully explain this logarithmic trend more clearly.

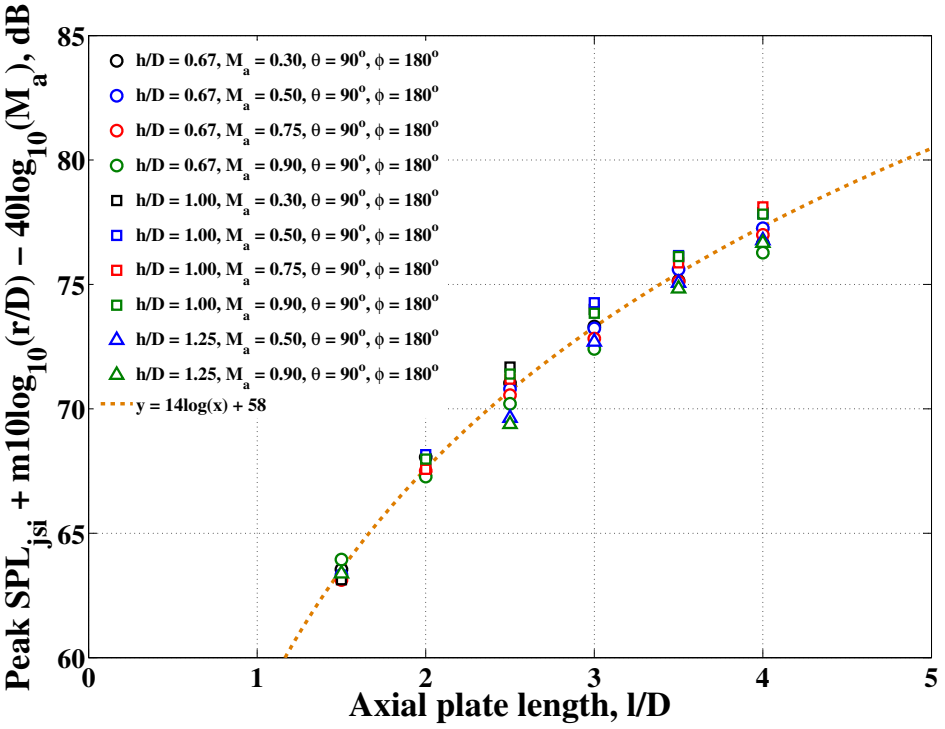

FIGURE 4.12: Far-field jet-surface interaction (JSI) noise peak SPL versus axial plate length (corrected for acoustic Mach number, M_a, and radial distance, r)

4.3.2.5 Polar directivity

If we recall Section 2.4, an empirical far-field frequency-dependent directivity function for installed jet noise was developed, in 1983, by Miller [1], see Equation 2.142. In this section, we will explore how Miller's model compares with the experimental data from the DOAK jet installed next to the horizontal flat plate. However, before we consider the single frequency JSI noise directivity, it is useful, first, to study the directivity of the frequency-integrated overall sound pressure level, or $\mathrm{OASPL}_{\mathrm{jsi}}(\theta_j)$. This quantity is defined simply by subtracting the isolated jet OASPL from the installed jet OASPL at each polar angle. In order to compare results from different jet-plate configurations and flow velocities, we can then use the following polar directivity factor,

$$D_{\mathrm{jsi}}(\theta_e) = \mathrm{OASPL}_{\mathrm{jsi}}(\theta_e) - \mathrm{OASPL}_{\mathrm{jsi}}(\theta_{e_{\max}}) \,, \tag{4.3}$$

where $\mathrm{OASPL}_{\mathrm{jsi}}(\theta_{e_{\max}})$ is the maximum OASPL measured over the complete range of polar angles.

Figure 4.13 shows the polar directivity patterns generated on both the unshielded and shielded sides of the DOAK jet (i.e. at $\phi = 0°$ and $\phi = 180°$, respectively) for four jet-plate configurations (subplots) and for the four acoustic flow Mach numbers (marker colours). Ideally, data from the shielded side of the jet should be used to investigate the 'pure' JSI noise source. This is so that one can neglect any contribution from the JSR source. Unfortunately, however, the quality of the $\mathrm{OASPL}_{\mathrm{jsi}}$ data on this side of the jet is low, particularly at the high flow acoustic Mach numbers where the difference between the installed and isolated jet levels is small. It is, thus, difficult to discern any robust directivity trends or patterns on the shielded side of the jet.

Figure 4.13 does, however, show a series of smooth directivity patterns on the unshielded side of the jet. This is particularly true of: 1) subplots (a), (b) and (d), where the jet is closest to the trailing edge of the plate, and 2) the black circle data series, where the acoustic Mach number is lowest. With these combinations of jet-plate geometry and jet flow velocity, the JSI noise contribution is substantially higher than that of the isolated jet noise (see also Figure 4.6). For the rest of this analysis, therefore, data from the closest-coupled jet-plate configuration (i.e. $h/D = 0.67$ and $l/D = 4$) and the lowest jet exit velocity flow condition (i.e. $M_a = 0.30$) will be studied to ensure that the peak JSI noise level is at least 10 dB above both the isolated jet and the JSR noise levels.

Figure 4.13 shows us that a $\sin^2(\theta_e/2)$ radiation pattern fits the unshielded data well. This is consistent with Ffowcs-Williams and Hall's semi-baffled dipole theory for a non-compact source in the vicinity of a semi-infinite half-plane [19].

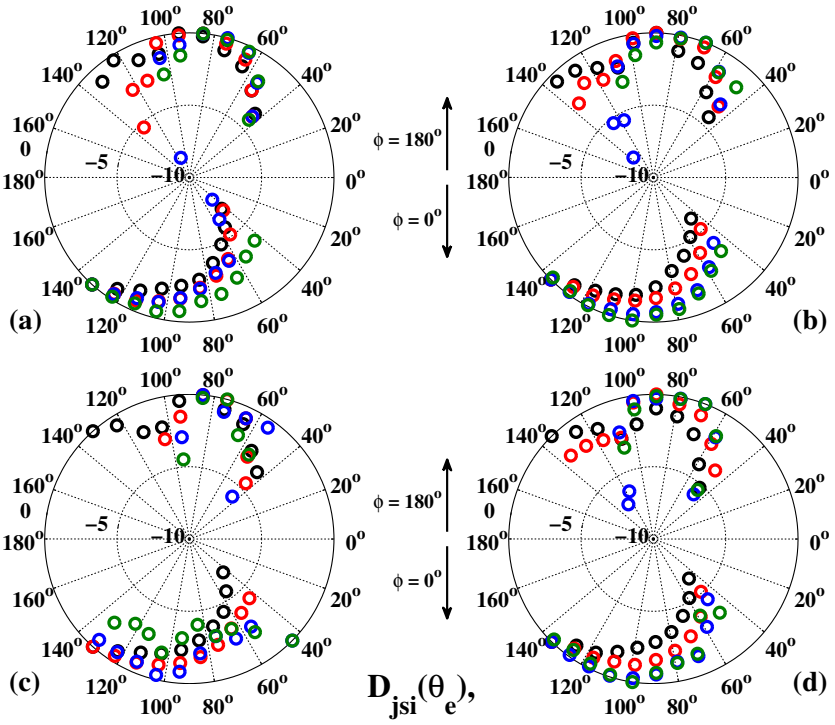

FIGURE 4.13: Far-field unshielded ($\phi = 0°$) versus shielded ($\phi = 180°$) JSI noise polar directivity factor, $D_{\text{jsi}}(\theta_e)$, for the horizontal flat plate installed at four locations next to the DOAK jet and operated at four subsonic acoustic Mach numbers: (a) $h/D = 0.67$, $l/D = 2$; (b) $h/D = 0.67$, $l/D = 4$; (c) $h/D = 1.00$, $l/D = 2$; (d) $h/D = 1.00$, $l/D = 4$; [black - $M_a = 0.30$; red - $M_a = 0.50$; blue - $M_a = 0.75$; green - $M_a = 0.90$]

If we now turn our attention to the single frequency polar directivity, we can repeat the above analysis using $\text{SPL}_{\text{jsi}}(f)$ instead of $\text{OASPL}_{\text{jsi}}$. Figure 4.14 shows a comparison between the DOAK jet data, Equation 2.142 from Miller [1] and Equation 2.136 from Roger and Moreau [64] at four separate frequencies. The frequencies chosen were logarithmically spaced across the JSI peak frequency range (i.e. between 400-4000 Hz) and the 'chord', c, was taken to be the total length of the flat plate, i.e. $c/D = 20$. As frequency increases (i.e. by moving from subplot (a) to (d)), we can see that each of the directivity factors tend towards the $\sin^2(\theta_e/2)$ limit for a fully non-compact, semi-baffled dipole. When studying Miller's result, we can appreciate the presence of his low frequency interference effect by the oscillations in the data at the high polar angles. While similar oscillations can also be seen in the DOAK data, the sparsity of the array makes it difficult to say definitively whether they are indeed real artefacts. Clearly, a smaller microphone spacing would be necessary in the forward jet arc for future experiments.

Finally, we can compare the DOAK directivity patterns with those derived by Roger and Moreau [64] for their modified Amiet finite geometry flat plate and 3D gust approach (as described in Section 2.3.3.2). The dotted red series in Figure 4.14 shows a less good match with the DOAK data compared with Miller. The potential problem

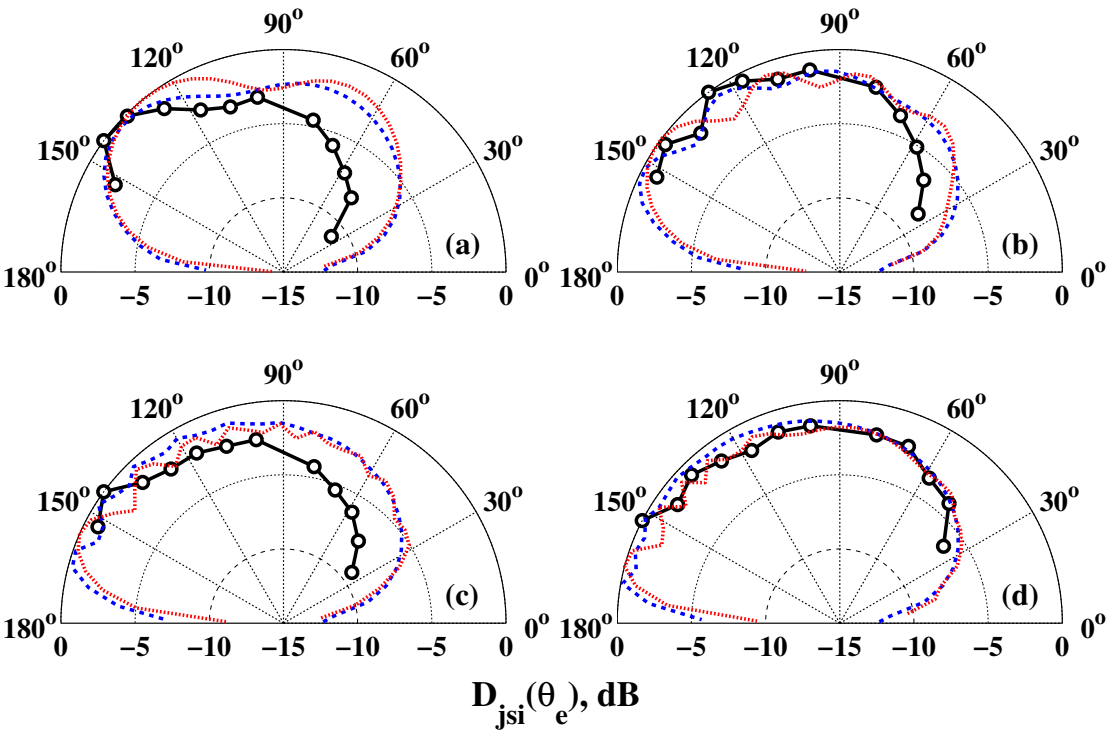

FIGURE 4.14: Far-field single frequency polar directivity comparison between the DOAK data (black) and both Miller's [1] (blue) and Roger & Moreau's [64] (red) theories at: (a) 400 Hz ($kc = 5.6$, (b) 860 Hz ($kc = 12.0$), (c) 1860 Hz ($kc = 25.8$) and (d) 4000 Hz ($kc = 55.6$); [$h/D = 0.67$; $l/D = 4$; $M_a = 0.30$]

with using this model is that it assumes that a uniform flow, containing frozen turbulence, passes both above and below the flat plate. Clearly, with the JSI situation, a non-uniform jet flow passes on just one side of the surface and over a small portion of the surface in the spanwise direction. The spanwise dimension, therefore, is particularly difficult to define. Perhaps if one were to split up the plate trailing edge surface into strips and apply a specific velocity profile to each gust along the span, it would be possible to better model the situation? The reader should also remember that there is a decay time constant associated with the turbulence generated within a jet shear layer. Is it safe to assume, therefore, that the turbulence passing the trailing edge of the plate is, in fact, frozen? This is another research topic currently being investigated.

4.3.2.6 Azimuthal directivity

If we plot the difference in decibels between the installed and isolated jet data at the five azimuthal angles between $0° \leq \phi \leq 180°$, see Figure 4.15, we notice a classic $\sin^2(\phi)$ figure-of-eight dipole radiation pattern for all jet-surface configurations and jet velocities. This result is consistent both experimentally, with Head and Fisher [67], and mathematically, with Curle [47] and Ffowcs Williams and Hall [19]. Only free turbulence quadrupole jet mixing noise is expected to radiate tangentially to the plate surface (i.e. at $\phi = 90°$). Any interpretations from the $\Delta\text{OASPL}_{\text{jsi}}(\phi)$ data plotted in Figure 4.15c at $M_a > 0.3$ are inconclusive because the decibel difference in decibel deltas are all less than 1. The only clear exception to the $\sin^2(\phi)$ trend appears for the slowest jet installed closest to the longest plate (i.e. when $h/D = 0.67$, $l/D = 4$, or the black line in Figure 4.15b), where a small amount of additional sound (approximately 2.5 dB) is radiated towards the $\phi = 90°$ observer angle. One hypothesis to explain this asymmetrical feature would be if the installed jet had been redirected upwards towards the plate via a Coandă-type effect. In this scenario, the quadrupole jet mixing noise sources would move closer to the $\phi = 90°$ observer position and, hence, increase the ΔOASPL between the isolated and installed jet cases. This point remains unsolved until further aerodynamic data confirms the presence of such a Coandă effect.

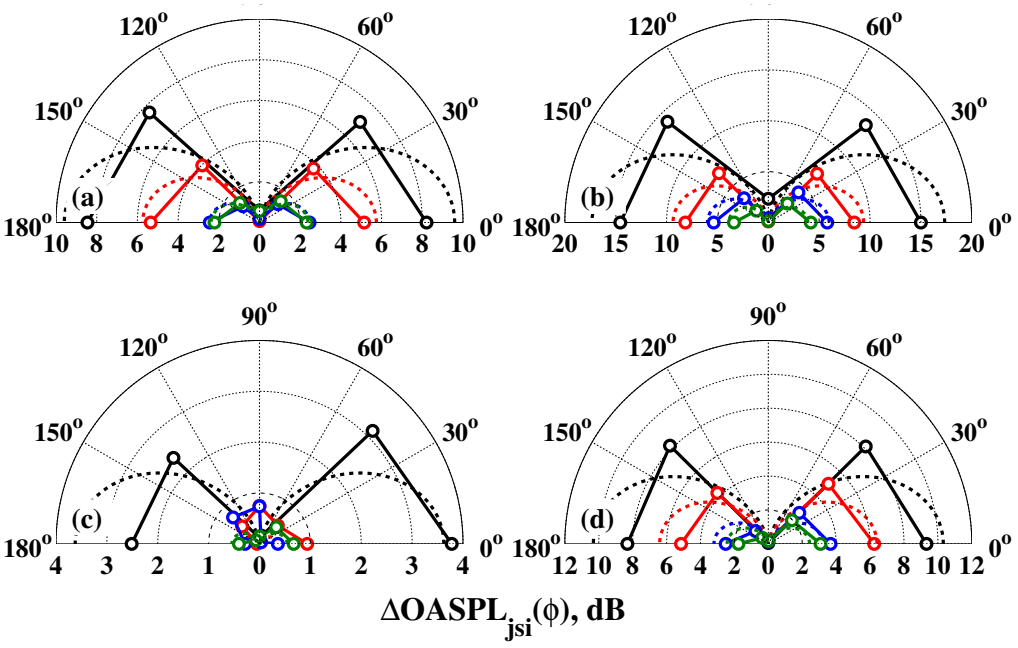

FIGURE 4.15: Far-field $\Delta\text{OASPL}_{\text{inst-isol}}$ azimuthal directivity for the horizontal flat plate installed at four locations next to the DOAK jet and operated at four subsonic acoustic Mach numbers: (a) $h/D = 0.67$, $l/D = 2$; (b) $h/D = 0.67$, $l/D = 4$; (c) $h/D = 1.00$, $l/D = 2$; (d) $h/D = 1.00$, $l/D = 4$; [black - $M_a = 0.30$; red - $M_a = 0.50$; blue - $M_a = 0.75$; green - $M_a = 0.90$; dotted lines - $A\sin^2(\phi)$ linear least-squared best-fit lines; $\theta_j = 90°$]

4.3.3 Near-field surface pressure results

In this section, data recorded by the near surface pressure array on the horizontal flat plate are analysed and discussed in order to reveal further details about the jet-surface interaction noise mechanism. There are five parts to this section. Firstly, an overview is given of the typical streamwise and spanwise spectra measured on the surface of the plate. Secondly, a comparison is made between the installed surface pressure spectrum and the (geometrically) equivalent isolated jet free-field spectrum. Thirdly, the phase relationship between the source pressure (measured at the plate trailing edge) and two far-field observer pressures (on opposite sides of the plate) is studied. The fourth part examines the frequency-dependent velocity with which the near pressure fields of the DOAK jet convect along the surface of the plate for different jet-plate configurations. Finally, a brief analysis of the spanwise correlation length-scale of the source pressure field at the plate trailing edge is presented and discussed with reference to Amiet's analytical 2D turbulent boundary layer gust solution [59] and Roger and Moreau's analytical 3D back-scattered gust solution [64].

A schematic of the near surface pressure array can be see below, in Figure 4.16. The locations of the transducers are defined relative to the centre of the plate's trailing edge and are displayed in Table 4.1.

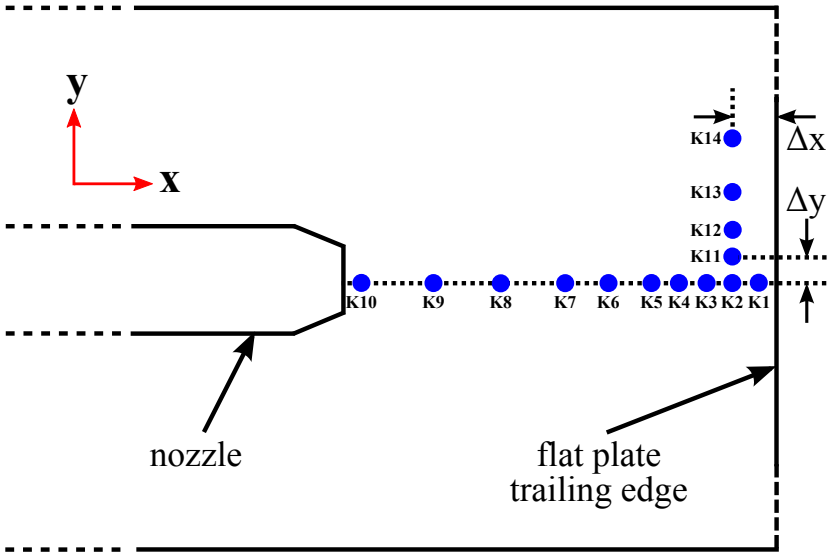

FIGURE 4.16: Schematic of the near-field Kulite array layout on the horizontal flat plate

4.3.3.1 General near-field installed jet noise results

Figure 4.17 shows the surface sound pressure levels measured along the centreline of the horizontal flat plate installed next to the DOAK jet. In this particular figure, the

Kulite ID	K1	K2	K3	K4	K5	K6	K7	K8	K9	K10	K11	K12	K13	K14
Δx (mm)	10	20	30	40	50	75	100	150	200	250	20	20	20	20
Δy (mm)	0	0	0	0	0	0	0	0	0	0	10	20	40	80

TABLE 4.1: Kulite locations relative to the trailing edge of the horizontal flat plate

jet acoustic Mach number is, $M_a = 0.30$. An amplitude correction factor of -6 dB has been applied to each installed surface pressure spectrum in order to account for the coherent addition of reflected pressure seen on the surface of the plate. Each data series has also been passed through a low-pass filter (or 'smoothed') for display clarity.

The reader will notice that as one moves upstream along the plate towards the nozzle (i.e. K1 $\rightarrow$ K7), the peak frequency of the spectrum increases. This behaviour is expected since the smaller eddies, which form within the upper jet shear layer close to the nozzle, dominate the hydrodynamic source field. One other observation is that the sub-peak (i.e. low wavenumber energy region) gradient of the installed near jet spectrum remains constant regardless of the axial position along the jet. In contrast, the sur-peak (i.e. inertial subrange energy region) gradient appears to steepen as x/D decreases. This observation essentially tells us that more high frequency energy is seen closer to the plate trailing edge than to the nozzle. Future planned aerodynamic investigation using hot-wires and five-hole probes should help to explain this observation fully.

If we non-dimensionalise the frequency axis using the Strouhal number, $\mathrm{St}_{r1} = fr_1/U_j$ (where $r_1 = 1$), and subtract a velocity amplitude correction factor, $m10\log_{10}(M_a)$, we can compare spectra measured at different flow velocities. Figure 4.18 shows us that the installed surface pressure spectral peaks collapse well when $m = 3$. It is thought that this cubic exponent relates to the near-field component of the dipole pressure field generated at the trailing edge. We can compare this result to the quadrupole-generated noise from the isolated jet case where the near-field spectral peaks collapse when $m \approx 4$, see Figure 3.21. It is also worth noticing at this point that both the sub-peak and sur-peak gradients of the near field surface pressure spectra are insensitive to the acoustic Mach number of the flow.

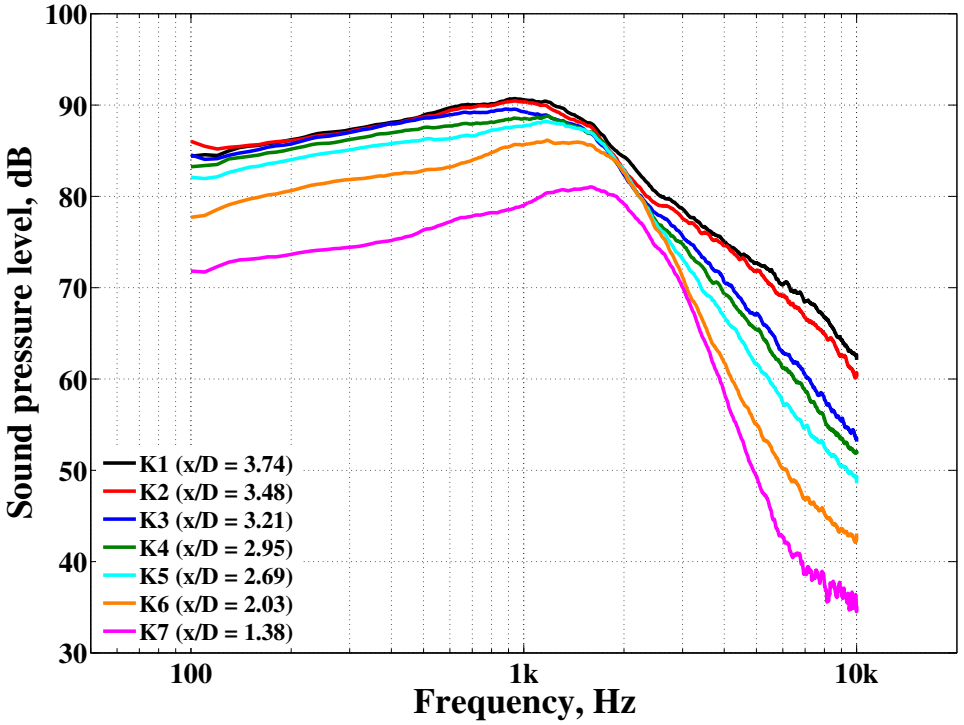

FIGURE 4.17: Streamwise Kulite smoothed narrowband surface pressure spectra on the horizontal flat plate installed next to the DOAK jet; [$h/D = 0.67$; $l/D = 4$; $y/D = 0$; $M_a = 0.30$]

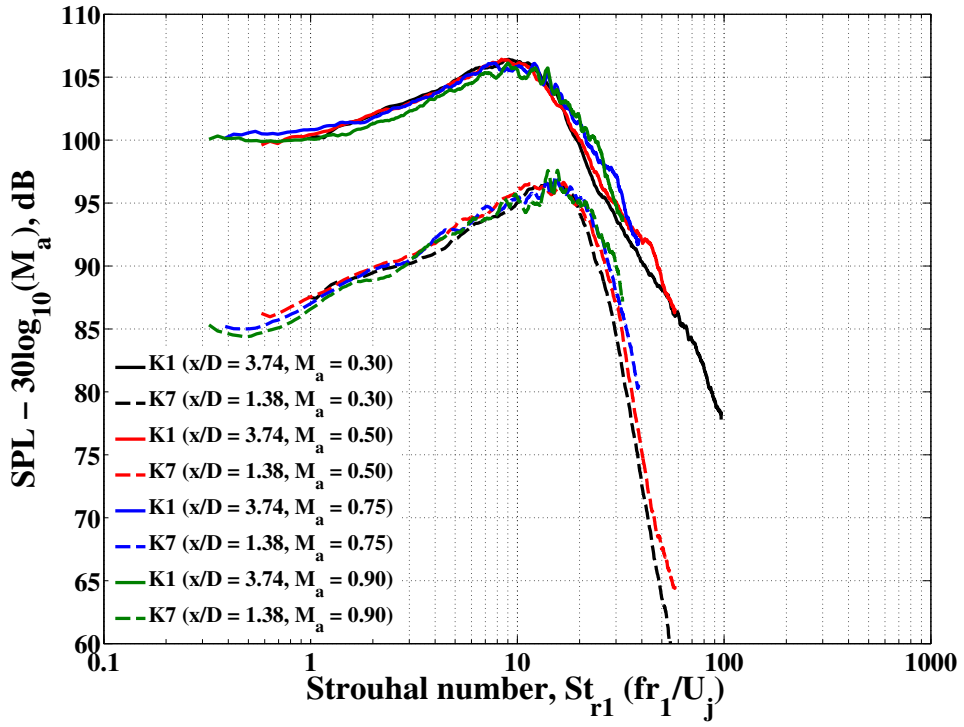

FIGURE 4.18: Velocity-corrected streamwise Kulite smoothed narrowband surface pressure spectra on the horizontal flat plate installed next to the DOAK jet; [$h/D = 0.67$; $l/D = 4$]

Regarding the spanwise surface pressure distribution on the horizontal flat plate, Figure 4.19 shows a typical example of the behaviour of the field at the trailing edge of the plate with increasing spanwise distance from the centre (i.e. as $y/D > 0$).

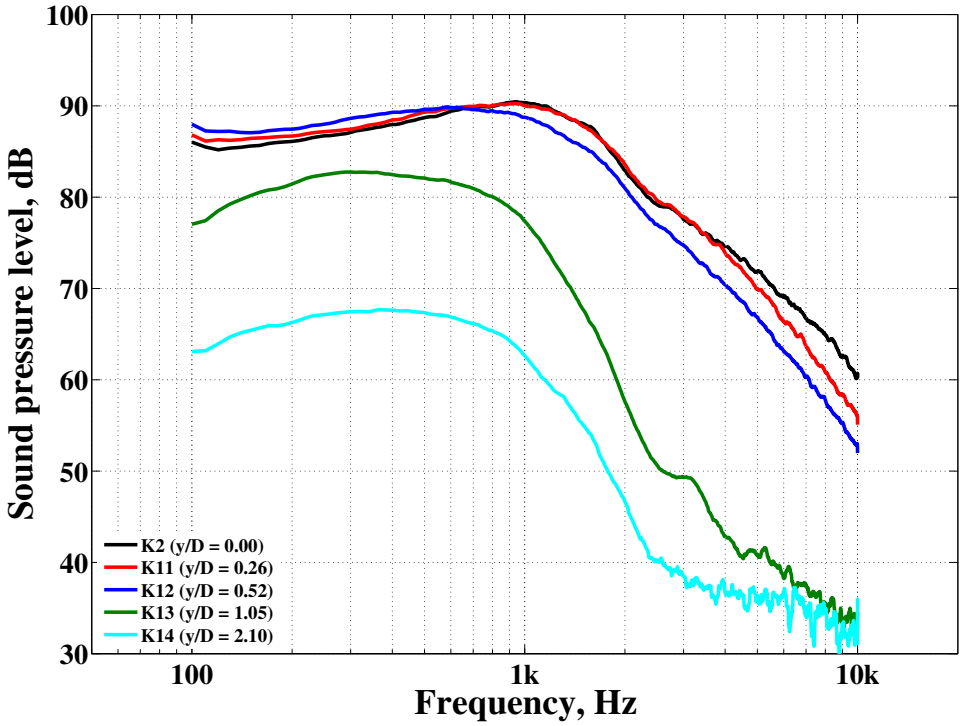

FIGURE 4.19: Spanwise Kulite surface pressure spectra on the horizontal plate installed next to the DOAK jet; [$h/D = 0.67$; $l/D = 4$; $x/D = 3.48$; $M_a = 0.30$]

4.3.3.2 Installed jet surface spectra versus isolated jet spectra

In this subsection, a near-field read-across is made between the isolated jet free-field spectra measured in Chapter 3 and the installed surface pressure spectra measured by the trailing edge Kulite (*K1*). As before, we will use the non-dimensional Strouhal x-axis, St_r, so that spectra from all four jet velocities can be compared. We can see from Figure 4.20 that at both the lowest and the highest frequencies, the installed and isolated spectra (i.e. the solid and dotted lines, respectively) tend to overlay. For the 100-10 kHz mid-frequency range, however, additional noise is recorded for the installed jet surface microphone compared to the isolated jet free-field microphone case. The maximum delta dB between the installed and isolated jet spectra, in fact, varies from approximately 6 dB at $M_a = 0.90$ up to 12 dB at $M_a = 0.30$. This result could be explained by the presence of a Coandă effect in the installed jet case. Such an effect would redirect the jet closer to the plate, reducing the radial separation, r, and, thus, increasing the strength of the hydrodynamic field incident on the surface of the plate. One other explanation involves a modification of the decay time constant of the

turbulence within the upper shear layer of the installed jet itself. Put simply, if the development of the jet is constrained by the presence of a solid surface, the intensity of the turbulence within the jet will likely increase as the upper shear layer is 'squashed' by the plate. Further aerodynamic investigation would help to answer this question.

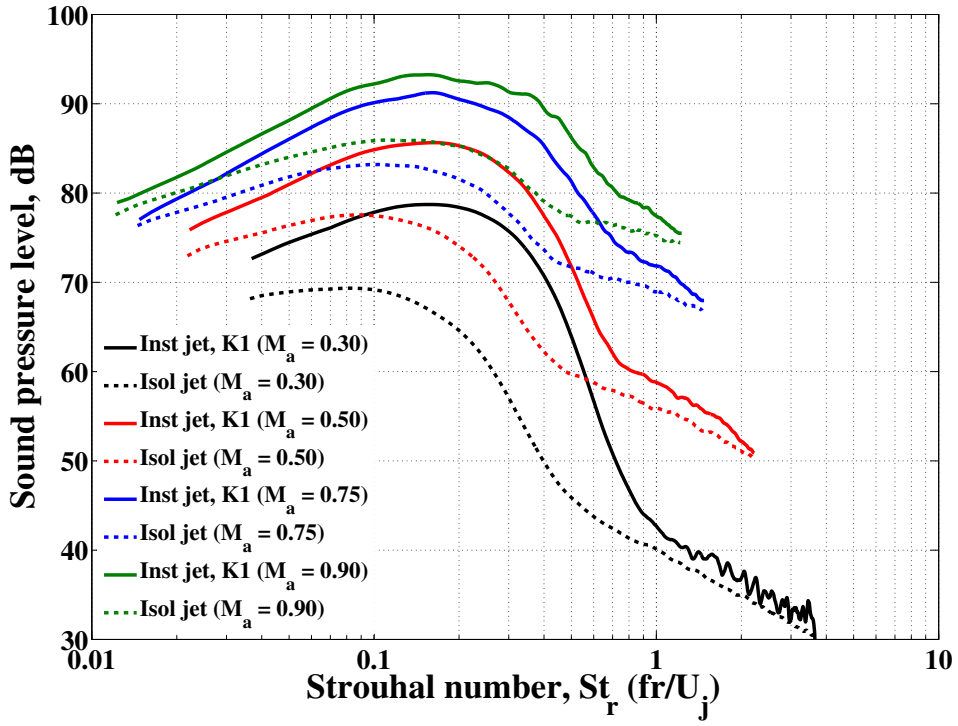

FIGURE 4.20: Near-field spectral comparison between an isolated jet and an jet installed next to the horizontal flat plate; $[h/D = 1.50;\ l/D = 4;\ x/D = 3.74;\ y/D = 0]$

The final observation concerns the location of the peak frequency. Figure 4.20 shows a slight mismatch between the installed and the isolated jet spectra. The installed jet spectrum peaks at $\mathrm{St}_r \approx 0.17$ compared to $\mathrm{St}_r \approx 0.1$ for the isolated jet. The constrained nature of the jet's development could, again, be responsible for this frequency mismatch.

4.3.3.3 Near-field to far-field phase analysis

This subsection compliments the work of Head and Fisher [67] and Yu and Tam [68], who have both performed experiments with an installed subsonic jet next to a flat plate. They both identified the presence of a highly coherent sound field in exact phase opposition either side of the plate's trailing edge when positioned in close proximity to the jet. If we look at the phase angle difference, $\Delta\varphi$, relationship between the pressure measured at the trailing edge of the horizontal flat plate and the pressure measured in the far-field on both the unshielded and shielded sides of the jet, we arrive at Figure 4.21.

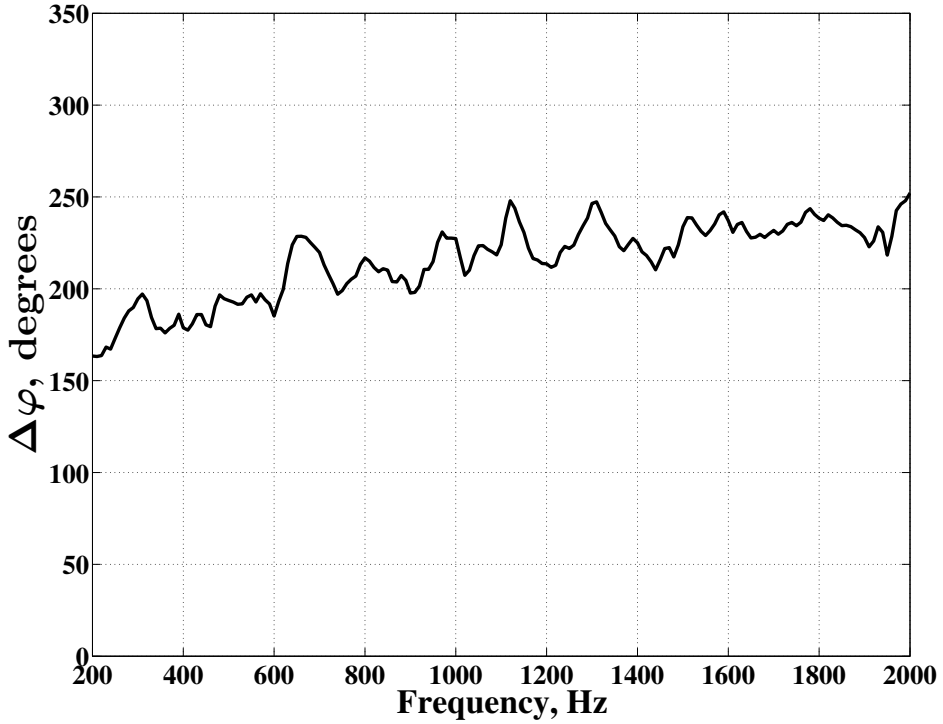

FIGURE 4.21: Phase angle difference between the trailing edge surface pressure near-field and the $\theta_j = 90°$ far-field pressures generated when a horizontal flat plate is installed next to the DOAK jet; $[h/D = 0.67; l/D = 4; M_a = 0.50]$

It is clear that a phase shift close to 180° does indeed exist between these two pressure signals. This result is consistent with previous research [67, 68] and confirms the presence of a dipole-type source. The same phase relationship is also observed for all of the other jet-plate configurations and acoustic Mach numbers tested.

4.3.3.4 Trailing edge convection velocity analysis

In this subsection, the term 'convection velocity' is defined as the phase velocity of the near surface pressure field as it propagates between two transducers spaced a distance, ϵ, apart. Mathematically, the streamwise convection velocity, U_c, is written as,

$$U_c = \frac{2\pi\epsilon_1}{\nabla\varphi} \tag{4.4}$$

where ϵ_1 is the streamwise separation distance between the two transducers, and $\nabla\varphi$ is the gradient of the phase angle versus frequency graph. An example of such a graph can be seen in Figure 4.22. The phase angles have been unwrapped for display clarity purposes. The two streamwise trailing edge surface pressure transducers ($K1$ and $K2$) are spaced at an interval of $\epsilon_1 = 10$ mm, (see Table 4.1). The quality of the phase information between these two transducers deteriorates above $\mathrm{St}_r = 0.3$.

While Figure 4.22 tells us that the ratio of the convection velocity to jet exit velocity is independent of acoustic Mach number, it appears that two separate gradients, or convection velocities, exist for $\mathrm{St}_r < 0.1$ and $\mathrm{St}_r > 0.1$. The low frequency hydrodynamic field seems to convect at 73% of the jet exit velocity whereas the higher frequency pressure field appears to convect more slowly at 44% of the jet exit velocity.

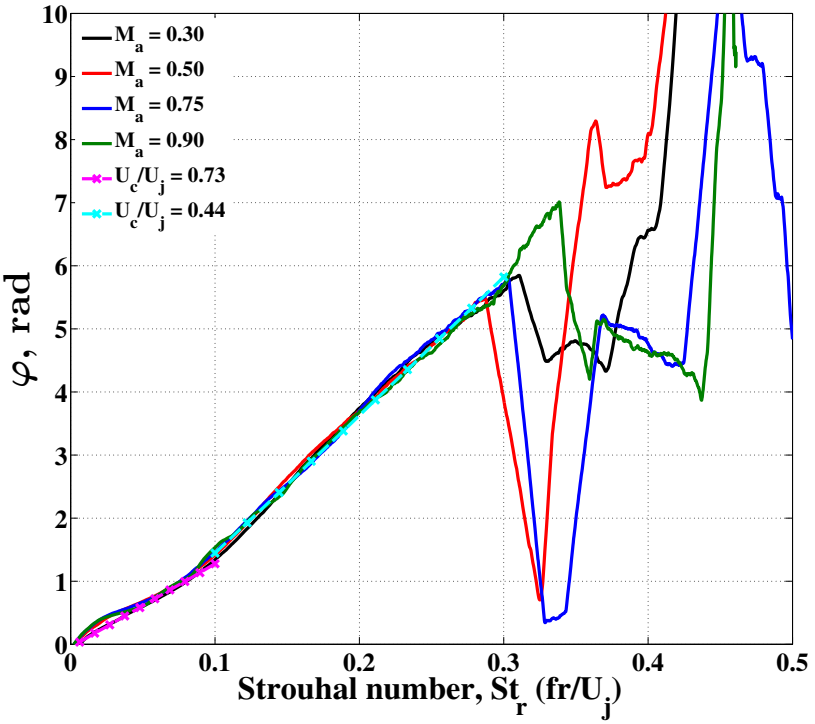

FIGURE 4.22: Unwrapped phase angle relationship between two trailing edge surface pressure transducers, $K1$ and $K2$, on the surface of the horizontal flat plate installed next to the DOAK jet at four acoustic Mach numbers; $[h/D = 0.67;\ l/D = 4]$

The pressure field convection velocity established by this measurement technique will form an essential input into future analytical models, based upon Amiet's theory for trailing edge noise. It will be essential to compare these data, however, with future aerodynamic hot-wire or five-hole probe measurements.

4.3.3.5 Spanwise correlation length analysis

It is important to appreciate the spanwise correlation length-scales of the wall pressures along the trailing edge of the plate when attempting to use analytical models (e.g. Amiet or Roger and Moreau) to predict the sound scattered to the far-field. As mentioned in Section 2.3.3, the expression for the spanwise correlation length is,

$$\Lambda_y(\omega) = \int_0^\infty \sqrt{\Gamma^2(\omega, \epsilon_2)} d\epsilon_2 \tag{4.5}$$

where Γ^2 is the coherence function between two surface pressure transducers, see Equation A.1, and ϵ_2 is the spanwise separation between the transducers. Figures 4.23-4.26 show the behaviour of this spanwise acoustic coherence function as the plate trailing edge is moved radially away from the jet and then axially upstream towards the nozzle exit.

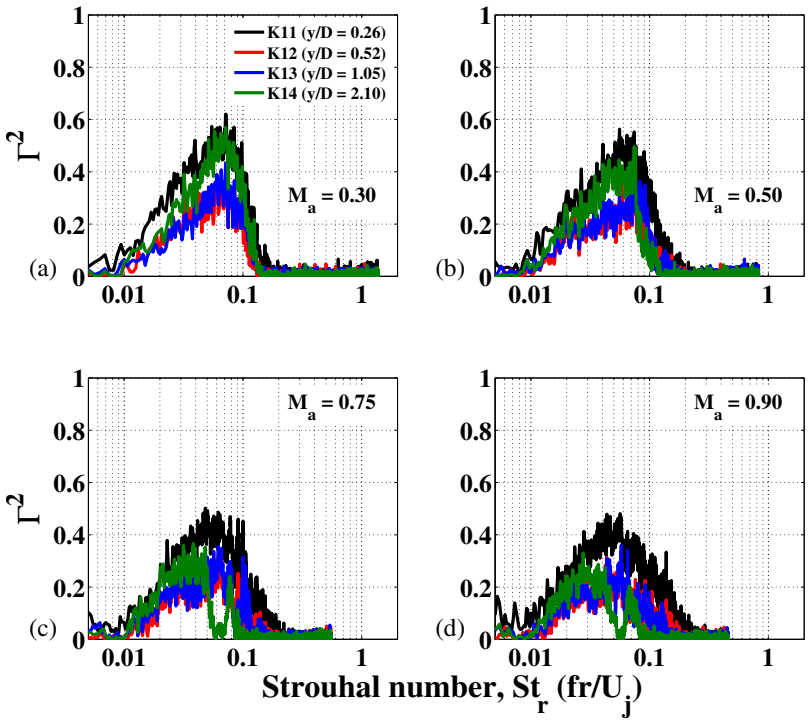

FIGURE 4.23: Acoustic coherence of the surface pressure field measured at multiple points along the span of the trailing edge of a horizontal flat plate installed next to the DOAK jet at four subsonic acoustic Mach numbers: (a) $M_a = 0.30$, (b) $M_a = 0.50$, (c) $M_a = 0.75$, (d) $M_a = 0.90$; $[h/D = 0.67; l/D = 4]$

While there are many features in these plots that require further analysis, the three main conclusions are as follows: (1) greater coherence is seen when the plate trailing edge is positioned further away from the jet (i.e. when the edge is within the irrotational region of the near pressure field); (2) the coherence between the centreline transducer and each of those along the span generally reduces (as expected) as transducer spacing increases; (3) when the trailing edge is placed within the rotational region of the near pressure field (see Figure 4.23), the coherence does not continue to reduce with increasing distance from the mid-span of the plate (as expected from the conclusion point (2)). It will be particularly important to better understand this third behaviour before the correlation length parameter can be fed into a modified-Amiet type model.

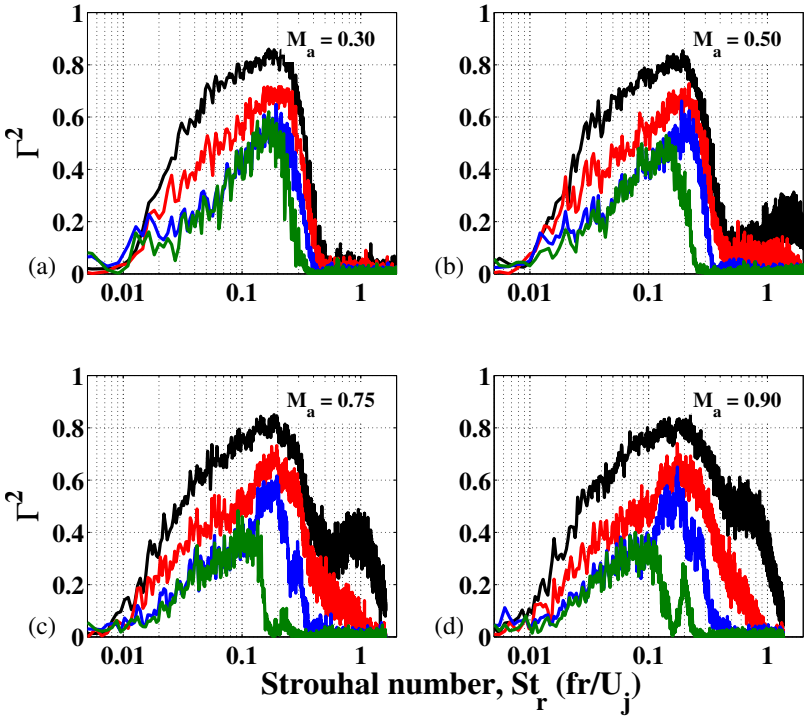

FIGURE 4.24: Acoustic coherence of the surface pressure field measured at multiple points along the span of the trailing edge of a horizontal flat plate installed next to the DOAK jet at four subsonic acoustic Mach numbers: (a) $M_a = 0.30$, (b) $M_a = 0.50$, (c) $M_a = 0.75$, (d) $M_a = 0.90$; $[h/D = 1; l/D = 4]$

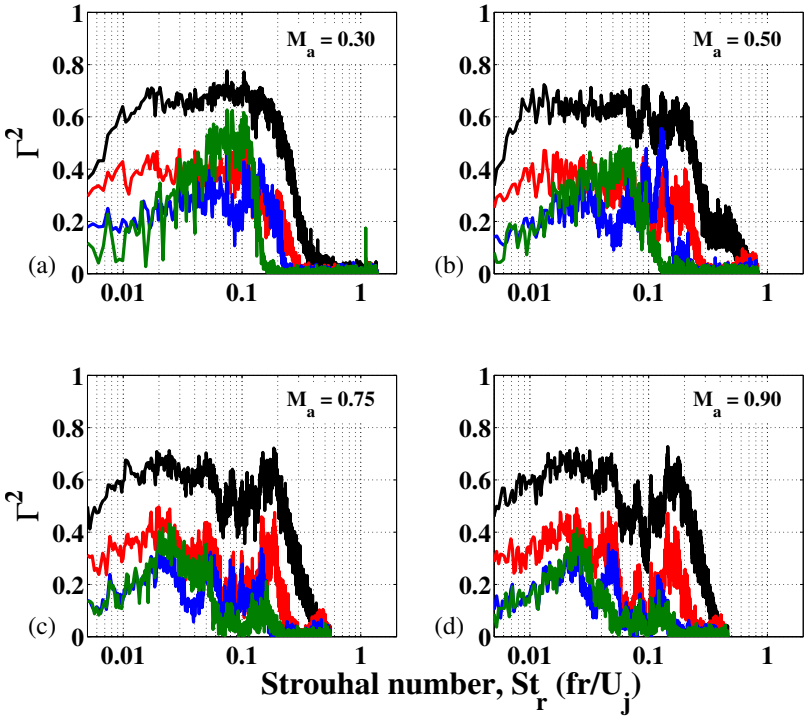

FIGURE 4.25: Acoustic coherence of the surface pressure field measured at multiple points along the span of the trailing edge of a horizontal flat plate installed next to the DOAK jet at four subsonic acoustic Mach numbers: (a) $M_a = 0.30$, (b) $M_a = 0.50$, (c) $M_a = 0.75$, (d) $M_a = 0.90$; $[h/D = 0.67; l/D = 2]$

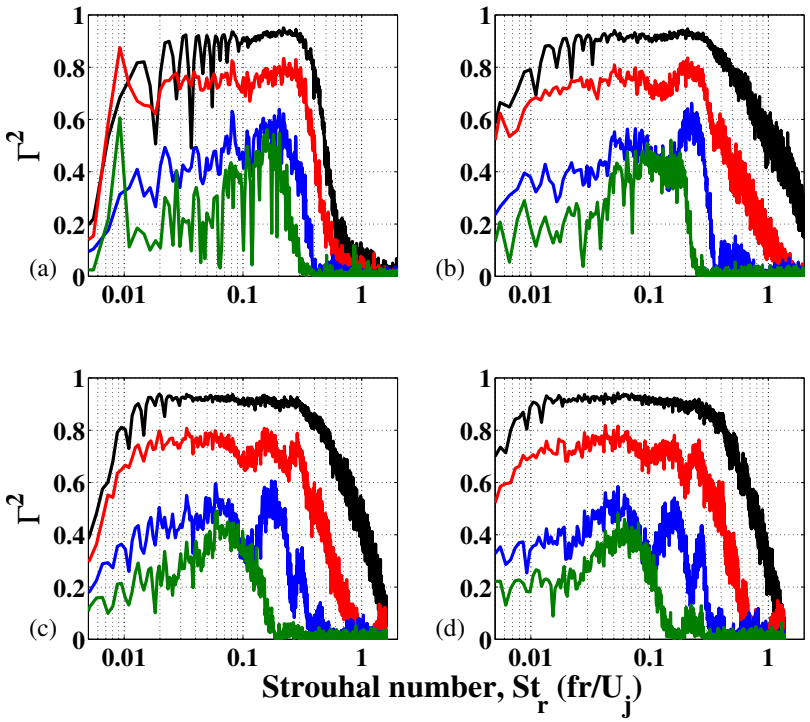

FIGURE 4.26: Acoustic coherence of the surface pressure field measured at multiple points along the span of the trailing edge of a horizontal flat plate installed next to the DOAK jet at four subsonic acoustic Mach numbers: (a) $M_a = 0.30$, (b) $M_a = 0.50$, (c) $M_a = 0.75$, (d) $M_a = 0.90$; $[h/D = 1; l/D = 2]$

4.3.4 Far-field jet-surface reflection noise results

As mentioned in Section 2.4.1, the best understood topic of under-wing-engine-mounted installation noise is the reflection (and shielding) of high frequency jet mixing noise by a surface, $\Delta\text{SPL}_{\text{jsr}}$. In this section, therefore, only a short discussion will be given regarding far-field JSR noise data at a single polar and azimuthal observer angle beneath a semi-infinite horizontal flat plate (i.e. at $\theta_j = 90°$ and $\phi = 0°$, respectively).

If we first study Figure 4.5, we can see that, at this closest-coupled radial configuration (i.e. $h/D = 0.67$), the JSR noise spectrum is also only visible above the low frequency JSI spectrum at $\text{St}_D > 1$. For these frequencies, the JSR noise also appears to have a constant ΔSPL above the isolated jet mixing noise. We can say, therefore, that the JSR noise is dependent neither on frequency nor acoustic Mach number at $\text{St}_D > 1$. If we then study the furthest-coupled configuration (i.e. $h/D = 4$), see Figure 4.8, where the $\Delta\text{SPL}_{\text{jsi}}$ source is almost negligible, we can see that the JSR source, in fact, can be seen almost over the entire installed noise spectrum, at $\text{St}_D > 0.3$. In this case, we can think of $\text{St}_D = 0.3$ as a 'cut-on' Strouhal number. Furthermore, at the low Strouhal numbers, at $\text{St}_D < 1$, the JSR noise spectrum shows a slight frequency dependence. If one thinks of the JSR noise as a distributed line of point sources located on a virtual jet lip-line, see Figure 4.27, then purely from a geometrical line-of-sight point of view, one would expect this cut-on frequency to be a function of the plate length, l. In other words, as the plate length increases and more downstream virtual sources are revealed to the surface, one would expect to see a lower JSR cut-on Strouhal number. Establishing the relationship between this cut-on Strouhal number and l/D, however, is outside the scope of this thesis and an area for further research.

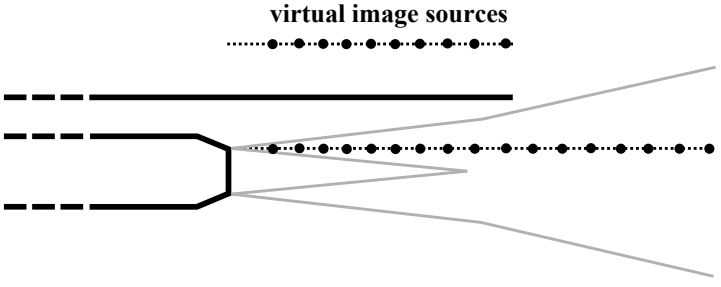

FIGURE 4.27: Schematic of jet surface reflection virtual image sources

The second observation to make is that, within each of the four figures (4.5-4.8), as we increase the axial length of the plate, l, horizontally downstream from the jet exit (i.e. as we look from subplot (a) through to (d)), the value of the $\Delta\text{SPL}_{\text{jsr}}$ typically increases from 1.5 dB, at $l/D = 2$, up to 3.5 dB, at $l/D = 10$. The first point worth mentioning here is that, for an incoherent addition of pressures (i.e. the reflected

sound generated from multiple distributed sources), one would not expect the total energy measured to exceed 3 dB. Perhaps a degree of partial coherent addition is being seen here for the most closely-coupled and longest plate lengths (i.e. for $h/d = 0.67$ and $l/d \geq 7$)? The fact that the $\Delta\text{SPL}_{\text{jsr}}$ value drops to 1.5 dB for the shortest plate length (i.e. $l/D = 2$) can be explained simply because fewer high frequency virtual sources, situated upstream of the end of the potential core (i.e. $\text{St}_D > 1$ at $x/D < 4$), can 'see' the $\theta_j = 90°$ observer. This also explains why a slightly positive gradient exists for the $\Delta\text{SPL}_{\text{jsr}}$ spectrum between $1 < \text{St}_D < 10$ for the $l/D = 2$ plate length at all four radial h/D positions (i.e. subplot (a) in each of the four figures). The highest frequency virtual sources furthest upstream for a $l/D = 2$ length plate clearly have the best chance to see the observer microphone at $\theta_j = 90°$ and, therefore, should get closest to $\Delta\text{SPL}_{\text{jsr}} = 3$ dB. Both of these observations are new pieces of information in the field of jet-surface reflection noise research and clearly both require further investigation before they can be modelled properly.

4.4 Conclusions

An extensive experimental investigation into the interaction between a subsonic jet and a flat plate has been successfully conducted and validated against historical data. Both near-field and far-field acoustic measurements have helped to confirm the presence of Ffowcs-Williams and Hall's scattered quadrupole source. Since the hydrodynamic source wavelengths involved are small compared to the length of the plate (i.e. $\lambda \ll L$), the overall sound pressure level jet-surface interaction trailing edge noise is seen to radiate with a non-compact, cardioid (or $\sin^2(\theta_e/2)$) polar directivity. When one studies the effect of the finite length of the plate on a single frequency basis, however, the data matches well with Miller's semi-empirical directivity model, which suggests that sound radiated above the wing diffracts around the topside of the plate and is back-scattered by the plate's leading edge.

An empirical expression to model the radial decay of the far-field JSI noise source has been found. It is hoped that future planned aerodynamic investigation of the installed jet turbulent velocity field will explain the logarithmic-type axial dependence of the peak JSI noise sound pressure level observed in the data.

A preliminary study of the convection velocity and the spanwise correlation length data has been performed. Further analysis and understanding of the acoustic coherence data, however, is needed before it can be used with confidence in a modified-Amiet analytical trailing edge noise model.

Further research into jet-surface reflection noise is required to understand how values ΔdB values higher than 3 can exist in installed jet data. A comparison with McLaughlin's [90] ray-based semi-empirical jet-surface reflection model would also be useful to establish whether his jet blockage model predicts the attenuation observed in the DOAK data.

Chapter 5

Large Model-Scale Installed Jet Noise

In this chapter, the design of and results from a new set of model-scale installed jet noise experiments are presented. The limitations of previous experimental work are initially reviewed followed by a description of the latest UK Technology Strategy Board (TSB) project SYMPHONY - SYstem Manufacturing and Product design tHrough cOmponent Noise technologY. Large, $1/10^{\text{th}}$-scale far-field acoustic experimental results, conducted at the QinetiQ Noise Test Facility (NTF) are analysed and compared to the smaller $1/50^{\text{th}}$-scale results from the Doak Laboratory (DOAK). It should be noted, at this point, that the author's involvement with the large-scale QinetiQ test campaign included: 1) designing the near-field flap surface pressure microphone array, 2) supervising the daily running of the facility, 3) checking that good quality data was being recorded, and 4) analysing both the acoustic and wing aerodynamic data sets after the test.

5.1 Introduction

The main problem with historical installed jet testing is that it has never been necessary to investigate very closely-coupled nozzle-to-wing configurations. Due to the ever-increasing bypass ratios of modern and future UWM turbofan aircraft, however, it has now become an important area for research. In addition to this limitation, typically only small amounts of forward arc acoustic data exist in jet noise research at all. This makes it difficult to characterise the jet installation noise sources fully. We saw, for example, in the previous chapter, how important the forward arc directivity pattern is in understanding the mechanism behind the jet-surface interaction (JSI)

noise source. We also know that the amplitude, frequency content and directivity characteristics of this source are all particularly sensitive to slight changes in the fundamental jet-wing geometry. Thus, a large-scale, parametric jet installation effects test campaign was designed for QinetiQ's NTF, in Farnborough. The campaign was funded by the UK Technology Strategy Board under a project called SYMPHONY - SYstem Manufacturing and Product design tHrough cOmponent Noise technologY.

The aim of this SYMPHONY test campaign was to simulate a modern day, generic 150-seater, regional civil aircraft. A nominal $1/10^{\text{th}}$-scale half-wing aerodynamic test model, therefore, was designed and positioned above a variety of different jet nozzles. Both acoustic and aerodynamic data were then acquired for a range of key close-coupled nozzle-to-wing configurations. Over the entire campaign, a comprehensive data set was recorded, comprising a total of eleven test builds and nineteen different flow conditions. Four separate far-field microphone arrays (azimuthal, polar, flyover and phased) were used to capture data, together with both static and dynamic near-field pressure measurements on the surface of the half-wing model. In this thesis, however, only far-field acoustic data from the test will be presented.

As one attempts to model a realistic installed jet situation, many questions arise. Some example questions include: What happens to the physics of the problem when one introduces an ambient flow (or flight stream) around the jet and the wing? Is the jet redirected due to the lift generated by the wing and flap? How is the hydrodynamic field of the jet altered when a flap is deployed into the upper jet shear layer? What diffraction effects would one expect to see from a 3D curved wing section with a finite chord? Will a tapered spanwise wing (or flap) trailing edge significantly alter the far-field directivity? What effect does the addition of a hot core flow have on the hydrodynamic field incident on the trailing edge of the wing (or flap)? Similarly, what happens when the nozzle no longer produces an axisymmetric flow field, for example, when the engine pylon is attached? Only a couple of these questions are actually investigated in this chapter. The first objective was to establish how well the $1/50^{\text{th}}$-scale DOAK data compared to the $1/10^{\text{th}}$-scale NTF situation.

5.2 QinetiQ Noise Test Facility

QinetiQ's Noise Test Facility (NTF), situated in Farnborough, Hampshire (UK), is a large high-quality anechoic chamber specifically designed for model-scale exhaust noise research. The facility has internal dimensions of 27 m long by 26 m wide by 15 m high, making it suitable for far-field noise measurements, see Figure 5.1. Twenty-two

thousand non-reflective, acoustic wedges line the chamber rendering it anechoic down to frequencies of 90 Hz. Positive ventilation prevents hot-gas recirculation, providing stable noise propagation paths.

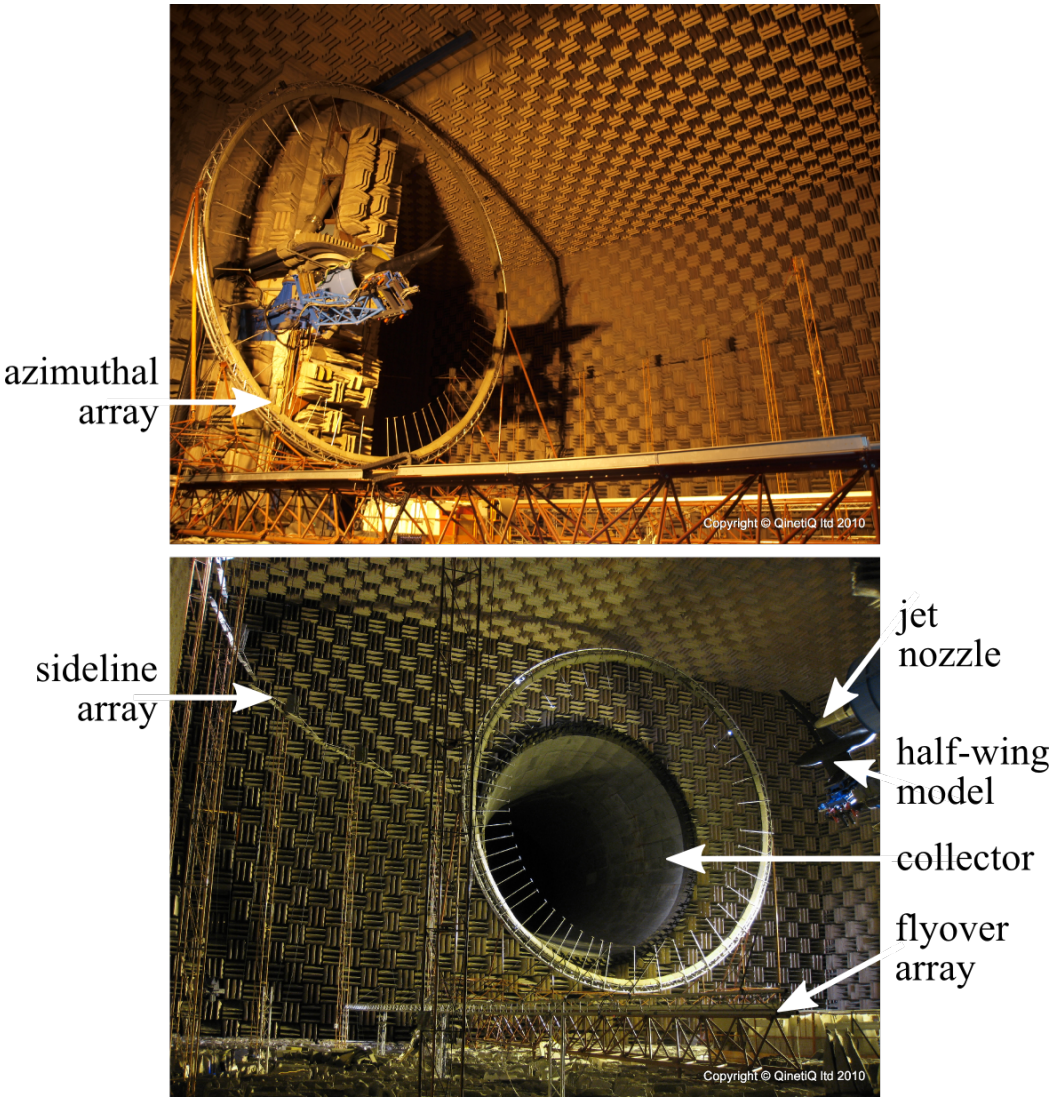

FIGURE 5.1: Photograph of the QinetiQ Noise Test Facility (NTF)

The facility rig protrudes into the chamber at a height of 8.73 m. Core and bypass air flows are supplied by a centrifugal compressor. A maximum combined mass flow of 15 kg/s at 3 bars can be achieved. Core air is then heated to jet exhaust temperatures using an 'Avon combustion can, specially modified to burn LPG. Bypass temperatures are controlled by mixing in cooler air from a heat exchanger system. Test models are mounted onto a sting assembly, which is cantilevered into the centre of a 1.8 m diameter open jet wind tunnel (i.e. the circular blue nozzle in Figure 5.1). This tunnel is used for in-flight simulation up to Mach 0.33. The air flow for this is supplied by a very large blower (350 kg/s) and passes through an extensive silencing arrangement such that the noise produced by the flight stream is effectively only due to that of the

fundamental jet mixing. The test model protrudes from the flight-simulation duct by about one duct diameter thereby enabling measurements to be made in the forward arc of the jet.

Target jet operating conditions are corrected for day conditions, such that the acoustic Mach number remains constant. In other words, the ratio of the jet velocity to the ambient speed of sound is kept constant as well as the ratio of the square roots of the jet temperature and the ambient temperature. When the flight stream is operational, ambient is taken to be the value within the flight-stream. Aerodynamic data, in the form of multiple total pressure, temperature and mass flow measurements are taken from probes and Venturi meters upstream of the nozzle. This data is used to compute real-time conditions, which are matched to the corrected target conditions. Jet conditions are matched to tolerances of ± 3 m/s on computed velocity and ± 5 K on total temperature. Accurate pressure measurements are ensured through regular weekly calibration. Dedicated boundary layer suction surfaces also feature on the sting assembly to minimise adverse aerodynamic effects inherent to the cantilevered design.

5.3 Experiment Hardware

Several new pieces of hardware were designed and manufactured for the SYMPHONY tests, including: two model-scale exhaust nozzles, a three-dimensional half-wing aerodynamic model and a three-axis traversable wing support structure.

5.3.1 Jet nozzles

Several generic nozzle geometries were chosen so that the fundamental jet installation noise mechanisms could be studied and published without infringing any commercial intellectual property rights. In this thesis, results from two axisymmetric nozzles are studied. The first nozzle is the single-stream S33-ASS nozzle, see Figure 3.11. This nozzle was chosen so that direct comparisons could be made with the DOAK jet. The second nozzle is the coaxial S33-A55 jet nozzle, see Figure 5.2, which housed a central bullet and both upper and lower bifurcations. This nozzle was chosen to act as the next step up in complexity en route to simulating the realistic full-scale engine situation. A comparison between these two nozzles, therefore, would reveal the effect of the core flow and bullet on the installed jet noise. A table outlining the key aerodynamic parameters of these two nozzles and the ambient flight stream nozzle is given in Table 5.1. Some asymmetrical nozzle features (e.g. the addition of the wing pylon) were also tested, however, further study into these effects is beyond the scope of this thesis.

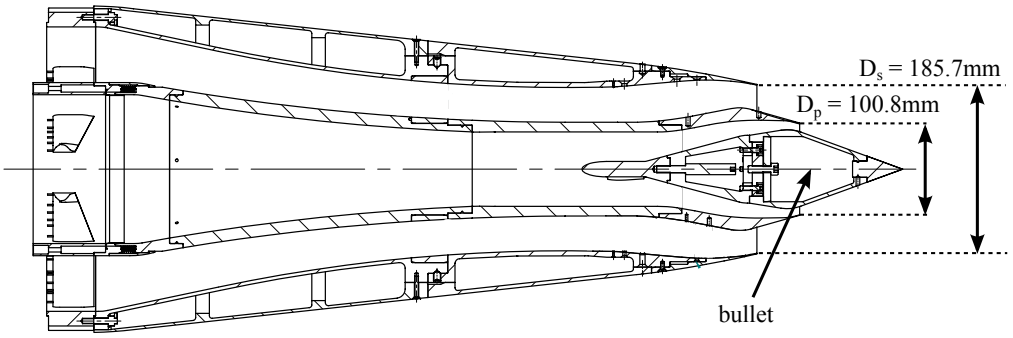

FIGURE 5.2: SYMPHONY S33-A55 185.7 mm diameter, axisymmetric, short-cowl coaxial nozzle with bullet schematic

S33-ASS bypass nozzle internal diameter (m)	0.1857
S33-ASS bypass nozzle exit area (m^2)	0.027084
S33-A55 core nozzle internal diameter (m)	0.1008
S33-A55 core nozzle exit area (m^2)	0.003073
S33-A55 bypass nozzle internal diameter (m)	0.1857
S33-A55 bypass nozzle exit area (m^2)	0.013828
S33-A55 core protrusion from bypass (m)	0.0471
S33 bypass protrusion from flight stream (m)	1.9450
Flight stream nozzle internal diameter (m)	1.80
Flight stream nozzle exit area (m^2)	2.54

TABLE 5.1: SYMPHONY key axisymmetric nozzle dimensions

5.3.2 Half-wing model

A half-wing (starboard) model was designed to represent a modern day generic 150-seater, civil transport aircraft powered by an under-wing-mounted (UWM) turbofan engine. The key scaling parameter used was the ratio of the jet bypass nozzle exit diameter to the wing chord. Nozzle operating constraints within the NTF lead to the design of a nominal $1/10^{\text{th}}$ scale aerodynamic test model.

5.3.2.1 Aerodynamic design

Previous jet installation noise test programmes [72, 73] have highlighted the importance of having a representative lift distribution around the wing because of its influence on the jet aerodynamics. The aerodynamic design activity was, therefore, required to create aerofoil sections and wings that, in combination with a deployed trailing edge flap, produced lift coefficients comparable to that of an aircraft at the take-off and approach conditions.

Simulating the wing at incidence to the ambient flight stream flow (i.e. when $\xi \neq 0$), however, proved to be the most problematic issue. Further investigation of the concept

highlighted the adverse implications of a deflected flight stream flow on the facility infrastructure as well as additional aerodynamic considerations arising from the design of a kinked nozzle assembly. A decision was taken, therefore, to realise a test solution which would produce the lift distributions, up-wash and down-wash associated with a wing at take-off and landing incidence, but with the wing positioned at zero incidence.

In addition, a decision to exclude leading edge slats was also made in order: (a) to reduce the geometric and aerodynamic complexity in the vicinity of the NTF nozzle installation and (b) to remove any unwanted acoustic effects arising from the slat cavity. Furthermore, to achieve an optimal lift distribution, a linear wing twist was applied to the planform (with zero twist at the crank position). A schematic of the baseline planform can be seen in Figure 5.3. The key planform dimensions are listed in Table 5.2.

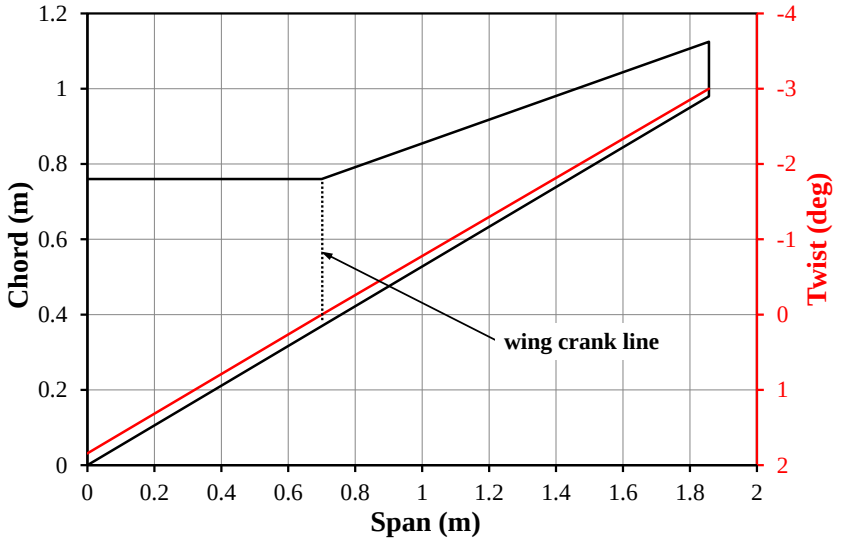

FIGURE 5.3: SYMPHONY baseline wing planform and twist distribution

Aspect ratio, AR	9.6
Taper ratio	0.193
Leading edge sweep (°)	27.8
Inner trailing edge sweep (°)	0
Outer trailing edge sweep (°)	17.6
Model semi-span (m)	1.858
Root chord (m)	0.763
Crank chord (m)	0.390
Tip chord (m)	0.147
Spanwise crank position (m)	0.707
Half-model reference area (m^2)	0.717

TABLE 5.2: SYMPHONY half-wing baseline planform dimensions

The initial baseline aerofoil section chosen was RAE model M2417C - a typical supercritical section optimised for transonic cruise performance. In order to produce

high-lift coefficients at low incidence but also to retain a geometrically representative lower (pressure) surface for the jet-wing interaction investigation, the upper (suction) surface profile was modified using the Flow Solutions 2D panel method, *Newpan*. The viscous-coupling capability contained in Newpan was used to provide viscous pressure distributions and surface boundary layer properties at the test free-stream Reynolds number ($\mathrm{Re} = 1 \times 10^6$). The boundary layer transition location was left free to vary.

Three separate configurations were designed: (1) a cruise (or clean wing) configuration, (2) a take-off configuration (with nominal 16° deployed flaps), and (3) an approach configuration (with nominal 32° deployed flaps). A series of increased camber aerofoil sections and trailing edge flap geometries were designed and evaluated in Newpan to meet the high-lift performance targets. The final two-dimensional geometries were then extruded into a three-dimensional configuration using the CAD design package *Catia V5*. Several 3D design features are worth mentioning at this point. Firstly, a representative wing tip geometry was created at the 94% span of the cruise wing profile. Secondly, the junction between the wing root leading edge and fuselage was blended, using an onglet, to reduce aerodynamic interference between the fuselage and the wing. Thirdly, from the initial planform dimensions, the wing was seen to extend radially across the shear layer of the ambient flight stream flow. Since this would generate unwanted aerodynamic noise, which would likely contaminate the measurements of the installed jet noise, the lift generated towards the edge of the flight stream was reduced by shortening and narrowing the outboard section of the wing. Finally, the cove between the wing trailing edge and flap was given a simple rear facing step geometry to represent current transport aircraft high-lift systems. All of these features are displayed in Figure 5.4.

The finite volume CFD flow solver *Fluent* was used to evaluate the full 3D performance of the final wing design to ensure that the required pressure coefficient, C_p, distributions could be achieved and that no flow separations were likely to occur on either the upper or lower wing surfaces. Prior to the numerical analysis, the geometries and surrounding flow field were discretised using the geometry meshing code *ICEM*. Tetrahedral volume meshes were employed with prismatic cells in the wall region to model the surface boundary layer. Density boxes were used to control mesh resolution in regions of interest such as the flap cove with each mesh containing approximately 5 million cells. The velocity and pressure distributions around each configuration were evaluated at each mesh point with a 2^{nd}-order discretisation scheme and a k-ϵ turbulence model with non-equilibrium wall functions. Figure 5.5 shows the final pressure coefficient results of the SYMPHONY wing for the take-off and landing configurations at ISA conditions, a flight stream Mach number of $M_f = 0.29$ and zero degrees incidence (i.e. $\xi = 0°$).

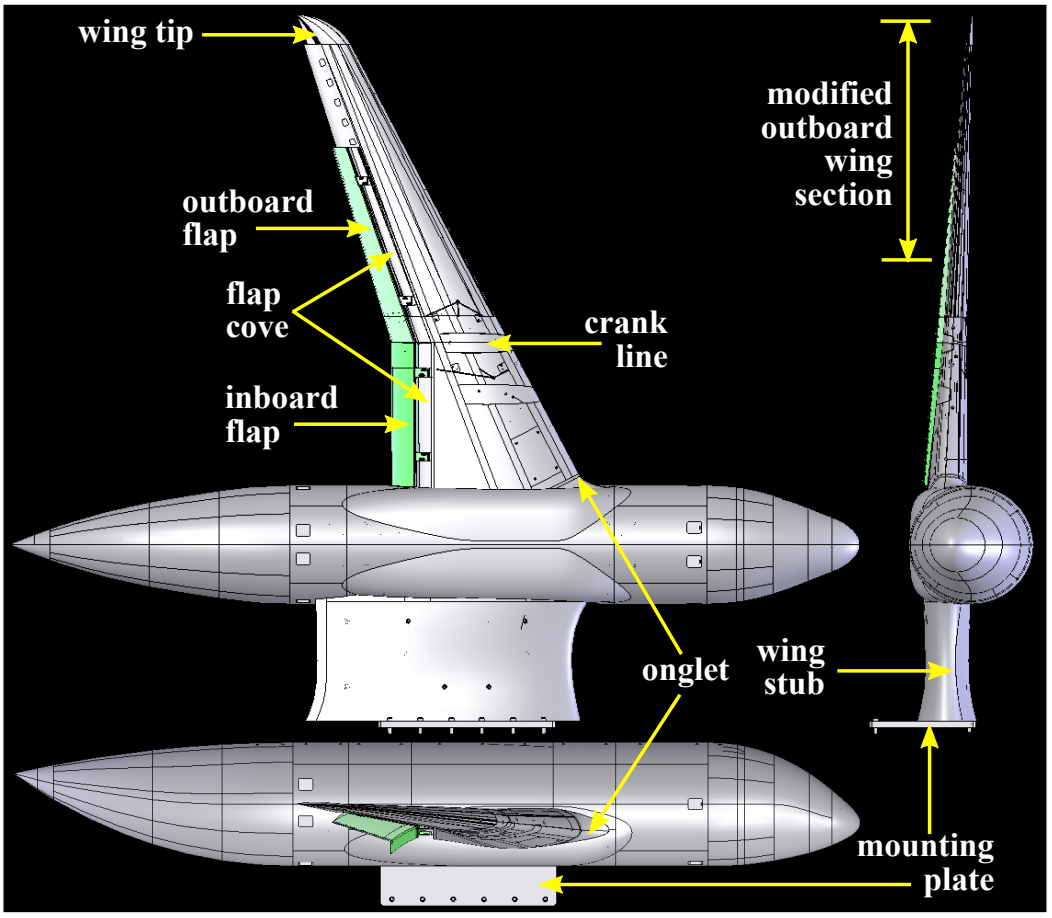

FIGURE 5.4: SYMPHONY final wing design

It should be noted that higher lift coefficients could have been achieved at zero incidence by increasing the aerofoil camber further but this would have introduced an undesirable level of risk of flow separation over the main wing element and, thus, a reduction in lift performance, buffet and unwanted aerodynamic noise. Finally, it is crucial to appreciate that the SYMPHONY wing was designed and evaluated in isolation both from an engine nacelle (and pylon) assembly and from any NTF support structures. These features are likely to modify the wing onset flow angle and velocity and, hence, the aerodynamic performance of the design.

5.3.2.2 Mechanical design

The wing mainly consisted of CNC-machined model-board with a supporting core of aluminium spars. In order to support both the structural and aerodynamic loads, the port wing of the aircraft model was replaced by a load-bearing stub and a mounting plate, see Figure 5.4. Since this stub was due to sit within the flight stream shear layer, it was necessary to profile the outer surface to minimise the potential generation of aerodynamic noise. The finite element analysis software *Cosmos* was used to ensure

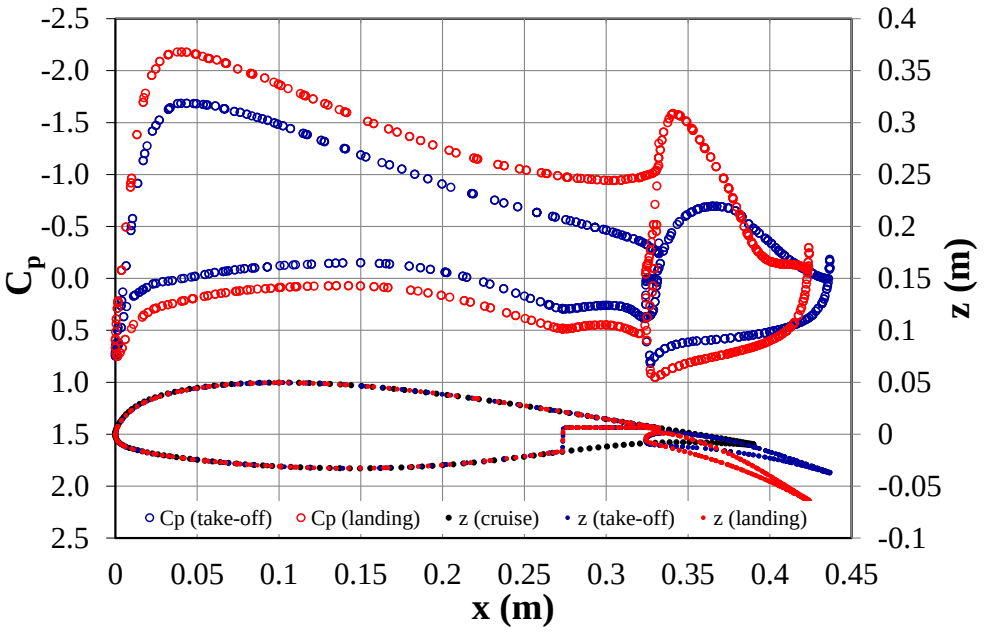

FIGURE 5.5: Lift coefficient (C_p) CFD results for the SYMPHONY wing at take-off and landing flap configurations; [$M_f = 0.29$; $\xi = 0°$]

the rigidity of the wing would allow no more than a 5 mm wing tip deflection under the maximum predicted lift force (i.e. 5.5 kN for the 32° deployed flap landing configuration). Removable cruise wing, 16° flap or 32° flap trailing edges were easily attached as required.

5.3.2.3 Wing installation and positioning

Both the height above the floor of the chamber and the azimuthal orientation of the wing presented a significant installation challenge. Structural modifications were made to the cantilevered wing support structure (WSS) lattice in order that the assembly could meet the safety requirements necessary to hold the model. Then, in order to position the wing model accurately and quickly during the test, a three-axis wing positioning system (WPS) was designed and fitted between the WSS and the mounting plate at the end of the port wing stub, see Figure 5.6.

Three linear variable differential transformer (LVDT) sensors were then used to log the precise coordinates of the wing with respect to the nozzle. Recalling Figure 2.24, the parameter Δx is defined as the axial (or streamwise) distance between the wing leading edge (LE) highlight point and the top dead centre (TDC) point on the lip of the bypass nozzle. Δy is the spanwise distance between the wing crank line and the nozzle lip TDC point and Δz is the vertical distance between the LE highlight point and the nozzle lip TDC point. While a variety of axial, spanwise and vertical

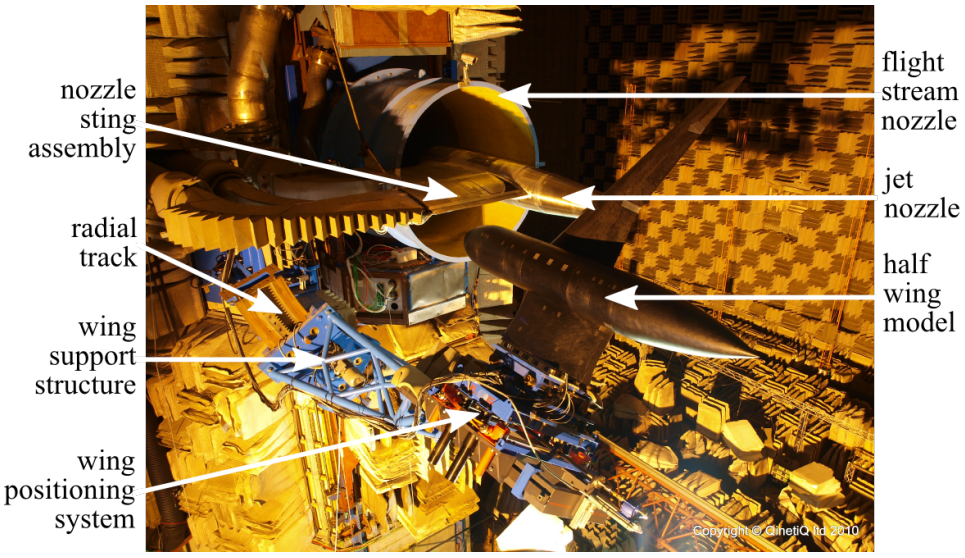

FIGURE 5.6: Photograph of the SYMPHONY wing installation in the NTF

nozzle-to-wing locations were tested in this campaign, we will refer only to a single *baseline* location in this chapter. The key coordinates of this baseline location, together with the h and l values for the different deployed flap configurations, can be seen in Table 5.3. The cruise wing configuration is defined when the flap deployment angle δ is equal to zero. When referring to these configurations later on in the thesis, the identifier (ID) will often be used.

Nozzle	δ	ID	x (mm)	y (mm)	z (mm)	h/D_s	l/D_s
S33-P51	0	1a	-46.4	0	-27.9	0.605	2.350
S33-P51	16	1b	-46.4	0	-27.9	0.453	2.604
S33-P51	32	1c	-46.4	0	-27.9	0.309	2.536
S33-A55	0	8a	-46.4	0	-27.9	0.605	2.350
S33-A55	16	8b	-46.4	0	-27.9	0.453	2.604
S33-A55	32	8c	-46.4	0	-27.9	0.309	2.536
S33-ASS	0	11a	-30	0	-70	0.724	1.939
S33-ASS	32	11c	-30	0	-70	0.428	2.125

TABLE 5.3: SYMPHONY baseline nozzle-to-wing configuration coordinates

Finally, due to the substantial amount of lift created by the flight stream flow over the wing (and, to a lesser extent, by the jet flow beneath the wing), it was important to monitor the vertical height LVDT sensor during the test to ensure the correct nozzle-to-wing separation distance was maintained.

5.4 Instrumentation

Acoustic data from five microphone arrays were acquired during the test programme together with corresponding nozzle aerodynamic data for each test condition. Wing surface static pressure measurements were also taken to compare with the simulated CFD data and to ensure the correct amount of lift was being generated. The measurement arrays and related acquisition systems are described in the following sections.

5.4.1 Aerodynamic measurements

Standard rig instrumentation rakes were used to measure the total pressure and temperature in the core, bypass and flight stream flows. All input aerodynamic measurement data were logged at a rate of 1 Hz, using the NTF Datascan system. The raw data were supplied to the aerodynamic logging facility software (ALF), for real-time computation of jet conditions and mass flows during the test.

Sixteen 1 mm diameter static-pressure tappings were installed in the surface of the wing model. Using the CFD pressure distributions as a guide, the tappings were positioned on both the upper and lower surfaces of the wing at two spanwise stations, as detailed in Figure 5.7. Each tapping was connected to a differential pressure transducer in the fuselage using 1 mm diameter length of hypodermic tubing. The static pressure in the fuselage was not considered to be stable enough to be used as a reference due to its close proximity to the flight stream flow. For this reason, the reference ports on the transducers in the fuselage were linked and piped to an ambient chamber position upstream of the flight stream nozzle exit. The transducer signals were logged at a rate of 1 Hz, using the Datascan system, and then displayed on a screen in the control room so that the performance of the wing could be monitored live.

Unfortunately, since the data from these transducers has not been processed, further analysis of the performance of the SYMPHONY wing in-flight compared to the CFD predictions cannot be made. Spanwise strips of cotton thread tell-tales, however, were attached to the suction side of the wing. This flow visualisation technique was indeed useful when trying to establish whether any unusual flow separation was occurring. At the worst case flight stream velocity (i.e. $U_f = 102$ m/s), both the cruise wing and 16° deployed flap configurations performed well. All tell-tales on the upper wing surface were straight and static, confirming the presence of laminar flow over the wing. For the 32° flap configuration, some flow separation was evident from the tell-tales on the upper surface of the flap, see Figure 5.8. This result, however, was deemed to be

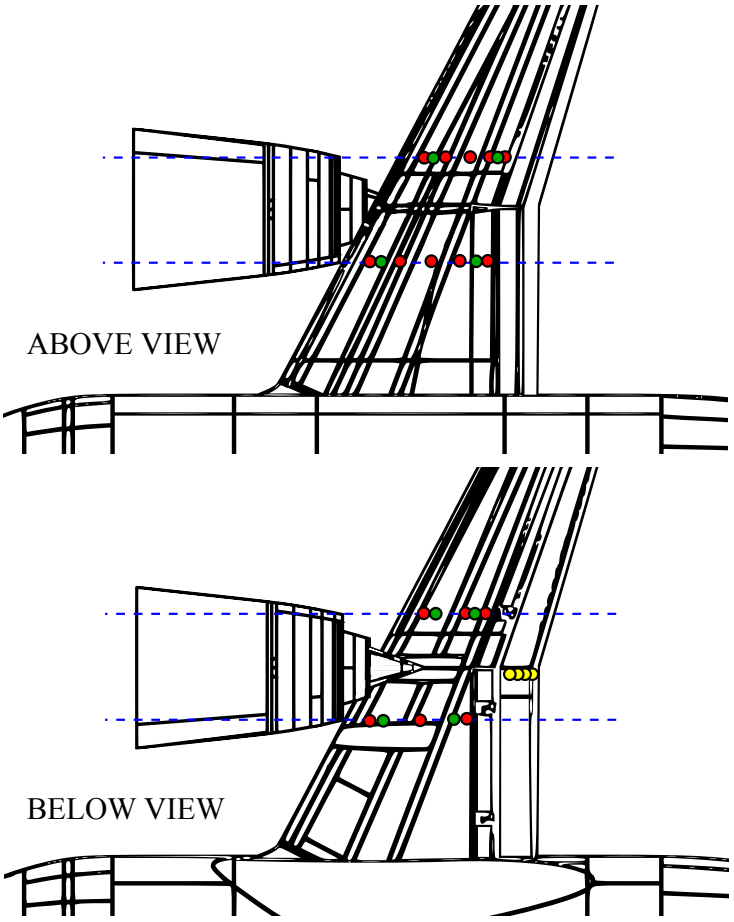

FIGURE 5.7: SYMPHONY wing instrumentation schematic [red dots - wing static pressure tappings; green dots - wing dynamic pressure tappings; yellow dots - flap dynamic pressure tappings]

suitably representative of a full-scale aircraft wing. No adjustments, therefore, were made to the angle or position of the 32° flaps.

5.4.2 Acoustic measurements

Acoustic data from four far-field microphone arrays and two near-field microphone arrays were acquired throughout the SYMPHONY campaign. The far-field arrays are referred to as the sideline, flyover, azimuthal and source location arrays. The locations of the far-field microphones in the test chamber are described in terms of a global chamber azimuthal angle Φ, a local model azimuthal angle ϕ, a polar angle θ relative to the downstream jet exhaust axis and a range R from the centre of the bypass nozzle exit plane. A schematic of the azimuthal angle convention is shown in Figure 5.9. For consistency between the NTF and Doak Laboratory set-ups, subsequent analysis will refer only to the local azimuthal angle, ϕ.

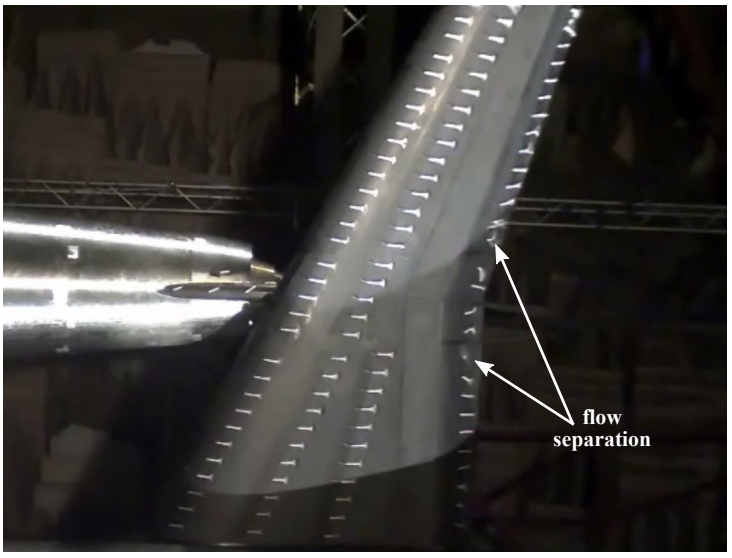

FIGURE 5.8: SYMPHONY wing tell-tale flow visualisation photograph for the 32° deployed flap configuration; [U_f = 102 m/s]

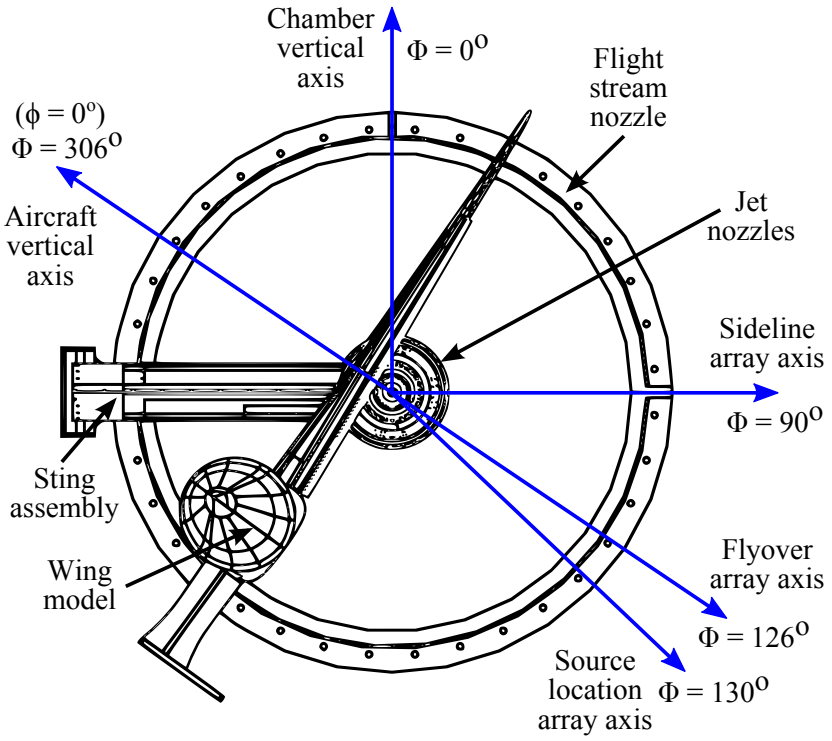

FIGURE 5.9: NTF azimuthal coordinate system schematic (looking upstream)

The far-field sideline array is a conventional, polar array centred on the bypass nozzle exit plane. The array is fixed on masts at rig height (approximately 9 m high) in the horizontal global chamber plane (i.e. $\Phi = 90°$) and at a nominal range of 12 metres, see Figure 5.1. Fifteen 1/4-inch free-field response condenser microphones, oriented at normal (i.e. 0°) incidence, were used to measure noise emitted at polar angles between $40° \leq \theta \leq 130°$.

Flyover measurements (i.e. directly under the aircraft) were made using a linear array. The array was installed on the floor of the chamber, parallel to the jet axis, and the microphones were elevated several meters above the acoustic wedges to minimise reflections. Sixteen 1/4-inch free-field response condenser microphones were mounted in the $\Phi = 126°$ azimuthal plane and each oriented at normal incidence to the centre of the bypass nozzle exit plane. The array measured noise emitted at polar angles between $50° \leq \theta \leq 140°$.

Measurements in the azimuthal plane were made using a large, nominal 9 m diameter circular array of microphones centred on the jet axis. At this distance, according to Arndt *et al.* [106], frequencies above 24 Hz could be considered to be in the acoustic far-field. The array was mounted on a linear traverse system parallel to the jet axis and positioned at eight stations corresponding to polar angles between $40° \leq \theta \leq 110°$, in 10° intervals. Thirty-six 1/4-inch and nine 1/2-inch free-field response condenser microphones were positioned on the circumference of the ring structure. To avoid unique incidence corrections at each traverse position, and to allow for the distributed and directional nature of the jet noise source, all microphones were installed at grazing (i.e. 90°) incidence to the jet axis. Each microphone axis tracked the circumference of the ring. Microphones were radially offset 1.4 m inside the ring structure and were held by 19 mm diameter supporting tubes in order to mitigate against the risk of reflections from the structure itself [115]. Microphone concentricity (with respect to the nozzle) was checked by positioning the ring closest to the bypass nozzle exit plane (i.e. at $\theta = 90°$) and then by measuring the distance to each microphone with a laser range-finder. The corresponding microphone ranges at all other axial traverse positions were calculated assuming a perfectly cylindrical traverse trajectory. Finally, the operation of the traverse was set to follow a gentle acceleration and deceleration profile (i.e. 10 mm/s^2) in order to minimise any microphone movement during each data acquisition.

The final far-field microphone array was a 1D polar source location array. Thirty-seven electret microphones were installed at a nominal radius of 11.5 m from the bypass nozzle exit plane and in the $\Phi = 130°$ global azimuthal plane. The microphones were elevated several metres above the acoustic wedges to minimise reflections and captured a polar aperture between $60° \leq \theta \leq 90°$ relative to the jet axis. In addition, a single 1/4-inch free-field response condenser microphone was installed at $\theta = 90°$ as a reference microphone. All microphones on the array were positioned at normal incidence to the bypass nozzle exit. Analysis of the data from this particular array, however, is beyond the scope of this thesis.

The two near-field arrays were known as the wing surface microphone array and the flap surface microphone array. The wing array consisted of eight 2 mm diameter Kulite Type XT-190 microphones embedded within the wing. These Kulites were the same transducers used in the near-field horizontal flat plate DOAK experiments described earlier in Chapter 4. The wing Kulites were located on both the top (suction) and the bottom (pressure) surfaces of the wing at the same two span-wise stations used for the static pressure tappings but at different chord-wise positions, as shown by the green dots in Figure 5.7. The microphone diaphragms were flush-mounted with the surface of the wing in order to minimise any adverse aerodynamic effects.

Regarding the flap array, four Kulite Type LQ-125 microphones were spaced at 5 mm intervals and embedded in a stream-wise line 12 mm inboard of the wing crank (or flap side edge) and 20 mm upstream of the TE of both the 16° and 32° flaps, as shown by the yellow dots in Figure 5.7. The thickness of the flap TE prevented any closer positioning of the transducers to the flap edges. Cabling from the transducers was laid in machined slots along the span of each flap and routed through a hole in the fuselage to connect to cabling from the conditioning and amplification equipment. The slots were filled flush with the flap surface to restore the original aerodynamic profile.

5.5 Data Acquisition and Processing

5.5.1 Data acquisition

In addition to the aerodynamic Datascan logging system mentioned in Section 5.4.1, two separate acquisition systems were used to record the data from the acoustic arrays. Firstly, a 32-channel RC Electronics Datamax 16-bit recorder was used to acquire data from both the sideline and flyover far-field arrays. The acquisition time for each test point was 18 seconds and the sample rate was 200 kHz per channel. All channels were connected to specially modified B&K NEXUS conditioning amplifiers with pre-emphasis and 200 Hz high-pass filters. Thus, it was possible to maintain the fidelity of the high frequency data measured at large distances in the jet far-field.

Secondly, a 96-channel Entegra Avocet 24-bit system was used to acquire data from the far-field azimuthal and source location arrays and from the near-field surface pressure arrays. The system comprised three 32-channel nodes, all of which were synchronised to less than 1° phase accuracy at 20 kHz. Data was sampled for 18 seconds and at a rate of 210 kHz. For the source location array, the electret microphones were connected to bespoke conditioning equipment with no filtering or signal gain. The reference microphone on this array was treated with the same

modified NEXUS conditioning as the sideline array (i.e. with pre-emphasis and 200 Hz high pass filtering). All azimuthal array microphones were connected to standard B&K NEXUS conditioning amplifiers with 200 Hz high-pass filters. The wing and flap surface pressure arrays were both connected to conditioning equipment, which included a 100 Hz high-pass filter. All 128 channels on the two acquisition systems were recorded throughout the whole test campaign.

5.5.2 Data processing

Data from the Datamax and Avocet recorders were processed using NTF bespoke software NAnSy v5.2 and NAnSy v6.3, respectively. Corrections for the measurement system response, microphone response and incidence were applied to all acoustic data. Each test point was also corrected for the chamber background noise using data measured on the day of testing. For the far-field data only, atmospheric attenuation was accounted for using the Bazley model [116] and a spherical spreading level correction to 1 m polar distance from the datum bypass nozzle exit was also applied. For the in-flight data, a correction for the transmission of the signal across the shear layer of the flight stream flow was also applied [117]. This correction includes both a level correction for astigmatism and an angle correction from observation (microphone) to sound emission angle.

5.6 Results and Discussion

In this section, results from both single stream and coaxial, axisymmetric installed jet nozzles are presented. Each set of figures is followed by a short discussion. It is worth stating at this point that several jet exit flow conditions are used throughout this analysis. These conditions are listed below in Table 5.4.

Description	ID	U_p (m/s)	T_p (K)	U_s (m/s)	T_s (K)	U_s/U_p	T_s/T_p
Sideline - single stream	20	289.30	330.0	289.3	330.0	1.0	1.0
Cutback - single stream	21	255.0	320.0	255.0	320.0	1.0	1.0
Approach - single stream	22	187.0	305.0	187.0	305.0	1.0	1.0
Sideline - coaxial	8	377.8	728.7	292.3	359.3	0.77	0.5
Cutback (hot) - coaxial	6a	267.6	696.1	244.5	346.6	0.91	0.5
Cutback (cold) - coaxial	6b	265.6	351.9	242.7	346.6	0.91	1.0
Approach - coaxial	2	146.0	672.7	176.7	332.5	1.21	0.5

TABLE 5.4: SYMPHONY jet operating conditions [ISA conditions - 101.325 kPa, 288.15 K]

Three ambient (or flight stream) flow conditions are also used in this analysis, see Table 5.5. For display clarity, the flow operating conditions for each test point, henceforth, will be referred to by combining the identifiers (ID) in each of these two tables. For example, the single stream cutback jet condition with high ambient flow will be referred to as condition *21F2*.

Description	ID	U_f (m/s)
Static	S	0
Low	F1	51
High	F2	102

TABLE 5.5: SYMPHONY ambient flow conditions

5.6.1 Scale-related effects

In this section, the SYMPHONY single stream, axisymmetric (i.e. the S33-ASS) nozzle is positioned beneath the SYMPHONY cruise wing in the baseline nozzle-to-wing configuration. Static ambient flow, far-field acoustic data from this test are then compared with data from the equivalent test build from the DOAK horizontal flat plate experiment. A schematic of the geometries involved in this read-across can be seen in Figure 5.10.

We have already seen, in Chapter 3, that a Reynolds number effect exists for the isolated DOAK jet flow at acoustic Mach numbers greater than $M_a = 0.50$ (see Figure 3.13). The only valid data comparison that can be made, therefore, must use the

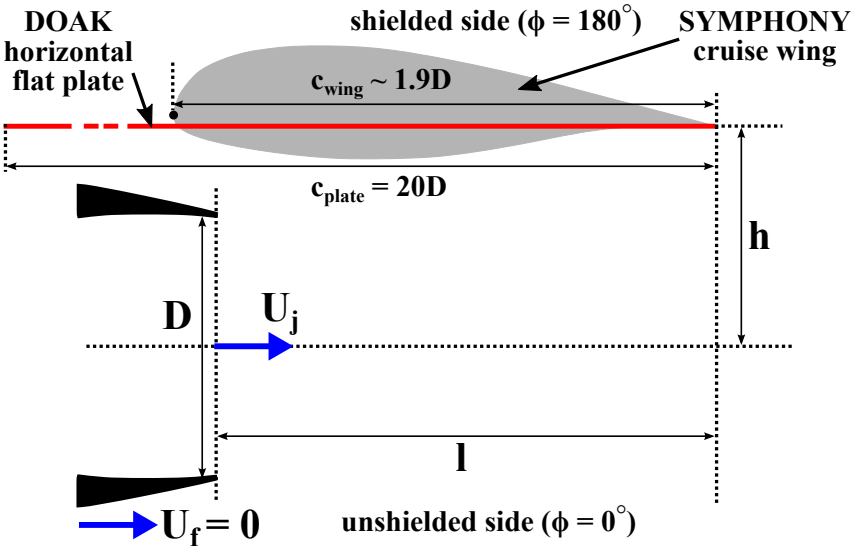

FIGURE 5.10: Schematic of the S33-ASS nozzle installed beneath the SYMPHONY cruise wing versus the DOAK nozzle installed beneath the horizontal flat plate (shown in red)

approach (i.e. the slowest) SYMPHONY jet operating condition (see Table 5.4). As with the previous isolated jet comparisons, the corrected sound pressure level, SPL_c, and Strouhal number, St_D will be used. The reader should be aware that the h and l values (i.e. the position of the wing trailing edge with respect to the nozzle) for the two cases are not completely identical. For the DOAK geometry: $h/D = 0.76$ and $l/D = 2.00$, but for the NTF geometry: $h/D = 0.72$ and $l/D = 1.94$.

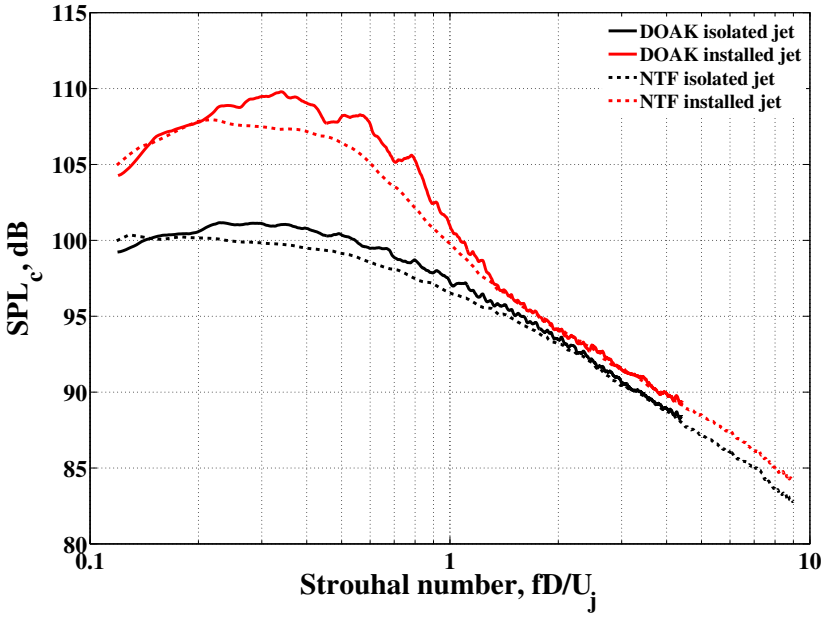

FIGURE 5.11: Far-field narrowband acoustic read-across between the S33-ASS nozzle installed beneath the SYMPHONY cruise wing and the DOAK nozzle installed beneath the horizontal flat plate; [$h/D \approx 0.76$; $l/D \approx 2$; $M_{a_{\mathrm{ref}}} = 0.50$; $U_f = 0$ m/s; $\theta = 90°$; $\phi = 0°$]

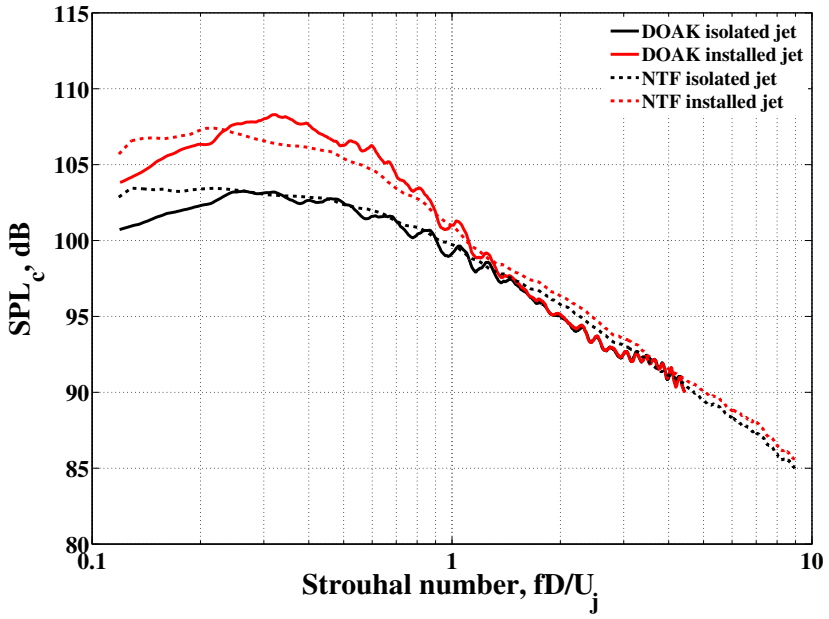

FIGURE 5.12: Far-field narrowband acoustic read-across between the S33-ASS nozzle installed beneath the SYMPHONY cruise wing and the DOAK nozzle installed beneath the horizontal flat plate; [$h/D \approx 0.76$; $l/D \approx 2$; $M_{a_{\text{ref}}} = 0.50$; $U_f = 0$ m/s; $\theta = 60°$; $\phi = 0°$]

Figures 5.12-5.13 all show very good agreement between the DOAK and SYMPHONY installed jets, both for the low frequency JSI noise source and for the high frequency JSR noise source. We can conclude, therefore, that no Reynolds number effects are present when one scales from a small university installed jet experiment up to an industrial rig five times larger. Furthermore, it is apparent that, under static ambient flow conditions, the curved 3D geometry of the SYMPHONY cruise wing makes little noticeable difference to the JSI noise observed in the far-field. In other words, the clean wing trailing edge behaves like a flat plate. One would, however, expect to see larger differences between these two spectra in the extreme forward arc polar angles (i.e. for $\theta > 130°$) due to the back-scattered interference pattern generated by the finite chord of the half-wing model. This result gives confidence to future small-scale installed jet testing.

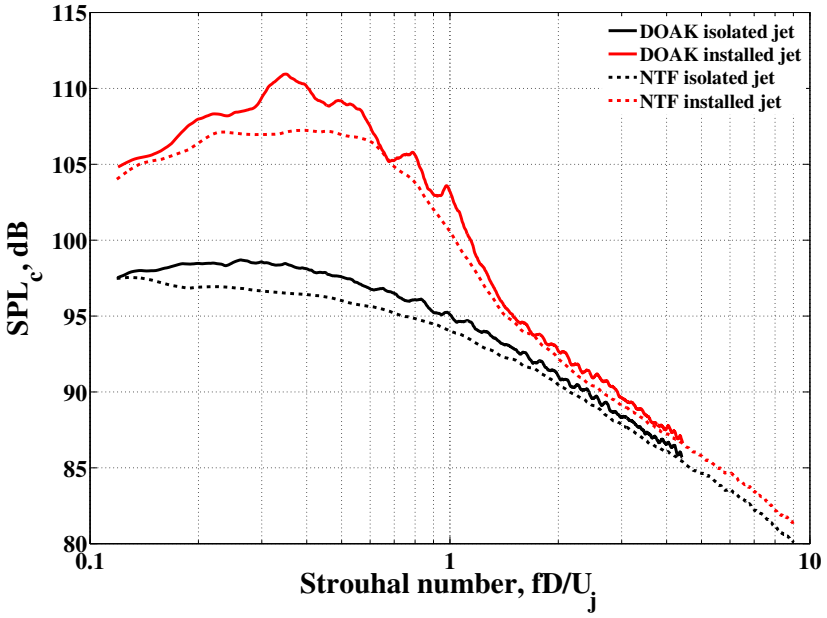

FIGURE 5.13: Far-field narrowband acoustic read-across between the S33-ASS nozzle installed beneath the SYMPHONY cruise wing and the DOAK nozzle installed beneath the horizontal flat plate; [$h/D \approx 0.76$; $l/D \approx 2$; $M_{a_{\text{ref}}} = 0.50$; $U_f = 0$ m/s; $\theta = 120°$; $\phi = 0°$]

5.6.2 Deployed flap effects

When the SYMPHONY cruise wing trailing edge is replaced with a deployed flap, an intriguing acoustic result is observed in the data. Due to the limited amount of single stream nozzle data available, the deployed flap analysis presented in this section will use data from the SYMPHONY coaxial, axisymmetric (i.e. the S33-A55) nozzle geometry instead. Figure 5.14 shows the far-field acoustic spectra as the flap deployment angle δ is increased.

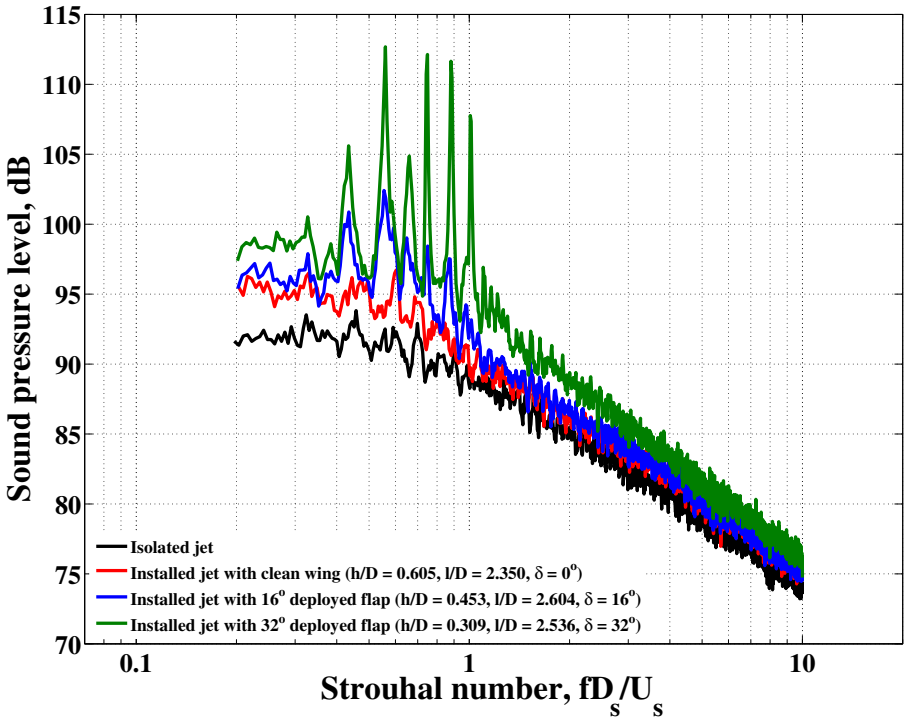

FIGURE 5.14: Graph showing the far-field acoustic effect of deploying a flap into the upper jet shear layer of the S33-A55 jet at flow operating condition 8S; [$\theta = 90°$, $\phi = 0°$]

It is clear to see that a series of tones are generated as the flap is deployed further into the jet flow. Upon first inspection, these tones increase both in number and in amplitude as the degree of impingement is increased, yet they do not appear to possess any harmonic relationship with each other. It should be noted that several diagnostic tests were conducted to ensure that neither cavities capable of sustaining resonances nor objects capable of shedding vortices were responsible for the generation of these tones. Weights were placed on the flaps, for example, to rule out any vibration-induced noise and the flap cove was also sealed up to rule out the presence of any cavity resonances. The impingement tones are only seen to appear between $0.2 < \mathrm{St}_{D_s} < 1.2$ and were capable of protruding up to 20 dB above the broadband JSI noise in some cases. The tones are clearly seen to increase in number and in amplitude as the degree

of impingement is increased. Further analysis of this tonal noise phenomenon will be presented in the following chapter.

A slight broadband lift can also be seen between $1.0 < \mathrm{St}_{D_s} < 4.0$ for the most aggressive flap impingement angle, $\delta = 32°$. Until this feature is understood, we will refer to this additional noise as jet-flap impingement broadband noise.

5.6.3 Static-flight effects

When an ambient flow is introduced around the wing and jet, the installed jet problem becomes much more complicated for two principal reasons. Firstly, the lift produced by the wing serves to bend, or redirect, the jet away from the wing/flap trailing edge. This fact is likely to change both the position and the strength of the quadrupole jet mixing sources beneath, and downstream of, the wing. The increase in radial distance from the trailing edge will also serve to reduce the magnitude of the JSI noise source. Secondly, it is well-documented that the turbulence kinetic energy in the upper jet shear layer decreases as the relative shear between jet and ambient flow decreases. Therefore, for a given axial distance downstream from the nozzle exit, the strength of the jet's hydrodynamic field, and thus the JSI noise source itself, will also decrease.

Due to the limited number of different in-flight flow conditions, it is difficult to establish any robust trends from the SYMPHONY dataset. If we couple this fact together with the absence of any aerodynamic flow data, this analysis becomes impossible to perform properly. Thus, in this section, only one test build will be presented and (briefly) discussed. The configuration with the most complete set of static-to-flight data is the most realistic (and most complex) test build of the campaign. Data from the SYMPHONY coaxial, asymmetric nozzle, complete with engine-to-wing attachment pylon (i.e. the S33-P51 nozzle) will be used in conjunction with the baseline SYMPHONY cruise wing and the standard deployed flap configurations. The operating jet flow condition will be the hot, cutback condition *6a*.

Figures 5.15-5.17 show the effect of the flight stream flow on the $\theta \approx 90°$ far-field acoustic spectra directly beneath the wing (i.e. at $\phi = 0°$). The polar angle is displayed in the captions as approximate due to the in-flight shear layer acoustic propagation correction [117, 118], which is applied to all data when $U_f \neq 0$ m/s.

If we study Figure 5.15, the data generally shows us that the peak frequency of the JSI noise increases with flight velocity. This is expected since the jet has effectively been stretched and the hydrodynamic field sources that were dominant in the static case have essentially now moved downstream from the trailing edge. The second observation is that the ΔSPL between the installed and isolated jet spectra does not noticeably increase for the clean wing, or *1a*, case. Clearly, however, when the flap is deployed (see Figures 5.16 and 5.17), the shape of the installed jet spectra changes substantially. More mid-frequency energy, between $0.5 \leq \mathrm{St}_D \leq 3$ in particular, is seen above the isolated jet levels. It is difficult to interpret exactly what is happening in these plots, particularly given the presence of the tones. In order to understand all of

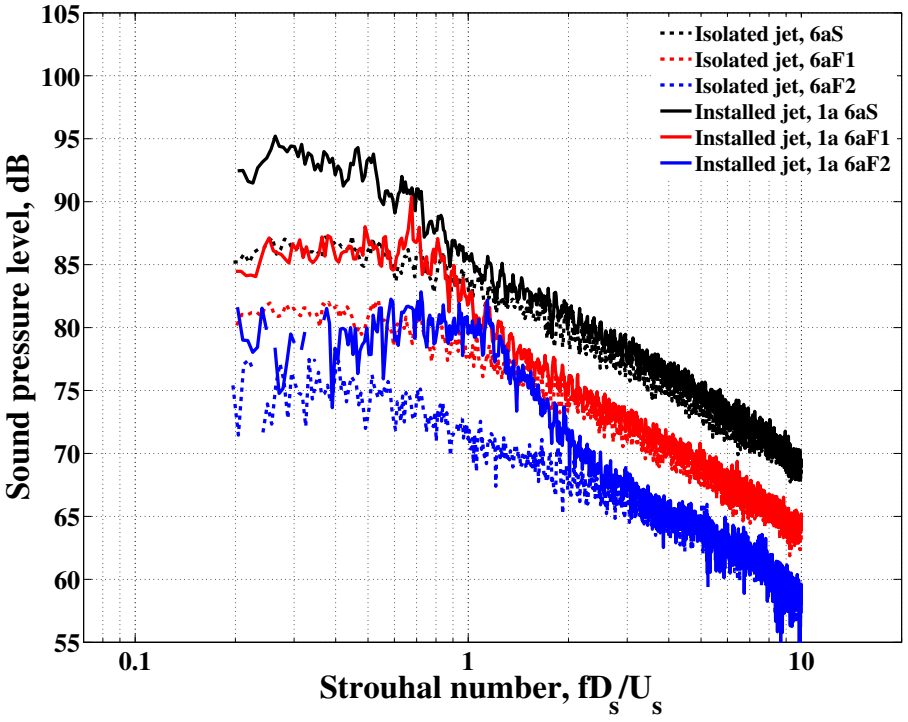

FIGURE 5.15: Graph showing the far-field acoustic effect of increasing the ambient flow around the S33-P51 nozzle when isolated and when installed beneath the SYMPHONY cruise wing at operating flow condition 6a; $[h/D_s = 0.605,\ l/D_s = 2.350,\ \delta = 0°,\ \theta \approx 90°,\ \phi = 0°]$

the physics within the in-flight situation, more information regarding the lift produced by the wing and the subsequent behaviour of the jet beneath is necessary.

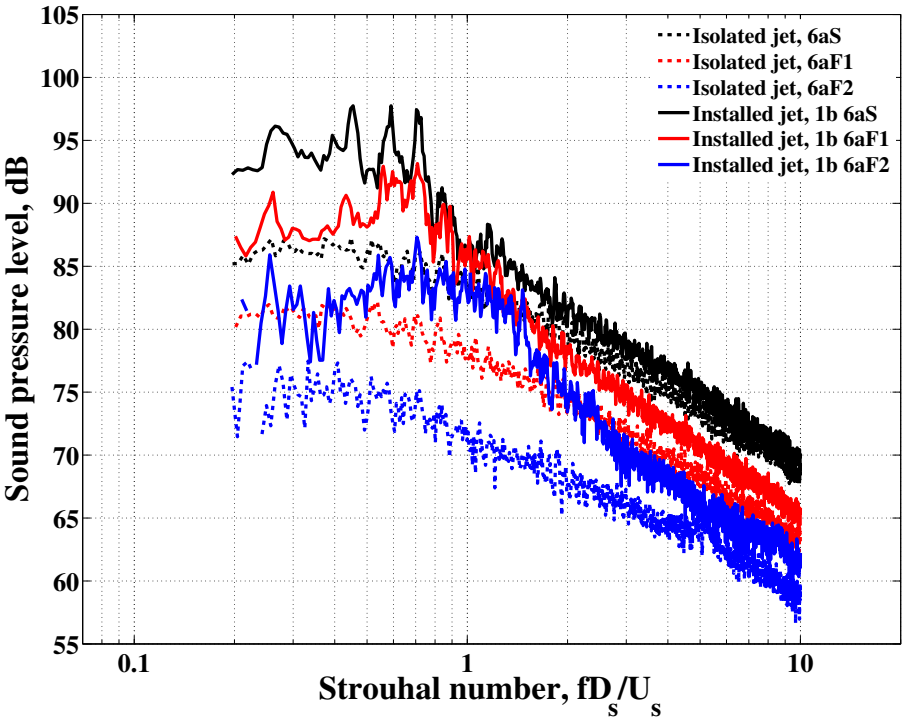

FIGURE 5.16: Graph showing the far-field acoustic effect of increasing the ambient flow around the S33-P51 nozzle when isolated and when installed beneath the SYMPHONY wing with deployed flaps at operating flow condition 6a; [$h/D_s = 0.453$, $l/D_s = 2.604$, $\delta = 16°$, $\theta \approx 90°$, $\phi = 0°$]

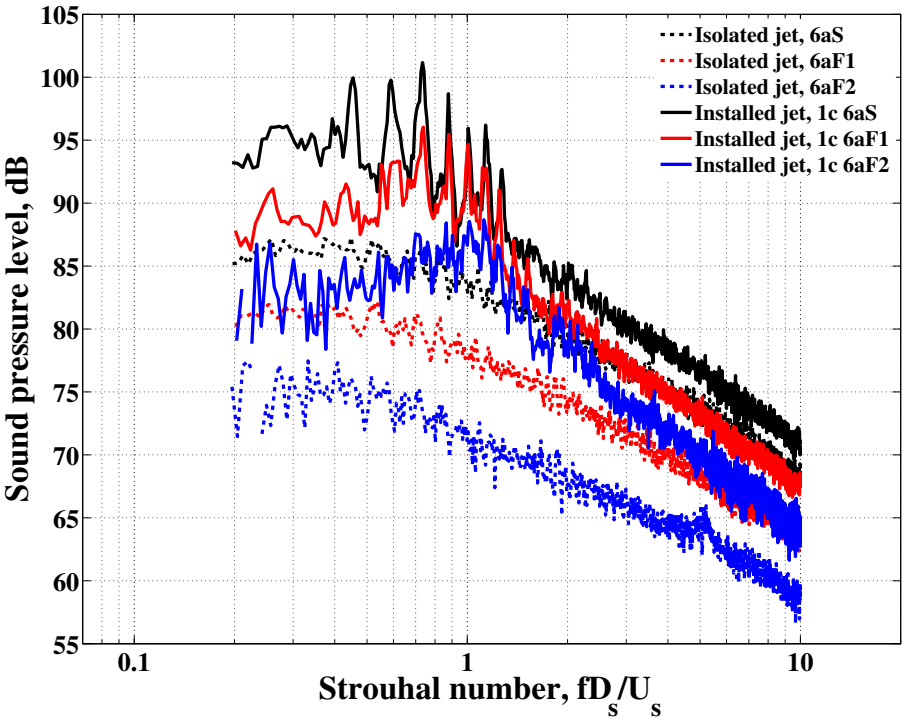

FIGURE 5.17: Graph showing the far-field acoustic effect of increasing the ambient flow around the S33-P51 nozzle when isolated and when installed beneath the SYMPHONY wing with deployed flaps at operating flow condition 6a; [$h/D_s = 0.309$, $l/D_s = 2.536$, $\delta = 32°$, $\theta \approx 90°$, $\phi = 0°$]

5.6.4 Propagation effects

An issue that has not yet been resolved in the field of installed jet noise research concerns the validity of using the propagation model proposed by Miller [1] and his polar directivity equation. The two principal questions are: (1) Do the acoustic waves radiated above the trailing edge of the wing (or flap) propagate upstream along the top surface of the wing (particularly when under in-flight conditions)? (2) Do these waves then scatter from the leading edge of the wing and propagate down beneath the wing to the far-field? Using data from the SYMPHONY test, it is now possible to answer these questions definitively.

The subsequent analysis is possible due to the synchronous acquisition capability of the Avocet data acquisition system and due to the fact that data from both the traversable far-field azimuthal array and the two near-field surface microphone arrays were recorded on the same system. Thus, the phase relationship between pairs of transducers, and hence the direction of acoustic propagation, can now be established. Due to the limited available testing time, it was not possible to collect a large amount of data using the traversable azimuthal array. Thus, as with the previous section, data from the S33-P51 nozzle will be presented. It should be noted that the presence of the engine-to-wing attachment pylon will not affect the fundamental findings of the following analysis. A schematic of the test configuration together with details of the key transducer locations can be seen in Figure 5.18.

The coaxial jet was operated at its sideline condition with no ambient flow (i.e. at condition 8S). For this particular nozzle-to-wing configuration and set of flow conditions, the JSI noise can be seen clearly above the isolated jet noise between 200 - 2000 Hz. If we look at the acoustic coherence (see Equation A.1) and phase relationships between pairs of transducers over this frequency range, we can establish: (a) whether a proportion of the acoustic energy propagates upstream from the flap trailing edge over the top surface of the wing and (b) whether the signals measured on the top surface of the wing correlate to those recorded in the far-field beneath the jet. Figures 5.19 and 5.20 show the acoustic coherence and phase results, respectively, for three different transducer pairs.

We can see from Figure 5.19 that a strong coherence exists between all three of the transducer pairs at the tonal frequencies. This fact alone is evidence that the same acoustic wave propagates past all four of these transducers. The direction of propagation is then clarified by Figure 5.20. The positive gradient the phase angle makes with frequency is evidence that sound is travelling from transducer 1 through to 4. This analysis, therefore, shows Miller's theory to be true. The component of JSI

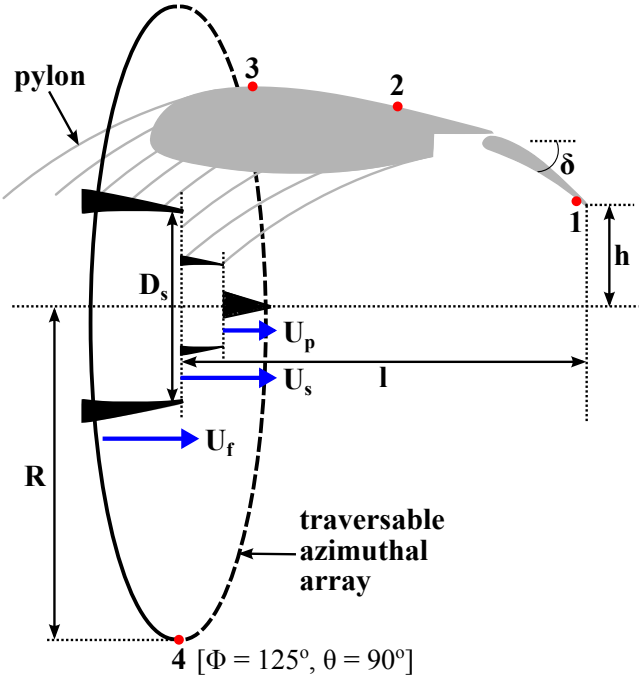

FIGURE 5.18: Schematic of the SYMPHONY S33-P51 asymmetric, short-cowl coaxial nozzle with bullet and pylon beneath the SYMPHONY wing in the deployed flap configuration. Approximate microphone transducer locations are shown as red dots

noise radiated above the flap trailing edge does indeed propagate upstream along the top surface of the wing, past the leading edge and then back down beneath the wing to the unshielded side of the jet.

The final observation to make is that if we compare the phase angle gradient of the (2,3) transducer pair in Figure 5.20 with the equivalent data for the high ambient flow velocity case, we find, as expected, that the velocity with which the sound convects upstream along the top surface of the wing decreases by approximately the same velocity as that of the incoming flight stream flow ($\Delta U_c \approx 95$ m/s), see Figure 5.21.

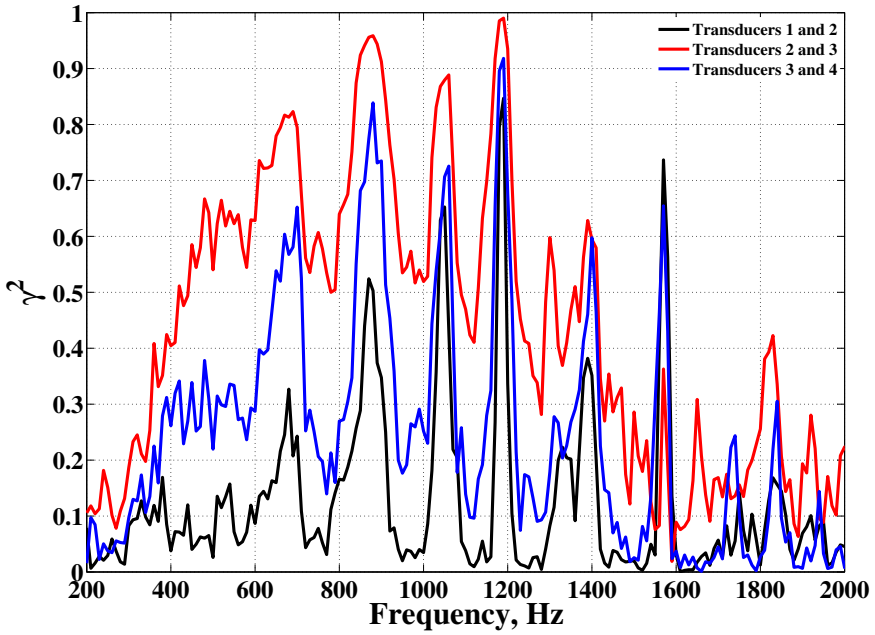

FIGURE 5.19: Coherence between the transducers defined in Figure 5.18

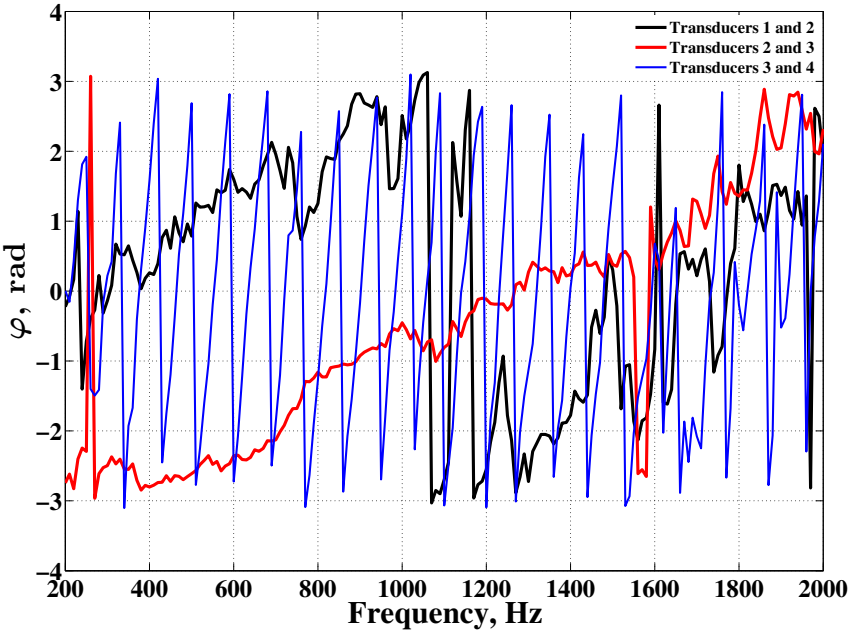

FIGURE 5.20: Phase angle relationship between the transducers defined in Figure 5.18

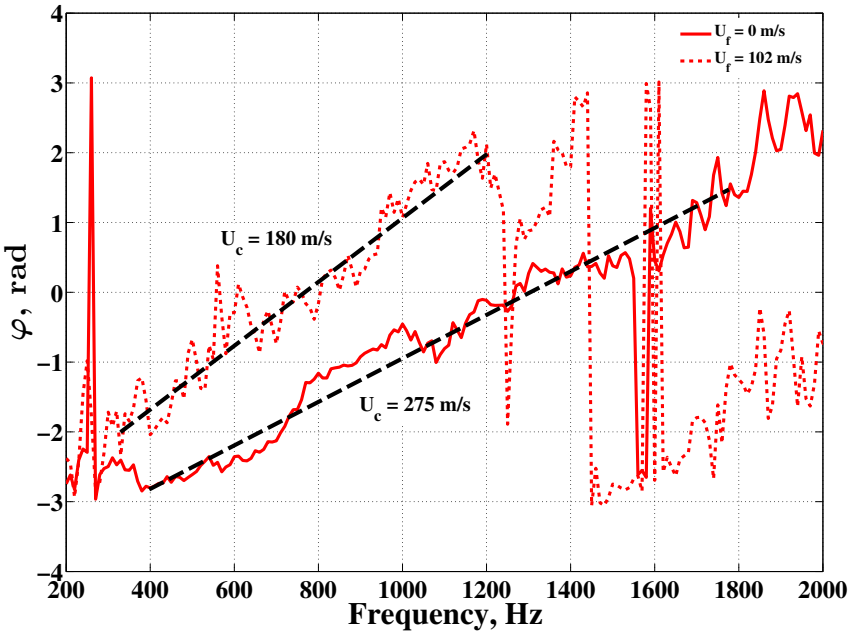

FIGURE 5.21: Static versus flight comparison of the phase angle relationship between the (2,3) transducer pair

5.7 Conclusions

An extremely demanding programme in terms of design, hardware installation and testing was successfully completed in the NTF. A comprehensive set of measurements was obtained using far-field azimuthal, sideline, flyover and source location microphone arrays as well as two near field surface microphone arrays.

Ignoring the Reynolds number effects inherent in the DOAK jet nozzle at flow acoustic Mach numbers greater than $M_a = 0.50$, no further scaling issues were seen to arise from simulating a static, installed jet with cruise wing experiment $1/5^{\text{th}}$ of the size of an industrial facility. The question of scaling up from $1/10^{\text{th}}$-scale to full-scale remains outstanding.

Strong jet-flap impingement tonal noise was observed in data when the flap trailing edge was deployed aggressively into the upper jet shear layer. Further investigation into this noise source is continued in the following chapter.

We know that the presence of ambient flow serves to reduce the mean turbulence kinetic energy in the outermost jet shear layer. This, in turn, will serve to weaken the hydrodynamic field seen by the wing/flap trailing edge. Thus, the jet-surface interaction noise source should also reduce. Substantial jet redirection effects would also effectively increase the radial separation between the jet and the wing/flap trailing edge resulting in a reduction of the JSI noise source. If the jet is redirected, however, the quadrupole jet mixing noise sources downstream of the wing TE will certainly move off the jet lip-line towards the observer on the ground. Both the directivity and strength of these sources, therefore, are also likely to change. Unfortunately, not enough aerodynamic information regarding the amount of lift produced by the wing and the subsequent position of the jet beneath exists to gauge the full extent of the flight effects in this problem. Small incremental increases in flight stream velocity in future experiments would help ascertain more of the physics involved in this situation, particularly for aggressively deployed flap angles. Therein lies a substantial field for further research.

One other effect that remains unstudied is the fact that the spans of the both the wing and the flap trailing edges are, in fact, tapered, not straight (as in the flat plate experiment). This will almost certainly change the directivity pattern of the JSI noise and would be another interesting area for further research.

Finally, evidence has been provided to support Miller's top side upstream-travelling acoustic wave propagation theory. An increased number of forward arc microphones, however, would be essential for future tests to validate this theory fully.

Chapter 6

Jet-Flap Impingement Noise

In this chapter, the tonal component of jet-flap impingement noise is investigated in more detail. As already mentioned in Chapter 5, multiple narrowband 'tones' with no harmonic relationship have been observed in model-scale experimental data for a closely-coupled, installed jet. Further fundamental experimental studies of these tones were carried out within a university laboratory setting in an attempt to establish the key parameters responsible for the generation of this noise source.

6.1 Introduction

We have already seen, in Figure 5.14, that when a jet flow impinges heavily upon a deployed flap, tones can protrude as much as 20 dB above the broadband noise level. In this chapter, after a brief review of the literature of edge-tones, further analysis of the data from the SYMPHONY large model-scale installed jet experiment campaign will be presented. Results from a smaller DOAK jet-flap interaction tonal noise study will then follow. Observations are made as to the frequency, amplitude and the directivity of the impingement tones relative to the following three parameters: (1) the radial separation between jet geometric centreline and flap trailing edge, h, (2) the axial separation between jet nozzle lip and flap trailing edge, or impingement distance, l and (3) the jet exit acoustic Mach number, M_a.

The problem of jet-flap interaction tones appears to be most similar to the *edge-tone* phenomenon, first reported by Sondhaus, in 1854 [119]. Classically, the edge-tone is the sound resulting from the action of a jet emerging from a slit orifice and impinging upon a fixed wedge placed downstream from the slit, see Figure 6.1. Since 1854, several jet impingement experiments have been investigated. In the 1950s, for example,

Von Gierke [120] and Powell [121] extensively studied this wedge configuration using a low-speed rectangular jet and concluded that the fluctuating fluid force on the edge served as a dipolar acoustical source. The fundamental (lowest) tonal frequency was then dictated not only by the mean jet velocity, U_j, and the orifice dimension, D, but also by the nozzle-edge impingement distance, l/D [122]. This finding suggested the presence of an instability feedback loop mechanism between the nozzle and the edge of the wedge.

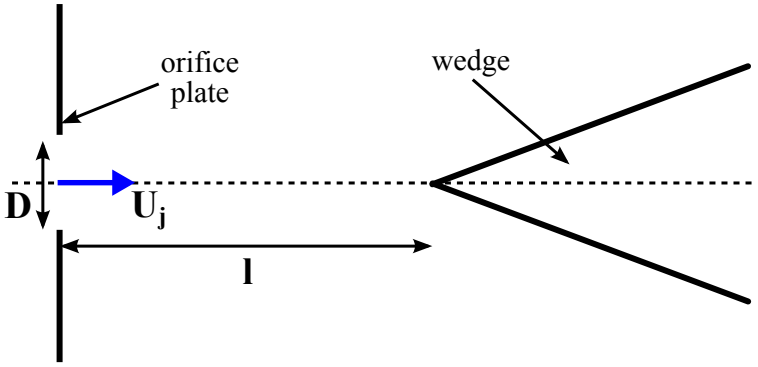

FIGURE 6.1: Schematic of the jet-wedge edge-tone set-up

Neuwerth [123] and Evertz *et al.* [124] were the first to observe jet-flap impingement tones in aviation, in the mid-1970s, when an impinging obstacle - a blown-flap - positioned less than five shock cells from an under-expanded jet, was seen to produce tones which masked the screech tones. In 1978, Hussain and Zaman [125] then observed impingement tones from the circular body of a hot-wire probe positioned within a shear layer. They concluded that the key parameters necessary to predict the fundamental edge-tone frequency are the free jet shear layer momentum thickness (i.e. a measure of the energy contained within the turbulent eddies), the jet nozzle lip-edge impingement length, l/D, and the characteristic shear layer velocity [125]. This prompted Umeda *et al.* [126] to perform a Schlieren flow visualization experiment for a high Reynolds number jet impinging upon a circular cylinder instead of an edge. Tones were found to be produced at jet Mach numbers greater than 0.60 and impingement lengths less than eight nozzle diameters [126].

Further impingement tone research featured Wagner [127], Ho and Nosseir [128], Landreth and Adrian [129] and Tam and Ahuja [130], who all focussed on vertical take-off and landing (VTOL) configurations involving a flat plate positioned normal to the direction of the jet flow. In support of Wagner [127] and Neuwerth [123], Tam and Ahuja's numerical simulations suggested that the acoustic feedback waves propagated upstream from the plate surface to the nozzle inside, rather than outside, the jet column [130]. This hypothesis was contrary to the suggestions of Ho and Nosseir [128] and Umeda *et al.* [126]. Tam and Ahuja also suggested that the reason no stable

impingement tones had been observed for cold, subsonic jets with Mach numbers less than 0.6 was because the Strouhal numbers of the upstream-propagating acoustic waves were larger than 0.7 and so were outside the Strouhal number range within which the Kelvin-Helmholtz instability waves of the jet exist [130].

Karamcheti *et al.* [131], Stegen and Karamcheti [132], Woolley and Karamcheti [133] and Ziada and Rockwell [134] all revisited Powell's jet-wedge experiment. Ziada and Rockwell concluded that small offsets between a vortex centre and the edge were responsible for shifts in oscillation frequency [134]. More recently, in 2001, Lin and Rockwell looked more closely at the fluctuating fluid force amplitude induced at the wedge edge [135]. High-image-density particle image velocimetry, together with surface pressure measurements on the leading edge of the wedge, were used to determine the instantaneous characteristics of the turbulent velocity field interacting with the edge and the resulting loading generated on the edge itself. It was suggested that the generation of multiple spectral peaks is due to the complex partitioning of large-scale elliptical vortices located within the shear layer by the impingement edge [135].

Most recently, in 2011, Mengle reported a peculiar spectral 'double-hump' in far-field third-octave band sound pressure level data from a model-scale installed aircraft engine test [81]. This chapter will provide evidence that jet-flap impingement tones, which are only clearly visible in narrowband data, are responsible for this particular spectral feature. Furthermore, the reader should appreciate that these tones pose a real threat to future closely-coupled low-noise aircraft.

6.2 Experiment Design

Installed jet noise has been the subject of recent research interest due to the addition of several new sources of noise. One such source involves the impingement of the upper free shear layer of the exhaust jet onto the trailing edge of the deployed aircraft flap resulting in the production of tonal noise. In this section, five separate installed jet experiments are designed to investigate the fundamental mechanism at the heart of this tonal noise phenomenon.

The first experiment involves the $1/10^{\text{th}}$-scale S33-P51 asymmetric, coaxial nozzle installed at the baseline nozzle-to-wing position 1c beneath the SYMPHONY wing with 32° deployed flaps, see Figure 6.2. The second experiment involves the same geometry but without the pylon (i.e. the S33-A55, axisymmetric coaxial nozzle at position 8c). Data from these two experiments will be compared in order to analyse the effect of the pylon on the tone generation.

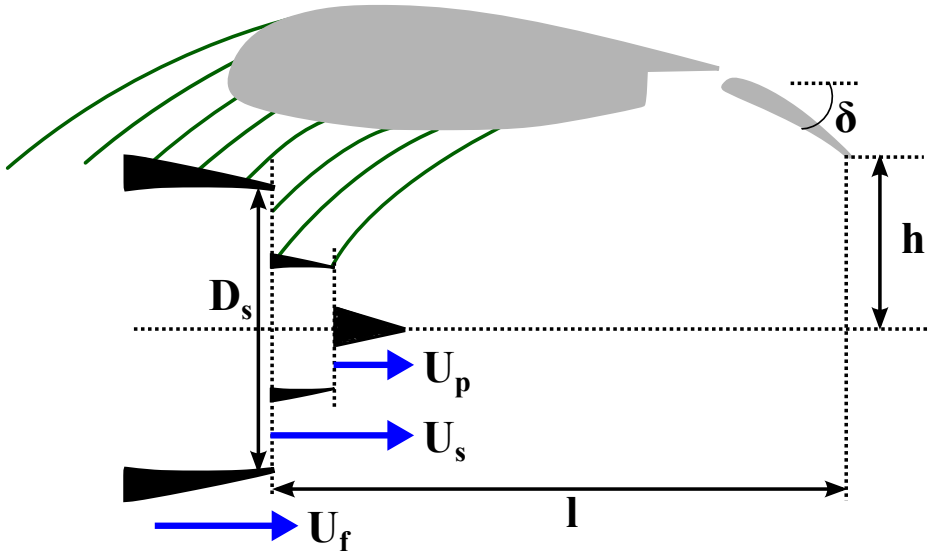

FIGURE 6.2: Schematic of the SYMPHONY S33-P51 asymmetric, coaxial nozzle with pylon (shown in green) installed beneath the SYMPHONY wing with deployed flaps

The third experiment involves the S33-ASS single stream, axisymmetric nozzle installed at position 11c beneath the SYMPHONY wing and 32° deployed flaps. The fourth experiment is a smaller and simplified $1/50^{\text{th}}$-scale model of experiment three involving the DOAK jet installed beneath a flat plate wing with a 30° angled flat plate flap. Data from both of the experiments will be compared to establish whether the impingement tones scale with Reynolds number. Figure 6.3 illustrates the two experiments.

Finally, the fifth experiment involves the DOAK jet installed simply beneath a 30° angled flat plate, see Figure 6.4. More detailed parametric investigation will be made

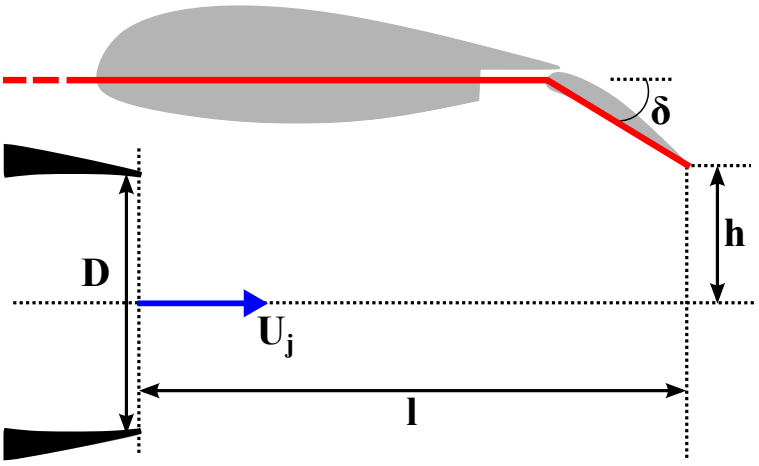

FIGURE 6.3: Schematic of the SYMPHONY S33-ASS axisymmetric, single stream nozzle beneath the SYMPHONY wing in the deployed flap configuration. The equivalent DOAK flat plate wing with angled flat plate flap geometry is shown in red.

with this geometry concerning the frequency and amplitude behaviour of the impingement tones relative to the following three parameters: (1) radial separation between jet geometric centreline and angled flat plate trailing edge h, (2) axial separation between jet nozzle lip and flap trailing edge (or impingement distance) l, and (3) jet exit velocity U_j.

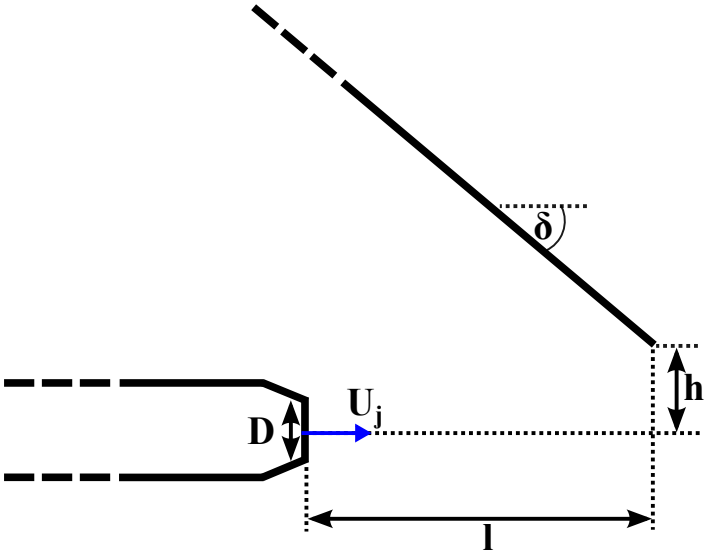

FIGURE 6.4: Schematic of the DOAK jet plus angled flat plate impingement experiment

6.3 Results and Discussion

In this section, 10 Hz narrowband far-field acoustic sound pressure level data from the five experiments above are interrogated. The section will be split into five subsections each to discuss a particular effect. First, the most complex S33-P51 asymmetric coaxial jet nozzle plus pylon geometry is compared with the S33-A55 axisymmetric coaxial jet nozzle without pylon geometry, under the static ambient flow condition 8S, in order to assess the effect of the pylon on the generation of the tones. Second, the flap trailing edge is moved incrementally radially down towards from the S33-A55 nozzle to assess the effect of the radial position of the trailing edge within the jet on the tones. Third, the flight effect on tone generation is discussed briefly using data from the S33-A55 nozzle set-up. The fourth analysis will compare the S33-ASS nozzle beneath the large-scale 3D SYMPHONY wing with the small-scale 2D DOAK flat plate and flat flap to investigate whether any scaling effects alter the generation of the tones. The fifth and final subsection will focus on the parametric variation of both the position of the 2D DOAK angled flat plate trailing edge within the jet and the velocity of the jet itself.

One important caveat must be stated before introducing the following analyses. Due to the lack of aerodynamic data, for each of these installed jet configurations we assume the entrainment and development properties of the jet do not change significantly over the first two jet diameters axially downstream from the nozzle lip.

6.3.1 Pylon effect

The most realistic aircraft configuration is the S33-P51 nozzle installed beneath the SYMPHONY wing with 32° deployed flaps. Figure 6.5 shows a far-field SPL comparison between the S33-P51 nozzle and the S33-A55 nozzle. The first observation to make is that the presence of the pylon appears to make little difference to both the amplitudes and frequencies of the tones. Having said that, however, it is possible to see that an additional tone is generated at 2400 Hz. Assuming that no significant change in convection velocity exists between the two builds, the fact that this tone is higher in frequency suggests that the particular feedback loop responsible occurs over a shorter distance. This hypothesis tallies with the fact that the pylon geometry extends axially downstream from the nozzle exit towards the flap trailing edge.

Classically, the frequency of edge-tones can be calculated by the following simple feedback loop expression,

$$f = \frac{n}{l} \Big/ \left(\frac{1}{U_c} + \frac{1}{U_a} \right) , \tag{6.1}$$

where U_c is the convection velocity of the instability which travels from the nozzle lip to the edge, and U_a is the velocity with which the acoustic wave travels back upstream to the nozzle. The impingement distance l for the baseline deployed 32° flap wing configuration (1c) is 471 mm (see Table 5.3). If we assume the instability travels at 60% of the bypass jet exit velocity (i.e. $U_c = 0.6U_s$) [30] and that the acoustic wave generated at the flap trailing edge travels back upstream to the nozzle within the bypass jet shear layer (i.e. $U_a = \sqrt{\gamma R_c T_s}$), as proposed by Tam and Ahuja [130], we arrive at a fundamental frequency of 257 Hz. Since neither this fundamental frequency nor its harmonics match any of the tones in Figure 6.6, it is clear that more subtle effects are responsible for the generation of the jet-flap impingement tones. One such factor could be the fact that different instability wavelengths are convected at different speeds [121]. Further aerodynamic investigation is required to understand this convection mechanism fully.

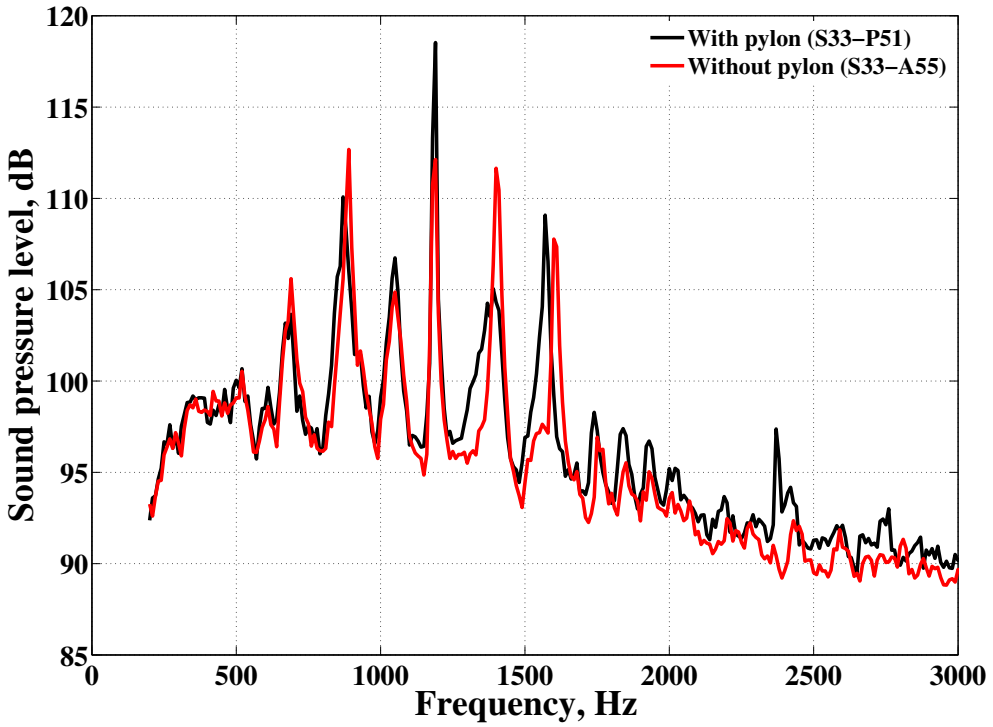

FIGURE 6.5: Graph showing the far-field acoustic jet-flap impingement tone pylon effect at flow condition 8S; [$h/D_s = 0.309$, $l/D_s = 2.536$, $\delta = 32°$, $\theta = 90°$, $\phi = 0°$]

Secondly, the addition of the pylon only appears to shift the frequency of the tone at 1600 Hz. Using the classical feedback loop expression (Equation 6.1), the change in impingement length Δl required to produce a 30 Hz change in frequency equates only to 1.45 mm. We can suggest, therefore, that extremely subtle changes in nozzle-flap geometry have the ability to produce significantly different results. Furthermore, since no obvious amplitude trend can be gleaned from these two seemingly identical test cases, this tonal noise source certainly highlights the need to study narrow, rather than

$1/3^{\text{rd}}$-octave, band data when attempting to understand future installed jet noise trends.

6.3.2 Vertical separation effect

Let us continue to study the S33-A55 nozzle installed beneath the SYMPHONY wing with 32° deployed flaps. As we move the trailing edge of the flap vertically down through the upper jet shear layer (in 9.3 mm increments) towards its baseline position (8c), we observe that the frequencies of the tones remain fixed, but that their amplitudes (above the broadband noise level) increase dramatically, see Figure 6.6. When the vertical distance between jet and flap is greatest (i.e. at $h/D_s = 0.559$), it is unclear whether the third tone in the figure is completely 'cut-off' or whether it is just masked beneath the broadband level. Clearly this sensitivity to vertical position is further evidence supporting the requirement to analyse narrowband jet-flap impingement data.

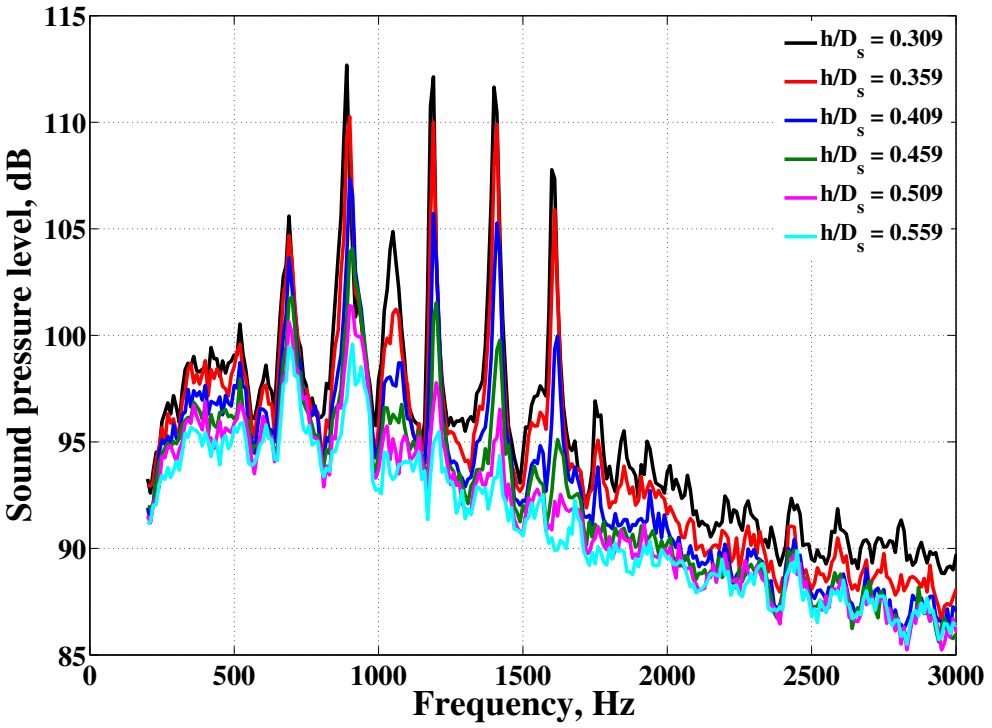

FIGURE 6.6: Graph showing the far-field acoustic jet-flap impingement tone vertical distance effect for the S33-A55 nozzle beneath the SYMPHONY wing at flow condition 8S; $[l/D_s = 2.536,\ \delta = 32°,\ \theta = 90°,\ \phi = 0°]$

6.3.3 Flight effect

When an ambient, or flight stream, flow U_f is gradually added to the jet-flap impingement tone problem, several effects can be observed, see Figure 6.7. Firstly, the five lowest frequency (i.e $f_1 = 690$ Hz, $f_2 = 890$ Hz, $f_3 = 1050$ Hz, $f_4 = 1190$ Hz and $f_5 = 1400$ Hz) tones all appear to stay at the same frequencies but reduce in amplitude between $U_f = 0$ m/s and $U_f = 52$ m/s. Two effects could be responsible for this attenuation: (1) the effective vertical distance between jet and flap increases due to the thinning of the jet by the surrounding flight stream flow, or (2) the flight stream flow reduces the mean turbulence kinetic energy (TKE) within the upper jet shear layer leaving less energy for each instability feedback loop to sustain itself. The author suspects that a combination of these two effects is more likely, however, further aerodynamic research is required to understand the situation fully.

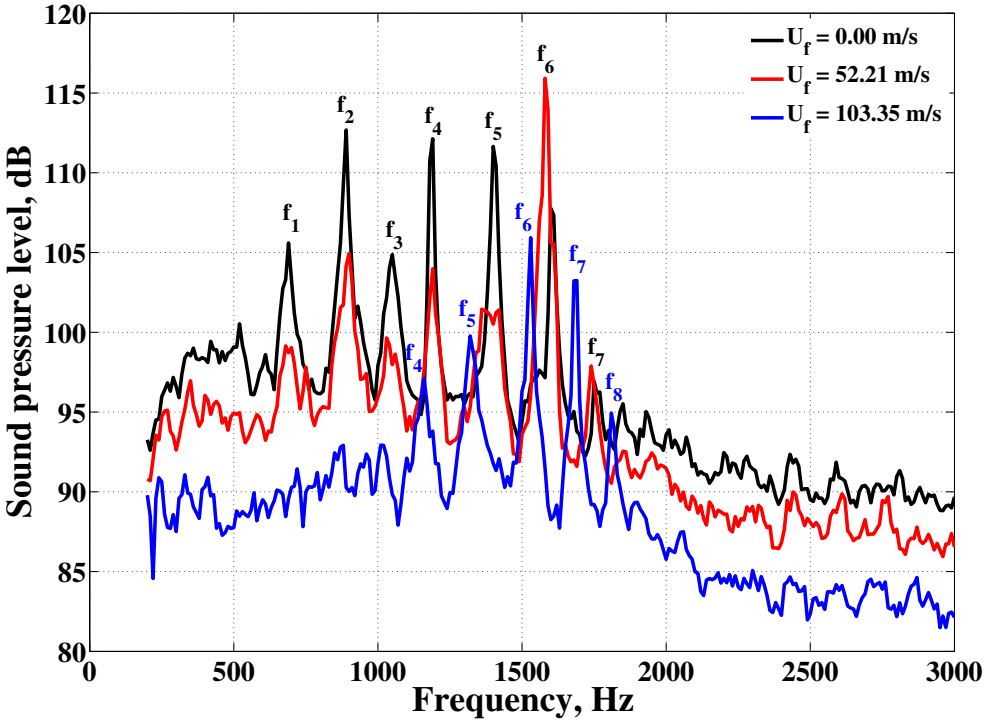

FIGURE 6.7: Graph showing the far-field acoustic jet-flap impingement tone flight effect for the S33-A55 nozzle beneath the SYMPHONY wing at jet flow condition 8; $[h/D_s = 0.309,\ l/D_s = 2.536,\ \delta = 32°,\ \theta = 90°,\ \phi = 0°]$

The clear exception to these two hypotheses concerns the sixth tone ($f_6 = 1580$ Hz), which appears to be amplified, by approximately 8 dB, in the presence of the 52 m/s flight stream flow. The reason why this particular instability grows in strength under these conditions is another area for further investigation. This sixth tone also appears to shift lower in frequency by 20 Hz when $U_f = 52$ m/s. On closer inspection of the bypass jet velocities of these two test points, however, a difference of 5 m/s was noted, which could, at least in part, explain the frequency shift.

When the flight stream velocity is increased further to $U_f = 103$ m/s, it becomes very difficult to track the behaviour of these six tones. It is unclear, for example, whether some of the tones have been: (1) 'cut-off' completely, (2) masked beneath the broadband level, (3) revealed above the broadband level (i.e. f_8) or (4) shifted in frequency. It should be noted that, based upon observations from the experimental data of Lepicovsky and Ahuja [136], Tam and Ahuja found little tonal frequency shift over their entire range of wind tunnel operating speeds (i.e. $U_f < 80$ m/s) [130]. At first sight, however, it would appear that tones f_4, f_5 and f_6 have all shifted lower in frequency, as labelled in blue on Figure 6.7? If this is the case, is this frequency shift caused by a reduction in instability convection velocity or a reduction in net upstream acoustic propagation velocity (if the acoustic wave, in fact, travels outside of the jet) or both? It is clear that data containing finer incremental increases in flight velocity are required to understand this effect properly.

6.3.4 Scaling effect

In order to establish if, and how, the jet-flap impingement tones scale with Reynolds number, a read-across experiment was performed with a smaller model-scale set-up in the Doak Laboratory. An horizontal flat plate wing and angled (deployed) flat plate flap were used to represent the equivalent NTF set-up, as detailed by the red lines in Figure 6.3. A far-field acoustic comparison between the NTF and DOAK experiments, under static ambient flow conditions, can be seen in Figure 6.8. As with previous read-across graphs, the corrected sound pressure level, SPL_c, and Strouhal number, St_D, variables are used.

Of the four most visible tones in this figure, it is interesting to observe that the first ($\mathrm{St}_1 = 0.60$) and fourth ($\mathrm{St}_4 = 0.95$) tones appear to scale well between the DOAK and NTF experiments. The same cannot be said, however, for the amplitudes of these tones. It should be noted that the geometries of the two experiments are not completely identical (as detailed in the legend of Figure 6.8). It is plausible that small details in the NTF wing and flap geometry may be responsible for the differences in tone amplitude as well for the generation of the second and third tones. Furthermore, any differences in the jet instability initial conditions at each of the nozzle lips will also decrease the likelihood of a perfect read-across. Clearly further aerodynamic investigation is required to get to the bottom of the physics responsible for these results.

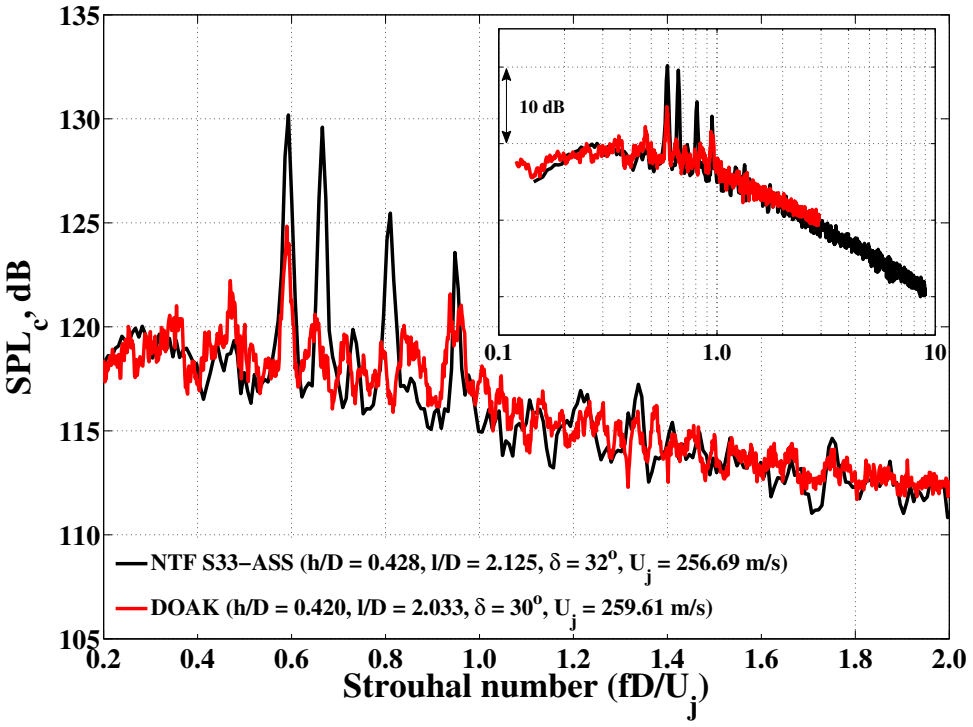

FIGURE 6.8: Far-field narrowband acoustic read-across between the S33-ASS nozzle installed beneath the SYMPHONY wing with deployed flaps and the DOAK nozzle installed beneath the horizontal flat plate wing and angled flat plate flap; [$M_{a_{\text{ref}}} = 0.75$; $U_f = 0$ m/s; $\theta = 90°$; $\phi = 0°$]

6.3.5 Angled plate geometry

Following the NTF-DOAK read-across test, one final experiment was conducted in the Doak Laboratory in order to interrogate the jet-flap impingement tonal noise mechanism further. A flat plate was angled at 30° to the jet axis and positioned at several axial, l, and radial, h, locations next to the same single stream, unheated, subsonic DOAK jet, see Figure 6.4. One read-across and three parametric analyses follow.

6.3.5.1 Read-across study

First, a far-field acoustic read-across experiment was performed between the previous horizontal flat plate wing with angled flat plate flap geometry and the new angled flat plate geometry, see Figure 6.9. The location of the angled plate TE and the deployed flap TE, relative to the jet, was kept constant between experiments.

In this figure, it is clear to see that the 4 kHz tone is produced in both experiments, albeit with a different amplitude. Generally, a greater number and strength of instability tones are visible for the angled plate case. The most plausible explanation

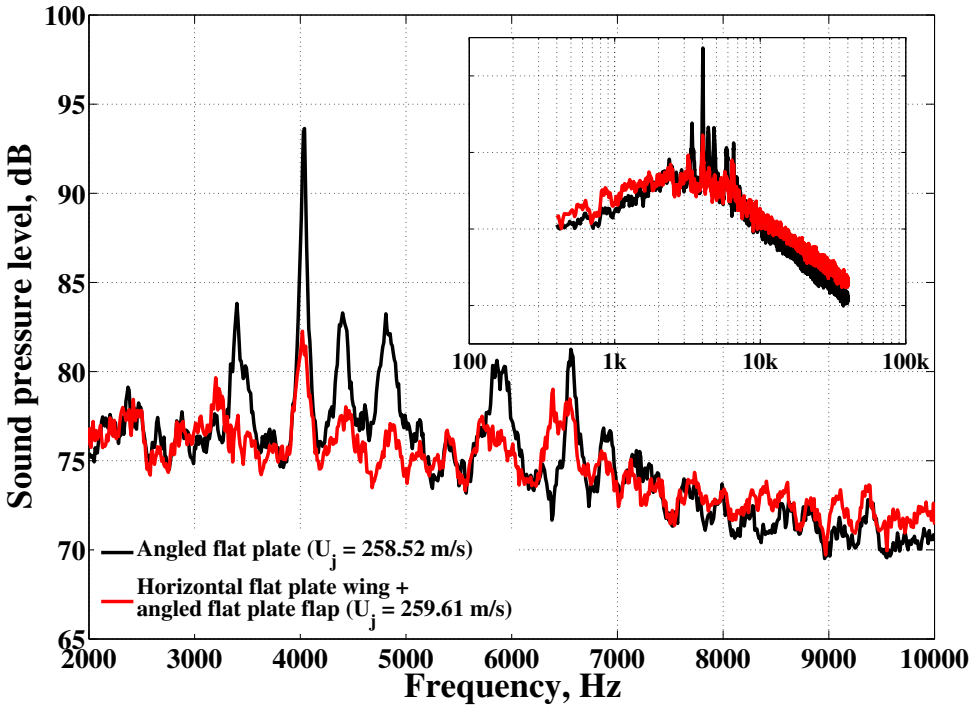

FIGURE 6.9: DOAK far-field acoustic read-across between an angled flat plate and an horizontal flat plate wing with angled flat plate flap; [$h/D = 0.42$, $l/D = 2.03$, $\delta = 30°$, $\theta = 90°$, $\phi = 0°$]

for this is that a number of jet instability modes are hampered from developing due to the presence of the horizontal flat plate wing. The entrainment of ambient fluid into the jet next to the angled plate is essentially unconstrained, which, therefore, provides all instability modes with the freedom to grow. A useful experiment to conduct in the future would be to force the jet, either using loudspeakers or actuators, in an attempt to prevent certain modes from forming.

6.3.5.2 Geometrical parametric study

A brief parametric study of the tonal behaviour was carried out for parameters l and h for the angled flat plate jet impingement set-up. Firstly, at one particular axial impingement location, $l/D = 1.50$, and for one jet acoustic Mach number, $M_a = 0.75$, the plate trailing edge was moved incrementally (in 3.8 mm steps) radially away from the geometric jet centreline through the upper shear layer of the jet. Essentially, this study was a repeat of the vertical separation effect experiment described above in Section 6.3.2. As before, the far-field acoustic data was measured beneath the plate at a single polar angle, $\theta = 90°$, and flyover azimuthal angle, $\phi = 0°$.

Figure 6.10 shows us that as the plate trailing edge is traversed radially across the jet shear layer away from the jet, the frequencies of the tones remain fixed and the

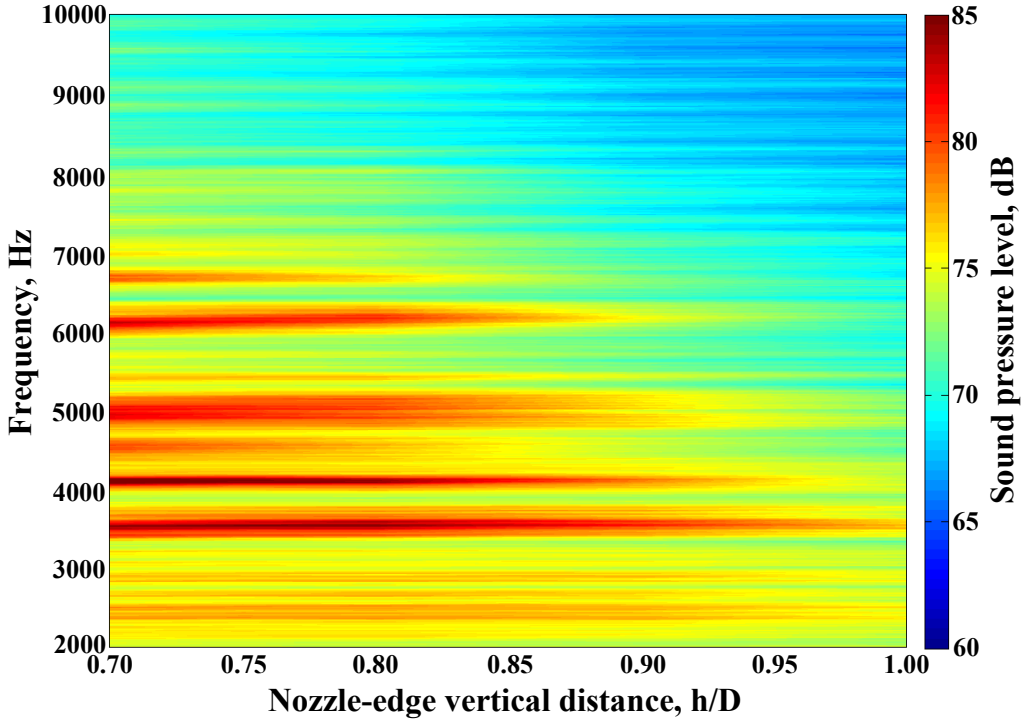

FIGURE 6.10: Far-field acoustic DOAK vertical separation parametric study of the jet impingement tonal noise using an angled flat plate [$l/D = 1.50$, $\delta = 30°$, $M_a = 0.75$, $\theta = 90°$, $\phi = 0°$]

amplitudes reduce. This result matches the behaviour found using the SYMPHONY deployed flap geometry but is contrary to the findings of Ziada and Rockwell [134], who reported that small transverse variations between a vortex centre and the edge (i.e. the change in the amplitude of the induced force on the edge) were responsible for shifts in tone frequency.

The second geometrical parameter in this study was the axial separation between nozzle and trailing edge, or impingement length, l/D. While the radial position was fixed (at $h/D = 0.67$), the axial location of the edge was increased (again, in 3.8 mm increments) downstream from the nozzle lip. The general trend, in Figure 6.11, is that the frequency of each instability tone decreases linearly with increasing impingement length. This is expected as, with increasing distance downstream from the nozzle, the edge-nozzle feedback loop will lengthen. Furthermore, the author would expect this decrease in frequency trend to continue for larger impingement lengths until each instability no longer has sufficient energy to sustain its own feedback loop.

One final observation to make is that the gradient of this linear relationship does not appear to be constant for each particular instability tone. The author suggests that this is due to the different velocities with which different instabilities convect downstream within the shear layer. It is hoped that this hypothesis can be explored

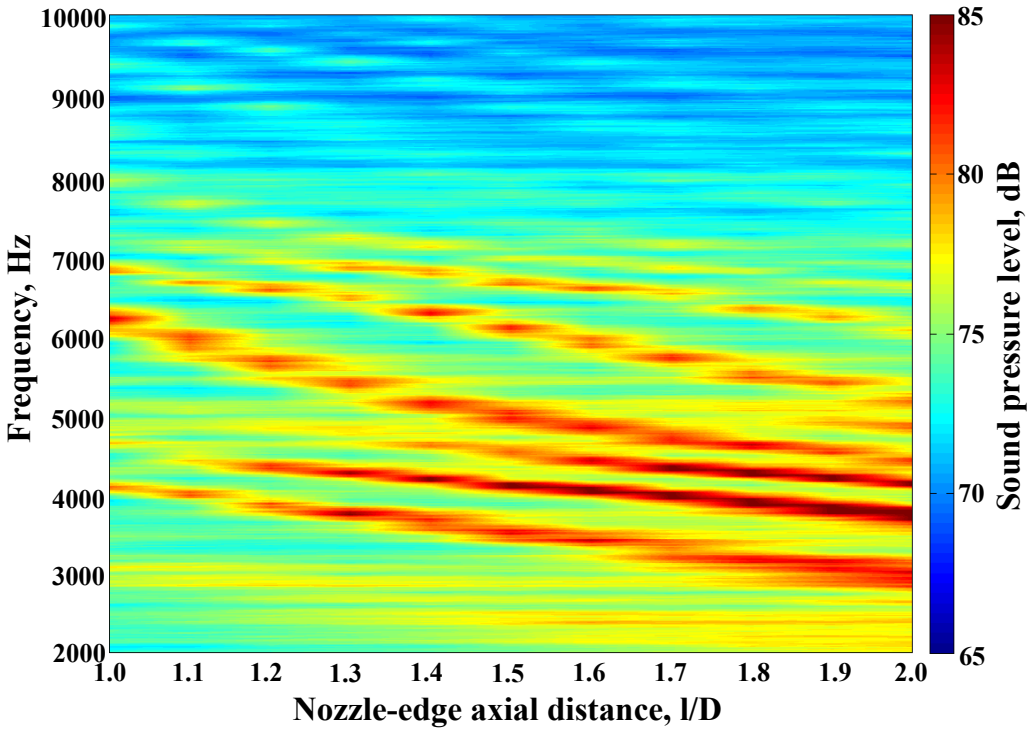

FIGURE 6.11: DOAK impingement length parameter study of the jet impingement tonal noise using an angled flat plate [$h/D = 0.67$, $\delta = 30°$, $M_a = 0.75$, $\theta = 90°$, $\phi = 0°$]

further in future aerodynamic test campaigns using PIV, hot-wire or 5-hole probe experimental techniques, for example.

6.3.5.3 Velocity parametric study

Finally, if we look at the jet acoustic Mach number dependence of the jet-flap interaction tones (plotted in 0.05 M_a increments), see Figure 6.12, we can see that $M_a = 0.60$ is a critical point above which the first jet instability has enough energy to sustain its own feedback loop. This result is consistent with previous research [126], in which a subsonic jet shear layer impinged upon a circular cylinder.

For acoustic Mach numbers greater than 0.80, however, it becomes increasingly difficult to identify any tonal protrusion above the broadband jet surface interaction and jet mixing noise. It also appears that the frequencies of the instability tones are independent of acoustic Mach number and that each tone has a critical range over which it can be sustained. A satisfactory physical explanation for this upper acoustic Mach number limit, however, has not yet been established. It is clear that further parametric acoustic and aerodynamic instability investigation is required to understand the intricacies of this tonal behaviour fully. The author also expects that

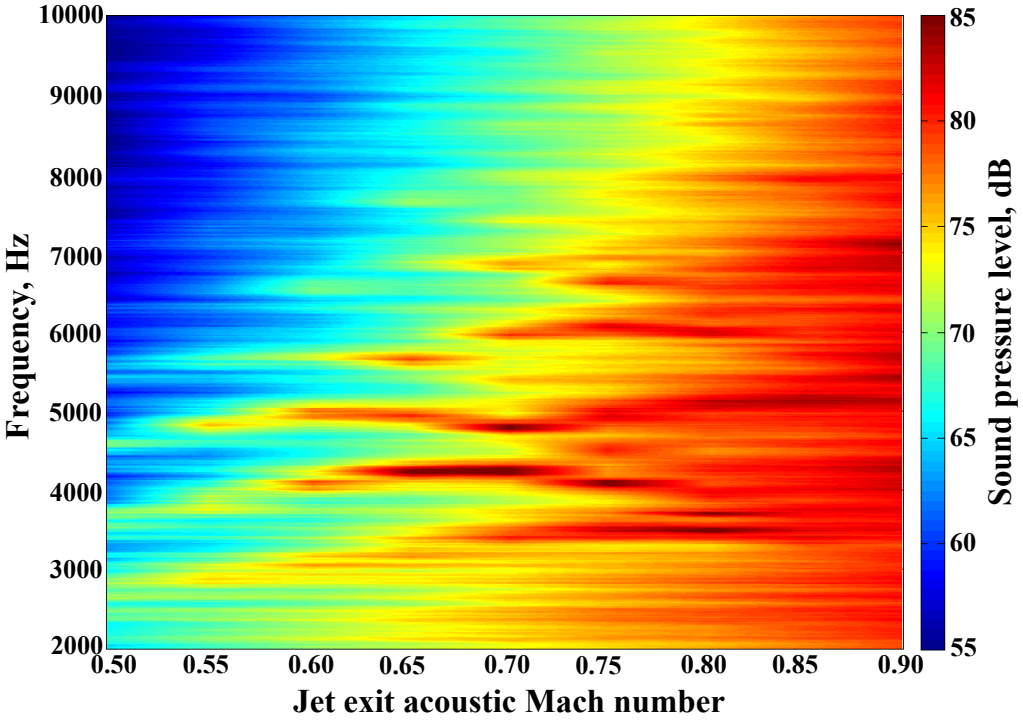

FIGURE 6.12: DOAK acoustic Mach number parameter study of the jet impingement tonal noise using an angled flat plate; [$h/D = 0.67$, $l/D = 1.50$, $\delta = 30°$, $\theta = 90°$, $\phi = 0°$]

the geometrical complexity relevant for realistic aircraft configurations will require an experimental and numerical two-pronged approach in the future.

6.4 Conclusions

Multiple tones bearing no clear harmonic relationship have been observed in several close-coupled, installed jet-flap experiments. It is suggested that the tones are generated by a jet instability feedback mechanism between the nozzle lip and the flap trailing edge. The frequency of the lowest visible tone was found to scale consistently from a large to a smaller model-scale experiment. It is believed that the higher frequency tones scale less well because they are inherently more sensitive to slight changes in the geometrical parameters of the experiment, as well as by the initial jet instability conditions imposed at the nozzle lip.

A parametric study of the key jet-flap geometries revealed, firstly, that the frequencies of the tones were found to be independent of the radial location of the flap trailing edge, h/D, when traversed across the upper jet shear layer. Intuitively, the amplitude of the tones was seen to reduce with increasing radial distance as the mean turbulent kinetic energy in the shear layer also decreases. Secondly, the fundamental tone frequency was observed to decrease linearly with increasing impingement distance, l/D. The higher frequency tones, however, decreased in a less linear fashion, again, suggesting a greater sensitivity to the fundamental parameters of the experiment, h, l and U_j.

The addition of flight stream results in three effects. Firstly, the three lowest frequency ($\mathrm{St} < 0.7$) shear layer instability tones lose the energy required to sustain the feedback mechanism and so reduce in amplitude until they are masked beneath the broadband jet-surface interaction noise. Secondly, due to the reduction in jet-surface interaction noise, higher frequency tones suddenly become visible above the broadband level. Thirdly, the frequencies of the tones decrease linearly with increasing flight stream. It is suggested that this is due to the reduction in the net upstream-propagating velocity of the acoustic wave generated at the flap trailing edge. This finding also suggests that the acoustic wave travels outside (rather than inside) the jet column.

Finally, each tone is seen to have a critical Mach number range between which it can sustain its own feedback loop. Typically, this appears to be between $0.6 < M_a < 0.8$, which is consistent with previous research. It is clear that further parametric acoustic and hot-wire or particle image velocimetry instability investigation is required to understand the intricacies of this tonal behaviour fully. It is also expected that the jet instability and geometrical complexity relevant for realistic aircraft configurations will require both an experimental and numerical approach in future.

Ways in which one could attenuate this source could involve forcing the jet acoustically at a different frequency. While one would clearly aim to destroy one particular

instability, it would be a difficult exercise not to excite any other instabilities at the same time. The only other practical option would be to remove the flap trailing edge from the situation completely. This could be an important factor for reintroducing a thrust gate, or gap, into the flap. One would obviously have to be careful, however, that additional side edge noise would not adversely affect the situation. This situation was, in fact, tested within SYMPHONY and did successfully remove the tones.

Chapter 7

Installed Jet Noise Modelling

In this chapter, a new, semi-empirical installed jet far-field noise prediction tool - SEmp version 1 - is presented. The model is described as *semi-empirical* because it has been developed principally using model-scale experimental data from the ISVR's Doak Laboratory and QinetiQ's Noise Test Facility. The current version of this engineering tool contains a series of scaling laws and curve-fits for the simplest installed jet configuration - a horizontal, semi-infinite flat plate positioned above an unheated, single stream jet under static ambient flow conditions. The term *semi-infinite* refers both to the total span of the plate, S, which extends 15 nozzle diameters, D, either side of the centre-line of the jet (minimising any side edge-generated noise), and to the total length of the plate, L, which extends $20D$ upstream of the nozzle exit (minimising any aeroacoustic leading edge effects). Predictions are made at a single azimuthal observer angle, $\phi = 0°$ (i.e. directly beneath the plate), and over a range of polar observer angles relative to the jet axis, θ_j. The tool is set within the wider context of the holistic, fully complex problem so that improvements to the fidelity of the model may be integrated easily in the future. Limitations, accuracy and opportunities for further development of SEmp v1 are also discussed.

7.1 Holistic Installed Jet Noise Prediction Strategy

It is important to appreciate the interdependencies between each noise source when attempting to capture the complete physics of the installed jet problem. First of all, therefore, a holistic installed jet noise prediction scheme is presented in Figure 7.1. Five key sources of noise have been identified: (1) isolated jet mixing noise, $\mathrm{SPL}_{\mathrm{isol}}$, (2) isolated wing airframe noise, $\mathrm{SPL}_{\mathrm{wing}}$, (3) jet-surface reflection noise, $\mathrm{SPL}_{\mathrm{jsr}}$, (4) jet-surface interaction noise, $\mathrm{SPL}_{\mathrm{jsi}}$, and (5) jet-flap interaction noise, $\mathrm{SPL}_{\mathrm{jfi}}$. In order

for these sources to propagate to the ground, each acoustic field will also need to pass through the hot, turbulent jet plume. They will all, therefore, be subject to a degree of attenuation, or blockage, $\Delta\text{SPL}_{\text{block}}(\omega, \theta_j, \phi, J_c)$, where J_c are the jet exit conditions (i.e. U_p, U_s, T_p and T_s). Any attempt to create a high fidelity acoustic far-field prediction code for most of these sources is not possible without knowledge of the flow field and jet blockage characteristics. A low fidelity, semi-empirical method, however, simply looks for overall trends in data to gain a quick appreciation of the sensitivity of each experiment parameter.

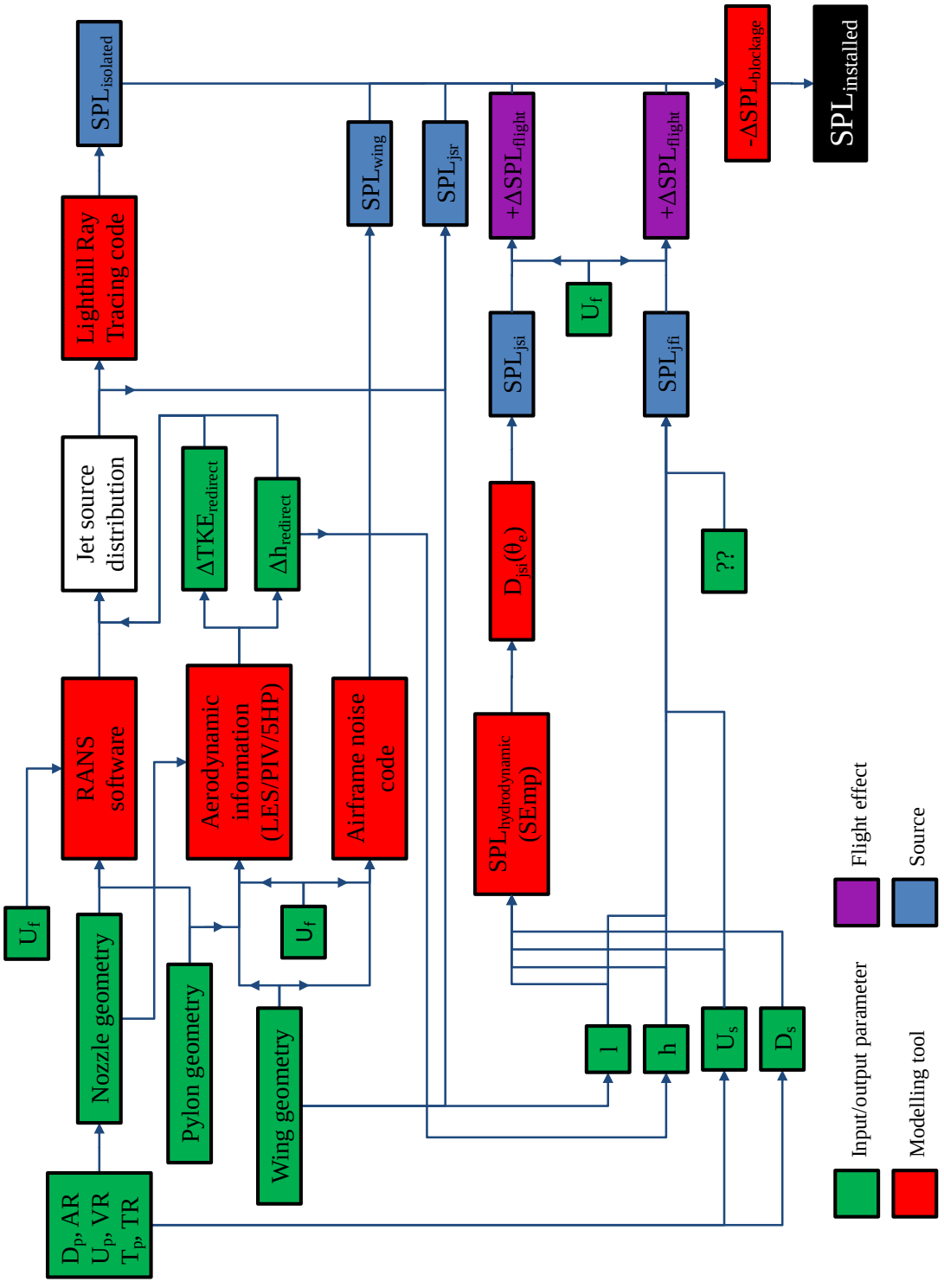

FIGURE 7.1: Structure of a holistic installed jet noise prediction scheme

7.2 SEmp v1 Methodology

The aim of SEmp is to produce a simple mathematical expression to predict the far-field strength and polar directivity of the jet-surface interaction source, $\mathrm{SPL_{jsi}}$, on the ground beneath a surface (e.g. an aircraft wing). Specifically, SEmp v1 predicts the ground-radiated noise beneath a horizontal, semi-infinite, flat plate (i.e. $\delta = 0°$) installed in close proximity to an unheated, single stream jet, under static ambient flow conditions (i.e. at $U_f = 0\mathrm{m/s}$). The schematic in Figure 4.2 on page 92 shows this scenario clearly. The parameter ranges over which SEmp v1 is valid are listed below in Table 7.1.

Parameter	Min	Max
h/D	0.67	1.50
l/D	1.50	4.00
$M_a = U_j/a_0$	0.50	0.90
θ_j (°)	30	150

TABLE 7.1: SEmp v1 valid parameter ranges

As established in Chapter 4, the dominant noise source mechanism for this configuration involves a scattering of the jet's hydrodynamic near pressure field by the trailing edge of the plate.

An initial analysis using the overall sound pressure level difference between the installed and isolated jets is used to establish the sensitivity of each fundamental parameter of the problem. Figure 7.2 shows the unshielded (i.e. $\phi = 0°$) $\Delta\mathrm{OASPL_{inst\ -\ isol}}$ far-field acoustic jet results from the ISVR's Doak Laboratory (DOAK) as a function of jet polar observer angle, θ_j. Least-squares best-fit trend lines have also been fitted to the data in the form, $A \sin^2 \theta_e/2$, where A is a scalar variable. This variable, therefore, relates to the difference between the strength of the jet's hydrodynamic field at the plate trailing edge when the jet is isolated and when it is installed.

It is clear to see that the majority of the experimental data fits well with Ffowcs-Williams & Hall's semi-baffled (i.e. $\sin^2 \theta_e/2$) directivity theory for a non-compact dipole source mechanism [19]. This agreement, however, is seen to deteriorate at the lowest jet acoustic Mach number (i.e. at $M_a = 0.30$) as more $\mathrm{OASPL_{jsi}}$ noise is generated than expected in the low polar angles. This directivity feature can be explained by remembering the wavelengths of the sound field scattered by the plate trailing edge. As velocity decreases, the peak frequency of the jet's hydrodynamic field (and thus the peak of the radiated JSI noise) also decreases. The source wavelengths, therefore, become more and more comparable to the total length

of the plate, L, (where $L = 0.762$ m ≈ 450 Hz). Thus, the lower frequency JSI noise will tend to radiate beneath the wing in a more omnidirectional fashion (i.e. as part of a classic compact dipole source pattern). At least, for realistic aircraft jet velocities, we can ignore this low speed (compact source) case altogether.

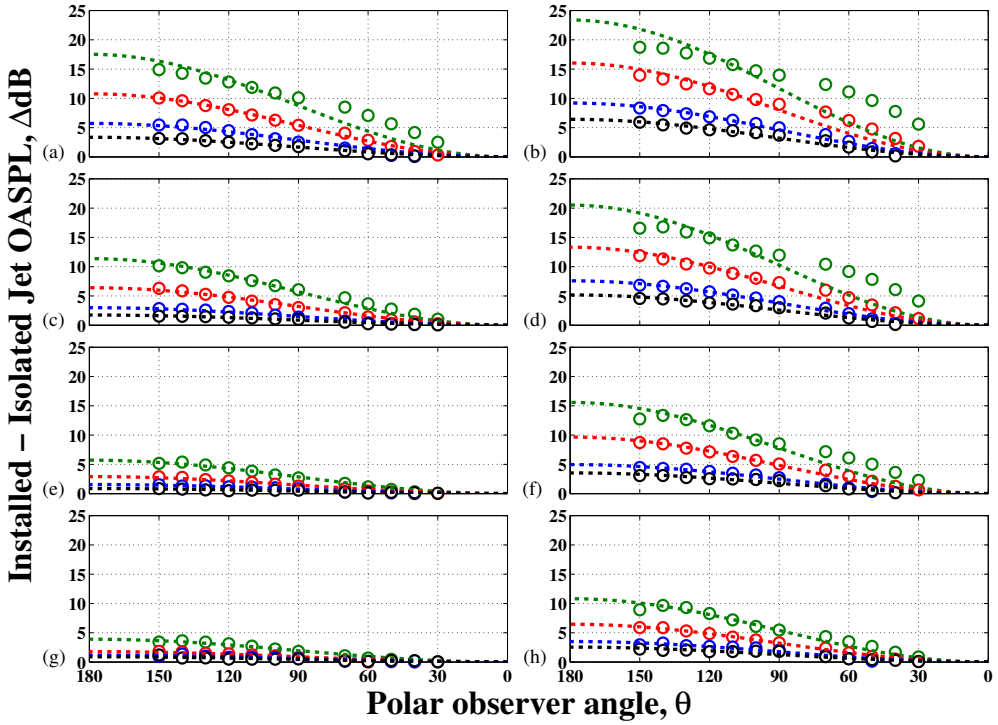

FIGURE 7.2: Polar directivity of a horizontal semi-infinite flat plate installed next to an unheated, single stream jet: (a) $h/D = 0.70$, $l/D = 2$; (b) $h/D = 0.70$, $l/D = 4$; (c) $h/D = 1.00$, $l/D = 2$; (d) $h/D = 1.00$, $l/D = 4$; (e) $h/D = 1.25$, $l/D = 2$; (f) $h/D = 1.25$, $l/D = 4$; (g) $h/D = 1.50$, $l/D = 2$; (h) $h/D = 1.50$, $l/D = 4$; [green - $M_a = 0.30$; red - $M_a = 0.50$; blue - $M_a = 0.75$; black - $M_a = 0.90$; circles - DOAK data; dotted lines - $A \sin^2 \theta_e/2$ least-squares best-fit; $\phi = 0°$]

If one then plots the relationship between the directivity amplitude parameter, A, and M_a, h and l, exponentially decaying relationships are seen to exist (see Figure 7.3). The subsequent plots (see Figures 7.4 and 7.5) show the curve-fits chosen to complete the prediction expression.

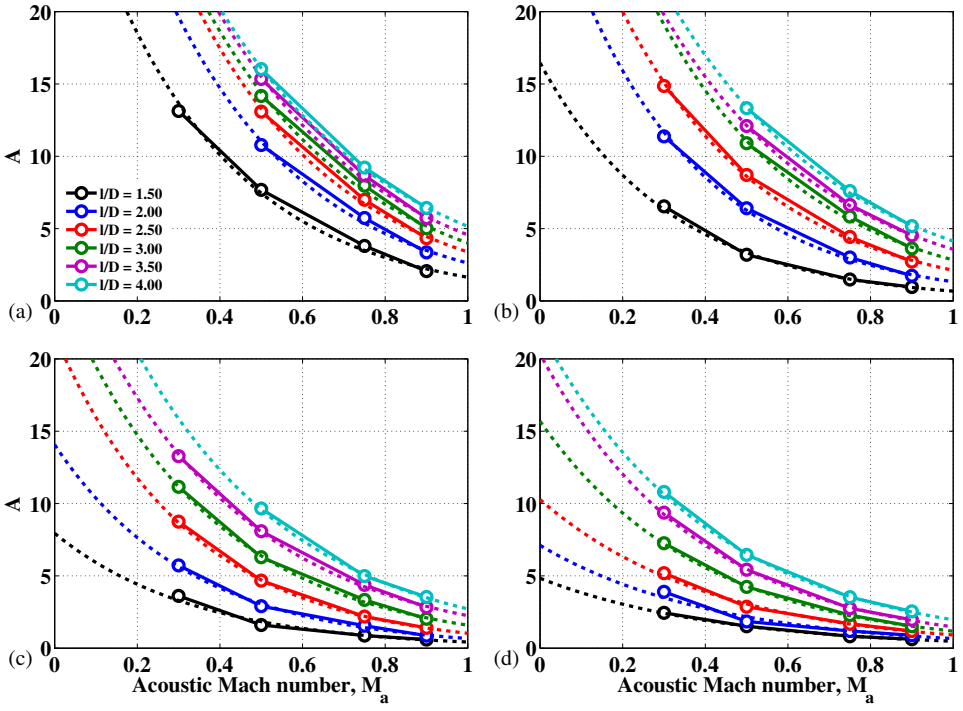

FIGURE 7.3: Polar directivity amplitude constant, A, versus jet acoustic Mach number, M_a, and axial distance from nozzle lip to plate trailing edge, l, for a single stream jet installed next to a horizontal flat plate: (a) $h/D = 0.70$; (b) $h/D = 1.00$; (c) $h/D = 1.25$; (d) $h/D = 1.50$; [dotted lines - $Be^{(CM_a)}$ exponential least-squares best-fit; $\phi = 0°$]

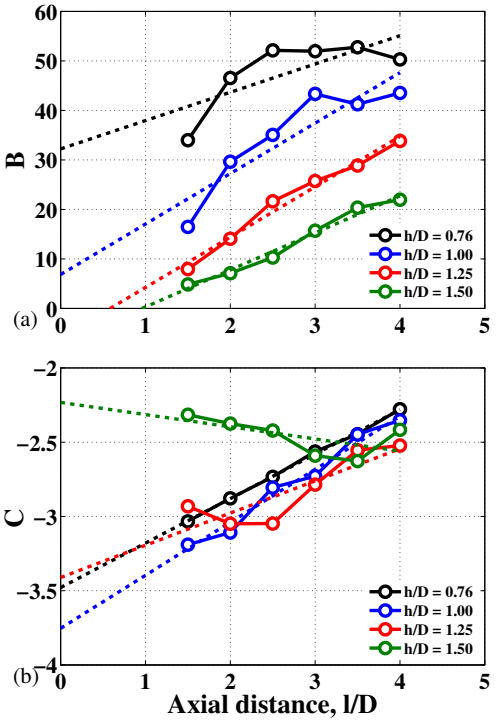

FIGURE 7.4: SEmp curve-fitting constants versus axial distance from nozzle lip to plate trailing edge, l: (a) B (dotted lines - $E(l/D) + F$ linear least-squares best-fit); (b) C (dotted lines - $G(l/D) + I$ linear least-squares best-fit; [$\phi = 0°$]

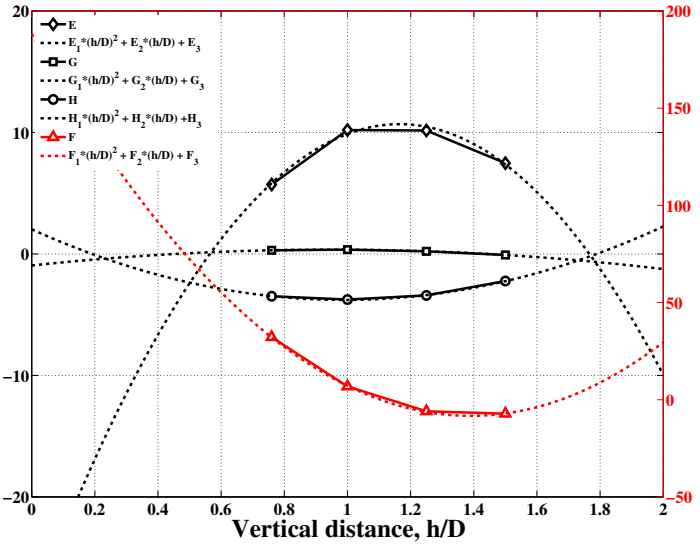

FIGURE 7.5: SEmp curve-fitting constants versus radial distance from jet geometric centreline to plate surface, h; [dotted lines - 2$^{\text{nd}}$ order polynomial least-squares best-fit; $\phi = 0°$]

In summary, the final expressions governing SEmp v1 can be written as follows,

$$\Delta\text{OASPL} = A\sin^2(\theta_e/2) \tag{7.1}$$

where,

$$A = Be^{C\cdot M_a} \tag{7.2}$$

where,

$$B = E(\frac{l}{D}) + F \tag{7.3}$$

$$C = G(\frac{l}{D}) + H \tag{7.4}$$

where,

$$E = E_1(\frac{h}{D})^2 + E_2(\frac{h}{D}) + E_3 \tag{7.5}$$

$$F = F_1(\frac{h}{D})^2 + F_2(\frac{h}{D}) + F_3 \tag{7.6}$$

$$G = G_1(\frac{h}{D})^2 + G_2(\frac{h}{D}) + G_3 \tag{7.7}$$

$$H = H_1(\frac{h}{D})^2 + H_2(\frac{h}{D}) + H_3 \tag{7.8}$$

The final twelve polynomial constants are displayed below in Table 7.2.

	1	2	3
E	-29.6	69.0	-29.5
F	101.7	-282.7	188.2
G	-1.4	2.7	-0.9
H	5.9	-11.7	2.0

TABLE 7.2: SEmp 2nd order polynomial least-squares best-fit constants calculated from DOAK data

7.3 SEmp v1 Predictions

As expected from a semi-empirical prediction method, very good agreement can be seen over the parameter range of interest, see Figure 7.6.

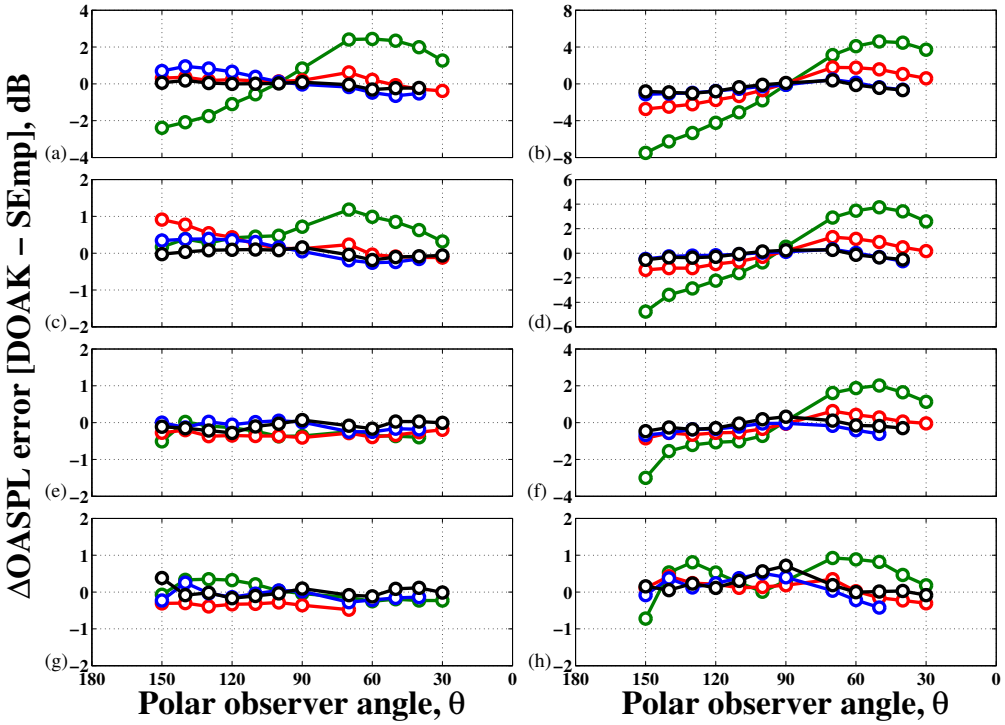

FIGURE 7.6: SEmp prediction versus $\Delta\text{OASPL}_{\text{inst-isol}}$ DOAK data for a horizontal, semi-infinite, flat plate installed next to an unheated, static, single stream jet: (a) $h/D = 0.70$, $l/D = 2$; (b) $h/D = 0.70$, $l/D = 4$; (c) $h/D = 1.00$, $l/D = 2$; (d) $h/D = 1.00$, $l/D = 4$; (e) $h/D = 1.25$, $l/D = 2$; (f) $h/D = 1.25$, $l/D = 4$; (g) $h/D = 1.50$, $l/D = 2$; (h) $h/D = 1.50$, $l/D = 4$; [green - $M_a = 0.30$; red - $M_a = 0.50$; blue - $M_a = 0.75$; black - $M_a = 0.90$; circles - comparison against DOAK data; squares = comparison against NTF data; $\phi = 0°$]

As previously identified, the only exception is when $M_a < 0.5$, when the full physics of the situation is not captured sufficiently.

7.4 Conclusions

A quick and robust semi-empirical prediction tool, SEmp v1, has been created and validated against the DOAK experimental data. This first version of SEmp is limited to the fundamental case of an installed horizontal, semi-infinite plate (or cruise wing) in close proximity to an unheated, single stream jet, under static ambient flow conditions. Clearly at particularly low jet acoustic Mach numbers (i.e. $M_a = 0.30$), the physics of the situation is not properly accounted for. At these flow speeds, SEmp v1 heavily under-predicts the installation noise in the rear jet arc and slightly over-predicts the installation noise in the forward arc.

The next step-up in model prediction accuracy (and complexity) requires a deconstruction of each individual source into its narrowband sound pressure level (SPL) spectral components. Regarding the $\mathrm{SPL}_{\mathrm{jsi}}$ source, and as mentioned at the end of Chapter 3, a semi-empirical model of the linear hydrodynamic near-field of a single stream jet is almost ready to predict the strength and frequency content of the field incident on a wing or flap trailing edge before it is scattered. Only then, together with a more sophisticated diffraction model for the wing geometry (like Miller's semi-empirical method or Roger and Moreau's analytical method), could the true far-field acoustic signature be reconstructed fully.

The next most significant improvements to the holistic installed jet noise prediction strategy would include high fidelity models for the jet-surface reflection source, $\mathrm{SPL}_{\mathrm{jsr}}$, and jet blockage propagation effect, $\Delta\mathrm{SPL}_{\mathrm{block}}$, as a function of polar observer angle and azimuthal angle.

A better understanding of the jet-flap interaction tones, $\mathrm{SPL}_{\mathrm{jfi}}$, is also clearly required before closely-coupled installed jets impinging onto deployed flaps can be modelled properly.

Finally, the extent to which the physics of each of these source mechanisms changes when under in-flight ambient flow conditions is still unknown. Careful analysis of static versus incrementally increasing flight velocity data, therefore, is required to help this understanding in the future.

Chapter 8

Conclusion

8.1 Summary of Key Findings

In this thesis, a several acoustic experiments have been conducted in order to investigate a variety of acoustic effects involving both isolated and installed subsonic jets. In Chapter 3, we have seen that some Reynolds scaling effects exist, at flow acoustic Mach numbers above 0.5, in the small Doak Laboratory university model jet compared to the large QinetiQ Noise Test Facility industrial model jet. A semi-empirical isolated jet hydrodynamic spectrum prediction method has been developed and a new velocity-dependent definition of the 'near-field' of an isolated jet has been found.

In Chapter 4, we have validated the jet plus flat plate experiment against historical data (for example, Head and Fisher [67]) and have matched far-field sound pressure level polar directivity data successfully to Miller's model [1]. Furthermore, the near-field analyses required to validate future Amiet-based analytical models have been performed.

In Chapter 5, a complex experimental test was designed and conducted successfully at QinetiQ's NTF. The static, cruise wing installed jet data was also found to scale well between the Doak and the NTF facilities giving confidence to future small-scale installed jet testing. Some simple static-to-flight effects were observed, but further physical understanding was deemed impossible without detailed wing lift performance and jet aerodynamic data. Phase analysis between transducers on the trailing edge of the flap, the forward top surface of the wing and the far-field below the wing have provided further evidence that jet-surface interaction sound produced at the flap trailing edge does, in fact, travel upstream above the wing and is then back-scattered by the leading edge back underneath the jet into the far-field.

In Chapter 6, a multiple tone jet-flap impingement noise source, originally discovered in the NTF, was investigated back in the Doak Laboratory. Certain tones were found to scale between the facilities and a simple parametric study with an angled flat plate revealed that a jet instability feedback mechanism between nozzle lip and flap trailing edge was the most likely mechanism responsible and that the tones only appeared above flow acoustic Mach numbers above .

Finally, in Chapter 7, a first version of a industrial installed jet noise prediction model was developed and validated against the Doak Laboratory data. This version of the method simply predicts the change in frequency-integrated overall sound pressure level noise produced when a horizontal flat plate is installed above a single-stream, subsonic, unheated jet. A higher fidelity narrowband prediction framework, however, has now also been designed, into which the isolated jet near-field hydrodynamic field method described in Chapter 3 will soon fit.

8.2 Future Work

There is much further research to conduct on this subject. Principally, more aerodynamic information (including both mean and turbulent velocity data) is clearly required to investigate the upper jet shear layer next to the wing, or flap, trailing edge. Clearly, h and l are very crude parameters to use for this type of problem and one would hope that the jet turbulent length and time-scales in the vicinity of the edge would make more sense to use in the future. This will be important too, further down the line, when attempting to study the asymmetric installed jet effects from the presence of the engine-to-wing support pylon.

It is clear also that wing lift effects will prove important to study as one attempts to increase the complexity of the problem by adding an ambient flight stream flow. Hot-wire and five-hole probe measurements, therefore, will be essential to map exactly where the jet is beneath the wing at various operating conditions and flap deployment settings.

Finally, the topic of jet-flap instability tones leaves much room for further study. The first step is to establish whether the mechanism is actually capable of scaling up to full-size aircraft geometries. If this is possible, then they will quickly become a serious concern to the aviation industry and will require further research. If a thrust gate approach is infeasible due to the loss in performance, for example, the next question will then be how does one best predict them. In this case, we must return to the physics of jet stability theory.

Appendix A

Appendix A - Kulite Calibration

A.1 Shock tube calibration

In order to establish the sensitivity, s_{kulite}, and phase response, φ_{kulite}, of the Kulite transducers over the frequency range of interest, in situ near-field dynamic pressure calibrations were performed for each transducer using a white noise loudspeaker shock tube set-up, see Figure A.1. This shock tube system was designed to generate a plane wave sound field incident on the diaphragm of the transducer. Two factors determine the maximum calibration frequency of such a system. Firstly, the width of the tube dictates the frequency above which standing waves will form across the tube. If standing waves exist, the incident sound field on the two microphones will no longer constitute a uniform plane wave and, thus, the calibration sensitivity values above that frequency will be invalid. Secondly, a frequency will exist above which the dynamic pressure responses of both the loudspeaker and the Kulite transducers will drop-off. At this point, a significant reduction in coherence between loudspeaker and microphone will occur and the calibration will be invalid. The 'coherence' between two signals, V_1 and V_2, is defined mathematically as,

$$\Gamma^2 = \frac{|\Psi_{V_1V_2}|^2}{(\Pi_{V_1V_1}\Pi_{V_2V_2})}\,, \tag{A.1}$$

where $\Psi_{V_1V_2}$ is the cross power spectral density between the two signals and $\Pi_{V_1V_1}$ and $\Pi_{V_2V_2}$ are the auto power spectral densities of signal 1 and 2, respectively.

In order to calibrate the Kulites with confidence over a broad calibration range, a GRAS Type 40BF condenser microphone was used as the reference microphone. This particular microphone was appropriate because its free-field frequency response is typically flat between 100 Hz and 20 kHz, see Figure 3.5. Using a pistonphone, the

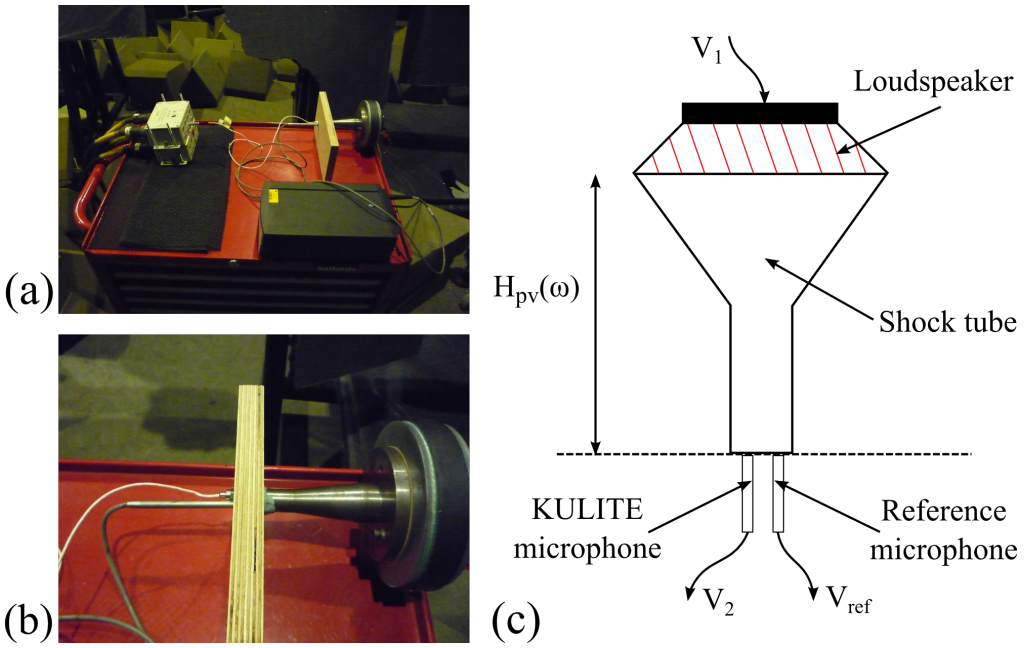

FIGURE A.1: (a) Shock tube calibration set-up; (b) close-up of calibration set-up; (c) schematic of calibration set-up

sensitivity, s_{ref}, of this reference microphone was measured (typically, $s_{\text{ref}} = 3$ mV/Pa at 1 kHz). This value could then be applied over the entire flat region of the frequency response spectrum.

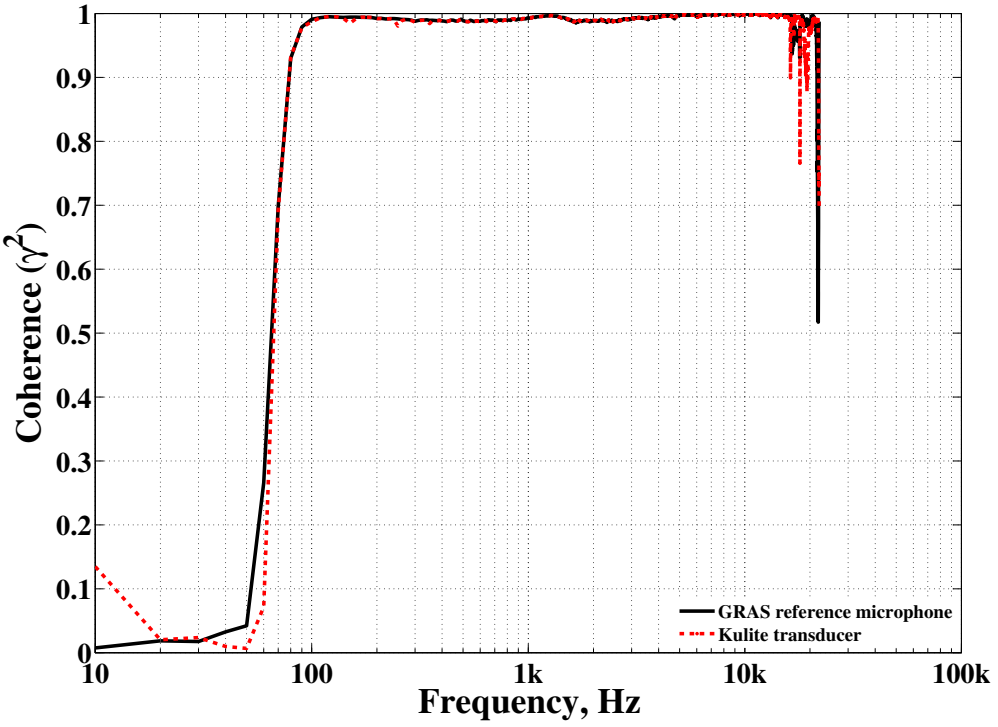

FIGURE A.2: Typical (measured) shock tube coherence between broadband loudspeaker input signal and transducer output signal

In order to account for the change in pressure between the loudspeaker and the transducers via the shock tube, the following transfer function, $H_a(\omega)$, is defined,

$$H_a(\omega) = H_{\text{ref}}(\omega) \cdot \frac{1}{s_{\text{ref}}} , \tag{A.2}$$

where

$$H_{\text{ref}}(\omega) = \frac{\Psi_{V_1 V_{\text{ref}}}(\omega)}{\Pi_{V_1 V_1}(\omega)} , \tag{A.3}$$

where $\Pi_{V_1 V_1}(\omega)$ is the auto power spectral density of the input broadband loudspeaker signal, V_1, and $\Psi_{V_1 V_{\text{ref}}}(\omega)$ is the cross power spectral density between V_1 and the output reference microphone voltage, V_{ref}. The sensitivity of the Kulite surface pressure transducer, $s_{\text{kulite}}(\omega)$, therefore, can be written down as,

$$s_{\text{kulite}}(\omega) = \frac{H_{\text{kulite}}(\omega)}{H_a(\omega)} , \tag{A.4}$$

where

$$H_{\text{kulite}}(\omega) = \frac{\Psi_{V_1 V_2}(\omega)}{\Pi_{V_1 V_1}(\omega)} , \tag{A.5}$$

where V_2 is the output Kulite voltage. The typical variation in Kulite sensitivity (relative to the GRAS reference microphone at 1 kHz) is shown in Figure A.3a. The corresponding variation in phase response can be seen in Figure A.3b. Finally, the spectral coherence between the input loudspeaker signal and both the GRAS (solid black line) and Kulite (dotted red line) transducer signals can be seen in Figure A.2. It is clear to see from these plots that the dynamic pressure signals recorded by the Kulites can be trusted across the 100 Hz-6 kHz frequency range. Typically, the sensitivity of each Kulite transducer was approximately 0.17 mV/Pa at 1 kHz. The sensitivity and phase response (relative to 1 kHz) of all Kulites in the array were within tolerances of ± 0.2 dB and ± 0.3 radians, respectively, over the 100 Hz-10 kHz frequency range of interest. Finally, the acquisition sampling rate for this array was set at 20 kHz, well above the Nyquist frequency, in order to account for the additional in-built analogue filter present in the NI acquisition cards.

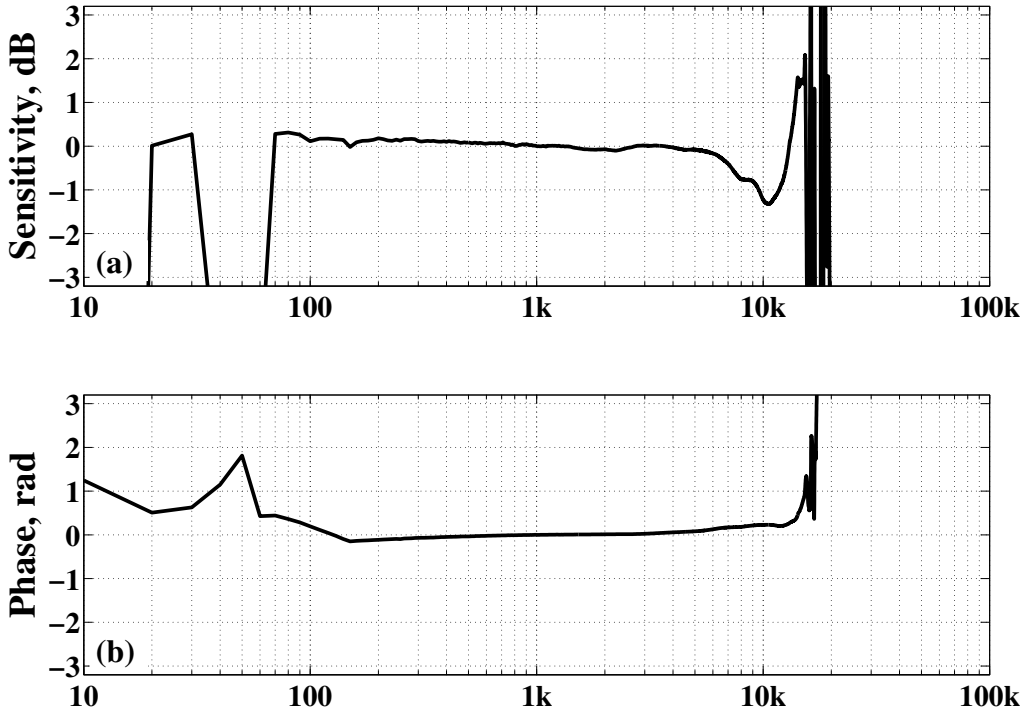

FIGURE A.3: Typical (measured) Kulite Type XT-190 surface pressure transducer variation in: (a) sensitivity and (b) phase angle; [relative to a GRAS Type 40BF reference microphone at 1 kHz]

Bibliography

[1] W. R. Miller. Flight effects for jet-airframe interaction noise. In *8th AIAA Aeroacoustics Conference*. AIAA Paper 1983-0784, 1983.

[2] Annual Report of the Council. International Civil Aviation Organization (ICAO), 2011.

[3] Environmental Report 2010. International Civil Aviation Organization (ICAO), 2010.

[4] Federal Aviation Regulations (FAR) - Part 36; Noise Standards: Aircaft Type and Airworthiness Certification. Technical report, U.S. Department of Transportation (DOT); Federal Aviation Administration (FAA), Washington D. C., 1969.

[5] Environmental Protection - Volume 1 - Aircraft Noise. International Civil Aviation Organization (ICAO), 2008.

[6] N. Dickson. ICAO Noise Standards. Technical Report May, 2013.

[7] European Aeronautics: A Vision for 2020. Technical report, Advisory Council for Aeronautics Research in Europe (ACARE), 2001.

[8] Environmental Report 2007. International Civil Aviation Organization (ICAO), 2007.

[9] Flightpath 2050 - Europes Vision for Aviation. European Commission (EC), 2011.

[10] G. M. Lilley. The prediction of airframe noise and comparison with experiment. *Journal of Sound and Vibration*, 239(4):849–859, 2001.

[11] D. P. Lockard, M. R. Khorrami, and F. Li. High resolution calculation of a simplified landing gear. In *10th AIAA/CEAS Aeroacoustics Conference*. AIAA Paper 2004-2887, 2004.

[12] M. J. T. Smith. *Aircaft Noise*. Cambridge University Press, New York, 1989.

[13] D. P. Lockard and G. M. Lilley. The airframe noise reduction challenge. NASA TM-2004-213013, 2004.

[14] Y. P. Guo, M. C. Joshi, P. H. Bent, and K. J. Yamamoto. Surface pressure fluctuations on aircraft flaps and their correlation with far-field noise. *Journal of Fluid Mechanics*, 415:175–202, 2000.

[15] Y. P. Guo, K. J. Yamamoto, and R. W. Stoker. Component-based empirical model for high-lift system noise prediction. *Journal of Aircraft*, 40(5):914–922, 2003.

[16] Y. P. Guo and M. C. Joshi. Noise characteristics of aircraft high lift systems. *AIAA Journal*, 41(7):1247–1256, 2003.

[17] R. W. Stoker, Y. P. Guo, C. Streett, and N. Burnside. Airframe noise source locations of a 777 aircraft in flight and comparisons with past model scale tests. In *9th AIAA/CEAS Aeroacoustics Conference*. AIAA Paper 2003-3232, 2003.

[18] T. F. Brooks and T. H. Hodgson. Trailing edge noise prediction from measured surface pressures. *Journal of Sound and Vibration*, 78(1):69–117, 1981.

[19] J. E. Ffowcs Williams and L. H. Hall. Aerodynamic sound generation by turbulent flow in the vicinity of a scattering half plane. *Journal of Fluid Mechanics*, 40(4):657–670, 1970.

[20] D. G. Crighton and F. G. Leppington. Scattering of aerodynamic noise by a semi-infinite compliant plate. *Journal of Fluid Mechanics*, 43(4):721–736, 1970.

[21] R. W. Stoker and R. Sen. An experimental investigation of airframe noise using a model scale Boeing 777. In *39th AIAA Aerospace Sciences Meeting & Exhibit*, Reno, 2001.

[22] G. N. Abramovich. *The theory of turbulent jets*. The MIT Press, 2003.

[23] I. Wygnanski and H. Fiedler. Some measurements in the self-preserving jet. *Journal of Fluid Mechanics*, 38:577–612, 1969.

[24] N. R. Panchapakesan and J. L. Lumley. Turbulence measurements in axisymmetric jets of air and helium. Part 1. Air jet. *Journal of Fluid Mechanics*, 246:197–223, 1993.

[25] H. J. Hussein, S. P. Capp, and W. K. George. Velocity measurements in a high-Reynolds-number, momentum-conserving, axisymmetric, turbulent jet. *Journal of Fluid Mechanics*, 258:31–75, 1994.

[26] A. Kolmogorov. The local structure of turbulence in incompressible viscous fluid for very large Reynolds numbers. *Dokl. Akad. Nauk SSSR*, 30(4):301–305, 1941.

[27] W. K. George and R. E. A. Arndt. The self-preservation of turbulent flows and its relation to initial conditions and coherent structures. *Advances in Turbulence*, pages 39–73, 1989.

[28] W. K. George and L. Davidson. Role of Initial Conditions in Establishing Asymptotic Flow Behavior. *AIAA Journal*, 42(3):438–446, 2004.

[29] T. Trüpel. Über die Einwirkung eines Luftstrahles auf die umgebende Luft. *Zeitschrift fur das gesammte Turbinewesen*, 1915.

[30] P. O. A. L. Davies, M. J. Fisher, and M. J. Barratt. The characteristics of the turbulence in the mixing region of a round jet. *Journal of Fluid Mechanics*, 15 (03):337–367, 1963.

[31] M. J. Fisher and P. O. A. L. Davies. Correlation measurements in a non-frozen pattern of turbulence. *Journal of Fluid Mechanics*, 18(1):97–116, 1964.

[32] J. A. B. Wills. On convection velocities in turbulent shear flows. *Journal of Fluid Mechanics*, 20(3):417–432, 1964.

[33] M. J. Lighthill. On sound generated aerodynamically. I. General theory. *Philosophical Transactions of the Royal Society A: Mathematical, Physical and Engineering Sciences*, 211(3):564–587, 1952.

[34] C. L. Morfey. *Dictionary of Acoustics*. Academic Press, 2001.

[35] P. A. Lush. Measurements of subsonic jet noise and comparison with theory. *Journal of Fluid Mechanics*, 46(9):477–500, 1971.

[36] W. A. Olsen, O. A. Gutierrez, and R. G. Dorsch. The effect of nozzle inlet shape, lip thickness and exit shape on subsonic jet noise. NASA TM-X-68182, 1973.

[37] A. M. Karchmer, R. G. Dorsch, and R. Friedman. Acoustic tests of a 15.2-centimeter-diameter potential flow convergent nozzle. NASA TM-X-2980, 1974.

[38] QinetiQ. JEAN static single stream jet noise test report. Technical report, 2003.

[39] J. E. Ffowcs Williams. The noise from turbulence convected at high speed. *Philosophical Transactions of the Royal Society A: Mathematical, Physical and Engineering Sciences*, 255:469–503, 1963. doi: 10.1098/rsta.1963.0010.

[40] N. Andersson. *A study of subsonic turbulent jets and their radiated sound using large-eddy simulation.* PhD thesis, Chalmers University of Technology, Sweden, 2005.

[41] M. J. Fisher, M. Harper-Bourne, and S. A. L. Glegg. Jet engine noise source location: The polar correlation technique. *Journal of Sound and Vibration*, 51: 23–54, 1977.

[42] J. P. Battaner-Moro. A large polar array for full-scale aero-engine noise source location and breakdown. In *12th AIAA/CEAS Aeroacoustics Conference.* AIAA Paper 2006-2652, 2006.

[43] S. A. L. Glegg. *Engine noise source location.* PhD thesis, University of Southampton, 1979.

[44] J. P. Battaner-Moro. Report on automated source breakdown for coaxial and single jet noise measurements. Technical report, ISVR, May 2003.

[45] O. M. Phillips. On the generation of sound by supersonic turbulent shear layers. *Journal of Fluid Mechanics*, 9, 1960.

[46] B. J. Tester and C. L. Morfey. Solving the Lilley equation with quadrupole and dipole sources. *International Journal of Aeroacoustics*, 9(4):419–460, 2010. doi: 10.1260/1475-472X.9.4-5.419.

[47] N. Curle. The influence of solid boundaries upon aerodynamic sound. *Philosophical Transactions of the Royal Society A: Mathematical, Physical and Engineering Sciences*, 231(1187):505–514, 1955.

[48] D. S. Jones. *Generalised functions.* McGraw-Hill, London, 1966.

[49] A. S. Hersh and W. C. Meecham. Sound directivity pattern radiated from small airfoils. *The Journal of the Acoustical Society of America*, 53(2):602–606, 1973.

[50] J. E. Ffowcs Williams and D. L. Hawkings. Sound generation by turbulence and surfaces in arbitrary motion. *Philosophical Transactions of the Royal Society A: Mathematical, Physical and Engineering Sciences*, 264(1151):321–342, 1969.

[51] H. M. Macdonald. Diffraction at a straight edge. *Philosophical Transactions of the Royal Society A: Mathematical, Physical and Engineering Sciences*, 212: 103–105, 1914.

[52] T. Pearcey. *Table of the Fresnel integral to six decimal places.* Cambridge University Press, 1956.

[53] D. M. Chase. Sound radiated by turbulent flow off a rigid half-plane as obtained from a wavevector spectrum of hydrodynamic pressure. *The Journal of the Acoustical Society of America*, pages 1011–1023, 1971.

[54] K. L. Chandiramani. Diffraction of evanescent waves with applications to aerodynamically scattered sound and radiation from unbaffled plates. *The Journal of the Acoustical Society of America*, 55(1):19–29, 1974.

[55] M. R. Fink. Investigation of scrubbing and impingement noise. NASA CR-134762, 1975.

[56] R. L. Underwood and T. H. Hodgson. Aircraft wing trailing-edge noise. NASA CR-164952, 1981.

[57] W. C. Meecham, T. D. Bui, and W. R. Miller. Diffraction of dipole sound by the edge of a rigid baffle. *The Journal of the Acoustical Society of America*, 70(5): 1531–1533, 1981.

[58] S. A. McInerny, W. C. Meecham, T. V. Ngo, and S. C. Liu. Diffraction of a baffled dipole: frequency dependence. *The Journal of the Acoustical Society of America*, 77(5):1713–1715, 1985.

[59] R. K. Amiet. Noise due to turbulent flow past a trailing edge. *Journal of Sound and Vibration*, 47(3):387–393, 1976.

[60] K. Schwarzschild. Die beugung und polarisation des lichts durch einen spalt. I. *Mathematische Annalen*, 55(2):177–247, 1901.

[61] M. S. Howe. A review of the theory of trailing edge noise. *Journal of Sound and Vibration*, 61(3):437–465, 1978.

[62] I. S. Gradshteyn and I. M. Pyzhik. *Table of integrals, series, and products.* Academic Press, 7th edition, 2007.

[63] M. Abramowitz and I. A. Stegun. *Handbook of mathematical functions.* Dover Publications, New York, 10th edition, 1972.

[64] M. Roger and S. Moreau. Back-scattering correction and further extensions of Amiet's trailing-edge noise model. Part 1: theory. *Journal of Sound and Vibration*, 286:477–506, 2005.

[65] R. K. Amiet. Acoustic radiation from an airfoil in a turbulent flow. *Journal of Sound and Vibration*, 41:407–420, 1975.

[66] M. Roger and S. Moreau. Trailing edge noise measurements and prediction for a subsonic loaded fan blade. *AIAA Journal*, 42(3):536–544, 2004.

[67] R. W. Head and M. J. Fisher. Jet surface interaction noise: analysis of farfield low frequency augmentations of jet noise due to the presence of a solid shield. In *3rd AIAA/CEAS Aeroacoustics Conference*. AIAA Paper 1976-502, 1976.

[68] J. C. Yu and C. K. W. Tam. Experimental investigation of the trailing edge noise mechanism. *AIAA Journal*, 16(10):1046–1052, 1978.

[69] K. W. Bushell. Measurement and prediction of jet noise in flight. *AIAA Journal*, 461, 1975.

[70] V. M. Szewczyk. Coaxial jet noise in flight. *AIAA Journal*, 636, 1979.

[71] W. D. Bryce. Experiments concerning the anomalous behaviour of aero-engine exhaust noise in flight. In *5th AIAA/CEAS Aeroacoustics Conference*, 1979.

[72] I. S. Southern. Exhaust noise in flight: the role of acoustic installation effects. In *6th AIAA Aeroacoustics Conference*. AIAA Paper 80-1045, 1980.

[73] D. J. Way and B. A. Turner. Model tests demonstrating under-wing installations effects on engine exhaust noise. In *6th AIAA Aeroacoustics Conference*. AIAA Paper 1980-1048, 1980.

[74] N. N. Reddy and H. K. Tanna. Installation effects on jet noise in flight. In *6th AIAA Aeroacoustics Conference*. AIAA Paper 1980-1044, 1980.

[75] M. E. Wang. Wing effect on jet noise propagation. In *6th AIAA Aeroacoustics Conference*. AIAA Paper 1980-1047, 1980.

[76] J. G. Shearin. Investigation of jet-installation noise sources under static conditions. NASA TP-2181, 1983.

[77] G. SenGupta. Analysis of jet airframe interaction noise. In *8th AIAA Aeroacoustics Conference*. AIAA Paper 1983-0783, 1983.

[78] B. N. Shivashankara and A. M. Blackner. Installed jet noise. AIAA Paper 97-1601, 1997.

[79] C. J. Mead and P. J. R. Strange. Under-wing installation effects on jet noise at sideline. AIAA Paper 98-2207, 1998.

[80] N. N. Pastouchenko and C. K. W. Tam. Installation effects on the flow and noise of wing mounted jets. *AIAA Journal*, 45(12):2851–2860, 2007.

[81] V. G. Mengle. The effect of nozzle-to-wing gulley height on jet flow attachment to the wing and jet-flap interaction noise. In *17th AIAA/CEAS Aeroacoustics Conference*. AIAA Paper 2011-2705, 2011.

[82] A. V. G. Cavalieri, P. Jordan, and Y. Gervais. Scattering of wavepackets by a flat plate in the vicinity of a turbulent jet. In *18th AIAA/CEAS Aeroacoustics Conference*. AIAA Paper 2012-2156, 2012.

[83] A. D. Moore and C. J. Mead. Reflection of noise from aero engines installed under an aircraft wing. In *9th AIAA/CEAS Aeroacoustics Conference*. AIAA Paper 2003-3151, 2003.

[84] A. D. Moore. A 3D prediction of the wing reflection of aero engine noise. In *10th AIAA/CEAS Aeroacoustics Conference*. AIAA Paper 2004-2865, 2004.

[85] J. J. Berton. Noise reduction potential of large, over-the-wing mounted, advanced turbofan engines. NASA TM-2000-210025, 2000.

[86] J. Chappuis, J. Ricouard, and M. Roger. Aft fan noise shielding by a lifting surface: analytical, numerical and experimental results. In *12th AIAA/CEAS Aeroacoustics Conference*. AIAA Paper 2006-2617, 2006.

[87] L. R. Clark and C. H. Gerhold. Inlet noise reduction by shielding for the blended-wing-body airplane. In *5th AIAA/CEAS Aeroacoustics Conference*. AIAA Paper 1999-1937, 1999.

[88] C. H. Gerhold, L. R. Clark, M. H. Dunn, and J. Tweed. Investigation of acoustical shielding by a wedge-shaped airframe. In *10th AIAA/CEAS Aeroacoustics Conference*. AIAA Paper 2004-2866, 2004.

[89] A. Agarwal, A. P. Dowling, H. Shin, W. Graham, and S. Sefi. A ray tracing approach to calculate acoustic shielding by the silent aircraft airframe. In *12th AIAA/CEAS Aeroacoustics Conference*. AIAA Paper 2006-2618, 2006.

[90] P. McLaughlin, R. H. Self, C. J. Powles, C. Wrighton, P. J. R. Strange, and A. D. Moore. High frequency jet noise installation effects for an under wing mounted aircraft. In *14th AIAA/CEAS Aeroacoustics Conference*. AIAA Paper 2008-2997, 2008.

[91] R. P. Young, R. J. Gaeta, and D. Mavris. Development of a prediction method for jet installation noise: reflection/shielding. In *16th AIAA/CEAS Aeroacoustics Conference*. AIAA Paper 2010-3919, 2010.

[92] C. M. Ho and B. Lafouasse. Hydrodynamic pressure field of an axisymmetric jet. In *9th AIAA Aeroacoustics Conference*. AIAA Paper 1984-2316, 1984.

[93] E. Gutmark and C. M. Ho. Near-field pressure fluctuations of an elliptic jet. *AIAA Journal*, 23(3):354–358, 1985.

[94] G. I. Taylor. Statistical theory of turbulence. IV. Diffusion in a turbulent air stream. *Philosophical Transactions of the Royal Society A: Mathematical, Physical and Engineering Sciences*, 151:465–478, 1935.

[95] G. I. Taylor. Statistical theory of turbulence. V. Effect of turbulence on boundary layer. *Philosophical Transactions of the Royal Society A: Mathematical, Physical and Engineering Sciences*, 156:307–317, 1936.

[96] W. Heisenberg. Zur statischen theorie der turbulenz. *Zeitschrift für Physik*, 124: 628–657, 1948.

[97] S. Chandrasekhar. On Heisenberg's elementary theory of turbulence. *Philosophical Transactions of the Royal Society A: Mathematical, Physical and Engineering Sciences*, 200:20–33, 1949.

[98] A. M. Obukhov. Pressure fluctuations in a turbulent flow. *Dokl. Akad. Nauk SSSR, Ser. Geofiz.*, 3:49–68, 1949.

[99] A. M. Yaglom. Acceleration field in a turbulent flow. *Dokl. Akad. Nauk SSSR*, 67:795–798, 1949.

[100] G. K. Batchelor. Pressure fluctuations in isotropic turbulence. *Mathematical Proceedings of the Cambridge Philosophical Society*, 47(02):359–374, 1951.

[101] G. K. Batchelor. *The theory of homogeneous turbulence*. Cambridge University Press, 1953.

[102] E. Inoue. The application of turbulence theory to oceanography. *Journal of Meteorological Society of Japan*, 28:441–456, 1954.

[103] R. H. Kraichnan. Pressure field within homogeneous anisotropic turbulence. *The Journal of the Acoustical Society of America*, 28(1):64–72, 1956.

[104] G. M. Lilley. On the noise from air jets. Technical report, Aeronautical Research Council, Technical Report 20376, 1958.

[105] W. K. George, P. D. Beuther, and R. E. A. Arndt. Pressure spectra in turbulent free shear flows. *Journal of Fluid Mechanics*, 148:155–191, 1984.

[106] R. E. A. Arndt, D. F. Long, and M. N. Glauser. The proper orthogonal decomposition of pressure fluctuations surrounding a turbulent jet. *Journal of Fluid Mechanics*, 340:1–33, 1997.

[107] P. M. Morse and K. U. Ingard. *Theoretical acoustics*. McGraw-Hill, 1968.

[108] M. Harper-Bourne. Jet noise measurements: past and present. *International Journal of Aeroacoustics*, 9(4-5):559–588, 2010.

[109] H. E. Bass, L. C. Sutherland, A. J. Zuckerwar, D. T. Blackstock, and D. M. Hester. Atmospheric absorption of sound: Further developments. *The Journal of the Acoustical Society of America*, 97(1):680–683, 1995.

[110] H. E. Bass, L. C. Sutherland, A. J. Zuckerwar, D. T. Blackstock, and D. M. Hester. Erratum: Atmospheric absorption of sound: Further developments. *The Journal of the Acoustical Society of America*, 99(2):1259, 1996.

[111] L. E. Kinsler, A. R. Frey, A. B. Coppens, and J. V. Sanders. *Fundamentals of acoustics*. John Wiley & Sons, 4 edition, 2000.

[112] J. Bridges and C. A. Brown. Validation of the small hot jet acoustic rig for jet noise research. In *11th AIAA/CEAS Aeroacoustics Conference*. AIAA Paper 2005-2846, 2005.

[113] H. K. Tanna. An experimental study of jet noise part I: Turbulent mixing noise. *Journal of Sound and Vibration*, 50(3), 1977.

[114] G. M. Lilley. *Jet noise classical theory and experiments*. 1991.

[115] J. L. T. Lawrence. Microphone holder reflections. Technical report, 2010.

[116] E. N. Bazley. Sound absorption in air at frequencies up to 100 kHz. Technical report, National Physics Laboratory, Teddington, UK, 1976.

[117] W. D. Bryce and R. A. Pinker. Shear-layer corrections for flight simulation including flight stream temperature effects. Technical report, RAE Noise Note 002/84, 1984.

[118] D. J. Way. On the correction of noise data measured outside an airstream used for flight simulation. Technical report, NGTE Note 1018, 1976.

[119] C. Sondhauss. Ueber die beim ausströmen der luft entstehenden töne. *Annalen der Physik*, 167(2):214–240, 1854.

[120] H. von Gierke. Edge tones from circular gas jets and two-dimensional sheets. *Journal of Applied Mathematics and Physics*, 2:97–106, 1950.

[121] A. Powell. On edge tones and associated phenomena. *Acustica*, 3:233–243, 1953.

[122] A. Powell. On the edgetone. *The Journal of the Acoustical Society of America*, 33(4):395–409, 1961.

[123] G. Neuwerth. Acoustic feedback phenomena of the subsonic and hypersonic free jet impinging on a foreign body. Technical report, NASA, 1974.

[124] E. Evertz, Y. Kloeppel, G. Neuwerth, and A. W. Quick. Noise generated by interaction between subsonic jets and blown flaps. Technical report, Institut für Luft- und Raumfahrt, Aachen, 1976.

[125] A. K. M. F. Hussain and K. B. M. Q. Zaman. The free shear layer tone phenomenon and probe interference. *Journal of Fluid Mechanics*, 87:349–383, 1978.

[126] Y. Umeda, H. Maeda, and R. Ishii. Discrete tones generated by the impingement of a highspeed jet on a circular cylinder. *Physics of Fluids*, 30(8):2380–2388, 1987.

[127] F. R. Wagner. The sound and flow field of an axially symmetric free jet upon impact on a wall. NASA TT-F13-942, 1971.

[128] C. M. Ho and N. S. Nosseir. Dynamics of an impinging jet. Part 1. The feedback phenomenon. *Journal of Fluid Mechanics*, 105:119–142, 1981.

[129] C. C. Landreth and R. J. Adrian. Impingement of a low Reynolds number turbulent circular jet onto a flat plate at normal incidence. *Experiments in Fluids*, 9:74–84, 1990.

[130] C. K. W. Tam and K. K. Ahuja. Theoretical model of discrete tone generation by impinging jets. *Journal of Fluid Mechanics*, 214:67–87, 1990.

[131] I. R. Schwartz. *Basic aerodynamic noise research: a conference held at NASA Headquarters*. Scientific and Technical Information Division, National Aeronautics and Space Administration, Washington D.C., 1969.

[132] G. R. Stegen and K. Karamcheti. Multiple tone operation of edgetones. *Journal of Sound and Vibration*, 12(3):281–284, 1970.

[133] J. P. Woolley and K. Karamcheti. Role of jet stability in edgetone generation. *AIAA Journal*, 12(11):1457–1458, 1974.

[134] S. Ziada and D. Rockwell. Oscillations of an unstable mixing layer impinging upon an edge. *Journal of Fluid Mechanics*, 124:307–334, 1982.

[135] J. Lin and D. Rockwell. Oscillations of a turbulent jet incident upon an edge. *Journal of Fluids and Structures*, 15:791–829, 2001.

[136] J. Lepicovsky and K. K. Ahuja. Experimental results on edge-tone oscillations in high-speed subsonic jets. In *8th AIAA Aeroacoustics Conference*, 1983.